Dynamic Interactions of a Double-stage Photovoltaic Power Converter: Modelling and Control

By

Rabab Y. A. Alsharif

A thesis is submitted for the degree of Doctor of Philosophy
Department of Electronic and Electrical Engineering
Faculty of Engineering
The University of Sheffield

January 2019

Abstract

Photovoltaic (PV) systems are a promising renewable source to achieve green energy targets and be part of the electricity generation. Lots of efforts have been devoted to increase the penetration level of PV systems and its share in the generated electricity. Power quality is one of the challenges that impact the penetration level of PV systems. It is important to ensure high power quality from PV systems to allow more installations to the grid. So, PV power quality issues have to be addressed properly.

It was reported that the poor power quality of the PV systems might be caused by many reasons such as the large amount of PV power fluctuation, the low level of current from the PV system, and large populations of PV inverters. In addition to the aforementioned reasons, recently it was suggested that perturb and observe (P&O) controller is another source of harmonics which result in a deprived PV power quality. This newly reported problem is based on experimental observations without full understanding of the generation mechanism of these harmonics in the PV system, the relation between the P&O controller design and the generated harmonics, and the effect of these harmonics on the rest of the system. Thus, in-depth analysis of the harmonics in PV systems due to P&O controller and a solution to eliminate these harmonics are demanded.

Therefore, in this research an investigation is carried out to explore P&O related harmonics in a double-stage grid-connected PV system. First, regarding the P&O related harmonics full explanation of how harmonics are generated due to the perturbing nature of the P&O controller is provided, a modelling approach is suggested to identify the frequency and the amplitude of the variations in the DC bus due to the P&O controller, the effect of different factors (e.g. weather conditions, system parameters, system operating point, and P&O architecture) on the induced harmonics are investigated. Secondly, regarding the effect of the P&O related harmonics on the rest of the system an intense simulation analysis is provided to explore the possible effect of the P&O related harmonics on increasing the interaction between the system power stages. This can help to set system design recommendations and guidelines such as sizing the dc-link capacitance and designing the system controllers. Finally, a novel mitigation solution is proposed to supress the P&O related harmonics. That can help to reduce the dynamic interaction between system power stages and improve the power quality of the PV system.

Table of Contents

Acknowledgement

First, I would like to thank my supervisor Dr Milijana Odavic for the continuous support of my PhD study. Her guidance helped me in all the time of this research and in writing this thesis. Without her precious support it would not be possible to finish this research.

Besides my supervisor, I would like to thank Prof Kais Attalla, who gave access to his laboratory equipment. Without his help, the practical part of this research would not have been possible to be completed on time.

My sincere thanks also go to Dr Keir Wilkie, Dr Rui Zhao and Dr Essam Hussain, for the stimulating discussions and for sharing their practical experience in the laboratory. I have learned a lot from you and that is very valuable to me.

I would like to thank the laboratory technicians for their help to make sure safe practice in the laboratory.

Thanks to my friend Val for all the love, care and efforts she gave for me and my family during my PhD study and especially during my thesis writing.

Last but not the least; I owe thanks to my husband Kurt for his continued spiritual support and understanding throughout my PhD study. I appreciate my little boys Omar and Eiaz for being my motivation to pursue my dreams. I am the luckiest in the world to have such a lovely family, standing beside me with their love and unconditional support.

Nomenclature

SYMBOL	Description	Unit
K_b	Boltzmann constant (1.38×10^{-23})	-
C_{in}	The input capacitance of the first-stage DC/DC boost converter	F
C_o	The output capacitance of the first stage DC/DC boost converter	F
C_{o_min}	The minimum output capacitance of the first stage DC/DC boost converter for the specified output voltage peak-peak switching ripple	F
C_{out_2}	The output capacitance of the second stage DC/DC boost converter	F
D_k	The duty cycle of an arbitrary SCPVM unit k	-
D_{max}	Maximum duty cycle of the first-stage DC/DC boost converter	-
D_{mppt}	The duty cycle of the maximum power point tracking controller	-
$D_{1\_pair\_i}$	The duty cycle of the first SCPVM unit of an arbitrary pair i	-
$D_{2\_pair\_i}$	The duty cycle of the second SCPVM unit of an arbitrary pair i	-
f_c	Cut-off frequency	H_z
f_g	The grid fundamental frequency	H_z
f_{low}	The lowest harmonic frequency induced by the P&O controller	H_z
f_{low_active}	The lowest harmonic frequency induced by the P&O controller when using the active filter	H_z
f_{MPPT}	The sampling rate of the MPPT controller	H_z
f_n	The frequency of the interharmonics in the grid current	H_z
f_{sw1}	The switching frequency of the first-stage DC/DC boost converter	H_z
f_{sw2}	The switching frequency of the second-stage DC/DC boost converter	H_z
G	Solar irradiation level	W/m^2
$\dot{G}$	The average rate change in solar irradiation inside a time interval of length equal to the sampling period of the P&O controller	$W/(m^2 . s)$
G_{STC}	Solar irradiation level at the standard test conditions	W/m^2
$H_c(s)$	The transfer function of the controller	-
$H_{ci}(s)$	The transfer function of the PI current controller of the cascaded current-voltage controller	-
$H_{cv}(s)$	The transfer function of the PI voltage controller of the cascaded current-voltage controller	-
$H_{i_{l2}d_2}(s)$	The transfer function of duty cycle to inductor current of the second stage converter	-
$H_{i_{scpvm\_out}^G d}(s)$	The duty cycle to SCPVM output current transfer function	-
$H_{v_{dc}d_2}(s)$	The transfer function of the second-stage converter duty cycle to DC-link voltage	-
$H_{v_{dc}i_{l2\_ref}}(s)$	The transfer functions of the reference current-to-dc-link voltage of the second-stage converter	-
I_{grid}	Grid current	A
I_h	The current of h harmonic	A
I_{MPP}	Maximum power point current of the photovoltaic module	A
I_{ph}	Photo-generated current	A
$I_{ph,STC}$	Photo-generated current at standard test condition	A
I_{pv}	Photovoltaic module current	A
$I_{pv\_left}^G$	The PV current at Left MPP and irradiation G	A
$I_{pv\_mpp}^G$	The PV current at MPP and irradiation G	A
$I_{pv\_right}^G$	The PV current at Right MPP and irradiation G	A
I_{sat}	Diode saturation current	A
I_{sc}	Photovoltaic module short circuit current	A
$I_{scpvm\_out\_max}^G$	The maximum value of the SCPVM output current for irradiation G	A
$I_{scpvmk\_out\_max}^G$	The maximum value of the output current of one arbitrary SCPVM unit k under solar irradiation G	A
$I_{scpvm\_out\_min}^G$	The minimum values of the SCPVM output current for irradiation G	A
$I_{scpvmk\_out\_min}^G$	The minimum value of the output current of an arbitrary SCPVM unit k under solar irradiation G	A
$I_{scpvm\_out\_left}^G$	The steady-state value of the SCPVM output current when the PV module operate at the left of MPP	A
$I_{scpvmk\_out\_left}^G$	The steady-state current of an arbitrary SCPVM unit k when the PV module operate at the left of MPP	A
$I_{scpvm\_out\_mpp}^G$	The steady-state value of the SCPVM output current when the PV module operate at MPP and under solar irradiation G	A

$I^G_{scpvmk\_out\_mpp}$	The steady-state output current of an arbitrary SCPVM unit k when the PV module operate at MPP and under solar irradiation G	A
$I^G_{scpvm\_out\_right}$	The steady-state value of the SCPVM output current when the PV module operate at the right of MPP and under solar irradiation G	A
$I^G_{scpvmk\_out\_right}$	The steady-state output current of an arbitrary SCPVM unit k when the PV module operate at the right of MPP and under solar irradiation G	A
$I^G_{1\_pair\_i\_left}$	The steady-state output current of the first SCPVM unit of an arbitrary pair i when the PV module operate at the left of MPP and under solar irradiation G	A
$I^G_{1\_pair\_i\_mpp}$	The steady-state output current of the first SCPVM unit of an arbitrary pair i when the PV module operate at MPP and under solar irradiation G	A
$I^G_{1\_pair\_i\_right}$	The steady-state output current of the first SCPVM unit of an arbitrary pair i when the PV module operate at the right of MPP and under solar irradiation G	A
$I^G_{2\_pair\_i\_left}$	The steady-state output current of the second SCPVM unit of an arbitrary pair i when the PV module operate at the left of MPP and under solar irradiation G	A
$I^G_{2\_pair\_i\_mpp}$	The steady-state output current of the second SCPVM unit of an arbitrary pair i when the PV module operate at MPP and under solar irradiation G	A
$I^G_{2\_pair\_i\_right}$	The steady-state output current of the second SCPVM unit of an arbitrary pair i when the PV module operate at the right of MPP and under solar irradiation G	A
i_{dc}	The instantaneous DC-link current	A
i^G_{pv}	The instantaneous PV module current at solar irradiation G	A
$i^G_{scpvm\_out}$	The instantaneous output current of a single SCPVM unit	A
$i^G_{scpvmk\_out}$	The instantaneous output current of an arbitrary SCPVM unit k	A
$i^G_{1\_pair\_i}$	The instantaneous output current of the first SCPVM unit of an arbitrary pair i	A
$i^G_{2\_pair\_i}$	The instantaneous output current of the second SCPVM unit of an arbitrary pair i	A
j	Total number of system pairs	-
K	Solar cell material constant	A.m^2/W
K_{ii}	Integral current gain of the cascaded controller	-
K_{iv}	Integral voltage gain of the cascaded controller	-
K_{pi}	Proportional current gain of the cascaded controller	-
K_{pv}	Proportional voltage gain of the cascaded controller	-
K_v	Voltage gain of the three-pole-two-zero controller	-
L	Inductance of the first-stage DC/DC boost converter	H
L_{min}	Minimum inductance of the first-stage DC/DC boost converter for a specified current switching ripple	H
L_2	Inductance of the second-stage DC/DC boost converter	H
$M(D)$	Voltage conversion ratio of a DC/DC converter	-
M_p	Maximum overshoot	%
N	An integer (N-1,2,3,… etc.)	-
N_s	Number of series cells in the photovoltaic module	-
n	Total number of SCPVM units	-
P_{pv}	The power of a PV module	W
q	The electronic charge (1.6×10^{-19})	Coulomb
R_s	The series resistance of the equivalent circuit of the solar cell	Ω
R_{sh}	The shunt resistance of the equivalent circuit of the solar cell	Ω
r_{pv}	Dynamic resistance of the photovoltaic module at the linearisation point	Ω
r_{pv_mpp}	Dynamic resistance at the maximum power point	Ω
S_{num}	The number of P&O duty cycle steps	-
SCPVM	Self-controlled photovoltaic module	-
$SCPVM_k$	One arbitrary SCPVM unit k out of n units	-
$SCPVM_{1\_pair\_i}$	The first SCPVM unit of an arbitrary pair i	-
$SCPVM_{2\_pair\_i}$	The second SCPVM unit of an arbitrary pair i	-
T	The control loop gain	-
T_IS	The control loop gain of the second-stage converter with ideal current source.	-
T_NIS	The control loop gain of the second-stage converter with non-ideal	-

	source.	
T_{mppt}	The sampling time of the MPPT controller	Sec.
T_{settle}	Settling time	Sec.
T_{temp}	The junction temperature of the solar cell	°C
V_{dc}	DC-link bus voltage	V
V_{eq}	Equivalent voltage	V
V_{grid}	Grid voltage	V
V_m	The amplitude of the PWM voltage carrier	V
V_{mpp}	Maximum power point voltage of the photovoltaic module	V
V_o	Output voltage of a DC/DC converter	V
V_{oc}	Open circuit voltage of a photovoltaic module	V
V_{pv}	Photovoltaic module voltage	V
V_{pv_left}	The PV module voltage at Left MPP	V
V_{pv_mpp}	The PV module voltage at MPP	V
V_{pv_right}	The PV module voltage at Right MPP	V
V_t	Thermal voltage of the solar cell	V
v_{pv}	The instantaneous PV module voltage	V
x	The perturbed variable of the maximum power point tracking controller	V
Δd	The amplitude of the duty cycle perturbation of the MPPT P&O controller	-
Δi_{dc}	The peak-peak steady-state ripple in the DC-link current without taking into account the peak values of the transient response	A
$\Delta i_{dc\_overall}$	The overall peak-to-peak variation of the dc-link current of n-parallel SCPVM units taking into account the maximum and minimum peaks of the transient response	A
$\Delta i_{dc\_overall}^{uniform}$	the overall peak-peak variation of the DC-link current under unifrom solar irradiation of multi-parallel connected SCPVM units	A
$\Delta i_{dc\_pair\_i}^{uniform}$	the peak-to-peak variation of the total output current of of an arbitrary pair i under uniform solar irradiation	A
$\Delta i_{dc\_pair\_i}^{non\_uniform}$	the peak-to-peak variation of the total output current of an arbitrary pair i under non-uniform solar irradiation	A
$\Delta i_{dc\_overall\_active}^{uniform}$	the peak-peak variation of the dc-link current for j pairs and under uniform irradiation on each pair with the proposed active filter	A
$\Delta i_{k\_ss\_mpp\_to\_left}^{G}$	the left steady-state peak amplitude of an arbitrary SCPVM unit k measured with respect to the desired operating point MPP	A
$\Delta i_{k\_ss\_mpp\_to\_right}^{G}$	the right steady-state peak amplitude of an arbitrary SCPVM unit k measured with respect to the desired operating point MPP	A
$\Delta i_{k\_trans\_right\_to\_max}^{G}$	the right transient peak amplitude measured with respect to the right steady-state values of the output current of an arbitrary SCPVM unit k	A
$\Delta i_{k\_trans\_left\_to\_min}^{G}$	the left transient peak amplitude measured with respect to the left steady-state values of an arbitrary SCPVM unit k	A
Δi_{L_pp}	Peak to peak inductor current ripple	A
$\Delta i_{scpvm\_out\_ss}^{G}$	Peak-peak amplitude of the steady-state variation of the SCPVM output current without taking into account the peak values of the transient response	A
$\Delta i_{scpvm\_out\_overall}^{G}$	The overall variation of the SCPVM output current taking into account the maximum and minimum peaks of the transient response	A
$\Delta i_{1\_pair\_i\_ss\_mpp\_to\_left}^{G}$	The steady-state peak amplitude of the first unit of an arbitrary pair i when the PV operate at Left MPP	A
$\Delta i_{1\_pair\_i\_ss\_mpp\_to\_right}^{G}$	The steady-state peak amplitude of the first unit of an arbitrary pair i when the PV operate at Right MPP	A
$\Delta i_{2\_pair\_i\_ss\_mpp\_to\_left}^{G}$	The steady-state peak amplitude of the second unit of an arbitrary pair i when the PV operate at Left MPP	A
$\Delta i_{2\_pair\_i\_ss\_mpp\_to\_right}^{G}$	The steady-state peak amplitude of the second unit of an arbitrary pair i when the PV operate at Right MPP	A
Δx	The amplitude of the perturbation applied to the control variable x	
ω_n	The natural frequency	rad/sec
ω_o	The second-stage double pole frequency	
$\omega_{p1}\ and\ \omega_{p2}$	The frequency of the poles of the three-pole-two-zero controller	rad/sec
$\omega_{z1}\ and\ \omega_{z2}$	The frequency of the zeros of the three-pole-two-zero controller	rad/sec
μ	The static gain of a second order system	-
μ_0	The DC gain of the duty cycle-to-input voltage transfer function of the DC/DC boost converter	-

η	Diode quality factor	-
η_{MPPT}	MPPT controller efficiency	%
ζ	Damping ratio	-

Abbreviation

Abbreviation	Description
CC	Constant Current
CV	Constant Voltage
FFT	Fast Fourier Transform
IS	Ideal Source
MPP	The maximum power point of the PV module
NIS	Non ideal source
PI	Proportional integral controller
PM	Phase margin
P&O	Perturb and Observe
PQ	Power quality
RHP	Right half plane zero
SCPVM	Self-controlled photovoltaic module
STC	Standard test conditions
3P2Z	Three-poles-two-zeros controller

1 INTRODUCTION

1.1 Background

The world is facing environmental and energy challenges: such as how to deal with climate change and energy security. Burning fossil fuel is one of the main reasons of global warming which causes climate change on the earth resulting in environmental and socio-economic difficulties. Many countries around the world follow policies to reduce greenhouse gases. At the same time, economic growth needs electricity which relies mainly on fossil fuels. The problem of using fossil fuels is not only related to the increasing emission of greenhouse gases, but also the fact that fossil fuel resources are depleting. These challenges make using renewable resources in generating electricity all the more urgent and require swift actions from governments and industry. Renewable energies are inexhaustible and clean (no emissions in the generation of electricity). It will make a significant contribution in reducing the creation of greenhouse gases and decreasing the depletion rates of fossil fuels. Therefore, governments try to achieve targets in generating energy from clean resources such as wind, photovoltaic (PV), fuel cells, geothermal and hydro energies. On the other hand, there are some challenges to overcome and manage when connecting distributed generators to the grid such as synchronisation with the main power network, harmonics and subharmonics, voltage rise, voltage flicker, circulating current, the instability of the main network caused by increasing the number of the connected distributed generations, power quality and efficiency.

Microgrids (AC and DC microgrids) were proposed as a new paradigm in order to deal with some of the aforementioned problems. Microgrids allow connecting distributed generation sources efficiently and avoid the problems of small and low voltage distributed generation sources such as PV when connecting it to the main power network [1, 2]. Adopting AC microgrid, where the distributed generation sources and loads are connected together through an AC bus, has solved many problems (e.g. circulating current, reactive power flow, and synchronisation) and remarkable research has been made to improve its performance [3-7]. However, power quality is still an issue in AC microgrid especially for those with sensitive power loads (e.g. power electronic and microprocessor based loads).

As shown in Figure 1 PV has experienced a huge growth in the last few years due to the increasing of efficiency and reducing the cost per watt [8]. The cost (in US dollars)

per watt of utility scale PV has decreased from 4.57$/W in 2010 to 1.03$/W in 2017 (see Figure 2, [9]) and the efficiency has increased from 13.8% in 2010 to 17.5% in 2016 for commercial PV module (see Figure 3, [9]).
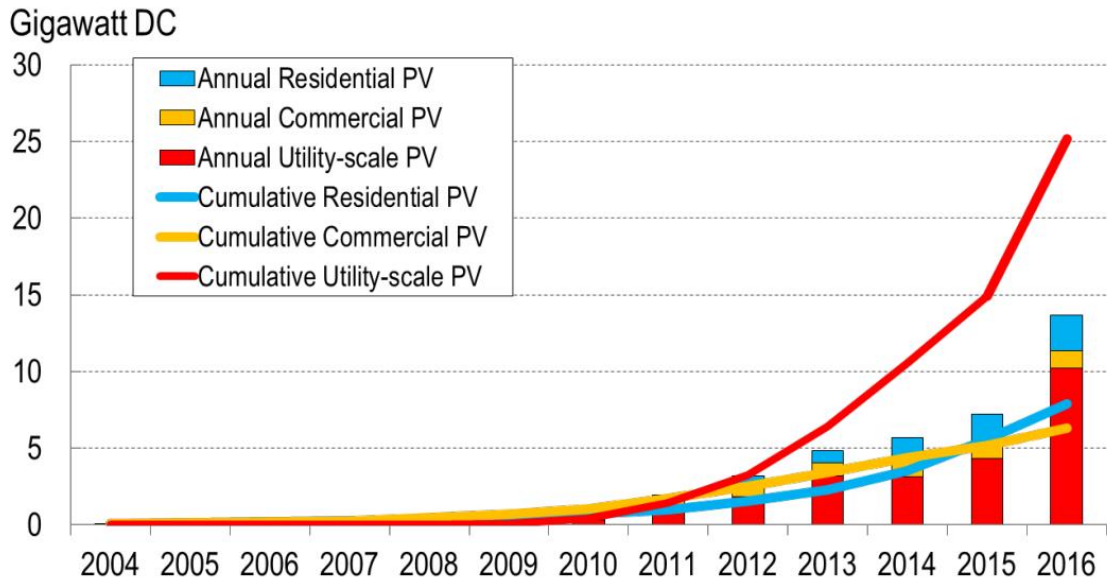

Figure 1: PV market growth in USA. 2004 – 2016 [9]
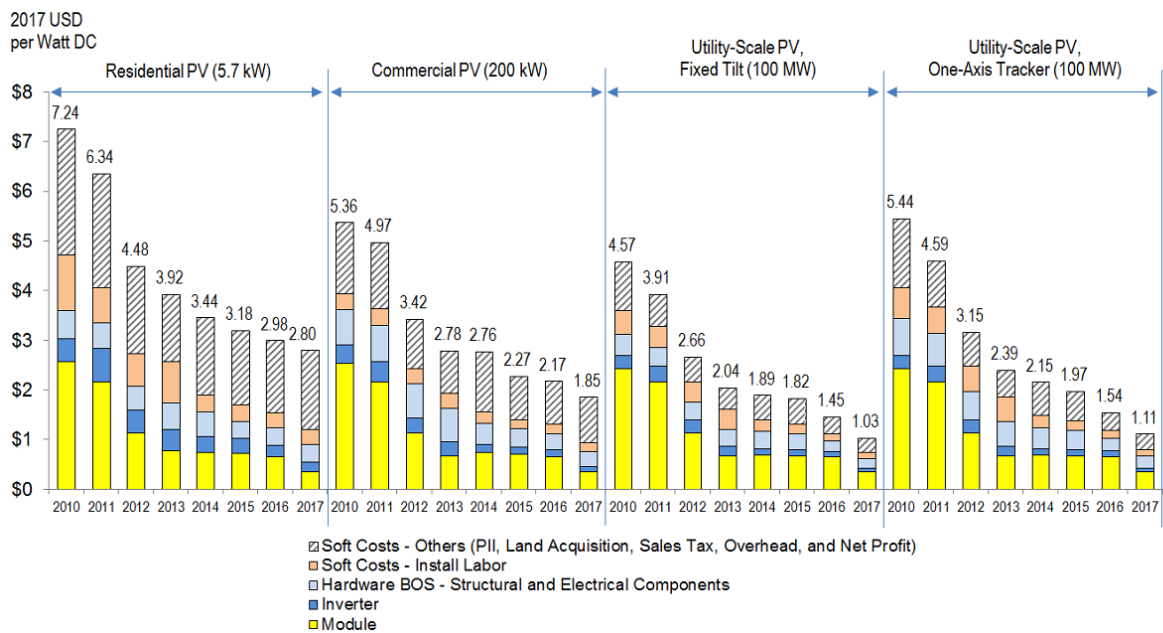

Figure 2: PV system cost benchmark summary in USA, 2010 – 2017 [9]
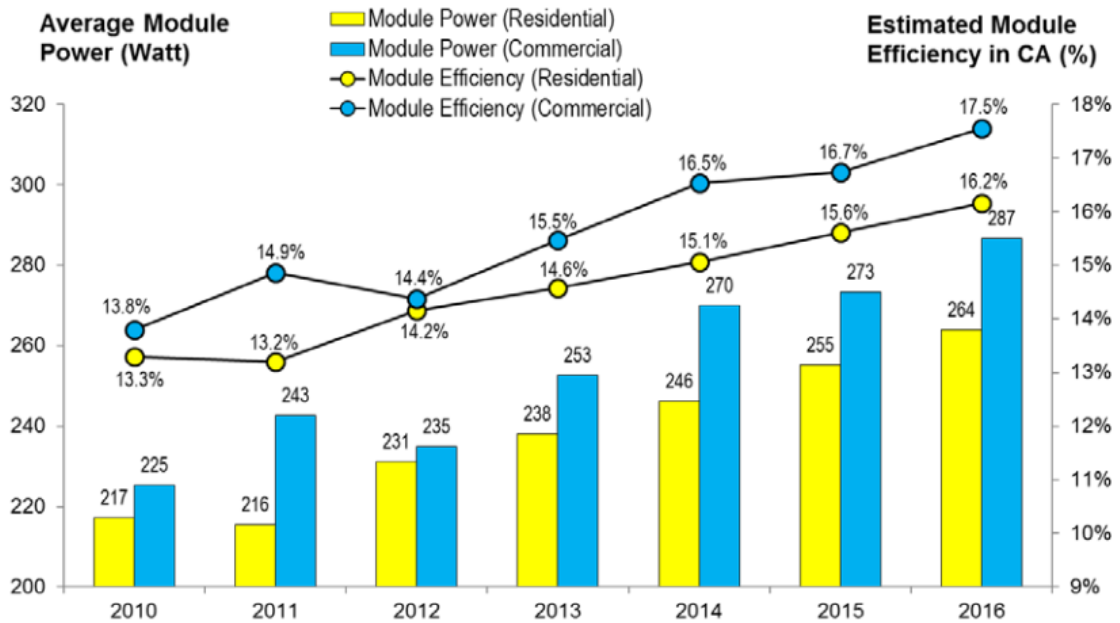
Figure 3: Module power and efficiency trends from the California NEM database, 2010–2016 [9]

Therefore, the effect of a PV system connected to an AC bus (e.g. AC microgrid) on the power quality has gained a high interest in recent studies. PV system can be interfaced in to grid through a single-stage converter or a double-stage converter as shown in Figure 4. Under mismatch phenomena due to shading from clouds or nearby building, dirt from dusty weather, manufacturing tolerances, PV module age, etc, the global MPP can be at the lower voltages than the normal MPP. In case of double-stage converter having a converter for MPPT tracking between the PV arrays and the grid converter (e.g. DC/AC converter) allows wider operating range of the PV voltage. Therefore, maximum power can be extracted at lower voltage than in the case of single-stage converter, where the PV voltage (v_{pv}) is constrained by the grid voltage as shown in Figure 4.

It has been reported that inverter based grid-connected PV systems are one of the sources which deliver harmonics to the grid [10-15]. It was found that harmonics increase due to large populations of PV inverters [10, 11], resonance between the power network and the PV inverter [10, 15], switching harmonics and its sidebands [11], in phase unwanted harmonics generated by multiple parallel connected PV inverters [11], low level of current fed by PV systems [12, 13], PV inverters operate with non-unity power factor (PF) for providing ancillary services (e.g. Volt-VAR control and PF-Watt control) [12], poor performance of the grid current synchronisation method in single-phase inverters [12], large amount of PV power fluctuations [12, 15],

impedance-based interactions especially when a PV system is connected to a weak grid [14], or Maximum Power Point Tracking (MPPT) controller as was observed recently in [16-18].
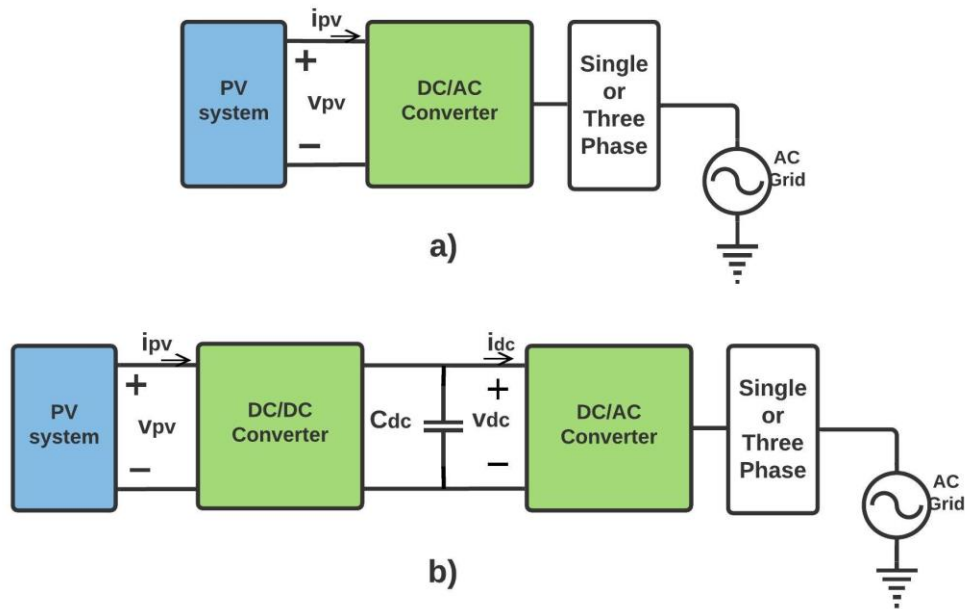
Figure 4: PV system interfaced in to grid (a) single-stage converter (b) double-stage converter

The author of [19] proposed what is a so-called 'DC type quality control centre' as a possible configuration to meet the needs of customers power quality. The configuration of their network is what is known today as DC microgrid, where the distributed generation sources and loads are connected together through a DC bus. A general structure of a DC microgrid is shown in Figure 5. DC microgrid has been recognised not only for high power quality but also for many other advantages such as small system size, high efficiency, a simple control system, and is compatible with DC output type distributed generation sources such as a PV source [20-27]. In DC microgrid there is no need for reactive power flow control, frequency regulation, and synchronisation control. Thus, unlike AC microgrid power quality issues due to a PV system that operates with a non-unity power factor and deprived performance due to a poor grid current synchronisation method are non-existent. Nevertheless, poor power quality in PV systems connected to a DC bus still may arise due to other issues such as large fluctuations in PV power, interaction between system power stages, or harmonics induced by MPPT controller as was observed in the case of a PV system connected to an AC bus.
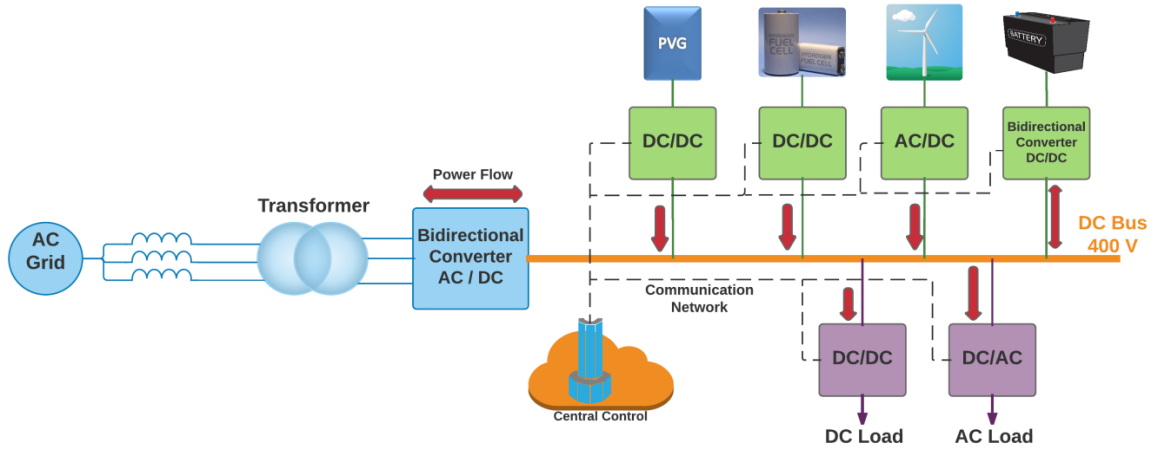
Figure 5: General structure of a DC microgrid

The poor power quality in PV systems due to MPPT controller, which is based on a perturbation technique such as P&O, is newly reported in the literature. It has been observed that harmonics are induced in a double-stage PV system connected to a DC bus (e.g. DC microgrid) due to the P&O controller which leads to a poor power quality as has been published in our papers [28, 29]. In parallel, the same observations were reported in other studies [16-18, 30, 31] which show interharmonics in grid-connected PV inverters due to the P&O controller. The analysis in [16-18] is based on experimental observations where the origin of the harmonics is suggested to be from the MPPT P&O controller. Although the aforementioned studies highlighted the origin of the interharmonics, still some issues are unclear and have not been investigated such as the generation mechanism of the P&O related harmonics, the effect of the P&O controller parameters on the characteristics of the harmonics, and the influence of these induced harmonics on the rest of the system.

Contrast with the analysis in [16-18] our published work in [28] demonstrates through simulation that the harmonics in the dc-link and grid currents increase due to the perturbing behaviour of the P&O controller in steady-state. In addition to that, it was shown that under specific operating conditions the interaction between the system stages increases due to the P&O related harmonics and that has been taken into account in designing the controller of the second-stage converter in the double-stage PV system. In another paper we published [29], the P&O related harmonics is expressed as a function of the P&O parameters (sampling period (T_{mppt})) and number of perturbation steps in steady-state) and it was shown that for optimal three duty-cycle steps operation the lowest harmonics frequency induced by the P&O controller is $f_{low} = 1/(4T_{mppt})$.

[31] is the latest research published in 2018 which is investigating the impact of the P&O controller on increasing the harmonics in a single phase grid-connected PV inverter. The frequency and the amplitude of the P&O related interharmonics in the grid current are expressed as a function of the P&O controller parameters (the sampling period and the perturbation step size). It was found that the perturbation step size of the P&O controller has a strong effect on the amplitude of the interharmonics components. While the sampling period affects both the amplitude and the frequency of the interharmonics. The findings in [30, 31] for single phase grid-connected PV inverter is in line with our simulation analysis in [28, 29] for a double-stage PV system connected to a main DC bus. In addition to that, our studies in [28, 29] provide an insight to the effect of the solar irradiation level and the dc-link capacitance size on the level of the P&O related harmonics and on the interaction between the system stages.

P&O technique is widely used in commercial products because of its low-cost implementations and simplicity which make the newly reported P&O related power quality problem a subject undergoing intense study and researchers are persuaded to find a solution. The first steps to do that is by understanding how the P&O harmonics are generated, identifying the factors that affect the P&O related harmonics, and assessing the effect of the P&O related harmonics on the rest of the system. To the best of our knowledge, only the generation mechanism of the P&O related harmonics is well covered in the literature through our research in [28, 29] and the studies in [30, 31]. With regard to the factors that affect the P&O related harmonics, the effect of the P&O parameters is well understood from [29-31]. However, other factors can affect the P&O related harmonics such as the solar irradiation level, the PV module operating region, and the adopted PV system configuration. Finally, the effect of the P&O related harmonics on the rest of the system has not yet been investigated in the literature. only brief simulations have been provided in our research paper in [28].

In addition to above, as the poor power quality in the PV system due to the P&O controller is only recently reported in the literature, there is no specific solution proposed.

1.2 Research Motivation

As discussed above, in order to improve the power quality of grid-connected PV systems several areas still need to be properly investigated such as identifying all factors that influence the P&O related harmonics and the effect of the P&O related

harmonics on the rest of the system. This will help to set system design recommendations to ensure minimum effect of the P&O related harmonics on system power quality and stability. That also will help to develop proper solutions to supress or eliminate these harmonics. With the improved PV system power quality more PV system can be connected to the grid and that will help meeting the targets in reducing the emission of greenhouse gases.

Thus, in this research an investigation is carried out to explore P&O related harmonics in a double-stage PV system connected to a DC bus. First, regarding the P&O related harmonics, a full explanation of how harmonics are generated due to the P&O controller is provided. A modelling approach is also provided to identify the harmonics frequency and the amplitude of the dc-link voltage and current variations. The effect of different factors such as weather conditions, system parameters, system operating point and P&O architecture on the induced harmonics is investigated as well. Secondly, regarding the effect of the P&O related harmonics on the rest of the system, an intense simulation analysis is carried out to explore the possible effect of the P&O related harmonics on increasing the interaction between the system power stages. Finally, a novel mitigation solution is proposed to supress the harmonics that are induced by the parallel-connected distributed P&O controller in the double-stage PV system. This will help to reduce the dynamic interactions between system power stages, improve the efficiency and power quality of the PV system.

1.3 Research Aim and Objectives

1.3.1 Aim

Investigate the dynamic interactions in a double-stage DC/DC PV system due to P&O related harmonics.

1.3.2 Objectives

The objectives of this PhD research can be summarised as follow:

1) Identify and analyse the impact of a P&O controller on the power quality of a double-stage DC/DC PV system.

2) Provide a procedure to predict the frequency and the amplitude of the dc-link current variation as a function of P&O parameters, solar irradiation level, and

the total number of parallel connected self-controlled PV modules (i.e. PV module with a dedicated MPPT converter).

3) Investigate the effect of the distributed P&O architecture and synchronisation between the distributed P&O controllers on power quality.

4) Explore the effect of the P&O related harmonics on increasing the dynamic interaction between system power stages in a double-stage DC/DC PV system.

5) Propose a solution to mitigate the harmonics induced by the P&O controller to improve the system's power quality and efficiency, and reduce the dynamic interaction between system stages in a double-stage DC/DC PV system.

6) Provide an experimental validation of the generated harmonics in the system due to the P&O controller, the proposed mitigation method, and the dynamic interactions between the system stages of the double-stage DC/DC PV system.

1.4 Thesis outline

This research is divided as follow:

Chapter 2: this chapter includes reviews on the PV source characteristics, maximum power point techniques, grid-connected PV system configurations in AC and DC microgrids, controller structure for grid-connected DC/DC PV systems, and the power quality of grid-connected PV systems. In addition to that, possible mitigation methods of P&O related harmonics are discussed.

Chapter 3: this chapter includes the adopted system configuration, system design considerations, controller design, and simulation results for the designed system.

Chapter 4: this chapter provides a procedure to predict P&O related harmonics in a PV system connected to a DC bus. The analysis includes investigating the effect of the following factors on the harmonics frequency and amplitude: (I) the P&O sampling period and the P&O perturbations step size, (II) solar irradiation level, (III) the non-linear characteristic of the PV source, (IV) the total number of parallel connected self-controlled PV modules, and (V) the synchronisation between the distributed P&O controllers

Chapter 5: through simulations analysis, this chapter explores the effect of the P&O related harmonics on the performance of a PV system that consists of a double-stage DC/DC boost converter connected to a DC bus. The dynamic interaction between the first stage; which consists of a PV module and its dedicated MPPT converter, and the second-stage dc-link voltage controller is analysed. The impact of the P&O controller on designing the second-stage controller is addressed. Also, this chapter investigates the effect of the controller parameters values (i.e. design specifications), the dc-link capacitance (C_{dc}) size, and the solar irradiation level on increasing the dynamic interaction between the system power stages.

Chapter 6: in this chapter a novel system-level controller named as "active filter" is proposed to reduce the progression of the P&O related harmonics into the dc-link bus and as a consequence improve the efficiency and power quality of the overall system.

Chapter 7: in this chapter experimental verification is provided to show the dynamic interactions in double-stage PV system due to P&O related harmoncis and to validate the proposed controller to supress P&O related harmonics.

Chapter 8: in this chapter the outcomes of this research, main contributions, and research prospective are summarised.

1.5 List of Publications

- R. Alsharif and M. Odavic, "Photovoltaic generators interfacing a DC micro-grid: design considerations for a double-stage boost power converter system," in *2016 18th European Conference on Power Electronics and Applications (EPE'16 ECCE Europe)*, 2016, pp. 1-10. (see Appendix A).

- R. Alsharif, M. Odavic, and K. Atallah, "Active suppression of photovoltaic system related harmonics in a DC microgrid," in *2017 IEEE Energy Conversion Congress and Exposition (ECCE)*, 2017, pp. 1594-1601. (see Appendix B).

2 LITERATURE REVIEW

2.1 Abstract

Currently there is a high concern about producing clean energy. Governments try to achieve targets in generating energy from clean resources such as wind, photovoltaic (PV) generator, fuel cell, geothermal, and hydro energies. Among these resources, PV has experienced the huge growth in the last few years due to the increasing of efficiency and reducing the cost per watt [8, 9]. Table 1 provide the Levelised Cost of Electricity (LCOE) for different energy sources technology [32].The LCOE is used to compare different energy sources technologies and it represents the total cost to build and operate a new power plant over its life divided to equal annual payments and amortized over expected annual electricity generation. It takes into account all the costs including initial capital, return on investment, continuous operation, fuel, and maintenance, as well as the time required to build a plant and its expected lifetime. It also takes into account carbon capture and sequestration. Table 1 show that the solar PV power plant is the second lowest cost energy source per watt compared with other energy technologies. This makes the PV a promising renewable source to achieve green energy targets and be part of the electricity generation.

Table 1: LCOE for different energy technologies[32]

Power Plant Type	Cost (LCOE) $/kW-hr
Nuclear	0.093
Wind onshore	0.059
Wind offshore	0.139
Solar PV	0.063
Solar Thermal	0.165
Geothermal	0.045
Biomass	0.095
Hydro	0.062

This chapter reviews the following: I) the electrical characteristics, equivalent circuit, and linearisation of a non-linear PV source; II) the most popular control techniques used for tracking the maximum power from a PV system; III) the configuration and topologies of grid-connected PV system in both AC and DC microgrids; IV) local control structures of the PV interface converter in microgrids such as voltage, current and droop control; V) and finally the effect of grid-connected PV system on power quality.

2.2 Photovoltaic Generator

2.2.1 Electrical characteristics and equivalent non-linear circuit

It is important to study the main electrical components of the PV cell in order to design a model that can be used in simulations tests for predicting the energy produced by PV, evaluating the converter performance, assessing power quality and testing control algorithms. The equivalent circuits of the PV generators proposed in the literature are categorised into two types: double diode model [33] and single diode model [34-37] as shown in Figure 6. The current-voltage characteristic for single diode model can be expressed by (2.1) [38]. For the double diode model, an additional current term shall be added to represent the second diode.
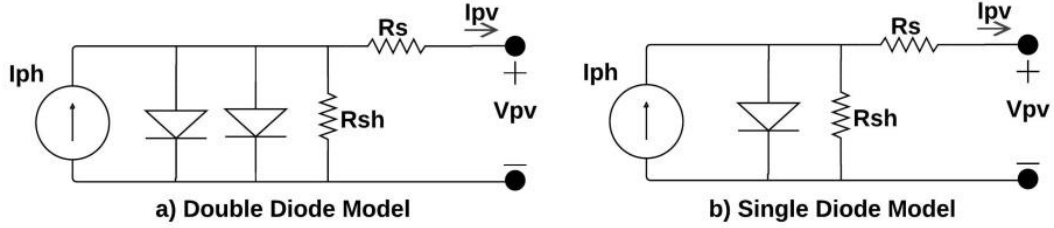

Figure 6: Equivalent non-linear circuit of solar cell (a) double diode (b) single diode model.

$$I_{pv} = I_{ph} - I_{sat} \cdot \left(e^{\frac{V_{pv} + I_{pv} \cdot R_s}{N_s \cdot \eta \cdot V_t}} - 1 \right) - \frac{V_{pv} + I_{pv} \cdot R_s}{R_{sh}} \tag{2.1}$$

where V_{pv} and I_{pv} are the Photovoltaic module voltage and current, respectively; I_{ph} is the photo-generated current (given in (2.2)); I_{sat} is the diode saturation current (I_{sat} is a measure of the "leakage" of carriers across the p-n junction in reverse bias.); R_s (given by (2.3)) and R_{sh} (given by (2.4)) are the series and shunt resistances, respectively; N_s is the number of series cells in the module; η is the diode quality factor (1.2 for monocrystalline solar panel) (η is a fitting parameter that describes how closely the diode's behavior matches that predicted by theory, which assumes the p-n junction of the diode is an infinite plane and no recombination occurs within the space-charge region); V_{oc} is the PV module open circuit voltage; I_{sc} is the PV module short circuit current; and V_t is the thermal voltage and given by ((2.5)), where K_b is Boltzmann

constant (1.38×10^{-23}), T_{temp} is the junction temperature, and q is the electronic charge (1.6×10^{-19}) coulomb.

$$I_{ph} = I_{ph,STC} \frac{G}{G_{STC}} \left[1 + \alpha_1 (T_{temp} - T_{temp,STC}) \right]$$

$$\alpha_1 = \left. \frac{dI_{pv}}{dT_{temp}} \right|_{STC} \quad (2.2)$$

$$R_s = - \left. \frac{dV_{pv}}{dI_{pv}} \right|_{V_{pv}=V_{oc}} - \frac{1}{I_{sat} \cdot \dfrac{q}{\eta.k.T_{temp}} e^{\frac{q.V_{oc}(T_{temp})}{\eta.k.T_{temp}}}} \quad (2.3)$$

$$R_{sh} = - \left. \frac{dV_{pv}}{dI_{pv}} \right|_{I_{pv}=I_{sc}} \quad (2.4)$$

$$V_t = \frac{K_b.T_{temp}}{q} \quad (2.5)$$

Electrical characteristics at standard test conditions (STC) cannot be usually measured. So, PV modelling tends to use data that provided by the module manufacturers. Normally, the manufacturer provides four values: the short circuit current I_{sc}, open circuit voltage V_{oc}, operating voltage and current at maximum power point (V_{mpp}, I_{mpp}). These four known values do not provide enough information to solve the five unknown parameters in a single-diode model which are I_{ph}, I_{sat}, η, R_s and R_{sh}. One possible solution is to fix one parameter value, e.g. the diode quality factor η or the shunt resistance [8], and solve the remaining parameters accordingly. In the double diode model the number of the unknown parameters increase with the additional current term for the second diode and that requires assuming more parameters which reduce its accuracy [8]. Moreover, the high-order model as double diode model is very sensitive to the selection of initial conditions, and failing in it may lead to the reduction of model accuracy. The double diode model requires generally more pre-assumed parameters and iterative tuning cycles than the single diode model parameterisation, because if the initial condition is not correctly selected, the accuracy of the double diode model will be low.

The single diode model is more popular than the double diode model. It is less complex since the number of the unknown parameters is lower. This makes it easier to be solved and more accurate with the least number of pre-assumed parameters. For this reason the single diode model is adopted in this research work.

Figure 7 and Figure 8 show the effect of solar irradiation level (G) and temperature (T_{temp}) on the current-voltage characteristic curve, respectively. There are three practical points to highlight on the current-voltage curve which are: short circuit current (I_{sc}), Maximum Power Point (MPP), and open circuit voltage (V_{oc}). These three points are illustrated in Figure 7 and Figure 8.
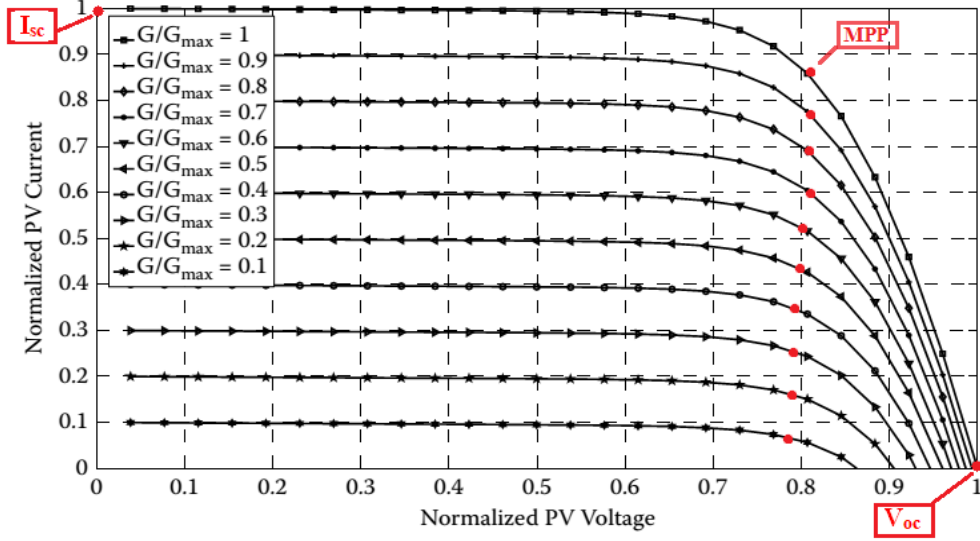
Figure 7: Effect of solar irradiation G on the PV current-voltage characteristic [38].
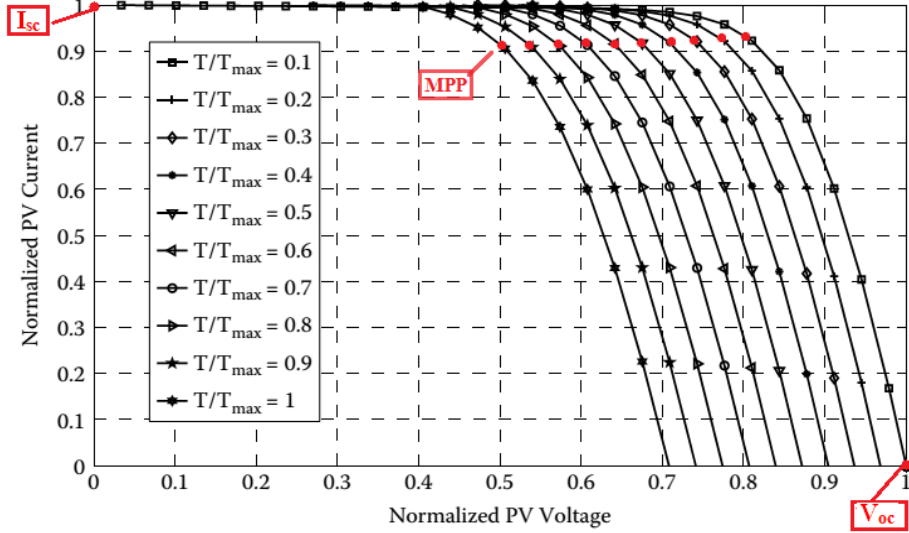
Figure 8: Effect of temperature on the PV current-voltage characteristic [38].

2.2.2 Equivalent linear model

The linear model of the PV is important for designing the system controllers, simplifying the analytical analysis of the effect of the PV source on the power electronic interfaced converter, and for the small signal analysis. A linear model of the PV is proposed in [39-41] which is described by the slope of the current-voltage curve at the linearisation point (e.g. MPP). The model is presented as a dynamic resistance (r_{pv}) connected in series with an equivalent voltage source $V_{eq} = V_{pv} + I_{pv} \cdot r_{pv}$ as shown in Figure 9. The PV current-voltage characteristic equation in (2.1) can be simplified to (2.6) as shunt resistance is assumed to be so high that it can be neglected. At the steady

state conditions both the solar irradiation and the cell temperature are constant which means that I_{ph} and I_{sat} are constant. Differentiating (2.6) and rearranging gives r_{pv} which is given by (2.7).

$$I_{pv} = I_{ph} - I_{sat} \cdot \left(e^{\frac{V_{pv} + I_{pv}.R_s}{N_s.\eta.V_t}} - 1 \right)$$ (2.6)

$$r_{pv} = \frac{\partial v_{pv}}{\partial i_{pv}} = \frac{-N_s.\eta.V_t - I_{sat}R_s \, e^{\frac{V_{pv} + I_{pv}R_s}{N_s.\eta.v_t}}}{I_{sat} \, e^{\frac{V_{pv} + I_{pv}R_s}{N_s.\eta.V_t}}}$$ (2.7)

From (2.7) it is clear that r_{pv} is a function of the PV voltage (V_{pv}), solar irradiation and temperature. Solar irradiation varies the value of I_{pv}. The cell temperature can vary the values of V_t, I_{sat}, and R_s. The rest of the research will focus on the influence of the irradiation and the PV module voltage on the dynamic resistance but not the temperature because during the day time the variation in the temperature is very slow [38].

The dynamic resistance for NU-E240 PV module [42]; its specifications are given in Table 2, under different V_{pv} and solar irradiation levels is shown in Figure 10. The lower the solar irradiation and/or the V_{pv}, the higher the r_{pv} becomes.

2.2.3   PV modelling for simulation studies

For this research work the model in [37] was chosen, since it is an accurate, simple and easy to be modified for implementing different PV modules.

The solar cell is modelled based on the Shockley diode equation with single diode solar cell for moderate complexity as shown in Figure 6.b. The model includes temperature dependent photo current (I_{ph}), diode saturation current (I_{sat}) and series resistance (R_s) but not a shunt resistance (R_{sh}). The shunt resistance is assumed to be so high that it can be neglected for simplifying the model. The model generates the output current from a selected PV panel depending on the weather data (solar irradiation (W/m^2) and temperature (°C)), the PV panel manufacturer's parameters, and the connected load. As shown in Figure 11 the PV model is implemented using a controlled current source and the control signal of the current source is computed based on (2.6). For connecting the PV model in Figure 11 to a DC/DC boost converter in simulink environment a capacitor is used at the output terminal of the current source.
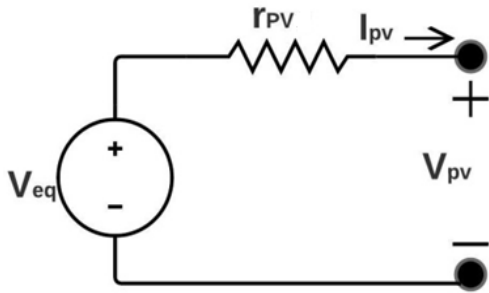
Figure 9: PV equivalent linear circuit.

NU-E240 (J5)	
Number of cells in series (N_s)	60
Maximum power	240 Wp
Open circuit voltage	37.3 V
Short circuit current	8.62 A
Standard operation condition temperature	25 °C
Maximum power point voltage (V_{mpp}^{STC})	29 V
Maximum power point current (I_{mpp}^{STC})	8.15 A
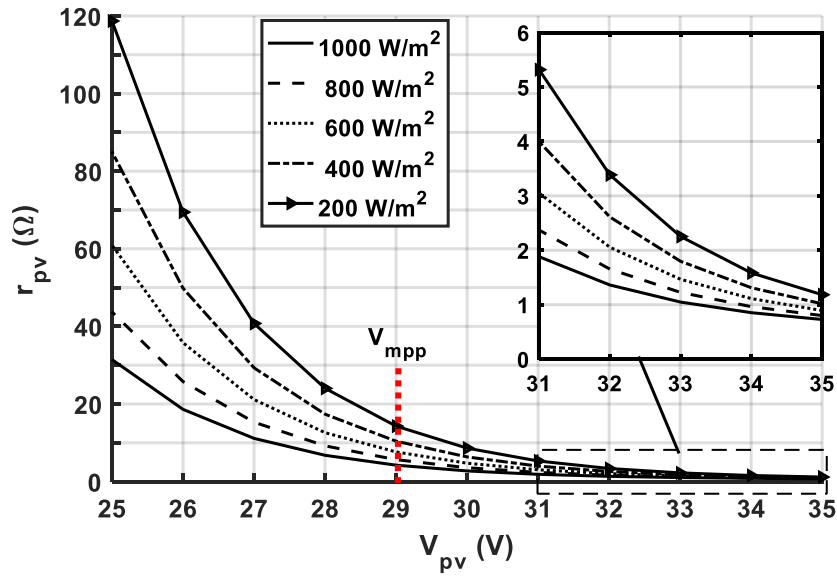
Figure 10: The dynamic resistance of NU-E240 PV model.

$$Equ.\,(2.6)$$
$$Ipv = f(Vpv, G, T, PVparameters)$$
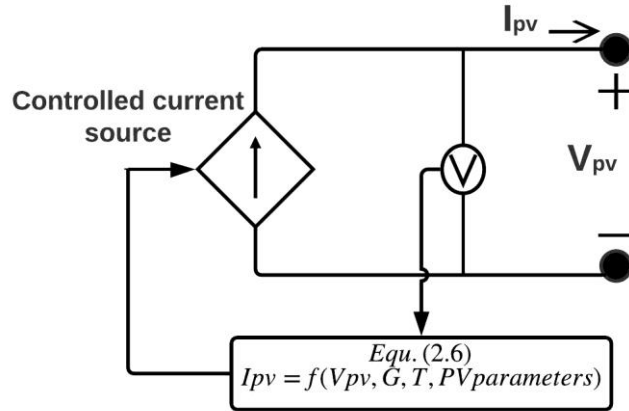
Figure 11: PV model.

2.3 Maximum Power Point Tracking Control

It is desired that PV operates at the maximum power point (MPP) to maximise the harvested power from a PV system. The maximum power point of the PV is a time-variant and depends on the operating conditions such as the uncontrollable weather conditions (i.e. solar irradiation and temperature) and on the connected load, so it is necessary to track the MPP continuously [43]. As a consequence, it is mandatory to use a converter stage between the PV array and the load/grid as the converter is capable of controlling its input voltage level to match the PV array MPP in the presence of time varying operating conditions.

A maximum power point tracking (MPPT) controller is employed to adjust the switching converter duty cycle to follow the MPP for whatever operating conditions. Different methods of MPPT have been addressed in the literature: examples of perturb and observe (P&O) [38, 39], adaptive step size P&O [44], incremental conductance (INC), hill climbing, particle swarm optimisation, the extremum seeking and ripple correction techniques [38, 43]. Under different operating conditions, the MPPT controller regulates either the voltage or the current to a value that gives the MPP. The current of MPP (I_{MPP}) is changing significantly with the solar irradiation (see Figure 7). Nevertheless, solar irradiation only slightly varies the voltage of MPP (V_{MPP}). Observing the effect of the temperature from Figure 8, it illustrates that the temperature is affecting V_{MPP} significantly but not I_{MPP}. The fact that during the day time the variation in solar irradiation is very high while the temperature is changing slowly and within certain limits makes controlling V_{MPP} possible and easier than I_{MPP}. V_{MPP} is

almost constant under different solar irradiation and it changes only with the temperature which has a very slow dynamic. That is why most of the researches such as [38, 40, 41, 45] prefer to control the PV voltage.

The most popular MPPT techniques will be reviewed in this section. Also, two different MPPT architectures which are used in the literature will be discussed.

2.3.1 Maximum power point tracking techniques

2.3.1.1 Fractional Open Circuit Voltage

The fraction open circuit voltage is one of the earliest and simplest proposed MPPT methods. It is based on approximating the MPP of the PV system as 76% of the open circuit voltage of the PV system [38, 46]. The drawback of this technique is that the MPP is not always at 76% of the open circuit voltage and keeping it unchanged under different solar irradiation levels and/or temperatures leads to very poor system efficiency.

2.3.1.2 Perturb and Observe (P&O)

2.3.1.2.1 P&O operation

The Perturb and Observe (P&O) method is the most popular technique for its simplicity and low cost. Basically the operation of P&O depends on a small perturbation injected to the system to drive the operating point toward the MPP. The PV operating point is perturbed periodically by changing the voltage at PV source terminals, and after each perturbation, the power generated by the PV before and after the perturbation are compared. If after the perturbation the PV power has increased, this means that the operating point has been moved toward the MPP; thus the following perturbation imposed to the voltage will have the same sign as the previous one. If after the perturbation the PV power has decreased, this means that the operating point has been moved away from the MPP. Therefore the next perturbation will have opposite sign of the previous one [38].

The PV operating points due to the P&O controller are shown in Figure 12. The P&O algorithm can be described using the following general equation [38]:

$$x[(k+1)T_{mppt}] = x[kT_{mppt}] \pm \Delta x$$

$$x[(k+1)T_{mppt}] = x[kT_{mppt}] + \left(\left(x[kT_{mppt}] - x[(k-1)T_{mppt}] \right).sign\left(P_{pv}[kT_{mppt}] - P_{pv}[(k-1)T_{mppt}] \right) \right)^{(2.8)}$$

where x represents the variable that is perturbed (e.g., the duty cycle or the reference voltage), T_{mppt} is the time interval between two adjacent perturbations and kT_{mppt} is the current sampling instant with $k = 1,2,..,etc.$; Δx is the amplitude of the perturbation applied to x; and P_{pv} is the output power of a PV module.
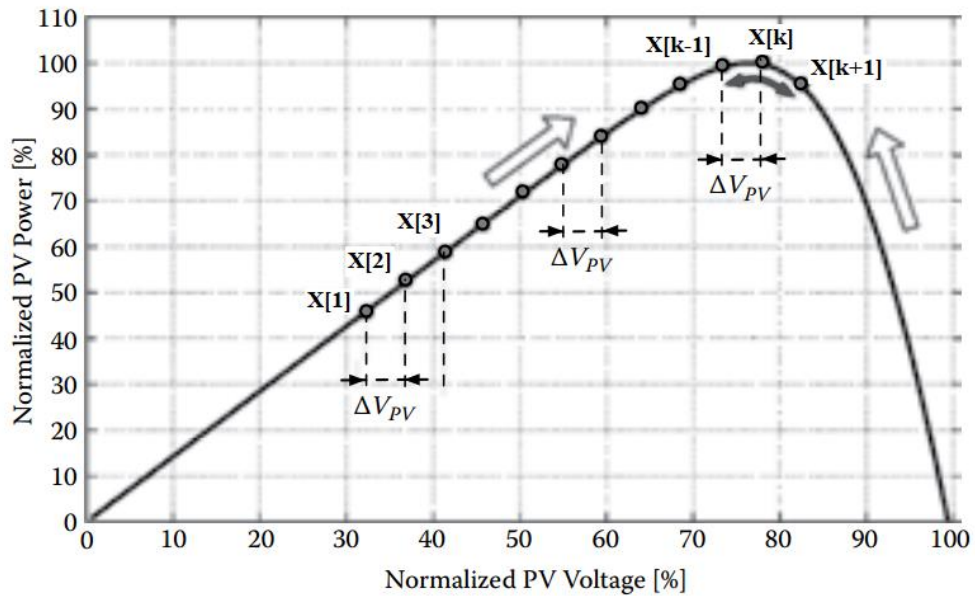
Figure 12: PV operating points imposed by the P&O controller [38]

Two P&O techniques can be used for controlling the switching converter and perturbing the PV voltage:

- Direct duty cycle P&O

  This involves direct perturbation of the duty-cycle of the switching converter. In this case the converter operates in open loop after each duty cycle perturbation.

- Voltage reference P&O

  In this case the converter operates under feedback voltage control loop and the perturbation is applied to the reference voltage of an error amplifier that generates the signal to control the duty cycle of the switching converter.

When the system approaches the MPP, the P&O algorithm continue oscillating about it. The optimal three-step P&O duty cycle oscillation; as shown in Figure 13, maximises the average power extracted from a PV module and ensures periodic and stable oscillation across the MPP [39].
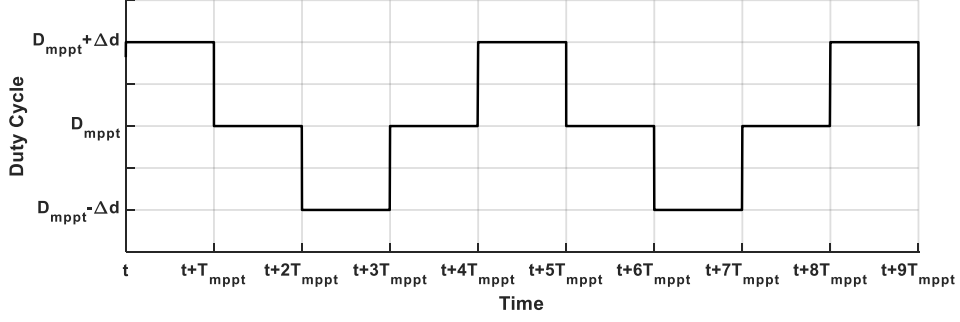
*Figure 13: Three-step duty cycle of P&O scheme.*

To guarantee optimal efficiency three-step P&O operation, the P&O parameters which are the amplitude of the perturbation Δx and the sampling period T_{mppt} have to be designed carefully. Guidelines for designing direct duty cycle and voltage reference P&O controllers are given in [38, 39]. In this research the direct duty cycle P&O controller is considered and designing both the duty cycle step size Δd and T_{mppt} are given in the following section.

2.3.1.2.2 Direct duty cycle P&O parameters optimisation

The basic version of P&O algorithm is designed with fixed duty cycle step Δd and its value is chosen to ensure a good compromise between the system transient and steady-state performance and to ensure that the P&O is not confused by the rapidly changing weather conditions (i.e. solar irradiation) [38, 39]. The P&O algorithm will not be confused only if during T_{mppt} the variation of the output power caused by the duty-cycle perturbations (ΔP_{pv_d}) is larger than the one caused by the solar irradiance (ΔP_{pv_G}) variation [39].

$$\left|\Delta P_{pv\_d}\right| > \left|\Delta P_{pv\_G}\right| \tag{2.9}$$

Based on the condition in (2.9), the author in [39] has derived the minimum duty cycle step size as follow:

$$\Delta d > \frac{1}{\mu_0}\sqrt{\frac{V_{mpp}K\left|\dot{G}\right|T_{mppt}}{HV_{mpp}+\dfrac{1}{r_{pv\_mpp}}}}$$

$$H = \frac{1}{2.\eta.V_t}\left(\frac{1-R_s}{r_{pv\_mpp}}\right)\left(\frac{I_{sat}}{\eta.V_t}e^{\frac{V_{mpp}+R_s.I_{mpp}}{\eta.V_t}}\right) \tag{2.10}$$

where K is a PV cell material constant 6.895×10^{-3} A.m^2/W, r_{pv_mpp} is the PV dynamic resistance at MPP, $\dot{G}$ is the average rate of change in the solar irradiation inside the time interval of length T_{mppt}, and μ_0 is the DC gain of the duty cycle-to-input voltage transfer function. Based on (2.10) the P&O algorithm controller is able to track without errors irradiation is characterised by average rate of change (within T$_{mppt}$) not higher than $\dot{G}$.

The sampling time T$_{mppt}$ is selected so that the P&O decision-making is not affected by transient response of the PV voltage and current after each perturbation [39]. It is necessary that the time period between two consecutive perturbations is long enough to allow the PV power to reach its new steady-state value. In order to find the minimum sampling period T$_{mppt}$ the dynamic behaviour of the whole system (i.e. the PV source and the interfaced switching converter) can be analysed by considering the system small-signal model evaluated around MPP.

Accordingly, and by assuming stationary weather conditions, the response of the PV power ($\hat{p}_{pv}(t)$) to a small step perturbation of amplitude Δd is derived in [38, 39] and given as follow:

$$\hat{p}_{pv}(t) = -\frac{\hat{v}_{pv}^2(t)}{r_{pv\_mpp}} \tag{2.11}$$

$\hat{v}_{pv}(t)$ can be found by analysing the step response of the control to PV voltage transfer function. Most of the DC/DC switching converter operating in open loop can be described by a second order transfer function as given in (2.12) [38].

$$G_{v_{pv},d}(s) = \frac{\hat{v}_{pv}(s)}{\hat{d}(s)} = \frac{\mu.\omega_n^2}{s^2 + 2\zeta.\omega_n.s + \omega_n^2} \tag{2.12}$$

Where μ is the static gain, ω$_n$ is the natural frequency, and ζ is the damping factor. The values of μ, ω$_n$, ζ can be expressed as a function of the converter parameters after the DC/DC converter topology is selected. From (2.12) the response $\hat{v}_{pv}$ to a small step perturbation of amplitude Δd is [38]:

$$\hat{v}_{pv}(t) = \mu\Delta d(1 - \frac{1}{\sqrt{1-\zeta^2}}.e^{-\zeta\omega_n t}.\sin(\omega_n t\sqrt{1-\zeta^2} + \arccos(\zeta))) \tag{2.13}$$

Inserting (2.13) in (2.11) the settling time T_ε which ensures the PV power oscillation is within a band of relative amplitude +/-ε around the steady state value is derived in [38, 39] and it results in:

$$T_\varepsilon = -\frac{1}{\zeta\omega_n} . \ln\left(\frac{\varepsilon}{2}\right) \qquad\qquad (2.14)$$

Accordingly the P&O sampling period has to be longer than the settling time in (2.14) so the algorithm is not affected by the transient oscillations of the PV system after each perturbation.

$$T_{mppt} \geq -\frac{1}{\zeta\omega_n} . \ln\left(\frac{\varepsilon}{2}\right) \qquad\qquad (2.15)$$

Where the value of ε=0.1 is a reasonable threshold to be considered based on the classical control system theory [39].

The parameters of the basic direct duty-cycle P&O technique (Δd, T_{mppt}) are fixed which are chosen to ensure a good compromise between the system speed under quick change in solar irradiation and the losses in steady state due to large perturbation step size. In [39] the authors recommend three-step P&O duty cycle operation as it maximises the average power extracted from a PV module and ensures periodic and stable oscillation across the MPP.

2.3.1.3 Advanced MPPT method

The performance of the P&O technique can be improved by modifying the basic algorithm. As an example in [44] P&O with adaptive step size is proposed. The duty cycle step size is automatically modified according to the derivative of power with respect to the PV voltage until the step size becomes very small around the MPP. This technique guarantees very good performance in the steady state. Other more advanced MPPT methods which can achieve a very small steady-state oscillation or even completely cancelling it can be used in order to improve the system performance in the steady-state. Example of these methods is: incremental conductance, particle swarm optimisation, extremum seeking, and ripple correlation [47-49]. In these methods once the system operation approaches the MPP and specific condition is fulfilled (depending on the employed method), the perturbation of the control parameter is stopped [47-49] to achieve high performance at steady-state.

Particle swarm optimization (PSO) is seen as a perturbative method with an adaptive amplitude of the applied perturbation. The particle velocity has been designed so that its value is close to zero when the system operation approaches the MPP and the value of the DC/DC converter duty cycle is approaching a constant. The application of the method requires a tuning of some parameters that strongly affect performances, some of them being dependent on the specific application.

Extremum seeking (ES) control uses a signal having a low-frequency oscillating component to detect whether the PV array is operating on its MPP or is on the right or left side of the MPP itself. In PV MPPT single-phase AC applications, ES can use the oscillating component at 100 or 120 Hz, depending on the frequency of the AC voltage, which can be 50 or 60 Hz, for tracking the MPP. Such an oscillation back propagates through the DC/DC converter and worsens the performances of the MPPT algorithm. Nevertheless, it can be used for tracking the maximum power point. In DC applications, a sinusoidal low-frequency disturbance can be injected for accomplishing the same work, but at the price of additional circuitry.

The ripple correlation control (RCC) technique uses the ripple at the switching frequency generated by the power electronic circuit to detect whether the PV array is operating on its MPP or is on the right or left side of the MPP itself.

Incremental conductance method is based on the observation that in the MPP, the following condition occurs:

$$\frac{dP_{pv}}{dV_{pv}} = \frac{d(V_{pv}.I_{pv})}{dV_{pv}} = 0 \tag{2.16}$$

By accounting for the dependence of the PV current on the voltage, it is possible to express such a condition as follows:

$$I_{pv} + V_{pv}\frac{dI_{pv}}{dV_{pv}} = 0 \tag{2.17}$$

so that the validity of condition (2.16) is equivalent to

$$\frac{I_{pv}}{V_{pv}} = -\frac{dI_{pv}}{dV_{pv}} \tag{2.18}$$

which means that, at the MPP, the absolute value of the conductance must be equal to the absolute value of the incremental conductance. Such a condition is the basis of the incremental conductance (INC) MPPT method. Condition (2.51) is verified through a

repeated measure of the conductance at two different values of the PV voltage. As a consequence, the method requires the application of a repeated perturbation of the voltage value, until the following condition occurs:

$$\frac{I_{pv}[k]}{V_{pv}[k]} = -\frac{I_{pv}[k] - I_{pv}[k-1]}{V_{pv}[k] - V_{pv}[k-1]} \qquad (2.19)$$

where the indices k and k− 1 refer to two consecutive samples of the PV voltage and current values.

2.3.2 Maximum power point tracking architectures

2.3.2.1 Centralised MPPT

The centralised MPPT is based on using one centralised switching converter and employs the MPPT for the whole PV arrays composed by paralleled PV strings as shown in Figure 14.

Under mismatch phenomena due to shading from clouds or nearby building, dirt from dusty weather, manufacturing tolerances, PV module age, etc., the power vs. voltage characteristic curve of the whole PV system may exhibit more than one peak which may confuse the centralised MPPT algorithms and make it fail [50-52]. In this case the centralised MPPT can cause a huge decrease in the overall system efficiency [50-52].
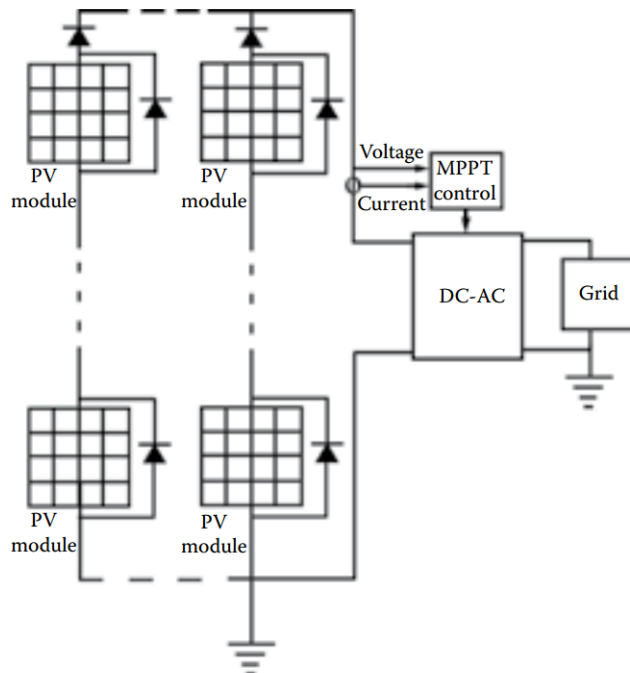

Figure 14: Grid-connected PV system with centralised MPPT. Strings of PV modules are put in parallel and connected to a single DC/AC inverter [38].

2.3.2.2 Distributed MPPT

The distributed MPPT is proposed to overcome the drawback of the mismatching phenomena in the centralised MPPT PV system. It is based on a dedicated switching converter for each PV module as shown in Figure 15 [38, 53-57]. Two different approaches can be implemented. The first one is based on dedicating MPPT DC/AC converter for each PV module [53, 54, 58], it is known as microinverter. The output port of the microinverters can be connected either in parallel or in series to the AC gird [38]. The second approach is based on dedicating MPPT DC/DC converter for each PV module [55-58]. The output port of the MPPT DC/DC converters can be connected in parallel or series to a common dc bus.
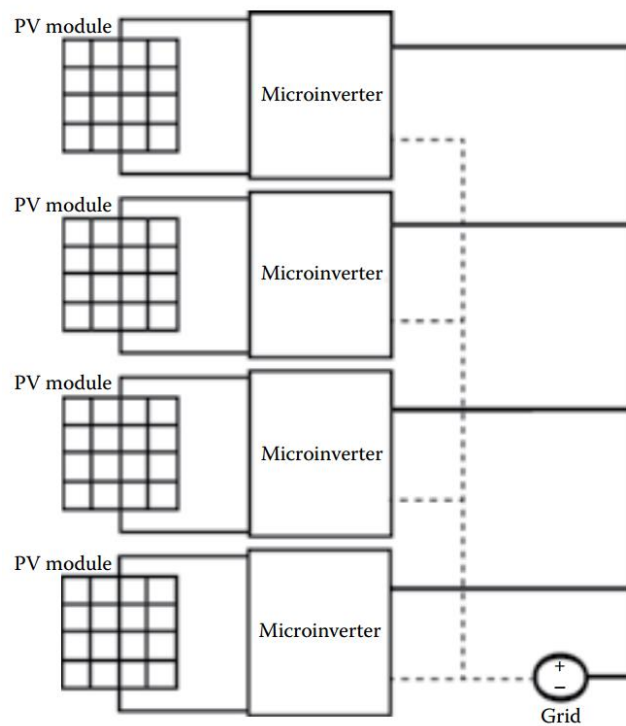

Figure 15: Grid-connected PV system with distributed MPPT. Approach based on the adoption of microinverters with the output ports in parallel to the grid [38].

2.4 Configurations and Topologies of Grid-connected PV Systems

2.4.1 Configurations in DC microgrids

When connecting PV system to DC microgrid, one of the major concerns is the need of a high output voltage (e.g. 380 V- 400 V) from low input voltage level (e.g. 30 V - 48 V) of a PV module. This problem can be solved by adopting different PV system configurations. The configurations can be classified into different categories based on

the method used to boost up the voltage and on the implemented MPPT configuration as shown in Figure 16 [20].

The most common configurations are the series centralised and string configurations as shown in Figure 16.(a) and Figure 16.(b), respectively. In these configurations the PV modules are connected in series to ensure sufficient voltage level and a centralised converter is used to implement MPPT. The advantage of these configurations is no need for a converter with a high-step-up voltage conversion ratio. However, these configurations are very sensitive to mismatching phenomena which increase the system power losses [38, 50-52].

To overcome the aforementioned drawback, PV system configurations based on distributed MPPT can be adopted [55-58]. Here and afterward will refer to the PV module with its MPPT converter as self-controlled photovoltaic module (SCPVM). The SCPVM can be connected in series directly to the DC microgrid as shown in Figure 16.(c), called series SCPVM configuration. This configuration provides lower sensitivity to mismatching phenomena, increase system modularity since it can be easily expanded by paralleling the series of SCPVM units, increase system redundancy in case of failure. However, under mismatching condition there is difficulty to achieve the desired output voltage of some SCPVM units. This is because voltage across each SCPVM (as given in (2.20) where V_{dc} is the dc-link voltage and V_{SCPVM} is the output voltage of a given SCPVM in the series connection) depends on the ratio of its output power with respect to the total output power of the whole string [38]. That means the output voltage of an SCPVM can vary in a wide range due to the imbalance power delivered by each PV modules. For example, if most of the modules in the system are totally under shading, the output voltage across the a few unshaded SCPVM units can become very large causing high switching stresses. To solve this problem an advanced and more complex control structure is necessary [55] or a parallel configuration could be adopted.

$$V_{SCPVM} = V_{dc} \frac{P_{out} \, of \, the \, Panel}{P_{total} \, of \, the \, string} \tag{2.20}$$

The new trend of connecting PV to the grid is the parallel configuration rather than series configuration to reduce the mismatching effect on the output voltage of the SCPVM units, improve the use of the PV power, and satisfy the safety requirement

during installation and maintenance; each converter module may be able to isolate its connected power source, so that the wiring parallel connections of these modules can be performed safely [57]. The power source—converter connection is a safe low voltage connection. However, in parallel connection one of the major concerns is the need to boost up the low PV voltage to a high output voltage (e.g. 400 V). Two solutions are proposed in the literature: Either boosting the voltage by using high-step-up boost converter, or by using multi stages of the conventional boost converter. Accordingly, single-stage and double-stage parallel SCPVM configurations are shown in Figure 16.(d) and Figure 16.(e), respectively. The new proposed high-step-up boost converters can be used for single-stage parallel SCPVM configuration such as coupled inductor, switched capacitor, integrated boost and switched capacitor, combined coupled inductor and switched capacitor, and interleaved boost converters [59]. However, the main problem with the single-stage parallel SCPVM configuration is the need for a DC/DC converter characterised by two contrasting requirements: a high-step-up voltage conversion ratio (about 10-15) and high conversion efficiency [38]. The double-stage parallel SCPVM configuration as shown in Figure 16.(e) can boost up the voltage by using two stages of conventional boost converter [59].
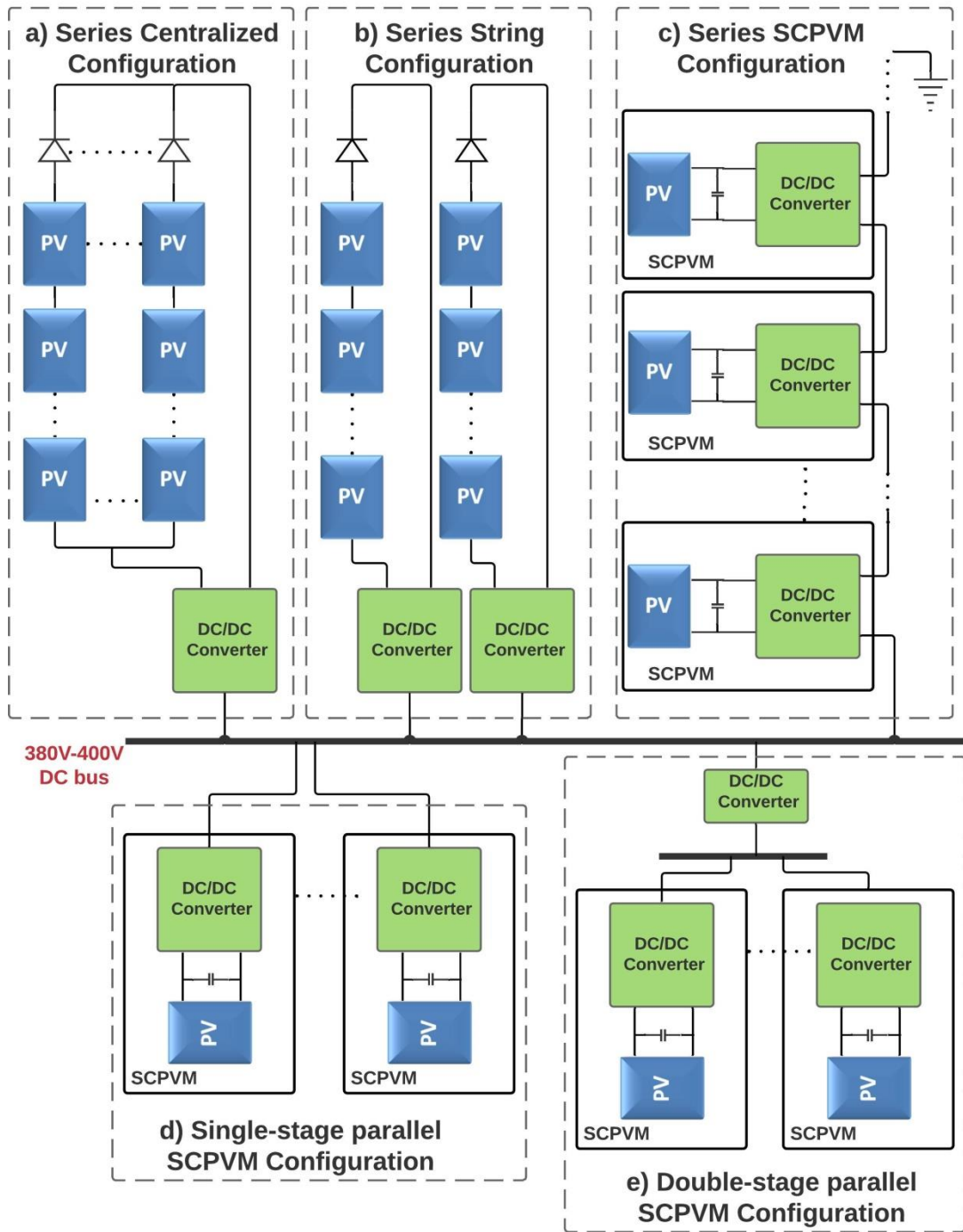
Figure 16: PV system configurations in DC microgrid.

Choosing between the single-stage and the double-stage parallel SCPVM configurations should be based on the configuration capability in providing: high-step-up voltage, high efficiency, low cost, simplicity, high MPPT efficiency, and high MPPT speed (as it was shown in previous section that the MPPT sampling time depends on the dynamic of the MPPT converter). The single-stage conversion is superior in its efficiency but the dynamic performance of the MPPT with the new proposed single-stage topologies has not been proven so far. Where in case of double-

stage based on using conventional boost converter: a high MPPT efficiency has been proven (more detail regarding MPPT efficiency is provided in section 2.4.3) [38], optimisation of the MPPT parameters and achieving high tracking speed are easy due to the simple structure of the boost converter.

It is important to mention that there are two issues to consider for two-stage boost converter: I) the stability of the cascaded structure which depends highly on the chosen controller structure [60]; II) for the second-stage boost converter the output-diode reverse recovery problem is severe and the voltage stress on the switch is high which have to be consider carefully in its design [59].

2.4.2 Configurations in AC microgrids

In any PV system connected to an AC microgrid it has to be provided with a DC/AC converter to invert the PV panels DC voltage to the grid AC voltage. Also, a DC/DC converter can be used between the PV panels and the DC/AC converter to maintain the DC voltage at the required level and to implement the MPPT controller. Figure 17 shows the most common PV system configurations in AC microgrid [8, 61]:

- Centralised configuration is where the PV modules are connected in series-parallel configuration to a centralised DC/AC converter.

- String configuration is where each string is connected to a DC/AC converter. If the string voltage does not have the appropriate value, then a boost DC/DC converter placed on the DC side or a step-up transformer placed on the AC side is required.

- Multistring configuration where is a DC/DC converter is placed between the PV string and the DC/AC converter. Each DC/DC converter implements the MPPT for the string. This configuration allows wider operating range of the PV voltage so the MPP can be extracted at lower voltage than in case of single-stage inverter, where the dc link voltage is constrained by the grid voltage.

- SCPVM configuration is where each PV module incorporates a DC/AC converter (single-stage) that implements an automatic control that performs the MPPT control at module level [58]. The DC/AC based SCPVM can be connected in parallel or series to the AC microgrid [38].

- Modular configuration, a conventional DC/DC converter and DC/AC converters (double-stage) sharing a common DC bus. Each DC/DC converter is connected to a PV string for MPPT implementation. High system reliability is guaranteed as the system is easy to maintain by only replacing the damaged converter.
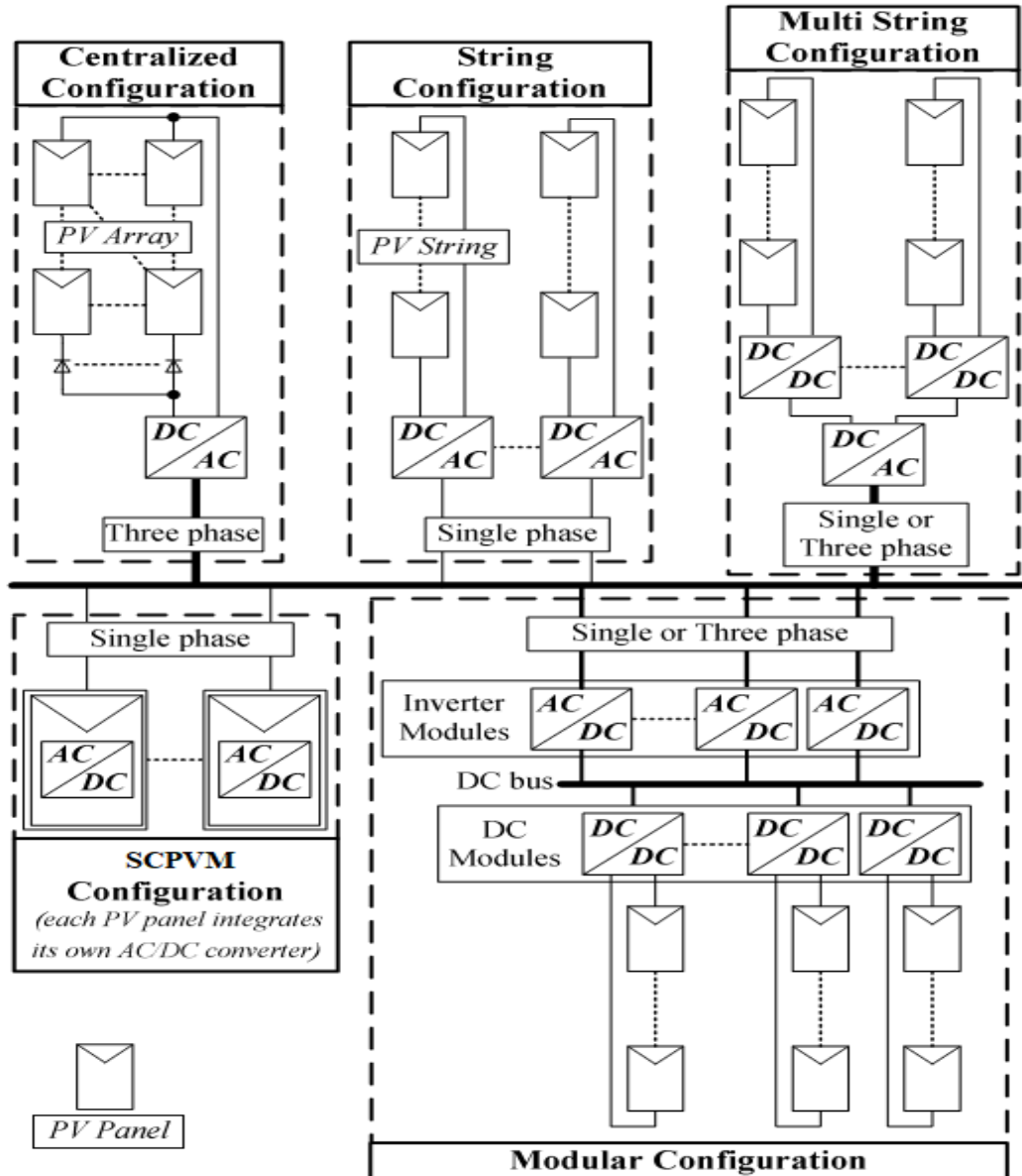

Figure 17: PV system configurations in AC microgrid [8].

The topologies used to interface the PV system to AC microgrid can be classified into categories based on using or not using an isolation transformer and on its location: either it is placed at the high frequency side ''high frequency transformer HFT'', or at the low frequency (60Hz or 50Hz) side ''low frequency transformer LFT''. Figure 18 summarises some of the PV system topologies in AC microgrid [8, 58].
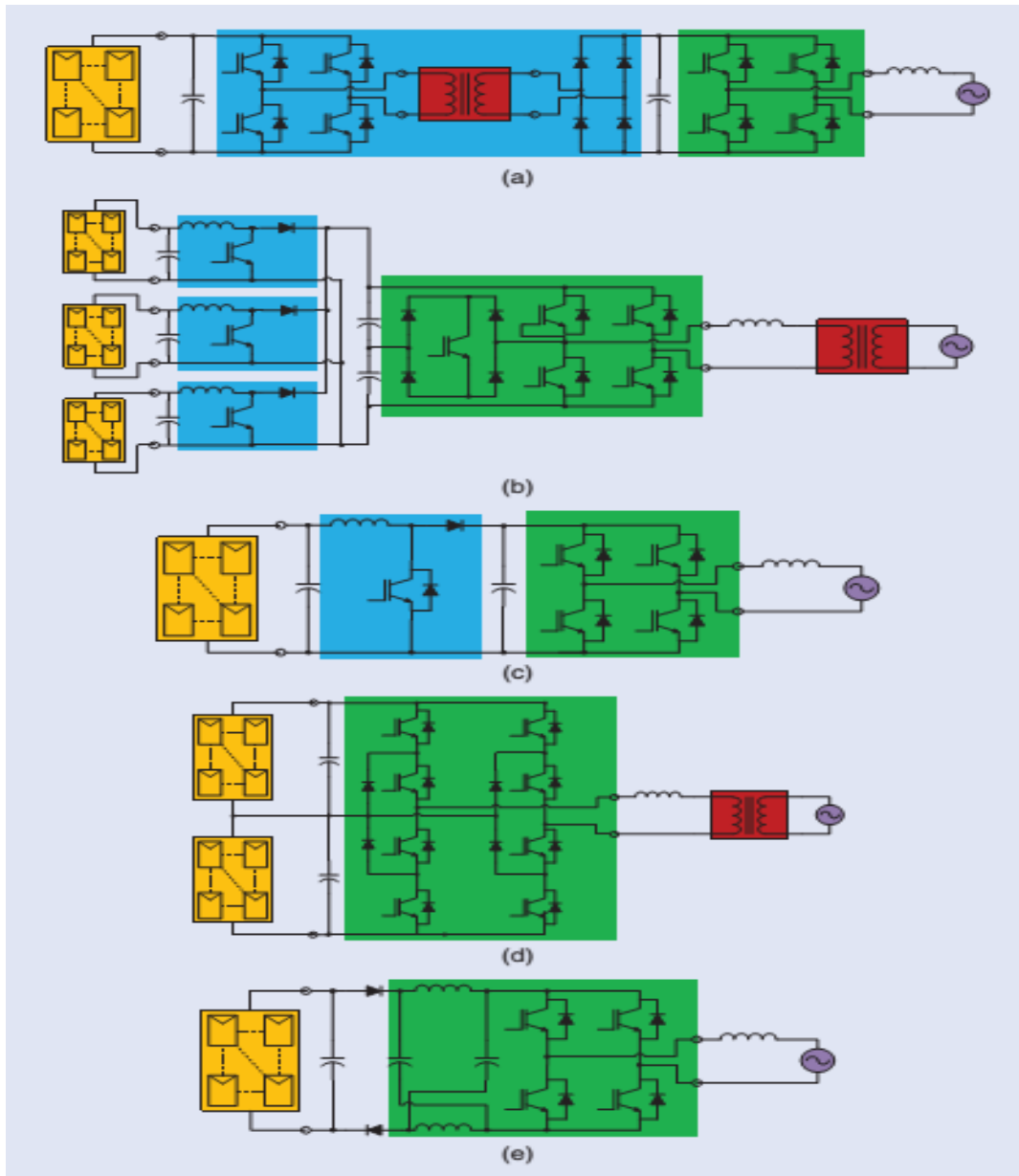
Figure 18: Example of PV system topologies in AC microgrid [8]. (a)DC/DC-DC/AC with HFT, (b) DC/DC-DC/AC with LFT, (c) DC/DC-DC/AC (boost and inverter), (d) DC/AC inverter with LFT, (e) DC/AC.

2.4.3 Converter topologies for SCPVM based DC/DC converter

DC/DC converters such as boost, buck, and buck-boost are widely used for SCPVM to implement the MPPT controller because of their simplicity and efficiency. There are very important key points to be considered when choosing between them such as the given application, efficiency, weight and size, input filter requirement, component stress level, cost, MPPT capability and efficiency, and matching the bus voltage regulation.

The authors of [62] compare different type of DC/DC converters buck, boost and buck-boost for implementing MPPT in stand-alone application, where the PV system is connected to a load. It was found that using buck converter for MPPT is better in case of inductive load because it keeps the system efficiency roughly constant as irradiation changes and shows better loop stability and dynamic response. However, large input filter is required for buck converter due to the discontinuous input current. In case of using boost converter for MPPT, it was found that it does not require input filter but the system efficiency is function of irradiation level (efficiency increases with decreasing irradiation). For the buck-boost converter it was found that it offers voltage gains larger or smaller than one, and therefore is more flexible in applications where the load varies widely. However, the switch and diode losses are greater than those of the basic buck or boost converters for same power level and voltage gain. For this reason the buck-boost type is not recommended for high power applications.

Different possible dc-dc converter topologies for PV applications such as buck, boost, buck-boost, Cúk converters are examined in [63]. The results reveal that: I) the boost converter is best if a significant step-up voltage is required with a short string of PV modules but cannot deliver all the power from the shaded modules, II) the buck converter can deliver any combination of module power but its required longer string of PV modules compared with boost converter; III) Buck-boost and Cúk converters are found to be the lower efficiencies and higher costs due to their high semiconductor conduction and switching losses.

A comparison between boost and buck converters was done in [64]. It states that the boost converter has several advantages over the buck as the following: I) the rms current through the inductor is much less; II) the required input filter (capacitance) is smaller and cheaper; III) current rating is lower which is better for selecting the power switches and drivers; IV) the boost diode acts as blocking diode to avoid the reverse current from the grid to the PV; V) the boost shows better dynamic characteristics: well damped, wider bandwidth and smaller resonance due to the small input capacitance.

The authors of [38] emphasise on all these aforementioned advantages mentioned by [64] for using boost converter in grid-connected PV applications. In addition to that, in [38] the effect of the DC/DC converter type on the MPPT efficiency is discussed. An expression of the MPPT efficiency as a function of the peak-peak voltage oscillation of

the output voltage and PV voltage conversion ratio (V_o/V_{pv}) of the DC/DC converter has been derived as given in (2.21).

$$\eta_{MPPT} = 1 + \frac{3.\alpha.V_{mpp} + \beta}{2.P_{mpp}.M^2(D)}.\Delta V_o^2 \qquad (2.21)$$

Where;

$$M(D) = \frac{V_o}{V_{pv}}$$

$$\alpha = \frac{1}{2}.\frac{\partial^2 I_{mpp}}{\partial V_{mpp}^2}$$

$$\beta = \frac{\partial I_{mpp}}{\partial V_{mpp}} - V_{mpp}.\frac{\partial^2 I_{mpp}}{\partial V_{mpp}^2}$$

It is important to highlight that α and β in (2.21) have negative values. The equation in (2.21) reveals that the MPPT efficiency is high as the output voltage oscillation is small and the voltage conversion ratio V_o/V_{pv} is high. This means that step-up DC/DC converters give better MPPT efficiency.

Accordingly and based on the discussion in this section for PV grid connected application the boost converter is preferred than the buck and buck-boost converters due to its advantages in boosting the voltage, allowing the use of small size input and output filters, and giving better efficiency of the MPPT.

2.5 Control Structure of PV Converters in Microgrid

In general, there are two control levels in microgrids [20, 65-67]:

- Local control level: This is applied on the interfaced converters of the distributed generators, storage systems and loads. Local control normally covers: a) voltage, current and droop control for each converter; b) special control functions such as maximum power point tracking (MPPT) for photovoltaic generators or state of charge for energy storage system; c) centralised such as master–slave or multi-master controllers in AC microgrid and decentralised coordination functions such as DC bus signalling, Power line signalling and adaptive adjustment of droop coefficients in DC microgrid; d)

Control the frequency and manage the output active and reactive power from the distributed generators in AC microgrid.

- Global control level (central control): A digital control and communication network can be applied to achieve advanced energy management functions. It uses information on load needs, power quality requirements, electricity cost, special grid needs, demand-side management requests, grid operating mode etc. to determine the coordinated control commands which is sent to the local controllers.

Figure 19 shows an example of a systematic control diagram in a DC microgrid.

In order to keep the scope of this research as focused as possible on the generation side of the microgrid and in particular on the PV source as the main renewable energy source used in this research, the rest of this section will be reviewing the local control of the PV source converter. More details about the global control principles can be found in [65] and references therein.

2.5.1 Operating modes of microgrids and the function of the PV source converter

The first time the concept of microgrid was mentioned in literature was by [2] in 2001. It has defined the microgrid as 'a cluster of loads and micro-sources operating as a single controllable system that provides both power and heat to its local area'. The main goals behind proposing this new paradigm were providing new way for connecting the distributed generation sources efficiently. An example of a DC microgrid is shown in Figure 19.The operating function of each converter in a microgrid to switch between different operating modes (i.e. operates as voltage source or current source) [66-70] depends on the microgrid operating mode (grid-connected or islanding mode), the power level from distributed generation sources, loads profile, and battery state [66-70]. At least one converter has to operate in voltage source mode to regulate the voltage and the frequency of the microgrid (in case DC microgrid only voltage regulation is needed), and then other distributed generation sources converters can be connected to the microgrid and function as current sources [66-70]. In order to assign the source converter which regulates the microgrid voltage, Table 3 summarises the operating modes of a microgrid and the function of the source converters for each mode [67, 68, 70].
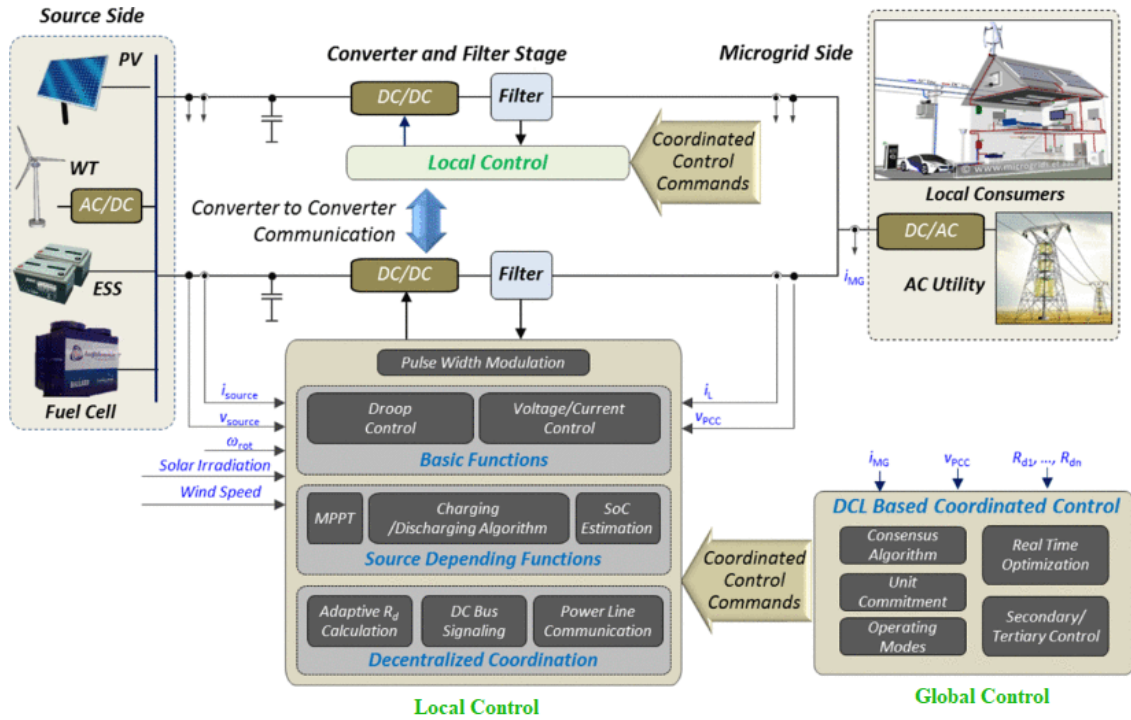
Figure 19: DC microgrid and control diagram of the local and global controllers [65]

In case of grid-connected mode the microgrid voltage is controlled by the main AC grid interfacing converter while the PV converter operates as a current source. In islanding mode; the distributed generator converter operates as a current source and the battery converter control the microgrid voltage unless the generated power by PV panels is higher than the load demand and the battery is fully charged (see mode VI in Table 3). In this case the PV converter operates as voltage source to regulate the microgrid voltage and ensure power balance in the system.

Based on the above discussion, the PV converter switches between current source and voltage source based on the operating mode of the microgrid as shown in Table 3. A general local control diagram of a PV converter connected to a DC bus is shown in Figure 20. The PV converter operates as current source (in Modes I – V) when the switch is at position 1. In this case the special MPPT control function is active. This operating mode will be called 'MPPT mode' and it is the desirable mode in grid-connected PV applications for higher energy harvesting. In case the switch is at position 2 the PV converter operates as a voltage source and controls the dc bus voltage (Mode VI). This mode will be referred as 'Droop mode'. It includes current and voltage controllers and droop control loop [65]. Switching between MPPT mode and Droop mode should be fast and smooth to provide bumpless transition and to guarantee the system efficiency and reliability. The decentralised coordination functions or the

central controller can be used to trigger the transition between different modes [65, 67, 69].
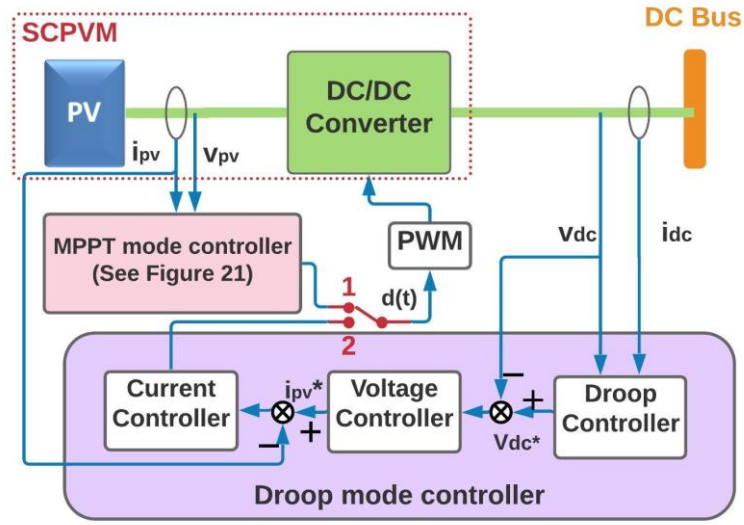

Figure 20: Local control diagram of PV converter connected to a DC bus.

Table 3: Microgrid operating modes and the function of the system's converters

Mode	Description	Functions of Power Converters (controller mode)		
		Main AC grid interfacing converter	PV converter	Battery converter
I	Grid connected, battery is not in full state, and $P_{PV} > P_L$ [(1)]	Voltage source (inverting)	Current source (MPPT)	Loading unit (charging)
II	Grid connected, battery is not in full state, and $P_{PV} < P_L$	Voltage source (rectifying)	Current source (MPPT)	Loading unit (charging) /Disconnected
III	Grid connected, battery is in full state, and $P_{PV} < P_L$	Voltage source (rectifying)	Current source (MPPT)	Disconnected
IV	Islanding mode, battery is not in full state, and $P_{PV} > P_L$	Disconnected	Current source (MPPT)	Voltage source (charging)
V	Islanding mode, battery is in full state, and $P_{PV} < P_L$	Disconnected	Current source (MPPT)	Voltage source (discharging)
VI	Islanding mode, battery is in full state, and $P_{PV} > P_L$	Disconnected	Voltage source (Droop)	Disconnected
VII	Islanding mode, battery is deeply discharged, and $P_{PV} < P_L$	Disconnected	Disconnected unless load shedding is applied	Disconnected unless load shedding is applied

Notes: (1) P_{PV} is the photovoltaic output power and P_L is the load power.

2.5.2 Local controller of a PV converter connected to a DC bus

General control structures when the system operates at MPPT mode are shown in Figure 21. The control structure in Figure 21.a is direct-duty-cycle MPPT controller and it was used by [38, 39, 71]. The voltage-reference MPPT controller in Figure 21.b has been used by [38, 40, 41, 71, 72]. It reduces the effect of r_{PV} on the system transient (see section 2.3.1.2.2), thus improve P&O performance. However this configuration is suitable only for low power application. The transient behaviour of the

current is uncontrolled and at high power application that affects the quality of the provided power and the system failure rate. This problem can be solved by using cascaded input-voltage controller structure which includes controlling the PV voltage and the inductor current as shown in Figure 21.c and it was used by [73].

Most of the studies on grid-connected PV system, where the PV converter operates at MPPT mode, use one of the above three discussed controller structures (Shown in Figure 21.a, b and c). The analysis is based on the assumption that main AC grid interfacing converter is responsible for controlling the dc bus voltage or in case islanding it is assumed that the storage system is large enough to store the excess energy from the PV resource and its converter is responsible to regulate the dc bus voltage.

The fact that the MPPT converter and PV source are both nonlinear makes it difficult to design the compensator. A solution for this problem is found in many references such as in [39-41]. Basically the nonlinear system (the PV and the switching converter) is formed as two linear models within a certain range and time period. The linearisation is based on the fact that the model is linear around the operating point within small operating range. Averaging and Linearising methods for DC/DC switching mode converter (e.g. state-space averaging method and circuit-averaging method) are well developed and are used for studying converter behaviour and designing linear controllers [74, 75]. An equivalent linear circuit of the PV source is proposed in [39-41] and was discussed earlier in Section 2.2.2, page 14. The linearised model of the PV source can be used for designing the associated PV system controllers and for simplifying the analytical analysis to show the effect of the non-linear PV source on the overall system dynamic.
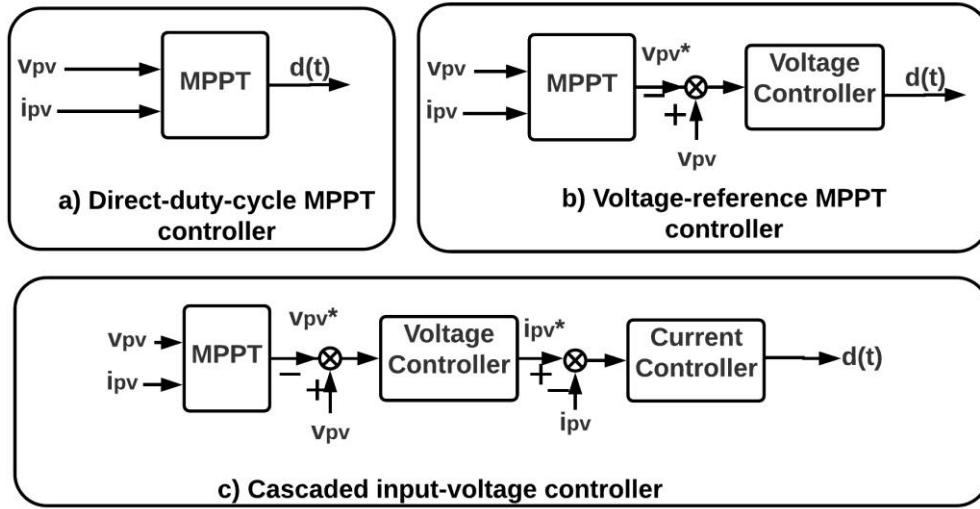
Figure 21: MPPT mode control structures.

In the next section the influence of the non-linear PV source on the controller performance and system dynamic will be explored based on using the linearised PV model.

2.5.3 Effect of the non-linear PV source on the controller performance

2.5.3.1 Regulating the input voltage of the PV interface converter

As the dynamic resistance of the PV source changes with the operating conditions (see Figure 10), the PV interfaced converter's dynamics is affected. In [38, 39] the dynamic behaviour of the PV voltage for a PV source connected to DC/DC boost converter with direct-duty cycle MPPT controller is studied for optimising P&O controller. It reports that the damping factor ζ of the control-to-input voltage transfer function depends on r_{PV}. It was found that as r_{PV} increases, because of a reduced in the solar irradiation level and/or a decrease in the PV voltage (see Figure 10), the damping factor reduces and that affects the system transient behaviour. Also, the authors in [38, 39] have showed that the effect of r_{PV} on the system transient can be reduced by using compensator in the feedback loop; voltage-reference MPPT controller as was shown in Figure 21.b. Figure 22 compares the system transient dynamic with and without compensator and it shows that with compensator the effect of r_{PV} is reduced and the settling time is much smaller than that for the open loop system.
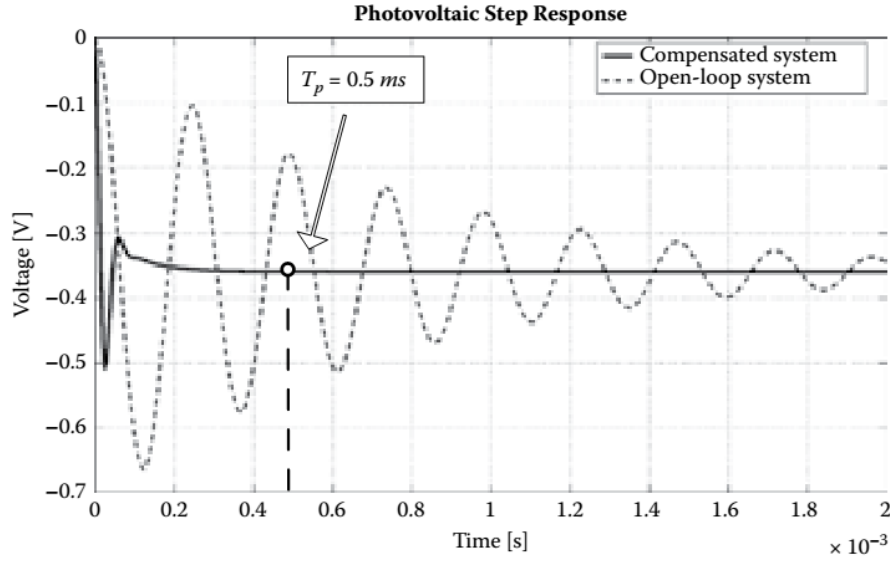
Figure 22: Step response of the PV voltage for low solar irradiation (100 W/m2). Black curve: closed loop step response, dashed curve: open loop step response [38].

For same system configuration (PV source connected to boost converter with voltage-reference MPPT controller), the authors in [40] have discussed the effect of changing the PV voltage on r_{PV} and eventually on the system dynamics under constant solar irradiation and temperature. The current-voltage curve of the PV source is divided into four regions; current source region, power region I, power region II, and voltage source region as shown in Figure 23. The frequency response of the control-to-input voltage transfer function in the four operating regions is shown in Figure 24. It shows that the change in the operating regions does not affect the dc gain, the natural frequency, and the cut off frequency. However, it affects the damping factor ζ. The system is well damped when the operating point is in the voltage-source region. The damping factor reduces, when r_{PV} increases by moving closer to the current-source region. So, the current-source region should be avoided to prevent the system from entering into oscillatory state and some control issues of the lightly damped system. In [40] two ways are suggested to avoid the current-source region. One way is a lower bound of the PV voltage, but the temperature affects the desired operating voltage (V_{mpp}) over a large range (see Figure 8) which makes it difficult to decide the lower bound. The other way is to use the lower bound of the r_{PV} under the lower limits of the solar irradiation and temperature.

39
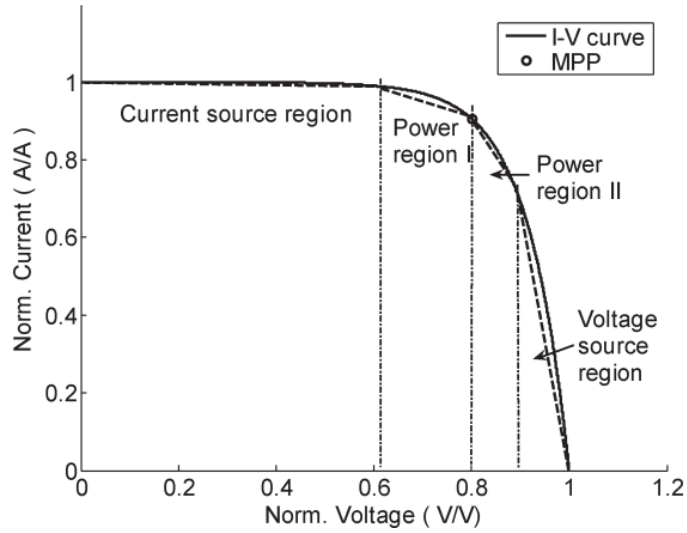
*Figure 23: Current-voltage characteristic curve of PV and the four operating regions as given in [40].*
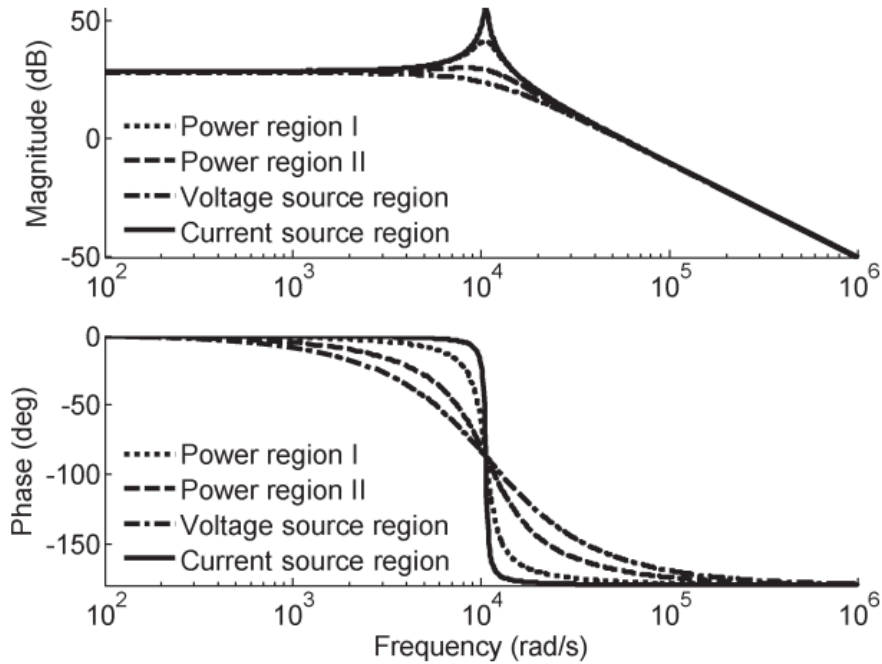
Figure 24: Bode diagram of the theoretical control-to-input voltage transfer function for voltage-reference MPPT controlled boost converter [40].The operating regions are shown in Figure 23.

The study in [41] is using voltage-reference MPPT controller to control a buck converter to interface the PV system to the load. The closed loop system performance is checked when the operating point moves between different regions (same regions shown in Figure 23: voltage-source, MPP and current-source region). The frequency response of the control-to-input voltage transfer function is shown in Figure 25. Its shows that the damping factor of the system is affected, where the current-source region presents the least damped operation, while the voltage-source region presents the

very damped operation. The cut-off frequency of the system for the different regions is the same.

Regulating the PV voltage by only considering a voltage control loop as was emplyed in [38-41] without an inner current loop is usually useful for small PV system (less than 1 kW). For higher power application, cascaded input-voltage control usually used to avoid current transient, reduce failure rates, and for overload protection [76]. Cascaded input-voltage control is implemented by using two control loops; the inner curent control loop and the outer voltage control loop as hown in Figure 21.c. In [41] the cascaded input-voltage control loop for a buck converter is analysed for three different PV operating regions. The bode diagram of the closed-loop system is shown in Figure 26. It shows that at low frequency region the dc gain and the phase are affected significantly. However, the design point of the closed loop control (i.e. cut-off frequency) is chosen at high frequency which guarantees proper control performance for the three operating regions. In fact, the effect of r_{PV} was hidden by the large input capacitance (connected across the PV terminal) and high cut-off frequency of the system.
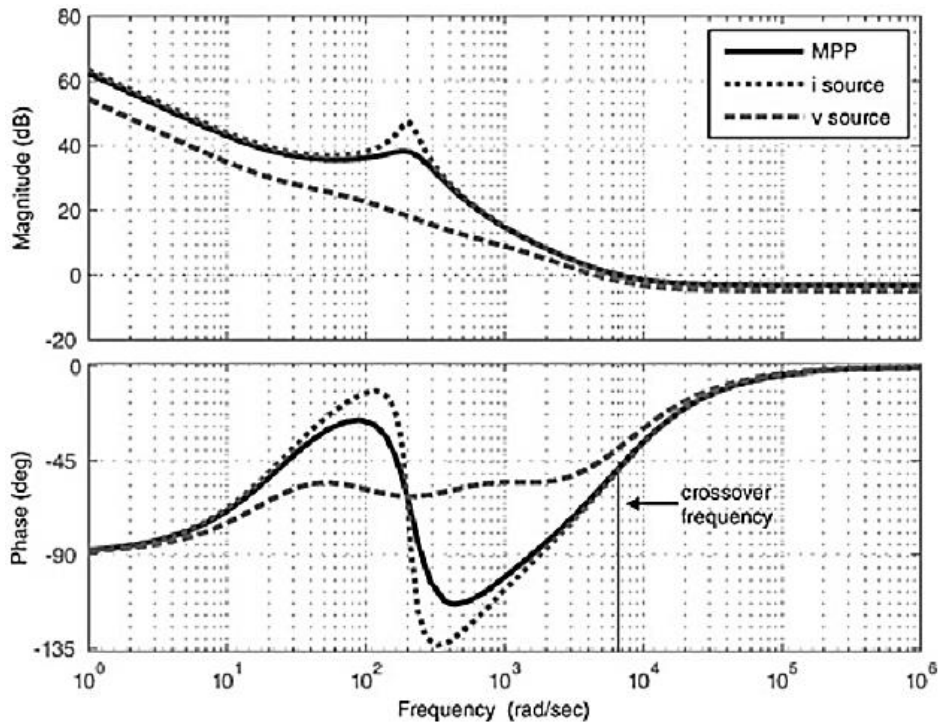

Figure 25: Bode diagram of the closed-loop system at three different operating regions for voltage reference MPPT controlled buck converter [41].

In the previous disscussed studies [38-41] the influence of the non-linear PV source (modelled as a dynamic resistance r_{PV}) on the PV voltage regulation results in different

damping factor. However, the resonance frequency is not affected by r_{PV} and the system can be easily controlled by two ways. One way is by designing the system with high cut-off frequency, where the system characteristics are less affected by r_{PV} as shown in Figure 24, Figure 25, and Figure 26. On one hand the high cut-off frequency helps to guarantee same system dynamic performance under different operating conditions, but on the other hand the high cut-off frequency will required higher switching frequency which increases the switching losses. Also in case cascaded input-voltage controller the cut-off frequency will be limited by the current controller. The other way is using large input capacitance C_{in} across the PV terminal to hide the effect of r_{PV}. However, large capacitance will reduce the system reliability [77] and will diminish the performance of the P&O controller [38].
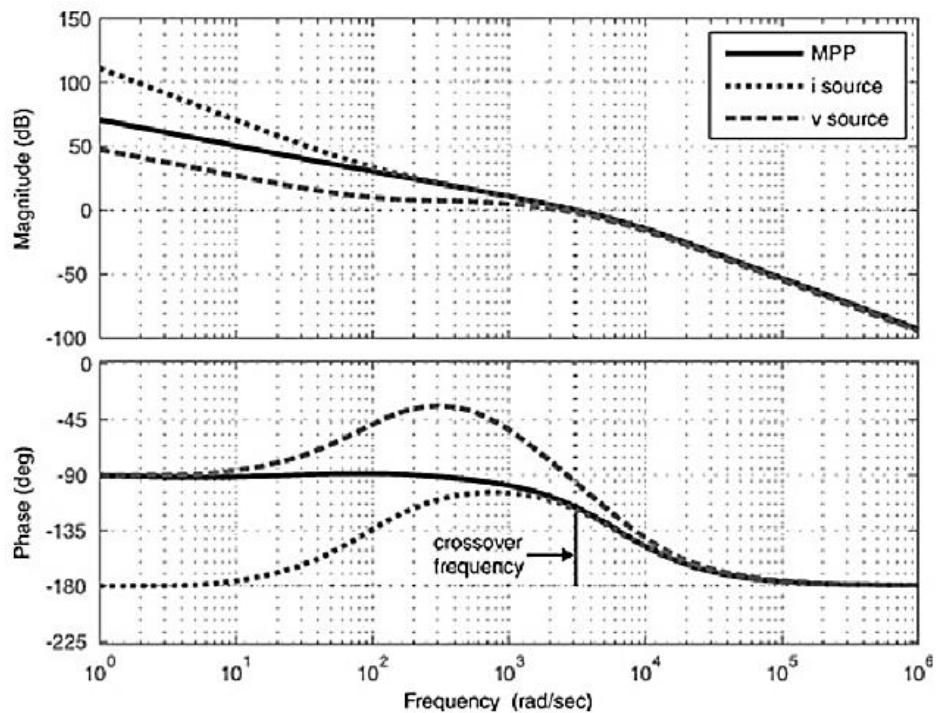

Figure 26: Bode diagram of the closed-loop system at three different operating regions for cascaded input-voltage controlled buck converter [41].

The influence of r_{PV} for cascaded input-voltage controlled boost converter with small input capacitance has been analysed in [73]. The PV voltage is controlled by means of inner inductor current loop. A small input capacitance and low cut-off frequency (~50Hz) are considered. It was found that r_{PV} variation affect the cut-off frequency and the phase margin of the system as shown in Figure 27. The impact of r_{PV} is very significant at MPP and CV regions. The performance of the controller becomes much slower as PV voltage increases which can cause problems such as low performance of the P&O controller [38], or no rejection of disturbances from weather variation or load side variation [76]. However, the effect on the stability is not critical as the phase

margin is improved. The author of [73] has proposed an adaptive voltage control based on estimating r_{PV} to adapt one parameter of the controller to overcome the slow regulation in the power and constant voltage regions and achieve same regulation performance at different regions.
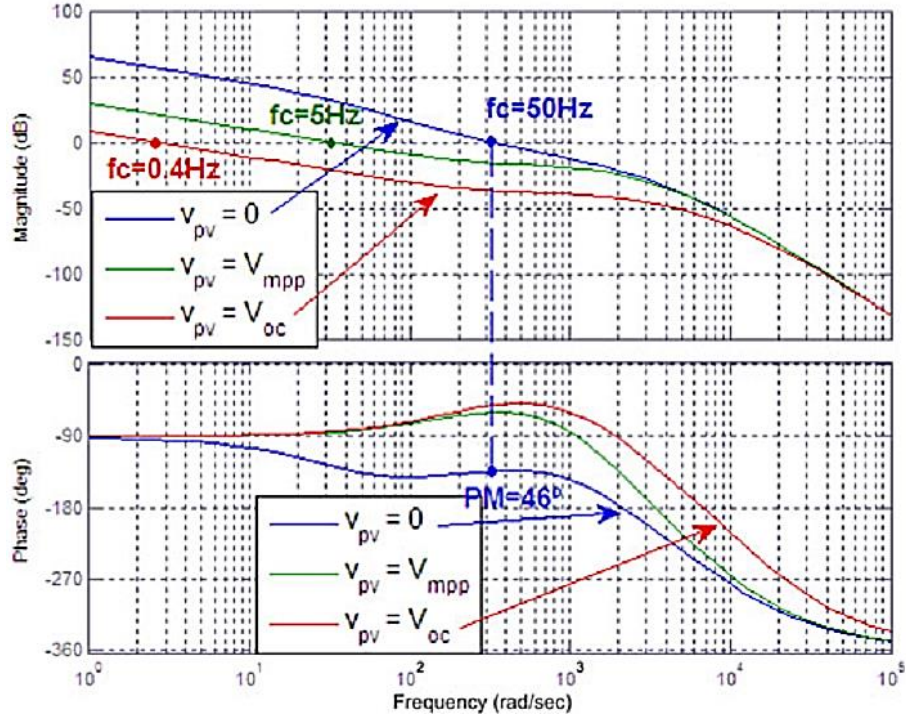

Figure 27: Bode plots of the cascaded input-voltage controlled boost converter at three different operating regions [73].

2.5.3.2 Regulating the output voltage of the PV interface converter

It was discussed in section 2.5.1, the outputs of the PV interfaced converter system (output voltage and current) need to be controlled under specific operating mode such as Mode VI (Droop mode). Output-side feedback control of buck type and boost type converters with a voltage source input (voltage-fed converter as shown in Figure 28.a) is completely developed. However, the existent of the current source input (current-fed converter as shown in Figure 28.b) such as PV source affects the dynamic representation of the conventional voltage-fed converter [78]. The main difference between the current-fed and voltage-fed converter is that the current-fed converter introduce a new state variable to the system which is the input capacitance C_{in} voltage. The input voltage of the current-fed converter is not constant as in the voltage-fed converter. The new state variable adds more complexity to the system and will also affect the dynamic of the system. Steady state mathematical model and the small signal frequency model in continuous conduction mode for current-fed buck and boost converters has been given in [78].

43
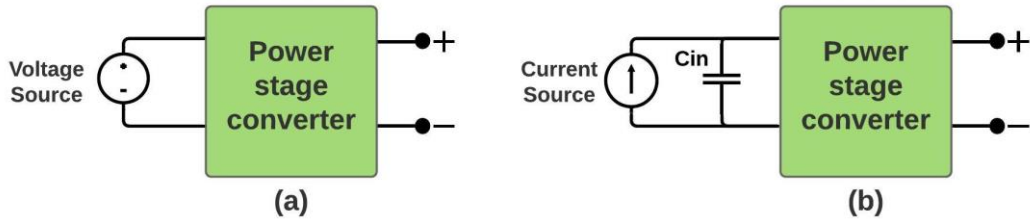
Figure 28:(a) voltage-fed converter (b) current-fed converter

The effect of the PV on the output-side control was tackled by [79, 80]. It was shown that the control loop gain of a peak-current-mode-controlled buck converter in PV application has a right half plane zero (RHP) when the PV operates in the current-source region. [80] also reveals that a RHP pole appears in the converter dynamic when the PV operates in the current-source region. The two earlier mentioned studies ([79] and [80]) have analysed the buck converter dynamics under output current control, the study in [81] is investigating the buck converter with output voltage control. It was found that the dynamics of the output-voltage-controlled buck converter, used in PV applications, contains RHP zero and duty-cycle-dependent resonant poles when the PV operates in the voltage-source region. Therefore, the controller design of an output-side-controlled buck converter used for PV applications is more complex than the conventional converter due to the appearance of the RHP roots.

Boost-type converters are preferred to connect PV to the DC microgrid, mainly because of its voltage boosting capability, small input filter and DC-link capacitance size, and high MPPT efficiency. However, the conventional voltage-fed boost, buck-boost and other boost-derived converters present considerable difficulties to the output-side controller design because they contain a RHP zero in their control-output transfer function [74]. In addition to the conventional RHP zero in boost type converters the recent investigation of PV interfacing boost converter [82] has showed that another RHP zero appears in the control-to-output transfer function when the PV operates in the current-source region. The second RHP zero is generated because of the non-linear PV source and the additional input filter at the output terminal of the PV.

Thus, to ensure good output-side-controller performance and stable control loop in PV application: In case output-voltage-controlled buck converter special care is required at the voltage-source region. For the peak-current-controlled buck converter, the attention is to be paid at the current-source region. In case of output-mode-controlled boost

converter for either output voltage or output current, the system is more sensitive at the current-source region.

2.5.3.3 Transient response specification under different damping ratio

In grid-connected PV system the interfacing converter operate at MPPT mode and control its input side by one of the structures shown in Figure 21. In section 2.5.3.1 it was discussed that the influence of the non-linear PV source on the input side control performance designed with a high cut-off frequency (at a frequency where the system characteristics are less affected by r_{PV} variation) affects only the damping ratio of the system [38-41]. The damping factor of the system affects the controller performance, especially its transient response [74, 83]. Consequently, this section reviews the effect of different damping ratio on the transient performance of a second order system focusing on the system settling time and maximum overshoot.

The closed loop transfer function of a DC/DC switching converter can be described by a second-order equation as given in (2.22):

$$\frac{C(s)}{R(s)} = \frac{\omega_n^2}{s^2 + 2\zeta\omega_n s + \omega_n^2} \tag{2.22}$$

Where; R(s) and C(s) are the input and output of the system, respectively. ζ is the damping ratio and ω_n is the natural frequency of the system. The step response curves of c(t) with different values of ζ is shown in Figure 29.

The settling time (t_s) is the time required for the response curve to reach a specified percentage of the final value (usually 2% or 5%) [74, 83]. The decay speed of the transient response depends on the time constant $\tau = \frac{1}{\zeta\omega_n}$ of the system. Therefore, for a given ω_n, the settling time is a function of ζ as shown in Figure 30.
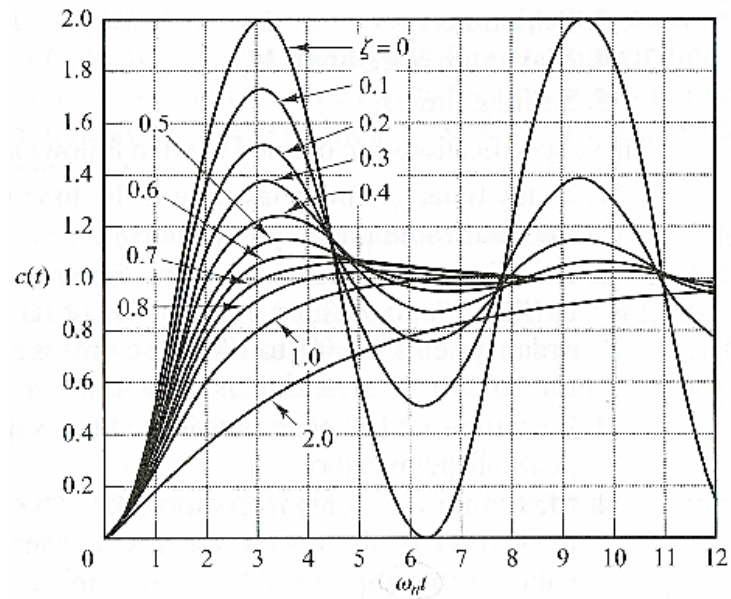
Figure 29: Unit-step response of the system given in equation (2.22) [83].

The maximum overshoot (M_p) is the maximum peak value of the response curve measured from unity [74, 83]. The relationship between the maximum percent overshoot and ζ is given in (2.23) and illustrated in Figure 31 [83].

$$M_p = e^{-\left(\zeta/\sqrt{1-\zeta^2}\right)\pi} \tag{2.23}$$
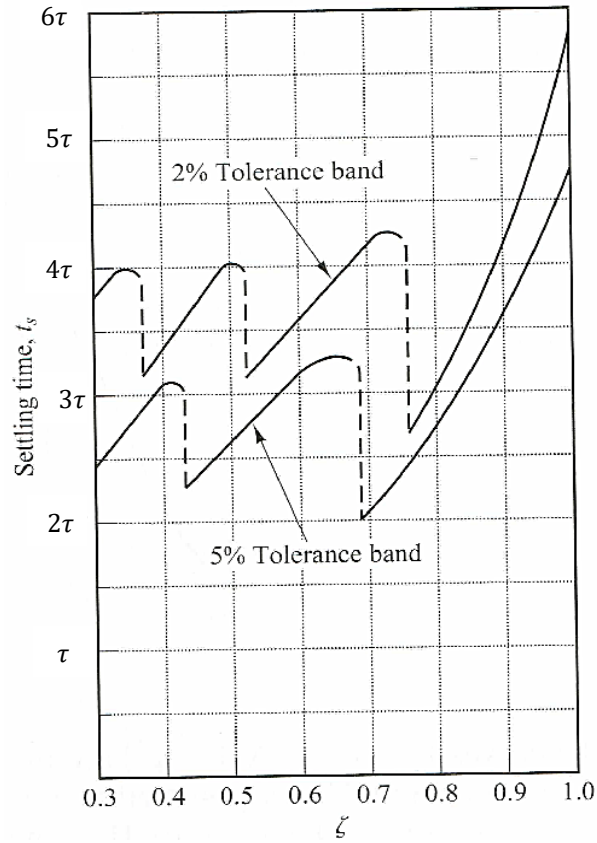
Figure 30: Settling time versus ζ [83].
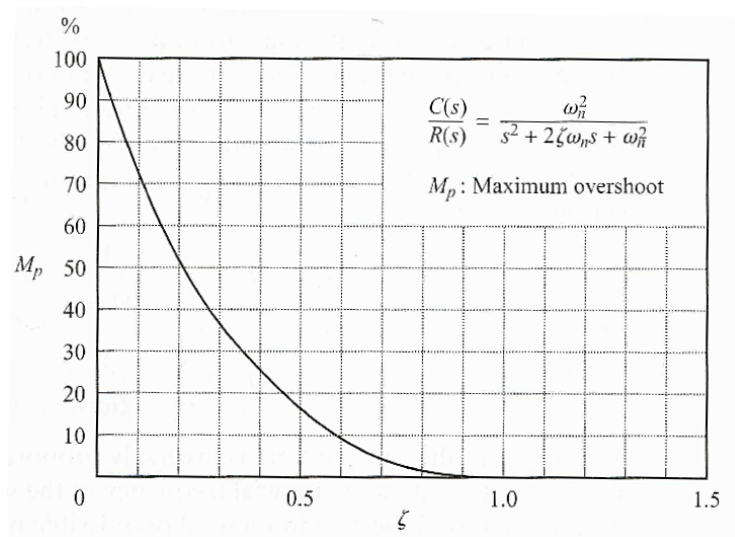
Figure 31: Overshoot versus ζ [83].

2.6 Power Quality of Photovoltaic Systems

One of the challenges the PV system bring to the grid is the power quality. Several origins of the poor power quality in grid-connected PV system are discussed earlier in

47

Chapter 1, Section 1.1. Recently, it was found that the MPPT controller that based on perturb and observe technique such as P&O controller induces harmonics in the grid and that impact the PV system power quality as reported in [16-18, 28-31]. In this section the impact of the P&O controller on PV power quality is reviewed in-depth and possible mitigation methods are discussed.

2.6.1   Impact of P&O controller on PV power quality

The investigations in [16-18, 30, 31] point to the impact of the P&O controller on the PV system power quality based on experimental results for single-stage centralised MPPT inverters. The study in [16] indicates significant power-dependent changes in harmonics emissions of the single-stage centralised MPPT inverters and states that harmonics emission increases in low power operating modes. The study suggesting that the increase in the harmonics is due to the P&O controller, but a clear explanation of how the P&O controller induces these harmonics is not provided. One of the experimental results of the study in [16] is shown in Figure 32 which show the harmonics in the dc-link voltage and AC grid current. Similarly, for the system shown in Figure 33 the authors of [17] reveal that rapid subharmonics have been observed in the experimentally measured DC and AC voltages and currents of the single-phase grid-connected PV inverters as shown in Figure 34. They comment that the cause of these subharmonics is the P&O controller, however proper explanation of generation mechanisms of these subharmonics is unclear. My published work in [28] shows that the harmonics in the dc-link and grid currents increase in the double-stage DC/DC boost converter due to the interaction between the system stages as the continuous perturbations from the P&O controller of the first-stage are seen as disturbances by the second-stage converter. The induced harmonics are shown in line with the P&O duty cycle perturbations as shown in Figure 35.
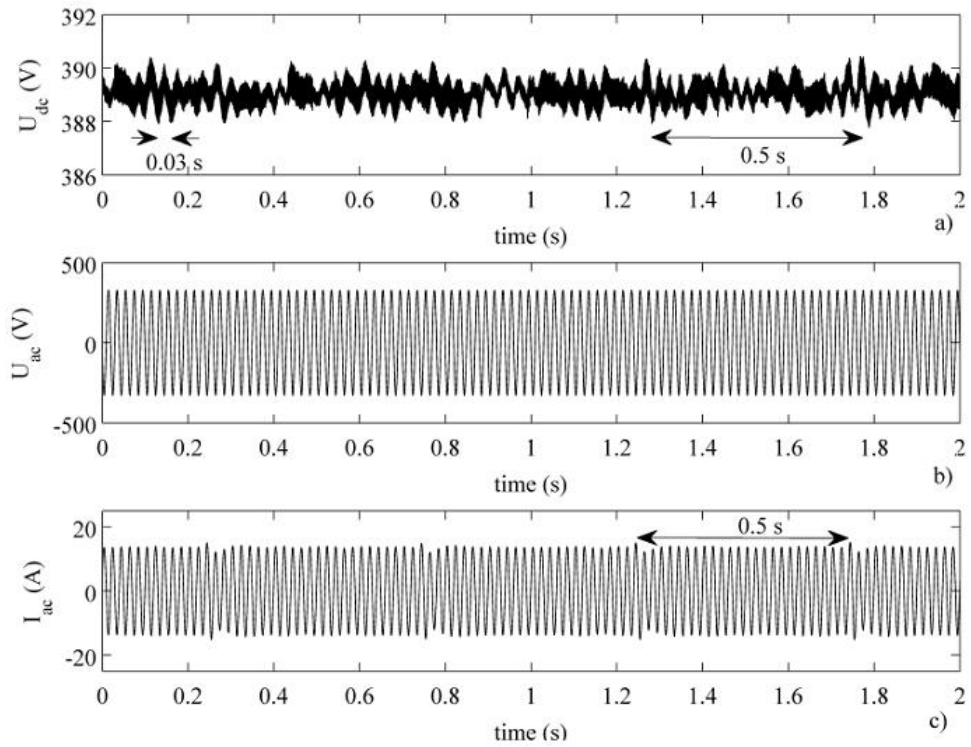
Figure 32: Experimental results of single-stage PV inverter (a) instantaneous input DC voltage, (b) instantaneous output AC voltage, and (c) instantaneous output AC current [16].


I_{sc} [A]	R_{tot} [Ω]	X_{tot} [Ω]	Z_{sc} [Ω]	R_{tot}/X_{tot}
1200 *)	0.19	0.025	0.19	7.6
650	0.349	0.025	0.35	13.9
488	0.380	0.276	0.47	1.4
250	0.898	0.276	0.94	3.2
*) inverters connected directly to point P0				
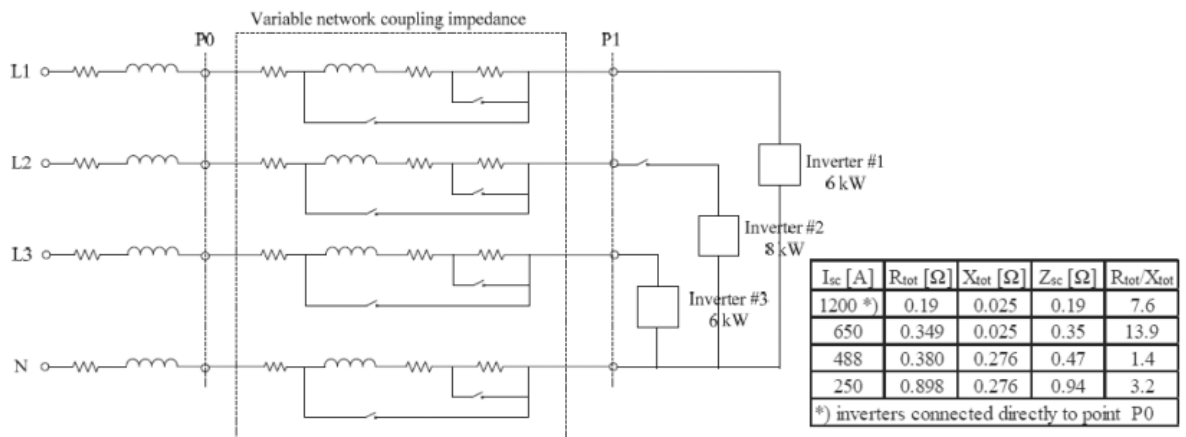
*Figure 33: Measurement setup and the network impedances*
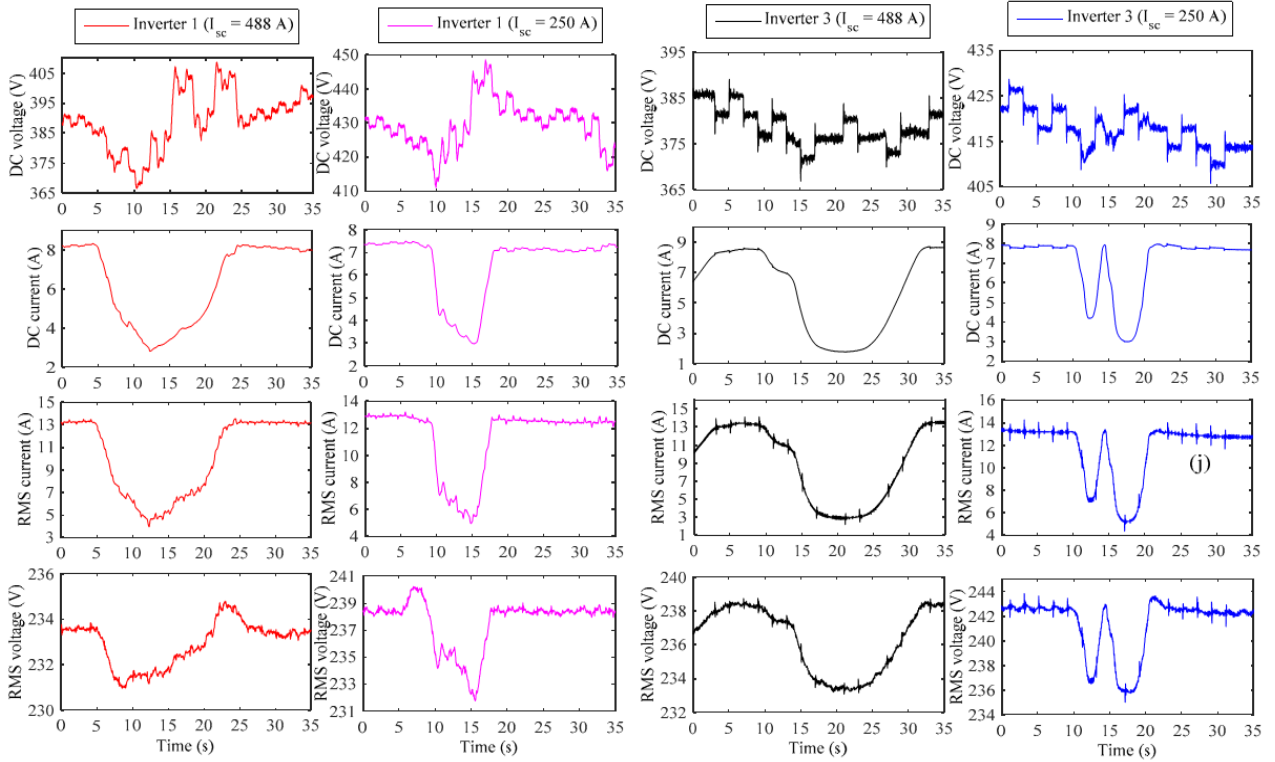
Figure 34: Experimental results of single phase single-stage PV inverters show the current and voltage variations related to the MPP tracker [17].
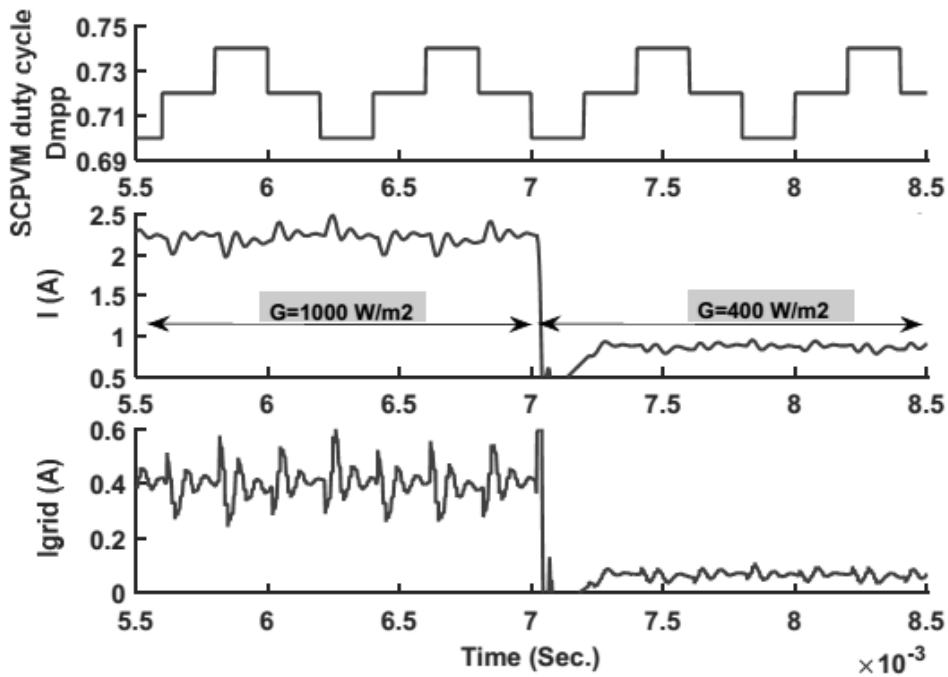

Figure 35: Harmonics in the dc-link current (I) and grid current (I_{grid}) in double-stage DC/DC boost converter [28].

Based on the earlier review on the P&O operation in section 2.3.1.2 and on the results shown at the DC side (i.e. the PV voltage and current) in [16] and [17] in Figure 32 and Figure 34, respectively, it seems that the P&O controller of their systems does not operate in three duty-cycle steps as shown in the DC voltage waveforms of inverter 1

and inverter 3; that might be another factor that increases the harmonics emissions in their systems. According to [38, 39] the perturbing behaviour of the P&O scheme introduces continuous PV power oscillations in the steady-state and transient-response oscillations at each time P&O perturbs. The steady-state oscillation depends mainly on the adopted P&O parameters which are the control parameter step size (e.g. duty-cycle step size in direct duty-cycle P&O controller) and the sampling frequency. The transient-response oscillations depend on the dynamics of the adopted converter topology and the PV module characteristics which is in turn a function of the solar irradiation level and the operating point of the PV module [38]. Accordingly, different converter topologies produce different transient-response oscillations under the same operating conditions. Proper optimisation of P&O controller to all possible operating conditions and to the dynamic behaviour of the specific converter adopted is very important to ensure least undesirable impact of the P&O on the rest of the system. The authors of [39] provide guidelines to properly optimise P&O controller (i.e. to operate in three duty-cycle steps in steady-state) and this also was covered in section 2.3.1.2 in page 18. The most important in the optimisation process is to make sure that P&O decision-making is not affected by transient-response oscillations of the PV voltage and current after each perturbation [39]. Therefore, the operating point leading to the longest transient oscillations (i.e. worst case scenario) must be used when optimising P&O parameters. Otherwise, the P&O controller can be confused leading to increased variations in the PV voltage and current and this give rise to the harmonics generated by the PV system.

The relation between the P&O controllers and the generated harmonics in double-stage parallel SCPVM system is discussed in my published paper in [29]. It highlights that the lowest harmonic frequency (f_{low}) generated in the dc-link and grid currents depends on the P&O sampling time (T_{mppt}) and the number of the P&O duty-cycle steps in steady-state. Thus, f_{low} is expressed as a function of the P&O parameters and it was shown that for optimal system efficiency and three duty-cycle steps operation $f_{low} = 1/(4T_{mppt})$. Some Fast Fourier Transform (FFT) results are provided in [29] as shown in Figure 36 and Figure 37 which show the P&O low-frequency related harmonics in the dc-link voltage and current of the double-stage parallel SCPVM system, respectively. Also, in my work in [29] the transient harmonics in the dc-link and grid sides due to the P&O perturbations are discussed.
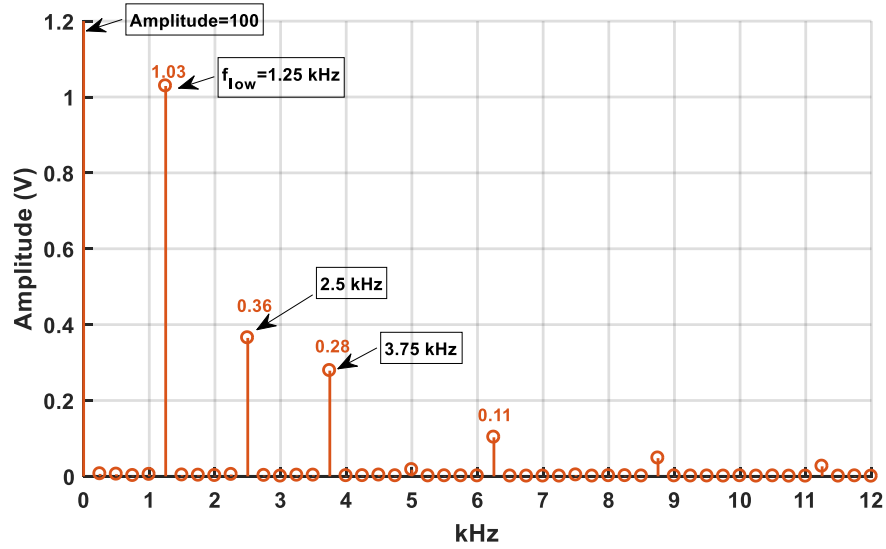
Figure 36: FFT of the dc-link voltage in double-stage parallel SCPVM system for four SCPVM units. System operates at three P&O duty-cycle steps in steady-state and T_{mppt}=0.2 ms [29].
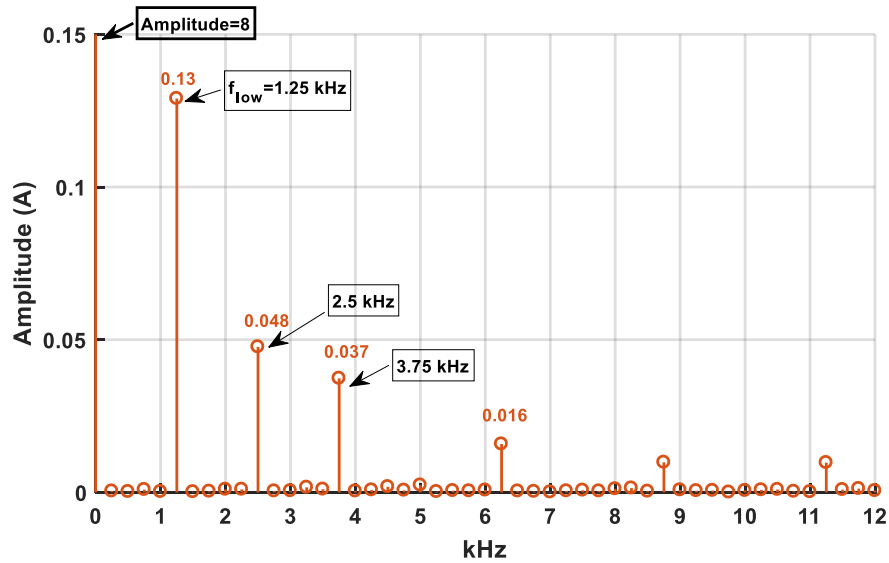

Figure 37: FFT of the dc-link current in double-stage parallel SCPVM system for four SCPVM units. System operates at three P&O duty-cycle steps in steady-state and T_{mppt}=0.2 ms [29].

[30, 31] are the latest studies published in 2018 which are investigating the impact of the P&O controller on increasing the harmonics in grid-connected PV system. In these studies the interharmonics from commercial PV inverter are observed experimentally as shown in Figure 38 and an approach to characterise the frequency and the amplitude of the P&O related interharmonics in the grid current is proposed for single phase PV inverter according to the P&O controller parameters. In [31] it was found that the frequency of the interharmonics (f_n) in the grid current can be expressed as a function

52

of the P&O sampling frequency (f_{MPPT}): $f_n = (2n-1)f_{MPPT}/4$, where n is an integer. Thus, the AC grid current will contain harmonics at $f_g \pm f_n$ frequencies after the amplitude modulation, where f_g is the grid fundamental frequency (e.g. f_g=50Hz). The variation in the grid current amplitude at each harmonics due to the variation in the dc-link voltage perturbations is predicted by decomposing the dc-link reference voltage into a summation of n frequency components (which is function of the P&O sampling frequency and the control-signal step size) and use it as an input to the system close loop transfer function between the dc-link reference voltage and the grid current amplitude. It was found that the perturbation step size of the P&O controller has a strong effect on the amplitude of the interharmonics components. While the sampling rate affect both the amplitude and the frequency of the interharmonics.
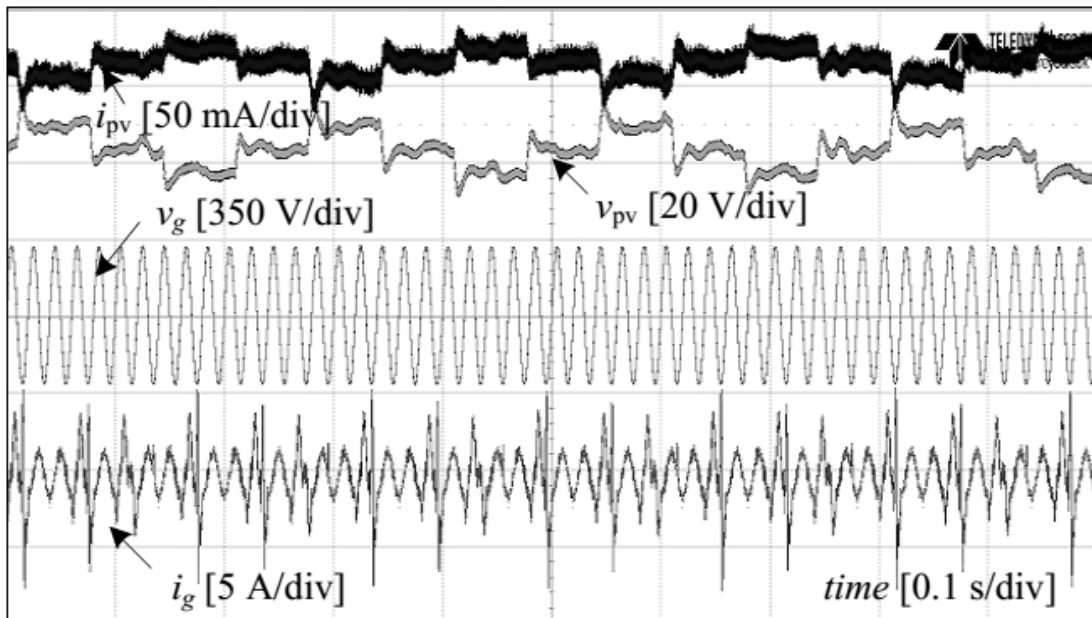

Figure 38: Experimental results from a commercial 15-kW PV inverter operating at 2% of the rated power, where v_{pv} is the PV voltage, i_{pv} is the PV current, v_g is the grid voltage, and i_g is the grid current [30, 31].

The adopted MPPT architecture; centralised or distributed MPPT (see section 2.3.2 page 24), is another factor to be considered when analysing P&O related harmonics in PV systems. From the P&O harmonic point of view, the distributed MPPT architecture is more critical than the centralised architecture because the number of the P&O controllers increases in the system.

2.6.2 Mitigation methods of P&O related harmonics

Since the main reason of the aforementioned generated harmonics in [16, 17, 28-30] is the repeated perturbations of the P&O control parameter, a possible solution could be adopting different MPPT method. As example, the fraction open circuit MPPT method (see section 2.3.1.1) can be used as suggested in [30]. It does not required perturbations in the PV voltage and current [38, 46]. However, this MPPT method leads to very poor system efficiency as the MPP is not always at 76% of the open circuit voltage and keeping it unchanged under different solar irradiation levels and/or temperatures decreases PV system efficiency. Other more advanced methods which can achieve a very small steady-state oscillation, or even completely cancelling it can be used such as, incremental conductance, particle swarm optimisation, extremum seeking and ripple correlation [47-49] as discussed in section 2.3.1.3. However, the implementation of these techniques is more expensive than P&O, sometimes required additional circuit, tuning their parameters is very complex and required more complex software which leads to increased computation time [38, 46]. In addition to that and as discussed in [39], in practice the specific condition which is required to be fulfilled to stop the perturbations is never exactly satisfied because of noise and measurement errors. As a result, it is usually required that such condition is approximately satisfied within a given accuracy and to that the operating point cannot be exactly equal to MPP but oscillates about it.

The P&O related harmonics problem is newly reported in the literature and a specific solution has not been proposed so far. However, some existing filtering methods can also be used to supress the voltage and current variations in the output side of the PV system due to P&O scheme such as passive filters, ripple eliminator circuits, or adopting new control techniques. The most common solution is using passive filters such as using bulk dc-link capacitor. This solution is not desirable as it reduces system reliability and increases losses and cost.

The bulky dc-link capacitor can be replaced by ripple eliminator circuit connected in parallel with a smaller dc-link capacitor. For instance, in the literature the ripple eliminator circuit is used to eliminate dc-link variations caused by a three-phase unbalanced ac load [84], switching ripple from an input source [85], second-order ripple power in a single phase PWM rectifier [86], and power fluctuations from renewable energy sources [87]. However, this solution required adding extra power

electronic circuit and control-loop to the system which increases system physical size, complexity and cost.

Alternative solutions might be new control techniques such as those proposed in [88], [89] and [90] to overcome dc-link variation caused by resonance under unbalanced loads condition, poorly damped *LC* circuit and interaction between micro-grid clusters, respectively. The advantages of these solutions are no additional power electronic circuit is required, power quality and efficiency are improved at low cost.

2.7 Conclusion

In this chapter the characteristics of the non-linear PV source, MPPT techniques, configurations and topologies of grid-connected PV system, and controller structures for different operating modes (i.e. grid-connected and islanded modes) have been studied. In addition to that, two concerns for grid-connected PV system have been discussed. The first concern is related to the effect of the non-linear PV source on the dynamic performance of the system such as system damping factor, phase margin, and cut-off frequency. It was found that the impact of the non-linear PV source depends on system controller structure in terms of controlling the input side or the output side of the PV interface converter. In case of controlling the input side the system damping factor and cut-off frequency are mostly affected. In case of controlling the output side (this is applied in case of islanded mode operation) the non-linear PV source changes the system dynamic and may generate a right half plane roots which affect system stability depending on the converter topology and the PV operating region. The second concern is related to the poor power quality from grid-connected PV systems. It has been reported that grid-connected PV systems is one of the sources which deliver harmonics to the grid due to[10-15][10-15][10-15][10-15][10-15] many reasons such as large populations of PV inverters, resonance between the grid and the PV inverter, or large amount of fluctuating in PV power[12, 15][12, 15][12, 15][12, 15][12, 15]. In addition to the aforementioned sources of harmonics in PV systems, recent studies have reported that there is possible impact of P&O controller on increasing the harmonics in PV grid-connected systems, which leads to a poor power quality from the PV system. P&O technique is widely used in commercial products, especially for low-cost implementations which make the newly reported P&O related harmonics problem a subject undergoing intense study and researchers are persuaded to find a solution.

As discussed in this chapter there are several configurations to connect a PV system to the grid and each configuration leads to different converter topologies and P&O architectures (centralised or distributed P&O). Therefore, it is difficult to generalise the effect of the PV system on the power quality in the grid. In this work, the main focus is on double-stage parallel SCPVM configuration connected to a DC bus. As has been discussed in section 2.4.1 this cofiguration is capable to provide: high-step-up voltage, low cost, simple and provide high MPPT performance.A DC/DC boost converter is considered for both system stages as will be shown in the next chapter.

3 DESIGN CONSIDERATIONS OF THE DOUBLE-STAGE PV SYSTEM CONNECTED TO A MAIN DC BUS

3.1 Abstract

In this chapter the design considerations of the SCPVM unit in double-stage DC/DC boost converter is discussed. First, the available range of the dc-link voltage for successful tracking of MPP has been identified. Then, the effect of that voltage range on the first-stage converter parameters (e.g. inductance and capacitance) under different weather condition is analysed. After designing SCPVM unit the P&O parameters (T_{mppt} and Δd) are optimised based on the dynamic behaviour of the first-stage converter and the adopted PV module. Then, a brief discussion of the different controller types that can be used to control the common dc-link bus in grid-connected mode such as the voltage mode and cascaded current-voltage controllers is provided with a summary of the designed controllers. Finally, time domain simulation for the designed system is provided and discussed.

3.2 Overall System Structure and Parameters

Different PV system configurations has been discussed in section 2.4, page 25, the double-stage parallel SCPVM configuration connected to a main DC bus, as shown in Figure 39 is investigated in this research. It offers advantages in minimising shading effects, improving system modularity, improving MPPT performance and efficiency, boosting up the voltage, and providing the same voltage level at the output of each SCPVM under mismatching conditions. Each SCPVM consists of a DC/DC boost converter, a PV module (type NU-E240 is used as an example; see Table 2, page 16 for its specifications) and a MPPT digital controller. For the second-stage converter a DC/DC boost converter is adopted in order to boost the dc-link voltage V_{dc} to the required main DC bus voltage V_{grid}. It is generally suggested that the main DC bus in a future DC system should be regulated at a voltage level in the range of 380-400V, since this voltage level can meet the industry standard for consumer electronics with the power factor correction circuit at the input [20, 91]. Also, this voltage level offers good efficiency when supplying high-demanding loads (e.g. hybrid electric vehicle chargers, washing machines) [20]. However, in this work V_{grid} is selected to be 200V due to some constrains in the practical work of this research such as the power rating of the programmable electronic load which is used to emulate the main DC bus voltage. This

is acceptable as V_{grid} level does not affect the main findings and contribution of this research.

The controller implementation is based on the assumption that the PV system is in grid-connected mode or in islanded mode and the storage system capacity is large enough to allow MPP tracking all the time. The first-stage controller is responsible for MPPT and a direct duty cycle P&O method is adopted. The controller of the second-stage converter controls the dc-link voltage V_{dc} at constant value. Some dc-link controllers for regulating V_{dc} such as voltage mode, and cascaded current-voltage controllers will be discussed in details in Chapter 5. The output voltage of the second-stage converter is controlled either by the bidirectional AC/DC inverter which connects the main DC bus to the AC network, or by a storage system converter.

The PV system standards require a very small tolerance between PV modules specifications and characteristics for high system performance [92]. In consequence, all the PV modules in this work are assumed to be identical and manufactured by the same firm.
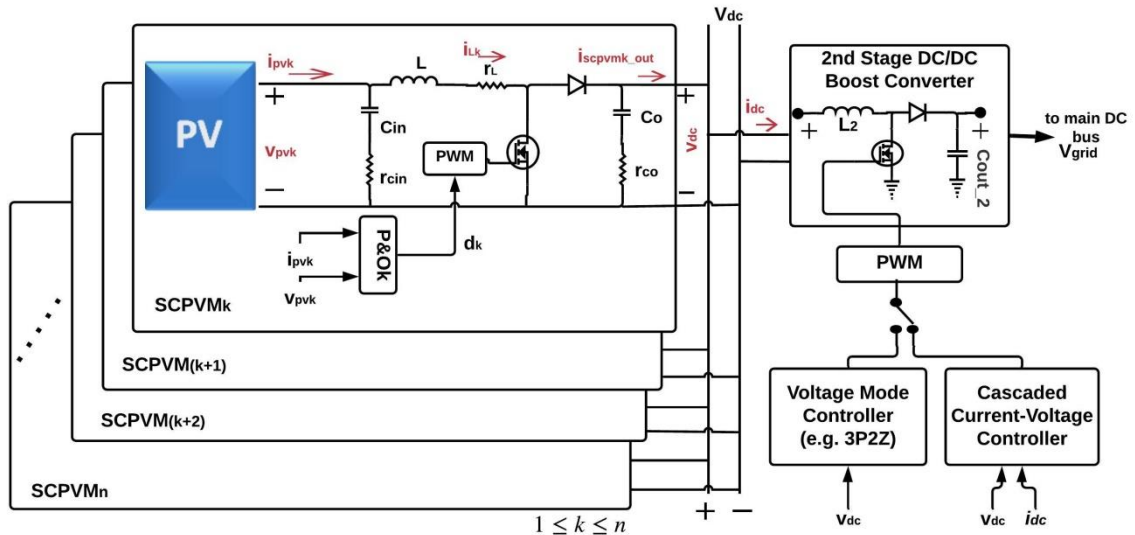

Figure 39: Double-stage parallel SCPVM configuration connected to a main DC bus.

3.3 Parameters and P&O Design of a SCPVM Unit

There are two key points to be considered when designing a SCPVM unit, namely the limitation on the output voltage to ensure the P&O is functioning under all weather conditions and the effect of changes in weather conditions and dc-link voltage V_{dc} on the first-stage converter parameters.

3.3.1 DC-link voltage selection for MPPT mode

This section shows that even when high efficiency DC/DC converter and high performance MPPT algorithm, the MPP cannot be achieved. This is because MPPT depends on the load profile and on the static features of the DC/DC converter. In [93] the authors present an analysis of MPPT limitation when different types of DC/DC converters (buck, boost, buck-boost, and cúk) are used. The analysis considered a resistive load at the output. Since the Boost converter is adopted in this work, the method in [93] was followed to check the limitation of the MPPT for the boost converter with constant voltage at the output. The maximum duty cycle limit is defined at 0.9. The required duty cycle (D_{mppt}) for the boost converter to obtain the maximum power from the PV module can be found from the basic voltage gain equation of DC/DC boost converter in [74].

$$\frac{V_{out}}{V_{in}} = \frac{1}{1-D}$$

(3.1)

If the system operates at MPP, the PV voltage will be $V_{in} = V_{mpp}^{STC}$ (the maximum power point voltage at Standard Test Conditions STC) and if the output voltage is regulated at constant voltage V_{dc}, then the output voltage is constant and $V_{out} = V_{dc}$. Assuming a converter efficiency of 100% ($i.e.$ $P_{in} = P_{mpp} = P_{out}$), the duty cycle is given by:

$$D_{mppt} = 1 - \frac{V_{mpp}^{STC}}{V_{dc}}$$

(3.2)

Under different solar irradiation levels and constant temperature conditions, V_{mpp} changes very slightly and can be assumed to be constant (equal to V_{mpp}^{STC}). This means that both the input voltage and the output voltage of the boost converter are constant, thus D_{mppt} is equal for the different solar irradiation levels. The situation will be different if the effect of changing the cell temperature is included because V_{mpp} will not be constant in this case.

Figure 40 shows the required duty cycle for the highest and lowest irradiation levels to achieve the maximum power point for different values of the output voltage V_{dc}. It shows that D_{mppt} is equal for different irradiation conditions for one output voltage level and it hits its maximum defined limit of $D_{max} = 0.9$ at 290V. Therefore, for the

tested system under constant temperature conditions, the dc-link voltage limit is given by:

$$V_{mpp}^{STC} < V_{dc} < \frac{V_{mpp}^{STC}}{1 - D_{max}}$$

(3.3)

And for NU-E240 PV module (see Table 2, page 16 for its specifications):

$$29V < V_{dc} < 290V$$

(3.4)

Therefore, V_{dc} is selected to be controlled at 50V.

3.3.2 Inductance and capacitance selection

In this part, first-stage converter parameters (i.e. inductance L and capacitance C_o) selection will be analysed considering the output voltage range in (3.4). The inductance L of the first stage converter can be found from the following equation [74]:

$$L \geq \frac{V_{in} D_{mppt}}{\Delta i_{L\_pp} f_{sw1}}$$

(3.5)

Where, $V_{in} = V_{mpp}^{STC}$, Δi_{L_pp} is the peak-peak inductor current ripple, f_{sw1} is the switching frequency of the first-stage converter.

In general, the peak-peak current ripple Δi_{L_pp} in (3.5) can be selected based on the minimum current ripple requirement for the highest PV module current (i.e. the highest solar irradiation) or for the lowest current (i.e. the lowest solar irradiation). Figure 41 shows the effect of changing the solar irradiation and SCPVM output voltage V_{dc} (within the limit in (3.4)) on L_{min} based on (3.6).

$$L_{min} = \frac{V_{mpp}^{STC}}{\Delta i_{L\_pp,max} f_{sw1}} \left(1 - \frac{V_{mpp}^{STC}}{V_{dc}} \right)$$

(3.6)

Where $\Delta i_{L_{pp},max}$ is defined as a percentage of the PV module current (a value of 13% is used in Figure 41). As shown in Figure 41 low solar irradiation conditions present the worse-case design requirement. However, other factors have to be considered such

as the inductance core size, and power production in deciding which operating point to use for the design.
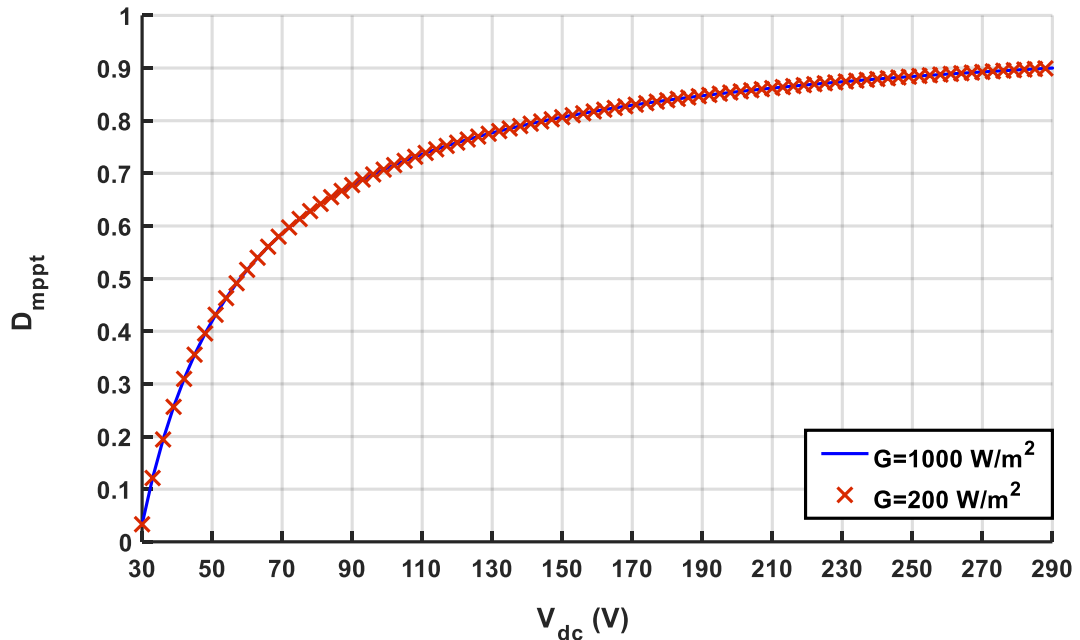

Figure 40: Effect of solar irradiation level ($1000\ W/m^2$ & $200\ W/m^2$) for different values of V_{dc} on D_{mppt} of the first stage converter.

If L is designed based on the highest irradiation, the result is smaller inductance than for the lowest irradiation as shown in Figure 41. In this case the core size will be smaller [94]. However, two key drawbacks can be identified. First, at lower solar irradiation the current ripple amplitude accounts for the higher percentage of the total current and thus the captured energy will be lower than in the case if the higher inductance were used [94]. Second, under the conditions of low input current (i.e. low solar irradiation) the converter might operate in discontinuous conduction mode (DCM).

If L is designed based on the lowest irradiation a higher inductance is needed, then the loss of the captured energy from PV is minimal at the low irradiation levels [94]. However, for this case the core size has to be designed for the highest current ($i_{l,max}$) to avoid magnetic saturation. As the core size is proportional to the stored energy in the inductor ($E = \frac{1}{2}i_{l,max}^2 L$), designing L based on the lowest irradiation will result in a bigger core size than the case if the higher solar irradiation were used for designing L [94].
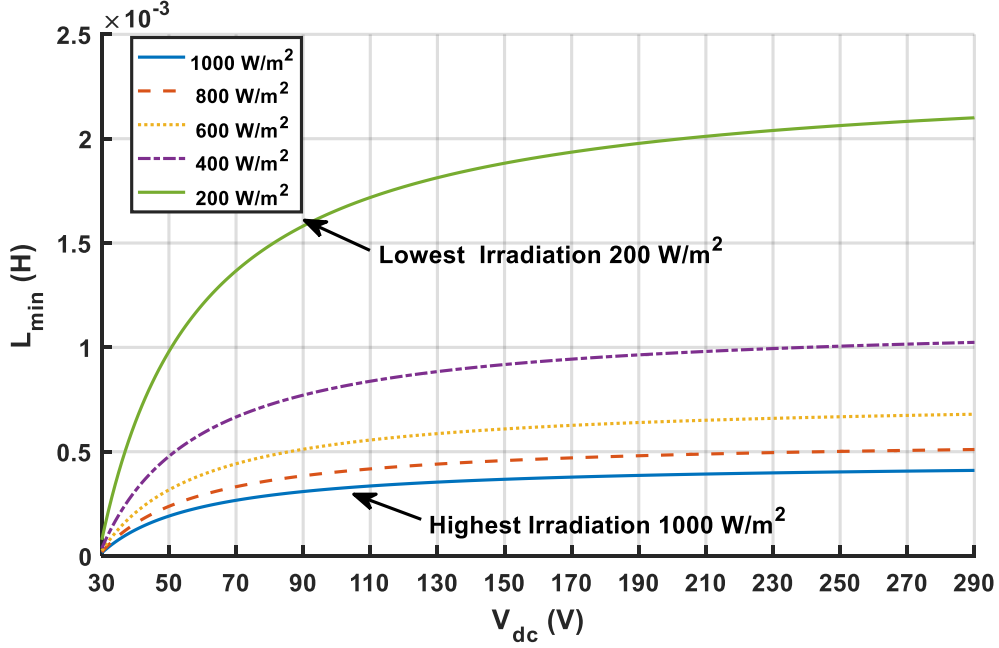
Figure 41: Effect of solar irradiation level ($1000\ W/m^2$ to $200\ W/m^2$) for different levels of V_{dc} on the first stage converter inductance value.(Δi_{L_pp} =13% and f_{sw1} =60kHz).

Thus, aiming for the small inductance core, high irradiation is used for designing L. DCM at low solar irradiation level can be avoided by opting for the current ripple to be less than twice the minimum current at the lowest irradiation. For instance, if the dc-link voltage is controlled at 50V, L should be equal or greater than 0.19 mH to ensure less than 13% peak-peak inductor current ripple at the high solar irradiation level (i.e. for NU-E240 and $G = 1000\ W/m^2$, $\Delta i_{L\_pp} = 0.13 \times 8.15 = 1.06A$) as shown in Figure 41. The PV current of NU-E240 at the lowest solar irradiation of 200 W/m^2 is 1.6A and since 2×1.6A=3.2A is higher than Δi_{L_pp}, the DCM is avoided. So, a value of 0.212 mH is selected.

The capacitance (C_o) can be found from equation (3.7) [74]. The effect of the irradiation level and the SCPVM output voltage V_{dc} (within the limit in (3.4)) on the capacitance value is shown in Figure 42 for a peak to peak dc-link voltage ripple $\left(\Delta v_{dc\_pp}\right)$ requirement of 3%. The highest irradiation level presents the worst case scenario.

$$C_{o\_min} = \frac{I_{scpvm\_out}\, D_{mppt}}{\Delta v_{dc\_pp} f_{sw1}} \tag{3.7}$$

62

where $I_{scpvm\_out} = (1 - D_{mppt})I_{pv}$. Figure 42 shows that increasing the output voltage will reduce the required capacitance; however, this will increase the duty cycle which affects the inductor copper losses and the semiconductor conduction losses [74]. Also, going back to the inductance design, increasing the output voltage will increase the inductance value. Another point that has to be considered when choosing the capacitance is the chosen PV system configuration. As example, in case of series connection of SCPVM, the voltage across each SCPVM will vary randomly in case of the non-uniform solar irradiation [38]. Therefore, in order to meet the minimum voltage ripple requirement the worst case operating condition has to be considered in the design of C_o. This limitation is not applied in the case of parallel connections which give more flexibility in choosing C$_o$ depending on the regulated DC-link voltage.
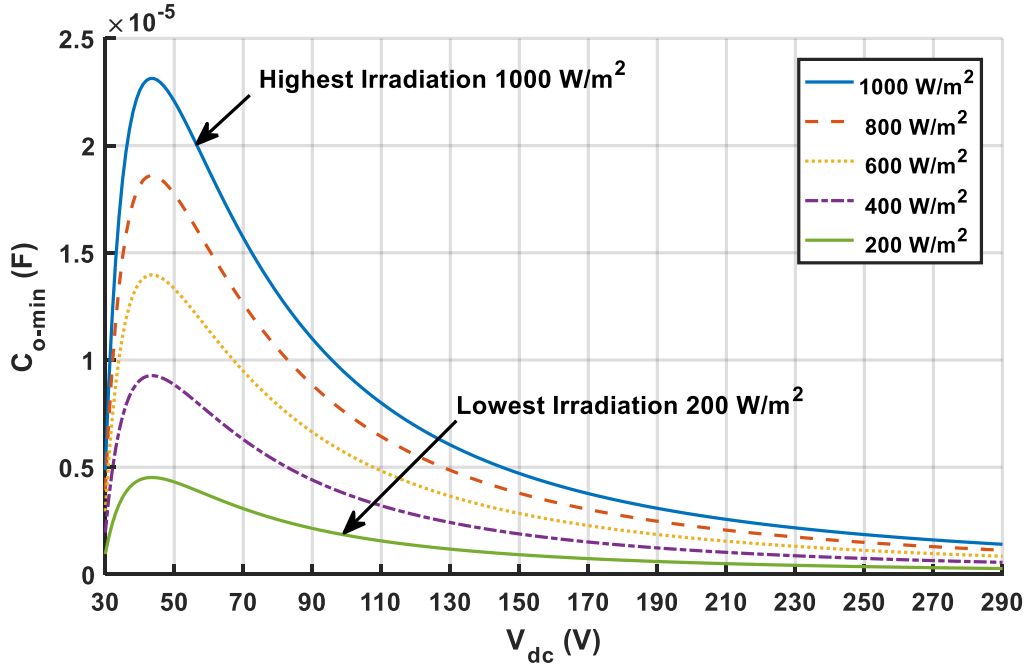

Figure 42: Effect of solar irradiation level ($1000 \ W/m^2$ & $200 \ W/m^2$) for different V_{dc} values on the first-stage output capacitance design. (Δv_{p-p}=3% & f_{sw1} =60kHz).

As the dc-link voltage is selected to be controlled at 50V, C_o is selected to be 22 µF and this will result in 1.5V peak-peak voltage ripple $(\Delta v_{dc\_pp} = 0.03 \times 50 = 1.5V)$.

Table 4 summaries the parameters of the first-stage DC/DC boost converter.

Table 4: Parameters of the first-stage converter

Symbol & Glossary		Value
L	Inductance of the first-stage converter inductor	0.212 mH
C_o	Capacitance of the output capacitor of the first-stage converter	22 μF
C_{in}	Capacitance of the input capacitor of the first-stage converter	2.2 μF[(*)]

[*] C_{in} value is chosen based on simulation tests to ensure a good value to fairly filter out the switching ripple of the inductor current and at the same time avoid worsening the dynamic performance of the system as MPPT sampling period is affected by its value.

3.3.3 P&O optimisation

Two parameters are required to be optimised: the sampling period (T_{mppt}) and the step size Δd. The sampling period has to be greater than the PV power settling time T_ε as was given in (2.15):

$$T_{mppt} \geq T_\varepsilon = -\frac{1}{\zeta \omega_n}. \ln(\varepsilon/2)$$

$\varepsilon = 0.1$ gives a reasonable threshold. The values of ω_n and ζ can be found from the small signal duty cycle to PV module voltage transfer function as given in (3.8) [38]; with reference to Figure 39.

$$G_{v_{pv},d}(s) = \frac{\hat{v}_{pv}(s)}{\hat{d}(s)} = -\frac{V_{dc}}{L.C_{in}} \frac{(1+r_{C_{in}} C_{in}s)}{\left(s^2 + 2\left(\frac{1}{2r_{pv}}\sqrt{\frac{L}{C_{in}}} + \frac{r_{C_{in}}+r_l}{2}\sqrt{\frac{C_{in}}{L}}\right)\left(\frac{1}{\sqrt{L.C_{in}}}\right)s + \frac{1}{L.C_{in}}\right)} \quad (3.8)$$

For ideal boost converter (3.8) can be assumed to be equal to (2.12). Therefore, ω_n and ζ can be expressed as the following:

$$\zeta = \frac{1}{2r_{pv}}\sqrt{\frac{L}{C_{in}}} + \frac{r_{C_{in}}+r_l}{2}\sqrt{\frac{C_{in}}{L}} \quad (3.9)$$

$$\omega_n = \frac{1}{\sqrt{L.C_{in}}} \quad (3.10)$$

Where, r_{pv} is given in (2.7) and the rest of the parameters in (3.9) and (3.10) are given in Table 4. The minimum T_{mppt} for boost converter can be found by inserting equations (3.9) and (3.10) in (2.15):

$$T_{mppt} \geq -\frac{2r_{pv}\sqrt{L.C_{in}}}{\sqrt{\dfrac{L}{C_{in}}} + \dfrac{r_{C_{in}} + r_l}{2}\sqrt{\dfrac{C_{in}}{L}}}.\ln(\mathcal{E}/2) \qquad (3.11)$$

As seen in (3.11) T_{mppt} is function of r_{pv} which in turn changes with solar irradiation level and PV module (v_{pv}) voltage as given in (2.7).

The results of the r_{pv} calculated based on (2.7) and the minimum sampling rate at different PV module voltages for the highest and lowest solar irradiation level are given in Table 5. Lower PV module voltage and/or solar irradiation level result in longer T_{mppt}.

Table 5: Minimum P&O sampling period (analytical calculation)

G (W/m²)	V_{pv}=27V		V_{pv}=29V (MPP voltage)		V_{pv}=31V	
	r_{pv} (Ω)	T_{mppt} (ms) ≥	r_{pv} (Ω)	T_{mppt} (ms) ≥	r_{pv} (Ω)	T_{mppt} (ms) ≥
1000	11.1	0.08	4.2	0.05	1.9	0.02
200	40.7	0.17	14.3	0.13	5.3	0.06

The PV module power settling times T_{ε} can be also estimated through simulating the SCPVM unit with a small unit step change in the duty-cycle. The simulation results in Figure 43 are determined by connecting a single SCPVM unit to a stiff 50V voltage. The duty cycle is adjusted to achieve the required testing point (i.e. the PV module voltage). The irradiation is kept constant (200 W/m² solar irradiation is considered) then a small step change in the duty cycle is applied (0.003 step change). The results in Figure 43 for G=200 W/m² show very close values to the analytical calculated values in Table 5. The slight difference is because in the analytical calculation an estimated values of r_{pv} and ζ were used, which were obtained based on the equivalent linear model while in the simulation a non-linear model of PV module was used. However, both results in Table 5 and Figure 43 show that the lower V_{pv} and/or G the longer time is required for the PV module power to settle and so longer sampling period T_{mppt} is needed. Therefore, for the adopted system to operate in three steps in steady state the minimum value of T_{mppt} is:

$$T_{mppt} \geq 0.2\,ms \qquad (3.12)$$

In this work 0.35 ms is considered for T_{mppt}.

The step size Δd can be found from (2.10). As the value of Δd depends on the average rate of change in the solar irradiation ($\dot{G}$) and that depends on the location site of the PV system, in this work it was assumed that the maximum $\dot{G}$ is 100 W/m^2.s. Table 6 shows the minimum value Δd for high, medium and low solar irradiation for the selected T_{mppt} of 0.35 ms. The solar irradiation leading to the highest value of Δd must be used which is the lowest solar irradiation as shown in Table 6. Therefore, the minimum value of Δd is as follow:

$$\Delta d \geq 0.006 \tag{3.13}$$
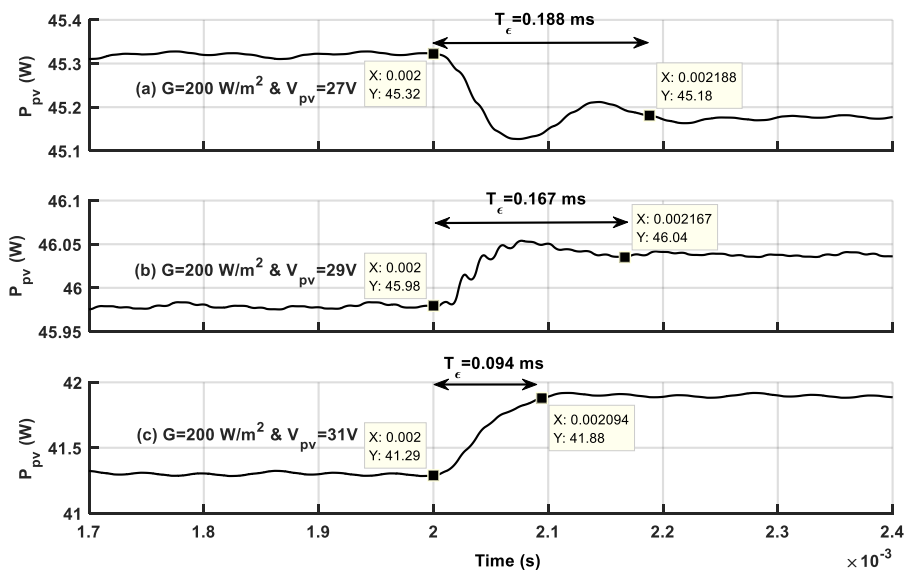
Figure 43: Duty-cycle step change of 0.003 to determine T_ε for G=200 W/m^2: top to bottom (a) V_{pv}=27V, (b) V_{pv}=29 V, and (c) V_{pv}=31V.

Table 6: Minimum P&O step size (Δd)

G	1000 W/m^2	700 W/m^2	200 W/m^2
$\dot{G}$	100 W/m^2.s	100 W/m^2.s	100 W/m^2.s
T_{mppt}	0.35 ms	0.35 ms	0.35 ms
Δd>	0.002	0.003	0.006

Figure 44 shows the simulation results of the first stage converter with Δd=0.006 and 200 W/m^2 solar irradiation.
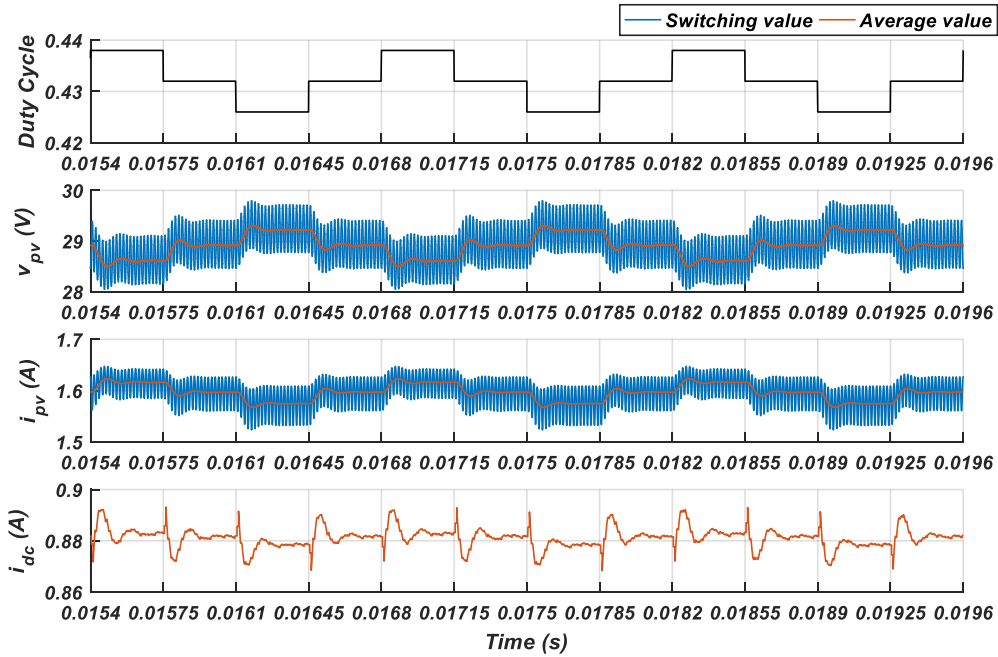
Figure 44: Simulation result of the first-stage converter with Δd=0.006,$T_{mppt} = 0.35ms$, and $G = 200\ W/m^2$.

It should be highlighted that the results in Table 6 only take into account the variation of the irradiance level. Other factors which affect the level of the PV power variation such as the variation of the input capacitor voltage, and measurement noise in the system have not been considered. So, in practice the value of Δd is most likely to be bigger than the analytical value given in Table 6. Also, as has been discussed in section 2.3.1.2 the value of Δd must be chosen to ensure a good compromise between the system transient and steady-state performance. Therefore, Δd is chosen to be 0.035 to ensure three-step P&O duty cycle operation. The parameters of the SCPVM unit are shown in Table 7.

3.4   Parameters of the Second-stage Converter

The second-stage converter is designed for a conversion ratio of 4 to boost up the voltage from 50V to 200V. Its power rating is based on a system that consists of two SCPVM units. The second-stage parameters C$_{out\_2}$ and L$_2$ are selected so that the peak-peak output voltage (V_{grid}) ripple is less than 1.5V (0.75% of V_{grid}) and the peak-peak current ripple is less than 1.2A (13% of I_{dc}), respectively for the case when the SCPVM units operate under the highest solar irradiation level. The minimum limit

values of the second-stage inductance and capacitance were found to be 0.52 mH and 11μF, respectively. Thus, 0.6 mH and 47 μF values are used for L₂ and C_out_2, respectively.

Table 8 summaries the parameters of the second-stage converter.

Table 7: SCPVM unit parameters

	Symbol & Glossary	Value	
L	Inductance of the input inductor of the first-stage converter	0.212	mH
$r_l^{(*)}$	Resistance of the input inductor of the first-stage converter	0.77	Ω
C_o	Capacitance of the output capacitor of the first-stage converter	22	μF
$r_{Co}^{(*)}$	Resistance of the output capacitor	1.2	Ω
$C_{in}^{(*)}$	Capacitance of the input capacitor of the first-stage converter	2.2	μF
$r_{Cin}^{(*)}$	Resistance of the input capacitor	2.5	Ω
f_{sw1}	Switching frequency	60	kHz
T_{mppt}	P&O sampling period	0.35	ms
Δd	P&O step size	0.035	

*The value is measured in the lab

Table 8: Second-stage converter parameters

	Symbol & Glossary	Value	
L_2	Inductance of the input inductor of the second-stage converter	0.6	mH
$r_{l2}^{(*)}$	Resistance of the input inductor of the second-stage converter	6.4	mΩ
C_{out_2}	Capacitance of the output capacitor of the second-stage converter	47	μF
$r_{Cout\_2}^{(*)}$	Resistance of the output capacitor of the second-stage converter	0.54	Ω
f_{sw2}	Switching frequency of the second-stage converter	60	kHz

*The value is measured in the lab

In grid-connected mode the second-stage converter is responsible for controlling the dc-link voltage V_{dc}. Chapter 5 provides full details of designing three different types of controller: Proportional Integral (PI), Three-pole two-zero (3P2Z), and cascaded current-voltage controllers. As it will be shown in Chapter 5 the traditional voltage mode PI controller is not suitable to control a second order power stage converter (as in our case), the -180° phase delay incurred by the power stage double pole result in an insufficient phase margin when the cut-off frequency is greater than the power stage double pole and that affect system stability. To overcome this problem a higher order voltage mode controller or a cascaded current-voltage PI controllers can be used, that depends on the power rating of the system. Typically a PV system over 1 kW is controlled by cascaded current-voltage controller to control the current transient and avoid failure due to high transient peaks. A voltage mode 3P2Z controller can be used in applications of less than 1 kW power rating. A summary of the designed 3P2Z and cascaded controllers is given in Table 9. More details on designing the controller will be provided in Chapter 5.

3.5 The dc-link Capacitance

The dc-link capacitance (C_{dc}) is defined as the sum of the capacitance values connected in parallel to the dc-link bus which depends on the output capacitance values of the SCPVM units (i.e. C_{o1}, C_{o2},…,C_{on}), thus for n-parallel connected SCPVM units the dc-link capacitance is:

$$C_{dc} = \sum_{k=1}^{k=n} C_{ok} \tag{3.14}$$

Table 9: 3P2Z and cascaded controllers specifications

Controller type	Designed controller	Specifications	
		f_c	PM
3P2Z	$H_c(s) = \dfrac{k_v}{s} \dfrac{(1+\frac{s}{\omega_{z1}})(1+\frac{s}{\omega_{z2}})}{(1+\frac{s}{\omega_{p1}})(1+\frac{s}{\omega_{p2}})} = \dfrac{-222}{s} \dfrac{(1+\frac{s}{4.9\times10^3})(1+\frac{s}{1.2308\times10^4})}{(1+\frac{s}{1.79\times10^4})(1+\frac{s}{1.0996\times10^5})}$	4.86 kHz	47.5°
Cascaded current-voltage	$H_{cv}(S) = K_{pv} + \dfrac{K_{iv}}{s} = -1 + \dfrac{-10^4}{s}$	3.91 kHz	67.8°
	$H_{ci}(S) = K_{pi} + \dfrac{K_{ii}}{s} = 38 + \dfrac{1.33\times10^6}{s}$	11.2 kHz	63.7°
	K_v : Voltage gain of the 3P2Z controller K_{pv}: Proportional voltage gain of the cascaded controller K_{iv}: Integral voltage gain of the cascaded controller K_{pi}: Proportional current gain of the cascaded controller K_{ii}: Integral current gain of the cascaded controller f_c : Control loop gain cut-off frequency PM: Phase margin		

3.6 Simulation Results

The system has been simulated using MATLAB Simulink software with the set of parameter values depicted in Table 7 and

Table 8 for the SCPVM unit and the second-stage converter, respectively. The simulink model of the whole system is shown in Appendix C. The model in [37] is used to implement the PV module as given in Appendix C.1. Direct duty cycle P&O MPPT controller as given in Appendix C.2 is used for the first-stage converter. The system is tested with single SCPVM unit and two SCPVM units connected to the second-stage converter.

3.6.1 Simulation results of a single SCPVM unit connected to the second-stage converter

Figure 45 shows simulation results of one SCPVM unit connected to the second-stage converter with a voltage mode 3P2Z controller. The results show the three-step operation of the P&O controller which results in a periodic oscillation across the MPP in the PV module voltage and current (v_{pv} and i_{pv}) in steady state. This periodic oscillation has been highlighted as the main disadvantage of the P&O controller that degrades its efficiency, as discussed in section 2.3.1.2, page 18. However, the P&O controller is widely used for its simplicity and low cost. The P&O is not only affecting v_{pv} and i_{pv}, from Figure 45 it can be seen clearly that oscillations are observed in both the dc-link and grid waveforms (referred to as low frequency oscillation (f_{low}) and transient oscillations in Figure 45). That mainly due to constant change in steady-state operating points of the SCPVM unit as the P&O controller perturbs every T_{mppt}.

Figure 46 shows the Fast Fourier Transform (FFT) analysis of the voltages and currents waveforms in Figure 45. It shows that the highest harmonic level of the dc-link and grid current occurs at a frequency (referred to as f_{low} in Figure 45 and Figure 46) associated with a time period equal to four times the P&O sampling period ($f_{low} = 1/(4T_{mppt})$). That is because under three-step P&O operation the overall waveforms shape will be repeated through time every $4T_{mppt}$. Figure 46 also shows that other dominant harmonics amplitudes occur at frequencies that are multiple of f_{low} (e.g. $2f_{low}$, $3f_{low}$, $4f_{low}$, $5f_{low}$,.. etc.).
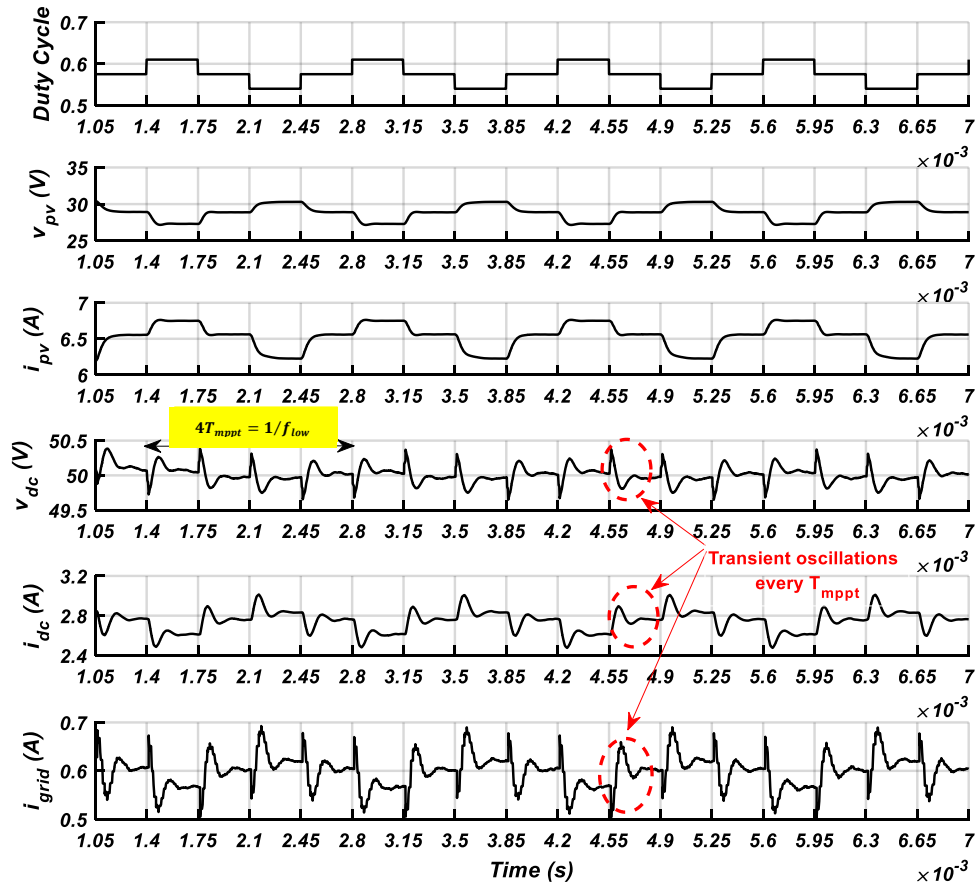
Figure 45: Simulation results of one SCPVM unit connected to the second-stage converter with 3P2Z controller (Table 9). $G = 800W/m^2$, $\Delta d=0.035$, $T_{mppt}=0.35ms$, $C_{dc}=C_o=22\mu F$, $V_{grid}=200V$.

71
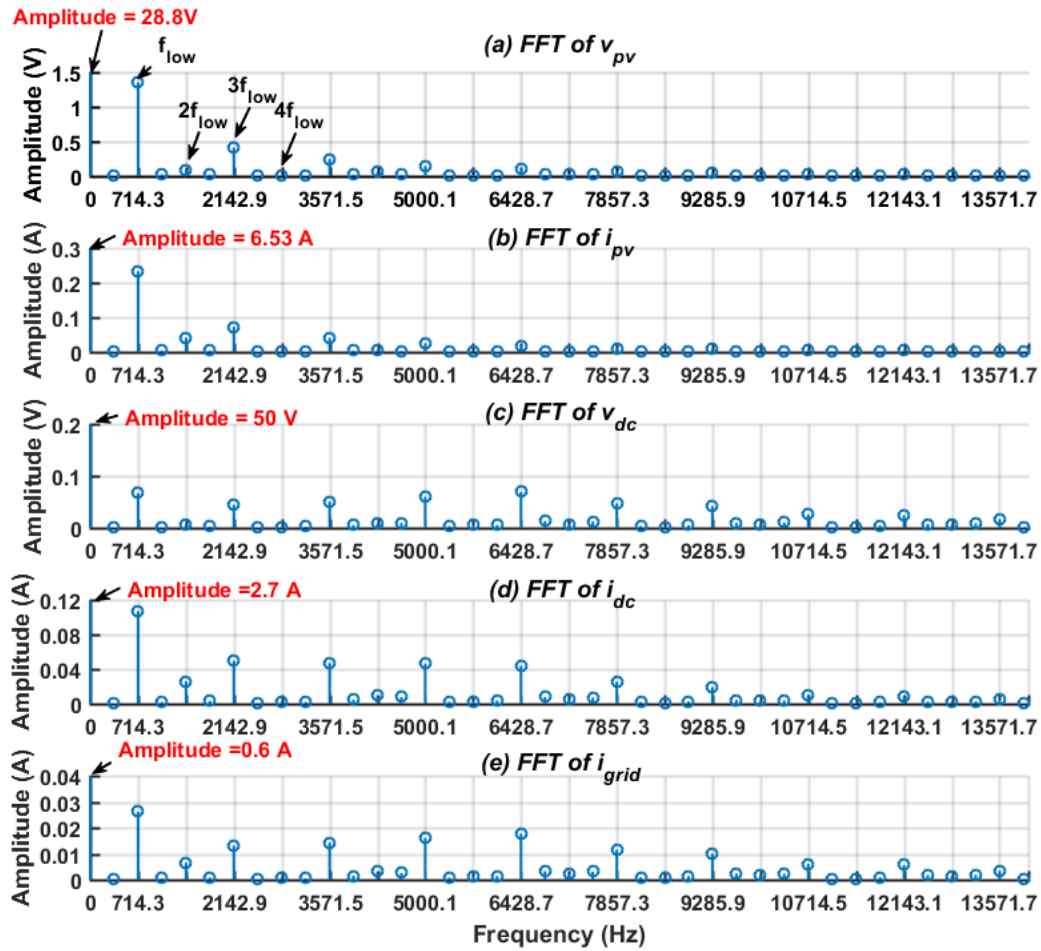
Figure 46: FFT of waveforms in Figure 45: from top to bottom FFT of (a) v_{pv}, (b) i_{pv}, (c) v_{dc}, (d) i_{dc}, and (e) i_{grid}

Another example of simulation results with a cascaded current-voltage controller employed for controlling V_{dc} is shown in Figure 47. Similar to the pervious simulation results steady-state oscillations at f_{low} and transient oscillations every T_{mppt} are observed in the dc-link and grid waveforms. Also, the FFT results in Figure 48 show the dominant harmonics at frequencies that are multiple of f_{low}.
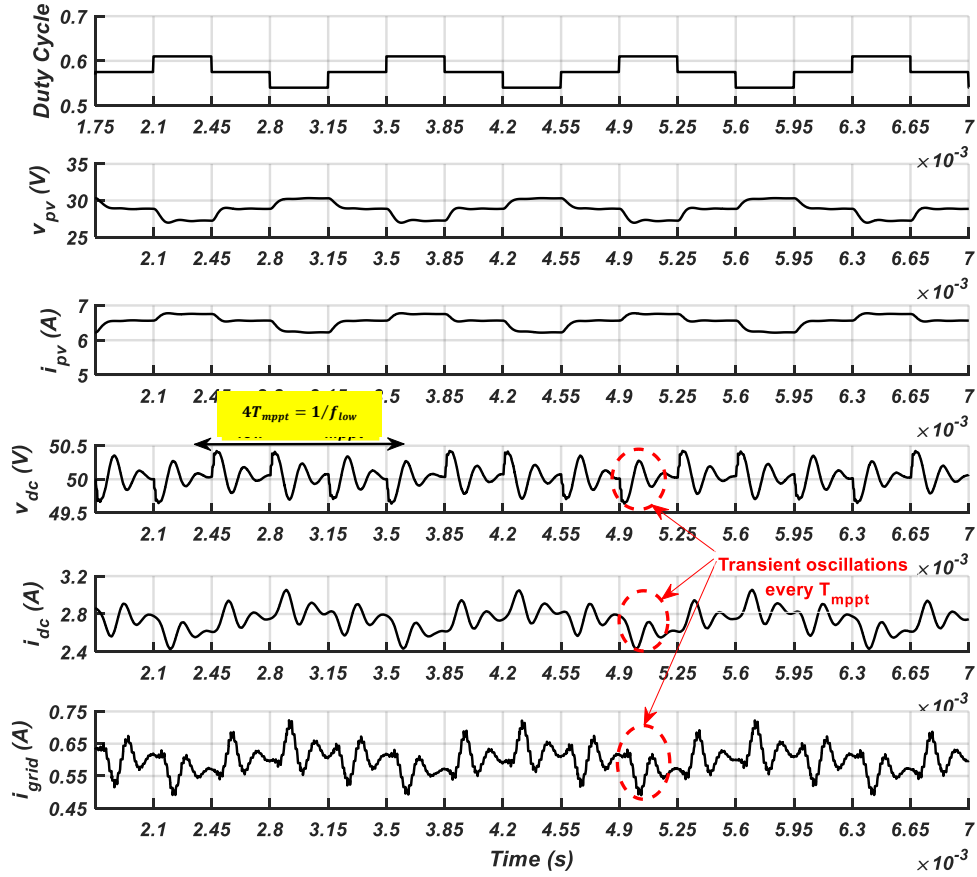
Figure 47: Simulation results of one SCPVM unit connected to the second-stage converter with cascaded current-voltage controller (Table 9). $G = 800\ W/m^2$, $\Delta d{=}0.035$, $T_{mppt}{=}0.35ms$, $C_{dc}{=}22\mu F$, $V_{grid}{=}200V$.

73
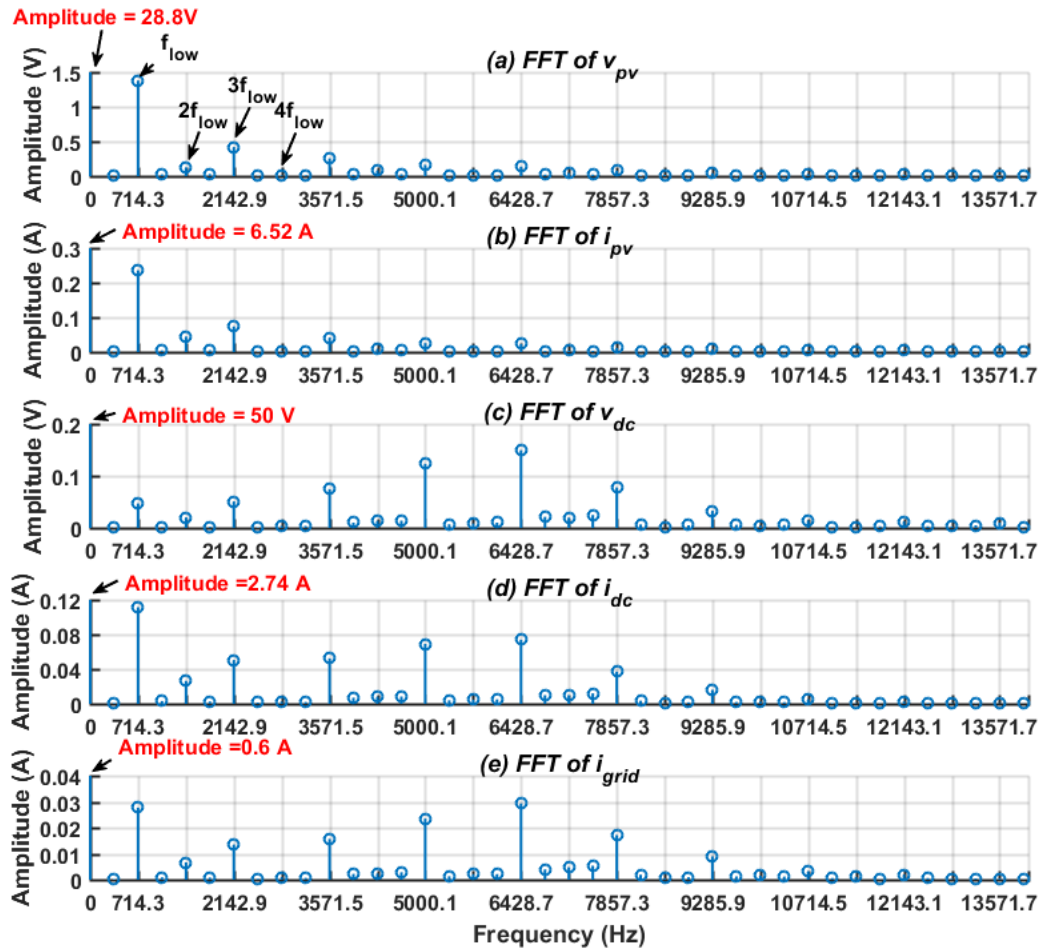
Figure 48: FFT of waveforms in Figure 47: from top to bottom FFT of (a) v_{pv}, (b) i_{pv}, (c) v_{dc}, (d) i_{dc}, and (e) i_{grid}

3.6.2 Simulation results for two parallel SCPVM units connected to the second-stage converter

The second-stage converter's parameters and controller are designed for the case of having two SCPVM units at its input. In order to validate the system operation with two units and under changes in dynamics due to the increase number of the SCPVM units, this section provide simulation results with the case of having two SCPVM units connected to the second-stage converter. The simulation results for two parallel SCPVM units connected to the second-stage converter for 3P2Z controller and cascaded current-voltage controllers are shown in Figure 49 and Figure 50, respectively. As has been shown for single SCPVM unit the P&O controller is affecting the dc-link and grid waveforms and continuous oscillations are observed in the steady state due to the constant change in the steady-state operating points of the SCPVM units.
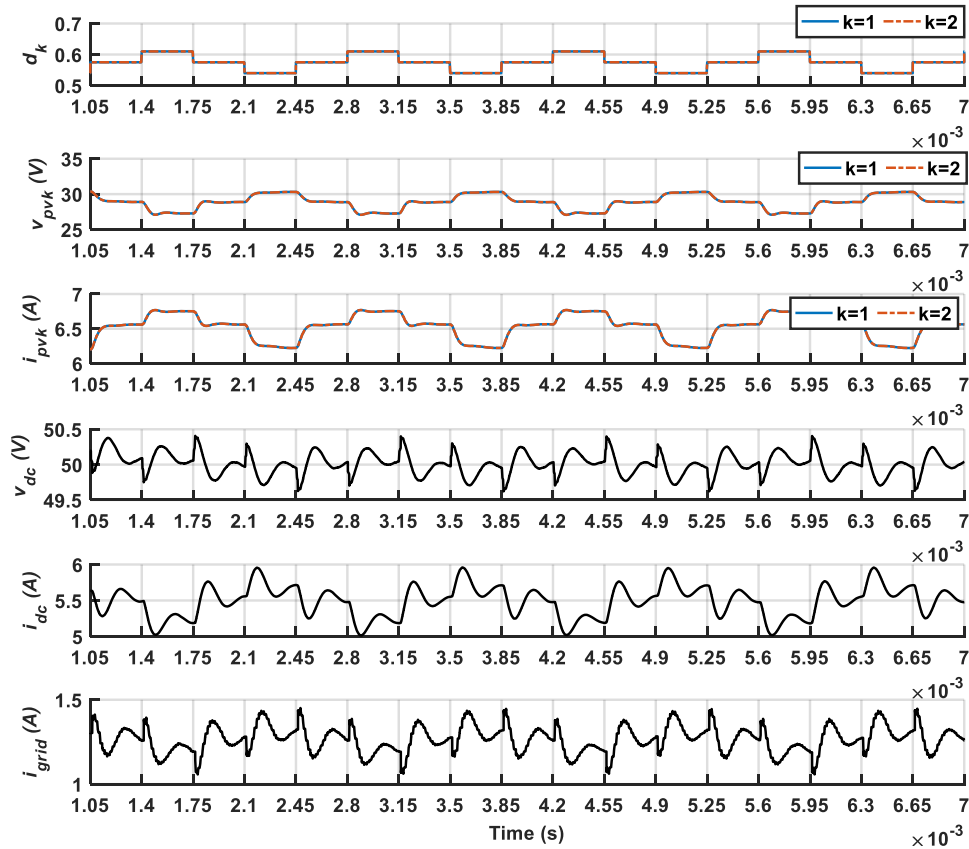

Figure 49: Simulation results of two SCPVM units connected to the second-stage converter with 3P2Z controller (Table 9). $G = 800W/m^2, \Delta d=0.035, T_{mppt}=0.35ms, C_{dc}=2 \times C_o=44\mu F, V_{grid}=200V$.

75
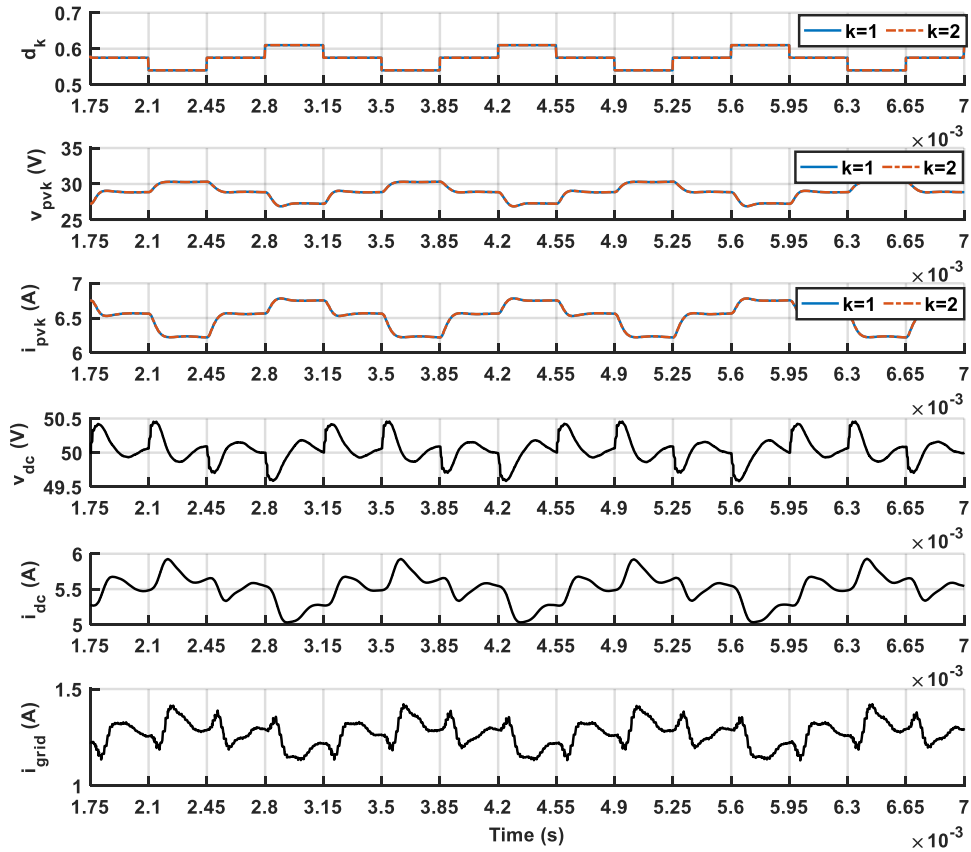
Figure 50: Simulation results of two SCPVM units connected to the second-stage converter with cascaded current-voltage controller (Table 9). $G = 800W/m^2$, $\Delta d=0.035$, $T_{mppt}=0.35ms$, $C_{dc}=44\mu F$, $V_{grid}=200V$.

The drawback of steady state oscillation in the PV module power due to the nature of the P&O controller is well known, but the impact of P&O controller on power quality in PV grid-connected system and dynamic interactions between the power stages of the double-stage system are not covered well in the literature. Therefore, chapter four and chapter 5 in this work analyse P&O related harmonics and their effect on the rest of the system in a double-stage parallel SCPVM configuration connected to a main DC bus, which is shown in Figure 39.

3.7 Conclusion

The design considerations of the double-stage DC/DC boost converter, P&O parameters optimisation, dc-link voltage control structures have been discussed. First, the available range of the dc-link voltage for successful tracking of MPP has been identified. Then, the effect of that voltage range on the first-stage converter parameters (L and C$_o$) under different weather condition is analysed. The converter parameters are

chosen based on the highest solar irradiation condition to ensure high performance of the MPPT and small inductance core size. Regarding P&O parameters (T_{mppt} and Δd), they are designed based on the dynamic behaviour of the first-stage converter and the adopted PV module to ensure three-step operation for optimal efficiency. In addition to that, a brief discussion of the different controller types that are used to control the common dc-link bus in grid-connected mode such as the voltage mode and cascaded current-voltage controllers are provided. Finally, time domain simulation and FFT results for the designed system are provided. The results show that the P&O controller is one of the sources that produce harmonics in the common dc-link bus and grid.

4 ANALYSIS OF P&O CONTROLLER RELATED HARMONICS

4.1 Abstract

In this chapter an analytical model of the PV related harmonics is provided as a function of P&O parameters (Δd and T_{mppt}), solar irradiation level, and number of the parallel SCPVM units in the system (considering single SCPVM unit and *n*-parallel-connected units). The analysis considers the dynamic behaviour of the non-linear PV source under different operating points and the synchronisation between the P&O controllers of the parallel-connected SCPVM units. The analytical model can be used to predict the harmonics frequency, explore the factors which affect the harmonics level induced by the P&O controller, and to understand the power quality degradation behaviour due to P&O related harmonics. The chapter starts with providing an analytical model of P&O controller related harmonics for parallel SCPVM units connected to a dc-link bus, and then MATLAB simulations and FFT analysis are provided under different operating conditions.

4.2 Simplified Double-stage Parallel SCPVM Configuration: Second-stage Converter modelled as Constant Voltage Source

Chapter 1, Section 1.1 and Chapter 2, section 2.6 discussed different causes that affect the power quality of grid-connected PV systems. One of them is the P&O scheme which is considered in this work. The impact of the P&O controller on the power quality of the adopted double-stage parallel SCPVM system configuration has been demonstrated in Figure 45 - Figure 50 in section 3.6. In this chapter, an analytical model of the PV related harmonics is provided as a function of P&O parameters (Δd and T_{mppt}), solar irradiation level, and number of the parallel SCPVM units in the system (considering a single SCPVM unit and *n*-parallel-connected units). In addition to that, the harmonics analysis considers the dynamic behaviour of the non-linear PV source under different operating conditions such as different PV voltage and solar irradiation level. The analytical model can be used to predict the harmonics frequency and explore the factors which affect the level of the harmonics induced by the P&O controller. Knowing the frequency of the P&O related harmonics and the factors that might worsen it can help in finding the most efficient method to eliminate it.

To carry on the aforementioned analysis first the configuration of adopted PV system in Figure 39 is simplified as shown in Figure 51. In grid-connected mode the second-stage

converter is designed so that it is capable to sink whatever current injected by the multiple parallel SCPVM units while keeping its input voltage regulated to a fixed average value (V_{dc}). So, it is possible to model the second-stage converter as a constant voltage source as will be considered in this chapter (see Figure 51). A very important advantage that the simplified PV system brings to the analysis is that the injected harmonics in the dc-link will be independent of the controller and impedance of the second-stage converter and it will clearly identify the harmonics frequency and levels that injected solely by the SCPVM units. Simulation results of the simplified system are shown in Figure 52. After ignoring the effect of the second-stage converter and its controller the transient behaviour of the dc-link current is defined by the dynamic of the first-stage converter and the connected load which is a stiff voltage in this study as shown in Figure 51, that makes the transient behaviour different than the earlier results shown in Figure 45 and Figure 47 where the transient behaviour were controlled and defined by the second-stage controller.
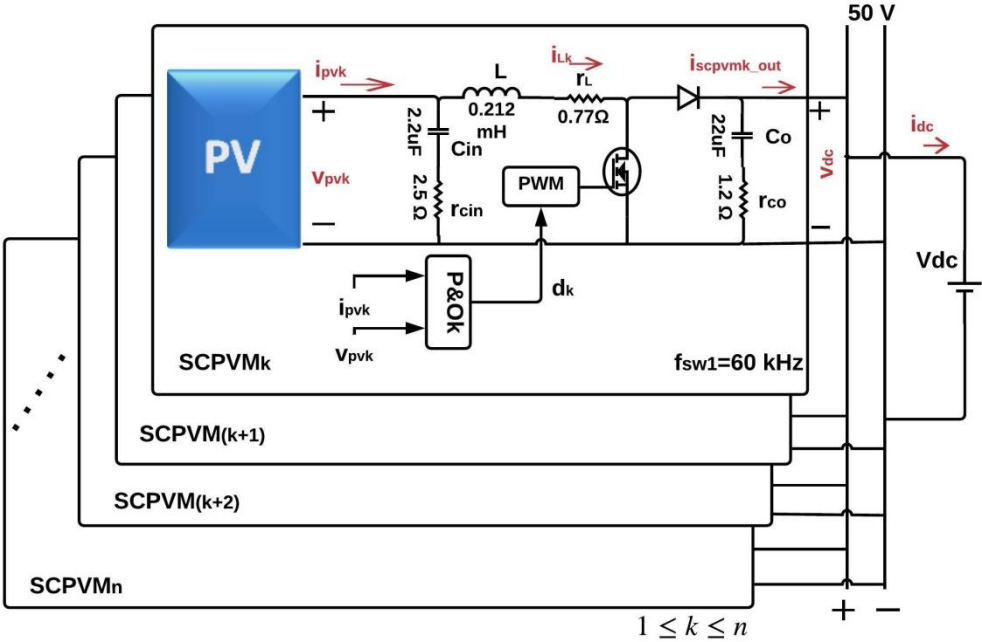

*Figure 51: Parallel SCPVM units connected to a dc-link bus.*
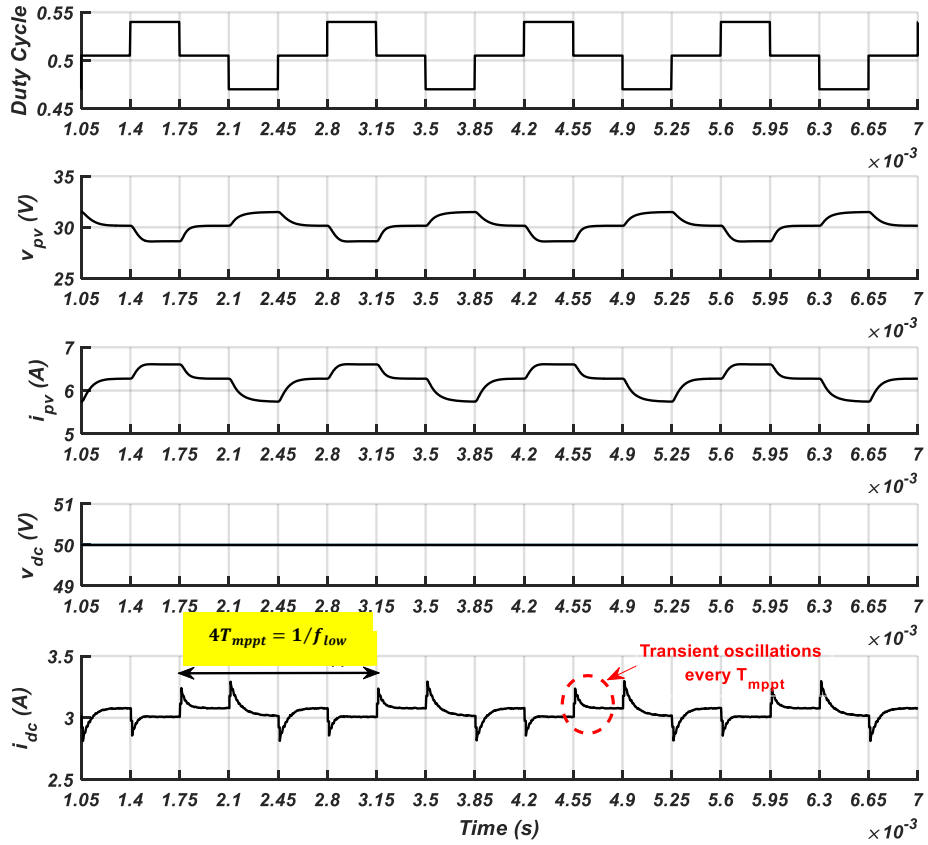
Figure 52: Simulation results of one SCPVM unit connected to a stiff dc-link voltage source. $G = 800\ W/m^2$.

The FFT analysis of the waveforms in Figure 52 is shown in Figure 53. The level of the harmonics has changed slightly compared with the results in Figure 46 and Figure 48 due to the absence of the dynamic and interaction with the second-stage converter. As shown in Figure 53 the system contains harmonics at $N \cdot f_{low}$ (N=1,2,3,..,etc.).
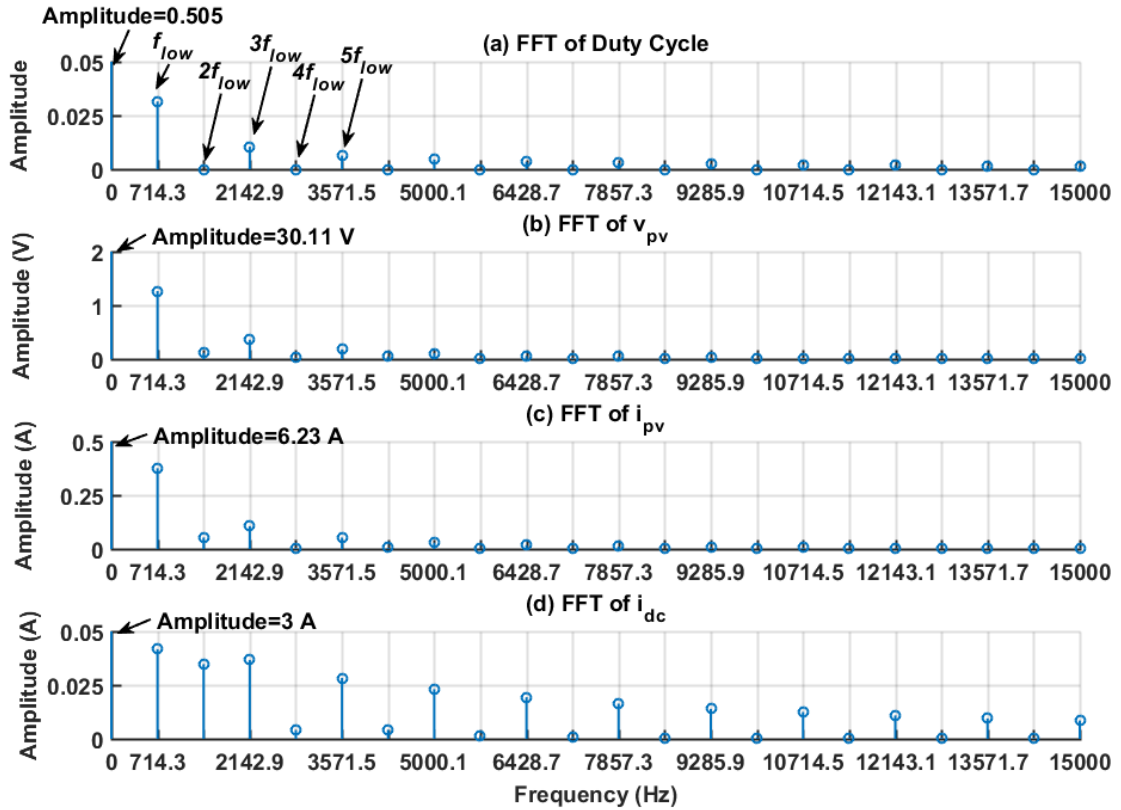
Figure 53: FFT analysis for (a) duty cycle, (b) v_{pv}, (c) i_{pv}, and (d) i_{dc} (waveforms are shown in Figure 52).

4.3 Analytical Modelling of P&O Related Harmonics

An analytical model of the P&O related harmonics can be useful to predict the frequency and the level of the harmonics induced by the P&O. Although the analysis is carried out for DC/DC boost converter, it can be easily done to any other DC/DC converter topology by considering the relevant equations and small signal model of the adopted topology. In this section the analytical analysis for multi parallel SCPVM considres synchronised perturbations times between the P&O controllers of the SCPVM units because it presents the worse case scenario of power quality and harmonics level. In addtion to that when the SCPVM units are non-synchronised its not easy to present their produced harmoics analytically as in this case it will be function of the time delay between the P&O perturbations time and that changes from one SCPVM unit to another due to connecting the units at different times (this can be the case when one or more units stop working and start again later).

81

4.3.1 Harmonics frequency

The frequency of the dominant harmonic (f_{low}) at the PV and dc-link sides can be defined as a function of T_{mppt} and the number of P&O duty cycle steps (S_{num}) in steady state as given in (4.1). As the oscillations at the PV and the dc-link sides due to the P&O controller are quasi-square waveforms, the system is expected to have harmonics at $N. f_{low}$ where N is an integer (N=1, 2, 3... etc.).

As the number of the P&O duty cycles steps increases from 2 steps (which is lowest number of steps that the system operate with) to S_{num} steps, the dominant lowest harmonic frequency is a sequence of $\frac{1}{2T_{mppt}}, \frac{1}{4T_{mppt}}, \frac{1}{6T_{mppt}}, \dots, \frac{1}{(2 \times S_{num}-2) \times T_{mppt}}$

Therefore the lowest harmonic frequency can be expressed as follow:

$$f_{low} = \frac{1}{\left(2 \times S_{num.} - 2\right) \times T_{mppt}} \tag{4.1}$$

Where S_{num} is the number of the P&O duty cycle steps. For three-step P&O operation as considered in this work f_{low} is $1/(4T_{mppt})$. Based on (4.1) one can conclude that when the P&O sampling period T_{mppt} is increased the frequency of f_{low} will be decreased and in this case it is harder to be suppressed and filtered.

4.3.2 Harmonics amplitude

There are two main factors that affect the amplitude of the dc-link voltage and current harmonics which are: (I) steady-state oscillations of the power fed by the SCPVM unit due to the P&O three-step operation; and (II) transient oscillations in the dc-link voltage and current due to the P&O duty-cycle perturbation every T_{mppt} (either increasing or decreasing).

In this analysis the peak-peak amplitude of the steady-state variation is measured based on the final average steady-state values after each P&O duty cycle step without taking into account the peak values of the transient response. While the overall dc-link variation takes into account the maximum and minimum peaks of the transient response. Figure 54 shows a general waveform of one SCPVM unit output current and the measurement reference points of both steady-state and overall variations. $I^G_{scpvm\_out\_max}$ and $I^G_{scpvm\_out\_min}$ are the maximum and minimum values of the

SCPVM output current for irradiation G. $I^G_{scpvm\_out\_right}$ and $I^G_{scpvm\_out\_left}$ are the steady-state values of the SCPVM output current when the PV module operate at the right and left of MPP, respectively.
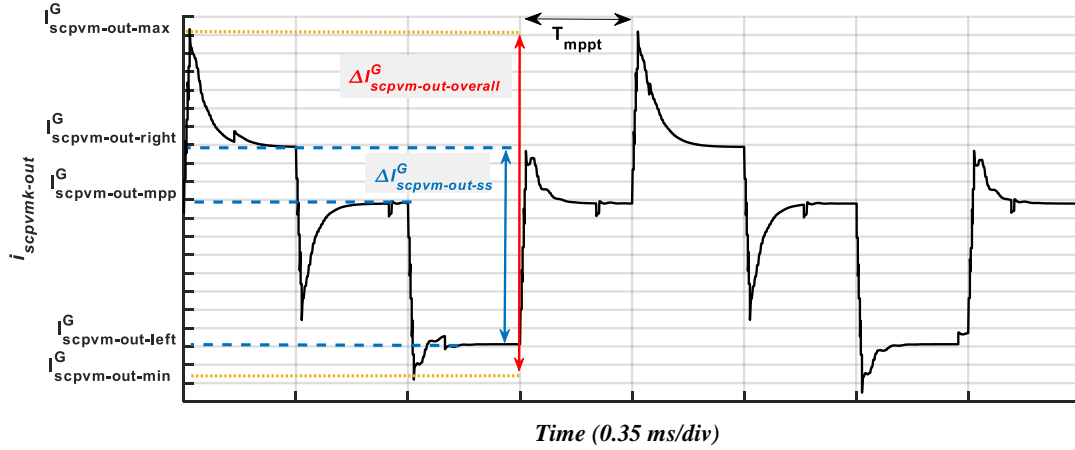

Figure 54: The steady-state and overall variations of the SCPVM output current.

4.3.2.1 Steady-state variation

The PV voltage and current variation due to the three-step P&O operation can be characterised by the following three points: Left MPP, MPP and Right MPP, as shown in green, red and yellow in Figure 55, respectively. The steady-state variation of the dc-link current depends on Δd, solar irradiation level, and the non-linear characteristics of the PV source as will be discussed herein. The analytical analysis in this section does not take into account the switching ripple to simplify the analysis.
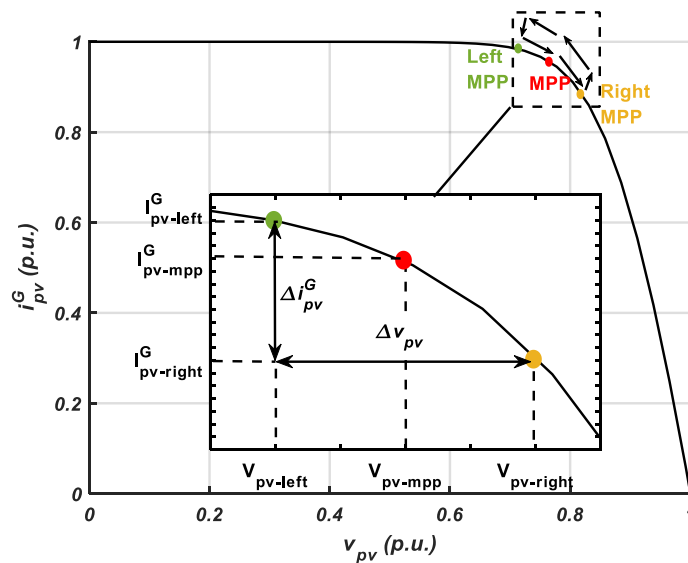

Figure 55: The location of the P&O operating points on the current-voltage characteristic curve of NU-E240 PV module (I_{rated}=8.62A and V_{rated}=37.3V).

4.3.2.1.1 Single SCPVM unit

From the basic current gain equation of a boost DC/DC converter, the output current of a single SCPVM unit for the three characteristic operating points (i.e. Left MPP, MPP, and Right MPP) can be defined as follow:

$$i_{scpvm\_out}^{G} = \begin{cases} I_{scpvm\_out\_mpp}^{G} = I_{pv\_mpp}^{G}(1 - D_{mppt}) \\ I_{scpvm\_out\_right}^{G} = I_{pv\_right}^{G}(1 - (D_{mppt} - \Delta d)) \\ I_{scpvm\_out\_left}^{G} = I_{pv\_left}^{G}(1 - (D_{mppt} + \Delta d)) \end{cases} \tag{4.2}$$

Where $I_{scpvm\_out\_mpp}^{G}$ is the SCPVM output current at MPP and irradiation G, $I_{scpvm\_out\_right}^{G}$ is the SCPVM output current at Right MPP and irradiation G, $I_{scpvm\_out\_left}^{G}$ is the SCPVM output current at Left MPP and irradiation G.

As specified in (4.2) the SCPVM output current varies between three values which are defined by D_{mppt}, Δd, and *PV* module current (i.e. solar irradiation) at the three P&O operating points. The associated PV module currents are defined as: $I_{pv\_mpp}^{G}$ is the PV current at MPP and irradiation G, $I_{pv\_right}^{G}$ is the PV current at Right MPP and irradiation G, and $I_{pv\_left}^{G}$ is the PV current at Left MPP and irradiation G as shown in Figure 55.

The PV module current can be approximated from the current-voltage characteristic equation of a single diode PV model as given in Chapter 2 in equation (2.1). Normally the shunt resistance R_{sh} is very high, so to simplify the analysis the last term in (2.1) can be neglected. Accordingly, the steady-state average values of i_{pv}^{G} at the three P&O operating points are as follow:

$$i_{pv}^{G} = \begin{cases} I_{pv\_mpp}^{G} = I_{ph}^{G} - I_{sat}^{G}.(e^{\frac{(V_{pv\_mpp} + I_{pv\_mpp}^{G}.R_s)}{(N_s.\eta.V_t)}} - 1) \\ I_{pv\_right}^{G} = I_{ph}^{G} - I_{sat}^{G}.(e^{\frac{(V_{pv\_right} + I_{pv\_right}^{G}.R_s)}{(N_s.\eta.V_t)}} - 1) \\ I_{pv\_left}^{G} = I_{ph}^{G} - I_{sat}^{G}.(e^{\frac{(V_{pv\_left} + I_{pv\_left}^{G}.R_s)}{(N_s.\eta.V_t)}} - 1) \end{cases} \tag{4.3}$$

All equations that required for calculating $I_{ph}^{G}, R_s, and\ V_t$ in (4.3) are given in Chapter 2, Section 2.2.1 and all required parameters for the adopted PV module is

provided in Table 2. As given in (4.3) the value of i_{pv}^G at the three P&O operating points depends on the PV module parameters, solar irradiation level and the PV module output voltage V_{pv_mpp} (PV voltage at MPP), V_{pv_right} (PV voltage at Right MPP) and V_{pv_left} (PV voltage at Left MPP) which are shown in Figure 55.

In this work PV grid-connected mode is considered where the DC-link voltage is controlled at constant value V_{dc}. Therefore, from the basic voltage equation of a boost DC/DC converter v_{pv} is:

$$v_{pv} = \begin{cases} V_{pv\_mpp} = V_{dc} \times (1 - D_{mppt}) \\ V_{pv\_right} = V_{dc} \times (1 - (D_{mppt} - \Delta d)) \\ V_{pv\_left} = V_{dc} \times (1 - (D_{mppt} + \Delta d)) \end{cases} \tag{4.4}$$

For a given PV module output voltage at MPP (V_{pv_mpp}) and dc-link voltage V_{dc}, D_{mppt} can be calculated and then for specific Δd the $V_{pv\_left,}$ and V_{pv_right} can be found.

Equations (4.4) and (4.3) can be substituted in (4.2) to find the values of $i_{scpvm\_out}^G$ at the three P&O operating points. Finally, $\Delta i_{scpvm\_out\_ss}^G$ can be estimated as follow:

$$\Delta i_{scpvm\_out\_ss}^G = \max\left\{ i_{scpvm\_out}^G \right\} - \min\left\{ i_{scpvm\_out}^G \right\} \tag{4.5}$$

A MATLAB m-file for calculating $\Delta i_{scpvm\_out\_ss}^G$ based on equations (4.2) - (4.4) is provided in Appendix D. Based on (4.5); Figure 56 shows $\Delta i_{scpvm\_out\_ss}^G$ under different values of Δd and solar irradiation level for the adopted PV module in Table 2, page 16. The results reveal that the steady-state variation increases as the solar irradiation and/or Δd increase. The decreased peak-peak variation at lower solar irradiation at fixed Δd and V_{dc} is related to the non-linear PV characteristic curve which becomes more flat around MPP at lower solar irradiations as shown in Figure 57.
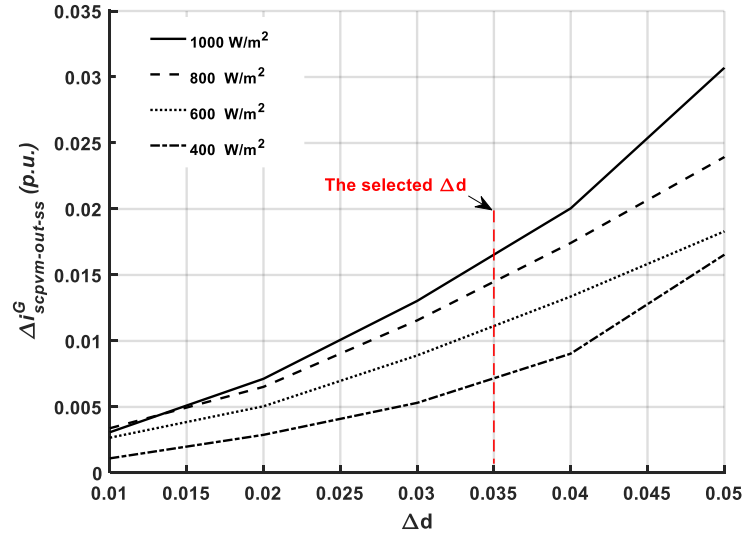
Figure 56: Effect of Δd and G on the peak-peak output current variation of one SCPVM unit. I_{rated}=8.15A. Results are obtained by (4.2) - (4.5).
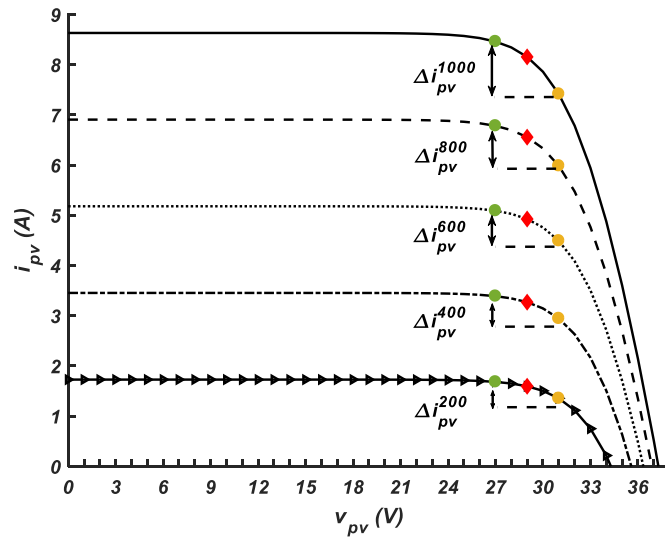

Figure 57: Simulation results: Effect of the non-linear PV source on the peak-peak PV current variation for NU-E240 PV module.

4.3.2.1.2 Multi-parallel connected SCPVM units

For multi-parallel-connected SCPVM units the steady-state variation and the level of the generated harmonics are dependent on the total number of the connected SCPVM units and synchronisation between their P&O controllers (i.e. Synchronised perturbations times).

Assuming that the P&O controllers of n-parallel connected SCPVM units are synchronised, the peak-peak dc-link current variation can be predicted and presented as a function of the variation of one SCPVM unit. The dc-link current in multi-parallel connected SCPVM units as shown in Figure 51 is:

86

$$i_{dc} = \sum_{k=1}^{n} i_{scpvmk\_out}^{G} \tag{4.6}$$

In case of synchronised P&O controllers of n-parallel connected SCPVM units the steady-state peak-peak variation of dc-link current is: (the transient dynamics are not included in this part)

$$\Delta i_{dc} = \sum_{k=1}^{n} \Delta i_{scpvmk\_out}^{G} \tag{4.7}$$

Under uniform solar irradiation ($G_k = G_{(k+1)} = ... = G_n$) it can be assumed that:

$$\Delta i_{scpvmk\_out}^{G} = \Delta i_{scpvm(k+1)\_out}^{G} = ... = \Delta i_{scpvmn\_out}^{G} = \Delta i_{scpvm\_out\_ss} \tag{4.8}$$

Thus, the dc-link current peak-peak variation of synchronised n-parallel SCPVM units can be written as follow:

$$\Delta i_{dc} = n \times \Delta i_{scpvm\_out\_ss} \tag{4.9}$$

It can be then readily concluded that by increasing the number of parallel connected SCPVM units, the variation level in the dc-link current is expected to increase substantially. Figure 58 shows the peak-peak steady-state current variation in the dc-link as the number of synchronised parallel-connected SCPVM units' increases (m-file for calculating Δi_{dc} is provided in Appendix D).
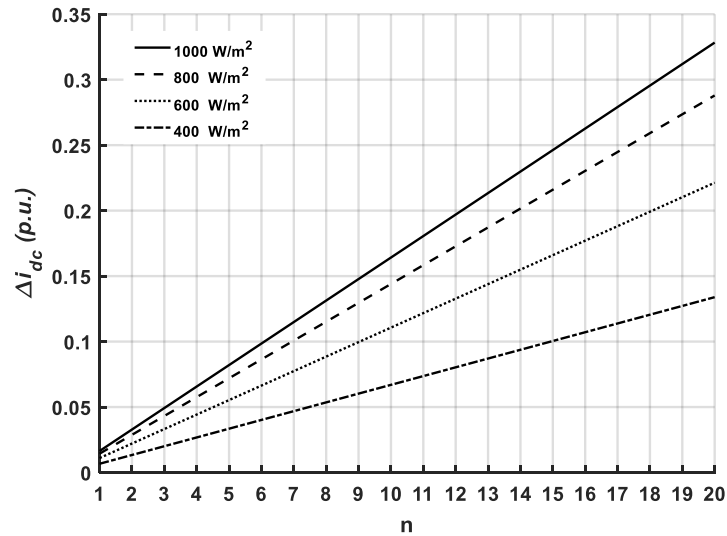

Figure 58: Effect of the total number of SCPVMs on Δi_{dc} under synchronised P&Os and uniform solar irradiation. $I_{rated} = I_{pv\_mpp}^{1000} = 8.15A$, $V_{dc} = 50V$, $\Delta d = 0.035$. Obtained by (4.9)

4.3.2.2 Overall variation

The overall dc-link variation takes into account the maximum and minimum peaks of the transient response as shown in Figure 54. The transient oscillations are induced by the perturbing nature of the P&O controller. At every duty-cycle perturbation the SCPVM current enters transient mode and oscillates until its new steady-state value is reached or the next perturbation occurs, depending on the P&O sampling period and the system dynamics.

It is possible to evaluate the transient behaviour of the SCPVM output current under different operating condition by analysing the small-signal unit step response of the duty-cycle-to-output current transfer function which is given in (4.10) [82]. This equation is obtained by using the small signal linear model of the non-linear PV source (see Figure 9, page 16) and the small-signal model of the DC/DC boost converter. The parasitic parameters of the inductance and the capacitance are ignored to simplify the analytical analysis.

$$
H_{i^G_{scpvm\_out}d} = \frac{\hat{i}^G_{scpvm\_out}}{\hat{d}}
$$

$$
= \frac{-i^G_{pv,0}\left(s + \dfrac{r_{pv,0}i^G_{pv,0}}{Li^G_{pv,0} - C_{in}v_{pv,0}r_{pv,0}}\right)\left(s + \dfrac{1}{r_{pv,0}C_{in}} - \dfrac{v_{pv,0}}{i^G_{pv,0}L}\right)}{s^2 + \left(\dfrac{1}{r_{pv,0}C_{in}}\right)s + \dfrac{1}{LC_{in}}} \tag{4.10}
$$

$r_{pv,0}$ is the PV dynamic resistance at the linearised operating point $(v_{pv,0}, i^G_{pv,0})$. The linearised model of a PV module is given in (2.7).

Based on (4.10) the dynamic behaviour of a SCPVM output current is affected by the boost converter parameters (L and C_{in}) and the PV dynamic resistance (r_{pv}) at the operating point. The parameters of the DC/DC boost converter (L and C_{in}) are assumed to be constant. Therefore, it is expected that changes in the system dynamic is mainly affected by r_{pv} which is solar irradiation and PV module voltage dependant parameter. From (4.10) it can be seen that r_{pv} has a direct impact on the location of the poles and zeros of $H_{i^G_{scpvm\_out}d}$ and in that affecting the transient behaviour of the SCPVM output current.

As given in (2.7) and illustrated in Figure 10, page 16 r_{pv} is function of v_{pv} , i_{pv}^G (i.e. solar irradiation) and the PV module specifications. Therefore, the SCPVM output current is expected to have different dynamic behaviour under different solar irradiation levels and P&O duty-cycle operating points (i.e. $D_{mppt} + \Delta d$, D_{mppt}, $D_{mppt} - \Delta d$).

The step function in MATLAB is used to plot the step response of $H_{i_{scpvm\_out}^G d}$ given in (4.10) to show the dynamic behaviour of i_{scpvm_out} for a sudden input d under different operating points such as different solar-irradiation levels and PV module voltages. Figure 59 shows the step response of $H_{i_{scpvm\_out}^G d}$ at MPP operating point for different solar irradiation levels (i.e. 1000 W/m^2, 800 W/m^2 and 600 W/m^2) of one SCPVM unit. It can be seen that the solar irradiation level affects the transient dynamic behaviour and at higher solar irradiation levels (i.e. lower r_{pv}) the system is more damped than at lower solar irradiation levels and it required longer time to settle.
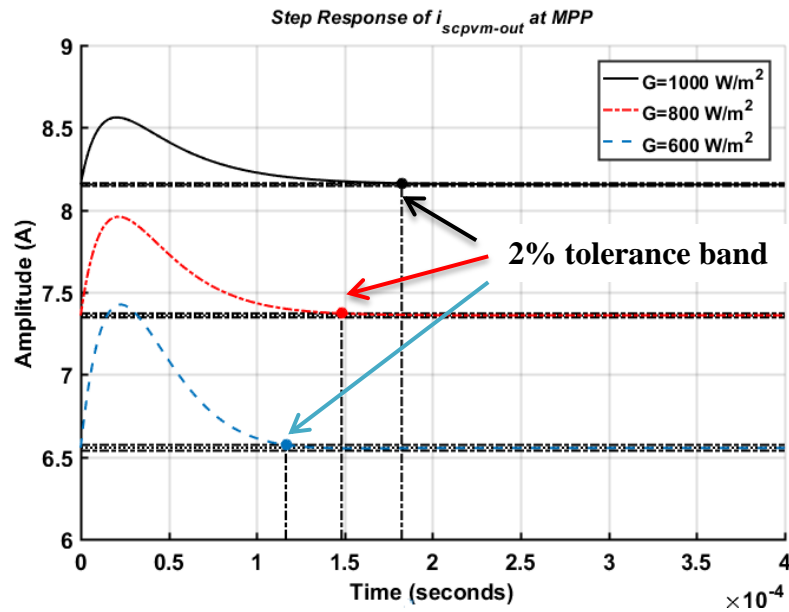

Figure 59: Step response of $-H_{i_{scpvm\_out}^G d}$ *at MPP for high, medium and low solar irradiation levels.*

The effect of different P&O operating points on the dynamic of $H_{i_{scpvm\_out}^G d}$ under the same solar irradiation is shown in Figure 60. As the P&O operating point varies between Left MPP, MPP and Right MPP, the value of r_{pv} changes and it becomes lower when moving to the right side of MPP which result in more damped system and longer settling time.
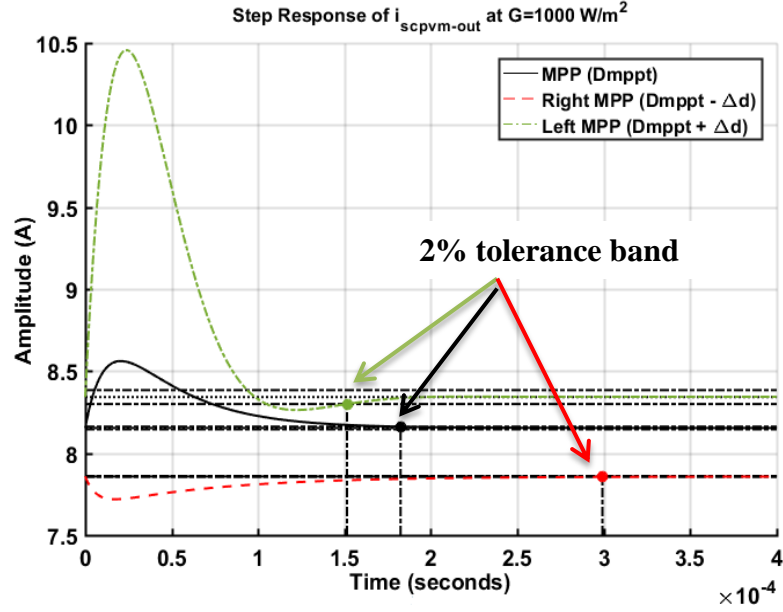
Figure 60: Step response of $-H_{i^G_{scpvm\_out}}d$ at the three operating points of the P&O controller under high irradiation ($1000\ W/m^2$). Δd=0.035, V_{dc}=50V.

Since the dynamic behaviour of transient harmonics depends on the operating point of the P&O controller (see Figure 60), for three-step P&O duty-cycle operation there will be four main intervals of transient modes which are then repeated every $1/f_{low}$.

4.3.2.2.1 Single SCPVM unit

As shown in Figure 54 when considering the transients peaks, the overall peak-to-peak variation of the dc-link current for a single SCPVM unit can be given as follow:

$$\Delta i^{:G}_{scpvm\_out\_overall} = I^G_{scpvm\_out\_max} - I^G_{scpvm\_out\_min} \tag{4.11}$$

4.3.2.2.2 Multi-parallel SCPVM units

The total dc-link current (i_{dc}) is the sum of the output currents of the multi-parallel SCPVM units as given in (4.6). Consequently, it will contain the transient oscillations induced by all SCPVM units. The overall dc-link current variation depends on the transient dynamic of $H_{i^G_{scpvm\_out}}d$ of each SCPVM unit, total number of the SCPVM units, and synchronisation between their P&O controllers.

Assuming synchronise P&O controllers the overall peak-to-peak variation of the dc-link current of n-parallel SCPVM units can be given as follow:

$$\Delta i_{dc\_overall} = \sum_{k=1}^{n} \left(I^G_{scpvmk\_out\_max} - I^G_{scpvmk\_out\_min} \right) \tag{4.12}$$

90

4.4 Simulation Analysis

In this section the system shown in Figure 51 is simulated to show the effect of different factors such as T_{mppt}, Δd, G, the number of SCPVM units and synchronisation between SCPVM units on the P&O related harmonics level.

4.4.1 Effect of T_{mppt} on f_{low}

Simulation results and FFT analysis of the dc-link current after increasing T_{mppt} are shown in Figure 61 and Figure 62 respectively. Comparing the FFT results in Figure 62 for $T_{mppt} = 0.9\ ms$ with Figure 53 for $T_{mppt} = 0.35\ ms$, increasing T_{mppt} from 0.35 ms to 0.9 ms has decreased f_{low} from 714.3 Hz to 277.7 Hz, respectively. This was expected from (4.1). Also, the FFT analysis in Figure 62 shows the harmonics in the dc-link current which are multiple of the 277.7 Hz for this case.
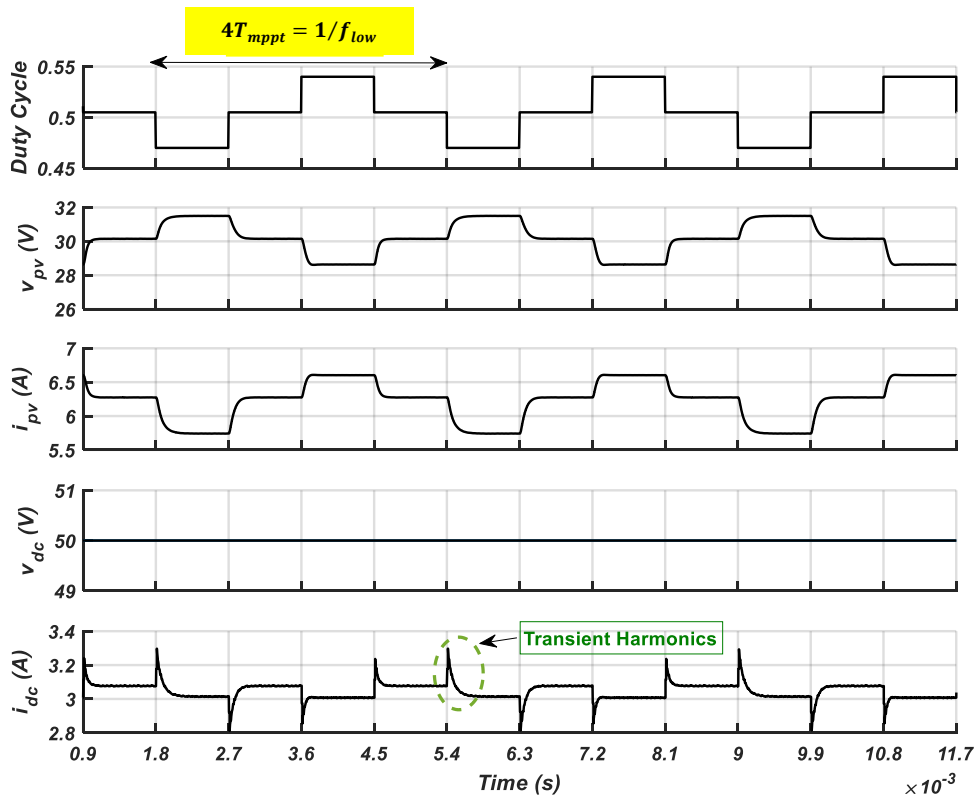
Figure 61: Simulation results of one SCPVM unit connected to a stiff dc-link voltage source. $G = 800W/m^2$, T_{mppt}=0.9ms, C_{dc}=22μF.
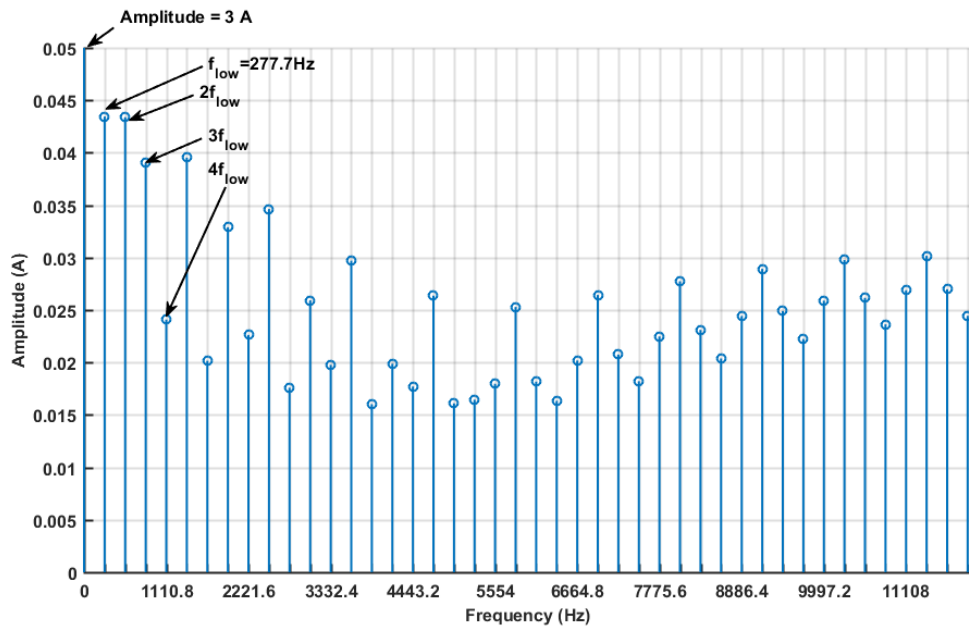
Figure 62: FFT analysis for the dc-link current i_{dc} *with* T_{mppt} *=0.9 ms (time domain waveform is shown in Figure 61).*

4.4.2 Effect of Δd on the harmonics amplitude

FFT results of the dc-link current i_{dc} for one SCPVM unit for two different values of Δd are shown in Figure 63. The results show that the harmonics levels decrease with smaller value of Δd. Considering f_{low} harmonic, this was expected analytically as was shown in Figure 56. Although the analysis in Figure 56 is considering only the steady-state peak-peak ripple of the output current for different values of Δd, it gives an indication about the effect of Δd on the amplitude of f_{low} harmonic.
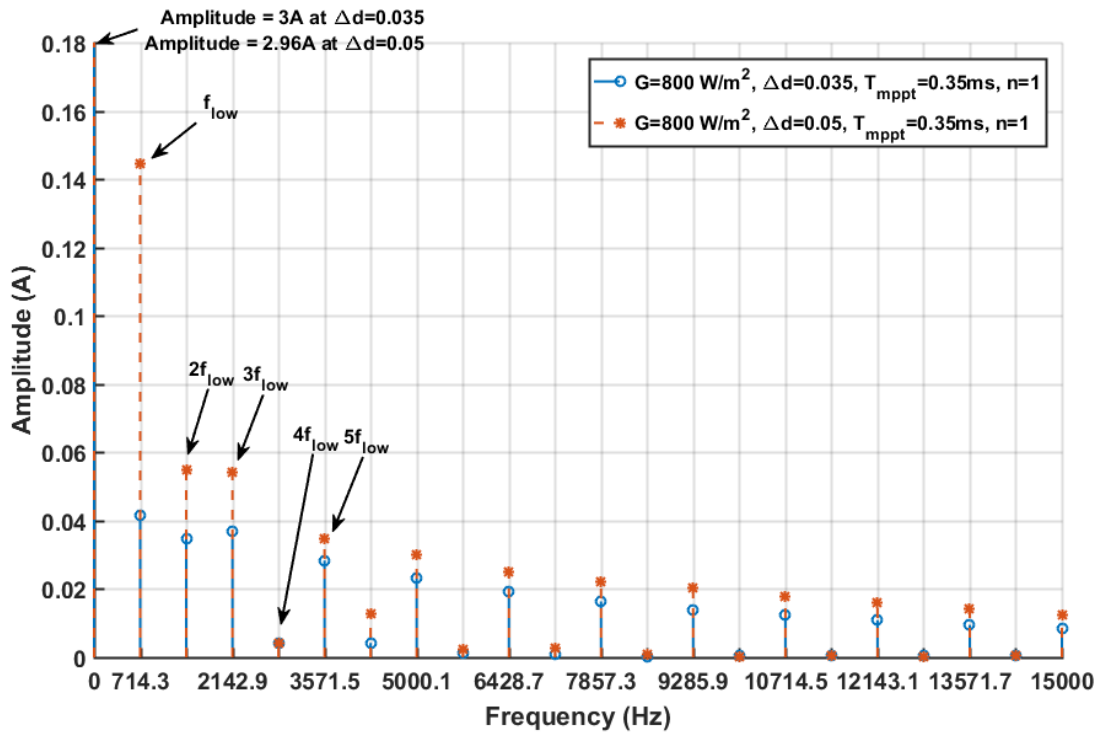
Figure 63: FFT analysis of i_{dc} for two different duty-cycle step size Δd=0.035 and Δd=0.05 of one SCPVM unit connected to a stiff dc-link voltage. $G = 800\ W/m^2$, T_{mppt}=0.35ms, C_{dc}=22μF.

4.4.3 Effect of solar irradiation on harmonics amplitude

FFT analysis of the dc-link current for one SCPVM unit when the solar irradiation level varies is shown in Figure 64. As expected the results show that the harmonics levels decrease under lower solar irradiation level.
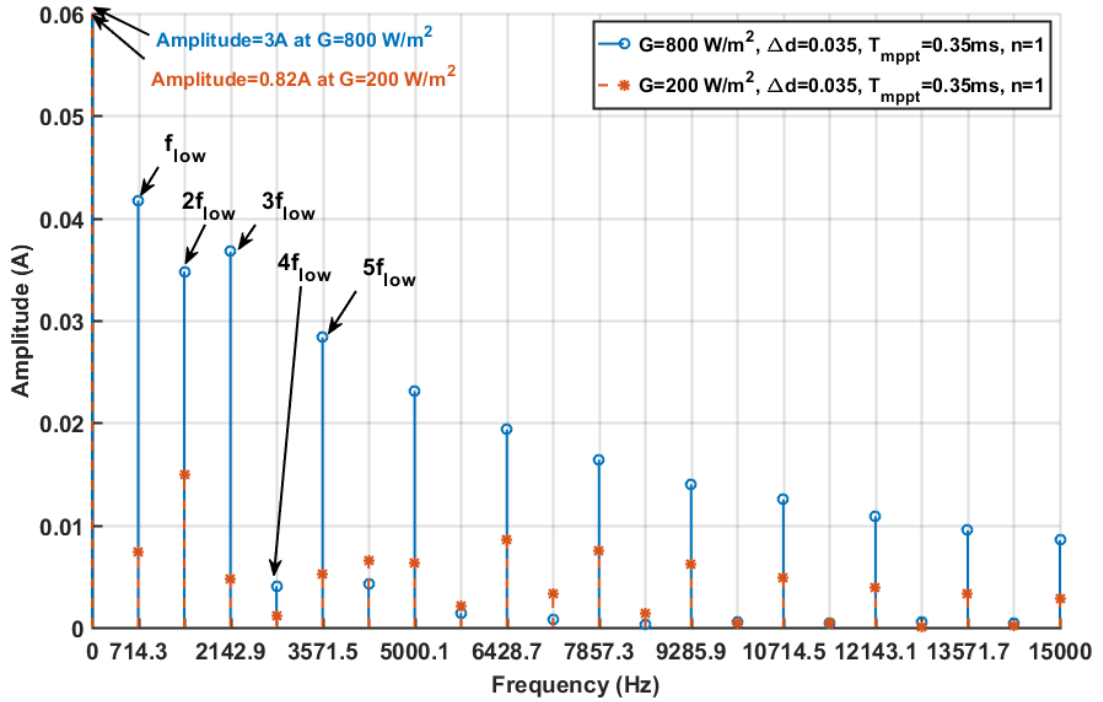
Figure 64: FFT analysis of i_{dc} for two different irradiation levels $G = 800\ W/m^2$ & $G = 200\ W/m^2$ of one SCPVM unit connected to a stiff dc-link voltage. Δd=0.035, T_{mppt}=0.35ms, C_{dc}=22μF.

4.4.4 Effect of increasing the number of the SCPVM units

4.4.4.1 Synchronised SCPVM units

In this test the identical distributed P&O controllers (i.e. their parameters Δd and T_{mppt} are the same) are assumed to communicate together and the perturbations of their duty cycles are forced to be synchronised in phase. The simulation results in Figure 65 and the FFT analysis in Figure 66 show that the in phase synchronised P&O controllers generate periodic harmonics in the dc-link current which are multiple of f_{low} (as predicted in section 4.3.1 and by (4.1)) which is the same as in the case of a single SCPVM unit.

Also, it can be observed from Figure 65 and Figure 66 the total peak to peak variation and the harmonics amplitudes are dependent on the number of the SCPVM units. As the units' number increases the overall variation increase and harmonics amplitudes increase as expected from (4.12). As an example and from Figure 65, for a single SCPVM unit $\Delta i_{dc\_overall} \approx 0.5\ A$ and for six SCPVM units $\Delta i_{dc\_overall} \approx 6 \times 0.5 = 3\ A$. The FFT results in Figure 66 show the increase in the harmonics amplitudes as the units' number increases.
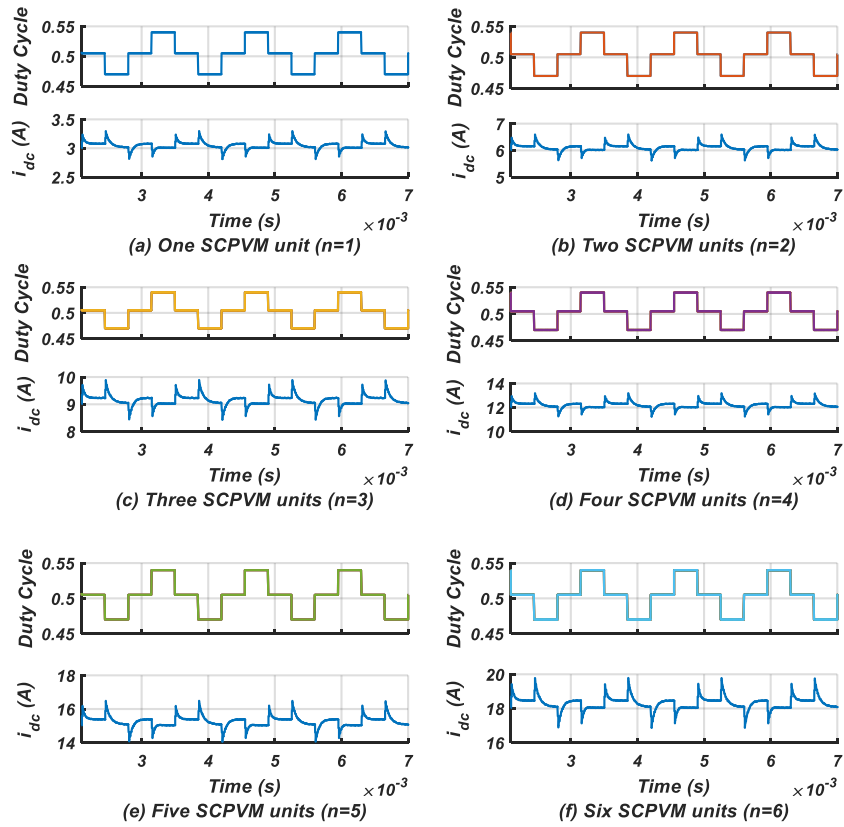
Figure 65: The dc-link current i_{dc} as the number of synchronised SCPVM units increases (a) n=1, (b) n=2, (c) n=3, (d) n=4, (e) n=5, (f) n=6. Δd=0.035, T_{mppt}=0.35 ms, $G = 800W/m^2$, $C_{dc} = n \times 22\mu F$, V_{dc}=50V.
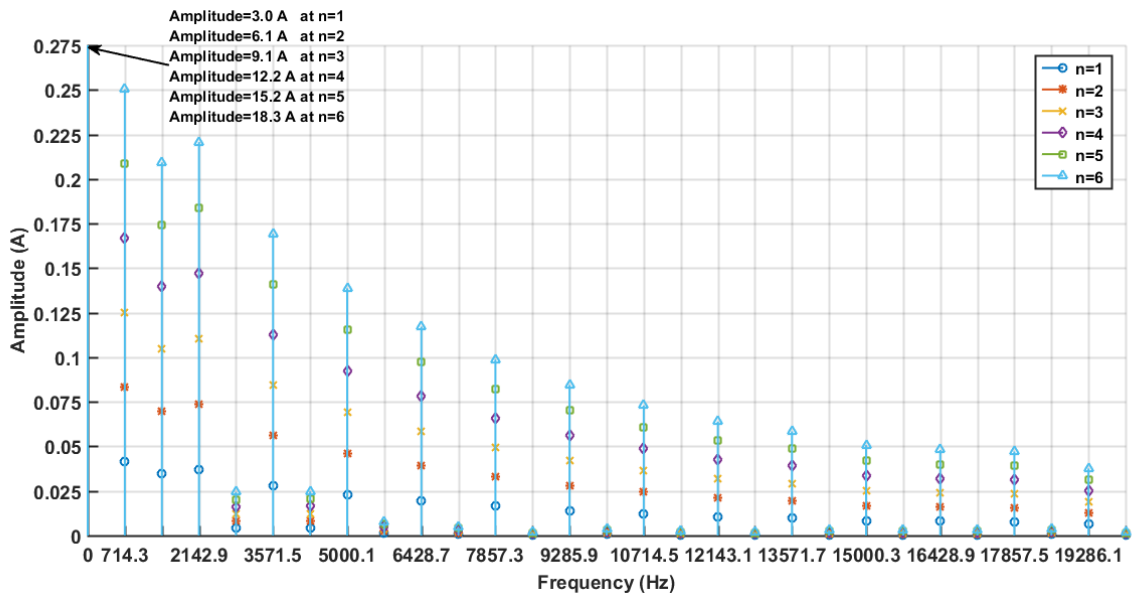

Figure 66: FFT analysis for the dc-link current i_{dc} as the number of the synchronised SCPVM units increases (time domain waveforms are shown in Figure 65).

4.4.4.2 Non-synchronised SCPVM units

In practise during the system operation if the SCPVM units are not forced to work in synchronised mode, the P&O perturbations time normally vary from one SCPVM unit to another due to connecting the units at different times (this can be the case when one or more units stop working and start again later), time delay which might be different due to non-identical measurement circuits design and unequal controllers computational times of the SCPVM units, delay between the P&O perturbation time, or the P&O controllers are designed with different sampling periods due to non-identical converters dynamics. Two examples of non-synchronised SCPVM units are shown in Figure 67 and Figure 71.

Figure 67 shows the variation in the dc-link current as the number of the asynchrounous SCPVM units increases (the units are not forced to work in synchronised mode). In this example the non-synchronisation is assumed to be caused by a time delay between the P&Os perturbation time. As the perturbations of the P&O controllers occur at different times, the steady-state and transient variations of the output currents of the SCPVM units does not happen at the same time for all SCPVM units. Thus, in non-synchronised mode the variations of i_{dc} cannot be mapped by the ones generated by a single unit as in the case of synchronised SCPVM units. For the considered example in Figure 67 the overall variation in the dc-link current for six non-synchronised SCPVM units is approximately 0.7A. That is 4 times less than the case of synchronised SCPVM units shown in Figure 65. However, this is only for this case and for asynchrounous SCPVM units the variation in the total dc-link current depends mainly on the relative time delays between the units. Other cases of different time delays between the units lead to a different results. As an example, Figure 68 shows the FFT results of i_{dc} for two SCPVM units for different time delay between their P&O perturbations. It can be seen that the amplitude of each harmonic is affected differently depending on the time delay between the units.

The FFT analysis of the dc-link current as the number of the non-synchronised SCPVM units increase (waveforms in Figure 67) is shown in Figure 69. It show that the harmonics amplitudes at $N. f_{low}$ are lower than the case of synchronised SCPVM units (see Figure 66) for the same number of SCPVM units.
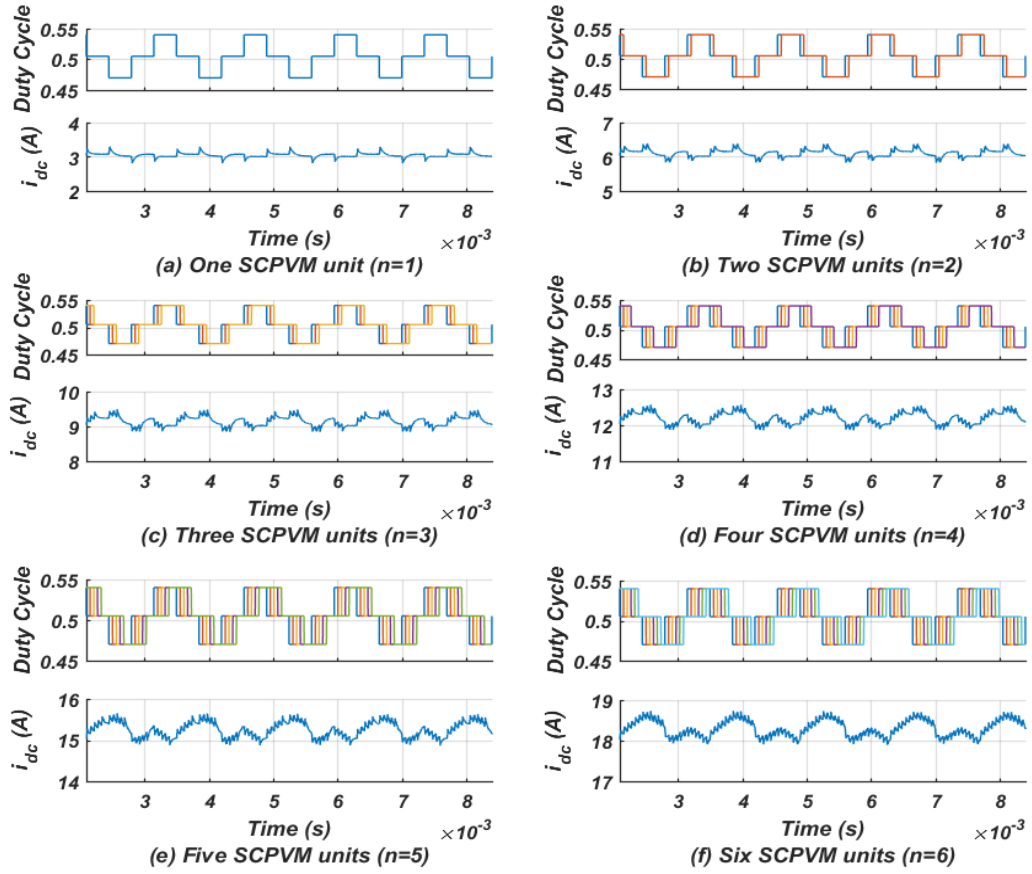
Figure 67: Simulation results of the dc-link current as the number of asynchronous SCPVM units increase (a) n=1, (b) n=2, (c) n=3, (d) n=4, (e) n=5, (f) n=6. Δd=0.035, T_{mppt}=0.35 ms, $G = 800W/m^2$, C_{dc}=n×22μF, V_{dc}=50V. Time delays with reference to SCPVM$_1$ are: 58.333μs, 2×58.333μs, 3×58.333μs,4×58.333μs and 5×58.333μs for SCPVM$_2$, SCPVM$_3$, SCPVM$_4$, SCPVM$_5$ and SCPVM$_6$, respectively.
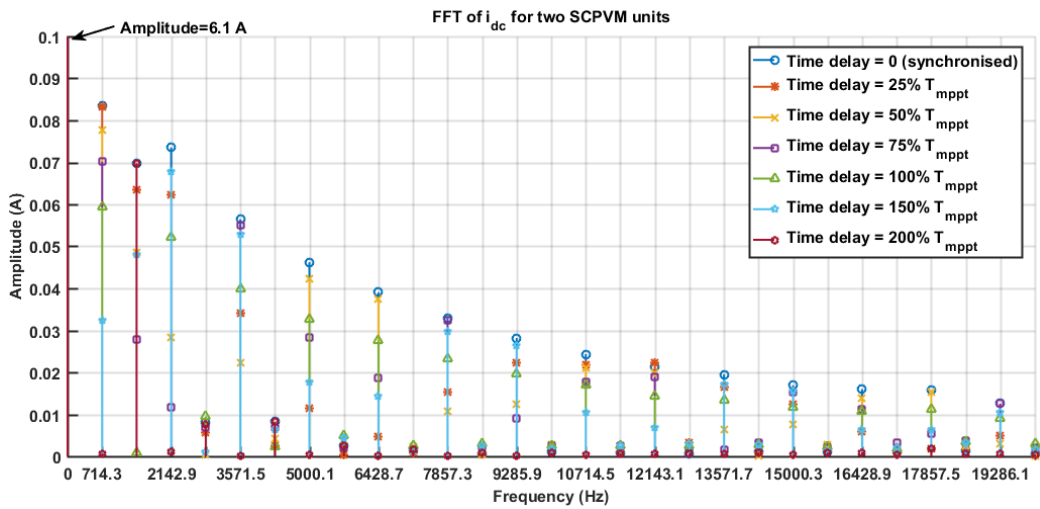

Figure 68: FFT of i_{dc} for two SCPVM units as the time delay between units varies.
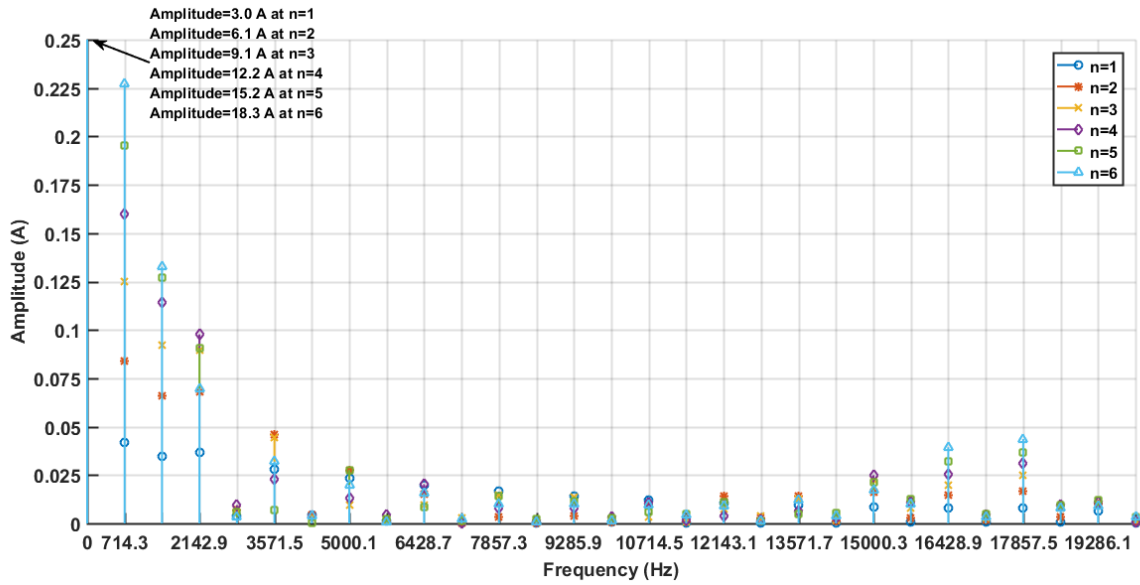
Figure 69: FFT analysis for the dc-link current as the number of the asynchronous SCPVM units increases (time domain waveforms are shown in Figure 67).

Figure 71 shows another example of non-synchronised SCPVM units. The non-synchronisation is caused by the non-identical optimisation of the P&O controllers sampling periods where the six SCPVM units are designed with different P&O sampling periods (this can be the case if non-identical PV modules and/or converters are used for the SCPVM units). It shows that the peak-peak variation in the dc-link current is time dependant and most likely to be non-periodic and inconsistent which make it difficult to predict. As example, the dc-link current waveform in Figure 71 is sectioned into 3 parts: Part A, Part B, and Part C. it can be seen that Part A present the worst case scenario with approximately 1A variation in the dc-link current. In Part B the current variation is getting smaller to almost 0.5 A. Then in Part C it is increasing slightly. That mainly caused by the relative time delays between the duty cycles perturbation times which are changing continuously during the time because of the non-equal sampling period of the P&O controllers (Figure 70 shows the changing in the time delay between the perturbations of the P&O duty cycles for two SCPVM units). Also, it can be seen that it is hard to distinguish the steady-state variation or the transient oscillations injected by the individual SCPVM units in the dc-link, especially if the delay between the units is very small where the transient oscillations of the SCPVM output currents overlap.

98
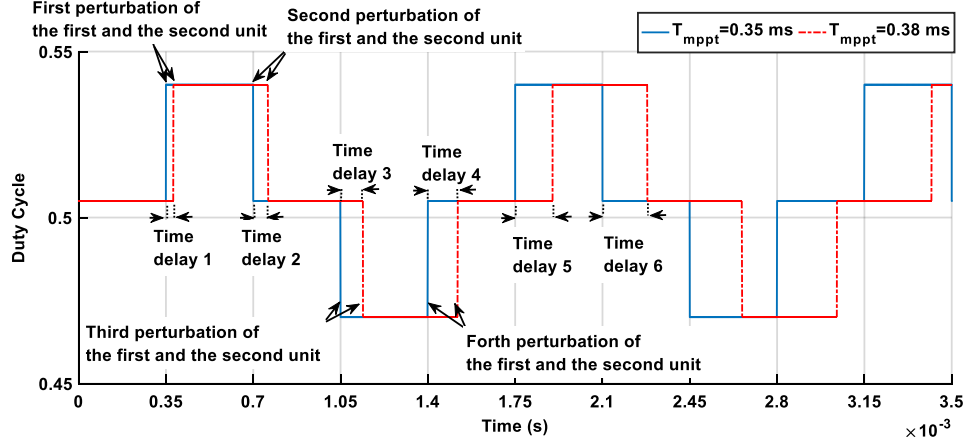
Figure 70: Changing in the time delay between the P&O controllers perturbations due to different design value for T_{mppt}.
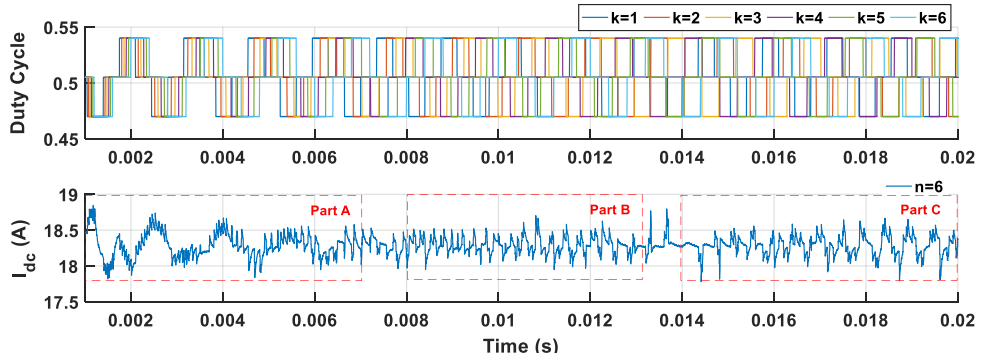

Figure 71: Simulation results of the dc-link current generated by 6-parallel SCPVM units operate with different sampling periods ($T_{mppt1} = 0.35ms$, $T_{mppt2} = 0.36ms$, $T_{mppt3} = 0.37ms$, $T_{mppt4} = 0.38ms$, $T_{mppt5} = 0.39ms$ and $T_{mppt6} = 0.4ms$). $\Delta d=0.035$, $G = 800W/m^2$, $C_{dc} = 6 \times 22\mu F$, $V_{dc}=50V$.

4.5   Conclusion

Based on the analysis in this chapter it was found that the periodicity of the harmonics in the dc-link bus which are generated by the distributed P&O controllers depend on their designed sampling periods T_{mppt}. If the distributed P&O controllers are optimised with different sampling periods, the result will be non-periodic and inconsistent variation in the dc-link bus. If the distributed P&O controllers are optimised with same sampling periods, the result will be periodic signal in the dc-link bus and if the sampling periods are synchronised the periodicity of the harmonics of n parallel SCPVM units is the same as one SCPVM unit. For synchronised identical sampling periods for the distributed P&O controllers it was found that the harmonics occurs at $N.f_{low}$ where N is an integer (N=1,2,3,.., etc.) and f_{low} is function of the P&O sampling period T_{mppt} and number of the P&O duty-cycle steps in the steady state. In addition to that, it was found that the harmonics levels increase as the P&O duty-cycle

99

step size (Δd), solar irradiation (G), number of the parallel SCPVM units increases, and when the P&O duty-cycles are synchronised in phase.

5 ANALYSIS OF THE DYNAMIC INTERACTIONS BETWEENT THE FIRST STAGE AND THE SECOND STAGE IN A DOUBLE-STAGE PV SYSTEM CONNECTED TO A MAIN DC BUS

5.1 Abstract

In this chapter the dynamic interaction between a SCPVM unit and the second-stage converter is analysed through simulations. The impacts of P&O controller on increasing the dynamic interaction between system stages and on designing the second-stage controller are highlighted. It is important to understand the possible interactions between a SCPVM unit and the rest of the system as that can help to set system design recommendations and guidelines. Three different types of dc-link controllers are considered: PI, 3P2Z, and cascaded current-voltage controllers. For each controller the dynamic interaction is explored in case of having an ideal current source (the SCPVM is modelled as a current source) connected to the second-stage converter and in case of having SCPVM unit connected to the second-stage converter. Also, this chapter investigates the effect of the controller parameters, C_{dc} size, and solar irradiation level on system stability. At the end of the chapter, the design recommendations are provided for the dc-link voltage controller of the second stage converter.

5.2 Simplified Double-stage Parallel SCPVM Configuration: Single SCPVM unit Connected to Second-stage Converter

In the previous chapter the second-stage converter of the double-stage parallel SCPVM configuration is modelled as a constant voltage source. On one hand that has helped to clearly identify and analyse the harmonics injected by the PV source and the P&O controller (the SCPVM unit), but on the other hand the effect of the PV related harmonics on the rest of the system was not included. It is important to understand the possible interactions between SCPVM unit and the rest of the system as that can help to set system design recommendations and guidelines.

In particular, this chapter explores the effect of the P&O related harmonics on the performance of a PV system consists of double-stage DC/DC boost converter connected to a DC bus (e.g. DC microgrid). The data and the simulation results in this chapter are obtained from a simplified system; the case when the system has only one SCPVM unit connected to the second-stage DC/DC boost converter as shown in Figure 72.a. However, the system can be scaled up for a higher power rating simply by

increasing the number of parallel SCPVM units, and increasing the power rating of the second stage converter. Three types of controllers will be considered PI voltage mode, 3P2Z voltage mode, and cascaded current-voltage controllers and all are designed for a dc-link capacitance of 44 μF (assuming having two SCPVM units connected to the dc-link bus, $C_{dc} = 2 \times 22\mu F$). For each controller the dynamic interaction is explored in case of having an ideal current source (the SCPVM is modelled as a current source and the value of the dc-link current is estimated based on the assumption that the SCPVM operates at the highest solar irradiation of 1000 W/m^2) and in case of having the SCPVM unit (the original source) connected to the second-stage converter.
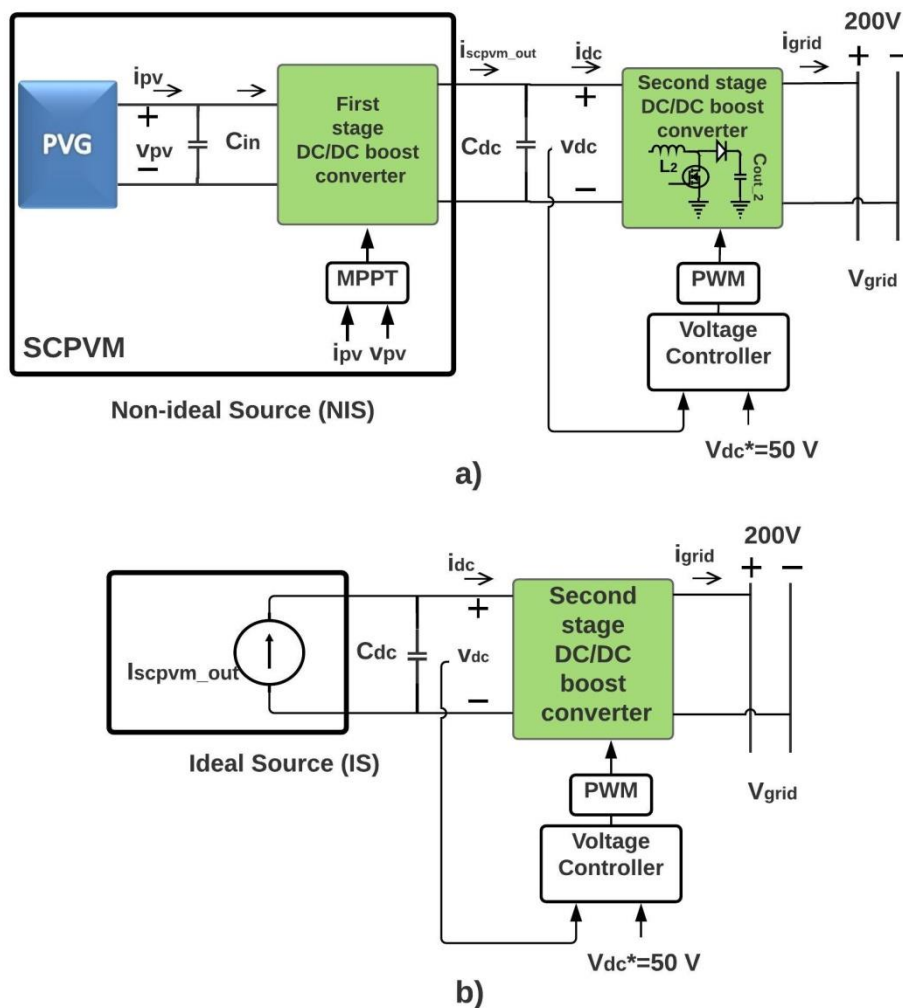

Figure 72: Voltage mode controller structure; (a) non-ideal source configuration, (b) ideal source configuration.

5.3 Voltage Mode Controller Design for Second Stage DC/DC Boost Converter

5.3.1 Proportional Integral (PI) compensation

In this section it will be shown that the PI controller is not suitable to control the input voltage of the DC/DC boost converter. Traditionally proportional integral (PI) controller is used for voltage regulation, since it is simple to implement and gives zero steady state error. The voltage mode control block diagram is shown in Figure 73. As a first attempt PI voltage mode controller is investigated to regulate V_{dc}. The voltage mode controller structure of the second-stage converter is shown in Figure 72.a. For designing the controller it is assumed that the first-stage converter is an ideal current source as shown in Figure 72.b. The transfer function of the duty-cycle-to-dc-link voltage $H_{v_{dc}d_2}$ of the second stage with ideal current source is [75]:

$$H_{v_{dc}d_2}(s) = \frac{\tilde{v}_{dc}}{\tilde{d}_2} = -\frac{V_{grid}}{L_2 C_{dc}} \frac{1 + r_{C_{dc}} C_{dc} s}{s^2 + \frac{r_{l2} + r_{C_{dc}}}{L_2} s + \frac{1}{L_2 C_{dc}}} \tag{5.1}$$
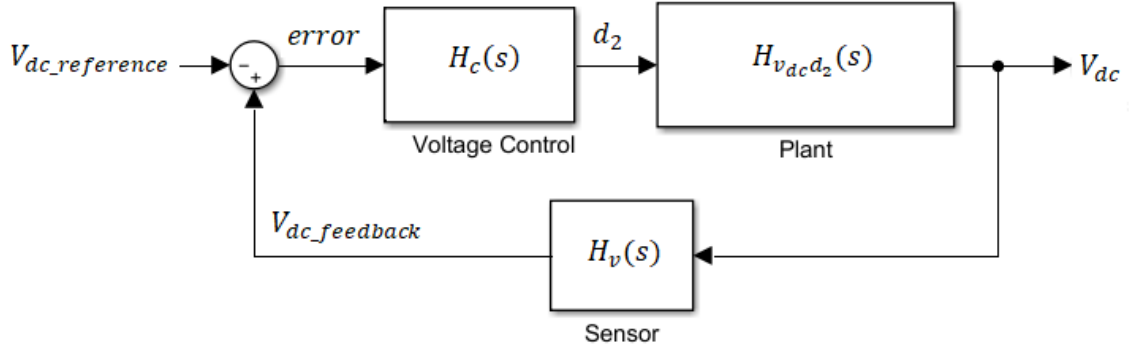

Figure 73: DC-link voltage mode control diagram

Figure 74 show the bode diagram of $H_{v_{dc}d_2}(s)$ for a system operating with the following parameters: C_{dc}=41 µF, L_2=1.5 mH, f_{sw1}=100 kHz, $r_{c_{dc}}$=1.2 mΩ and r_{l_2}=0.01 mΩ. Although the parameters in this section are different from those designed in Chapter 3 which is used for the rest of this research work, the main discussion and finding can be applied on a boost converter with any other parameters. As shown in Figure 74 the transfer function $H_{v_{dc}d_2}$ is a second order with a double pole at ω_0 where an additional -180º phase delay occur (at ω_0 the phase changes from 180º to 0º).
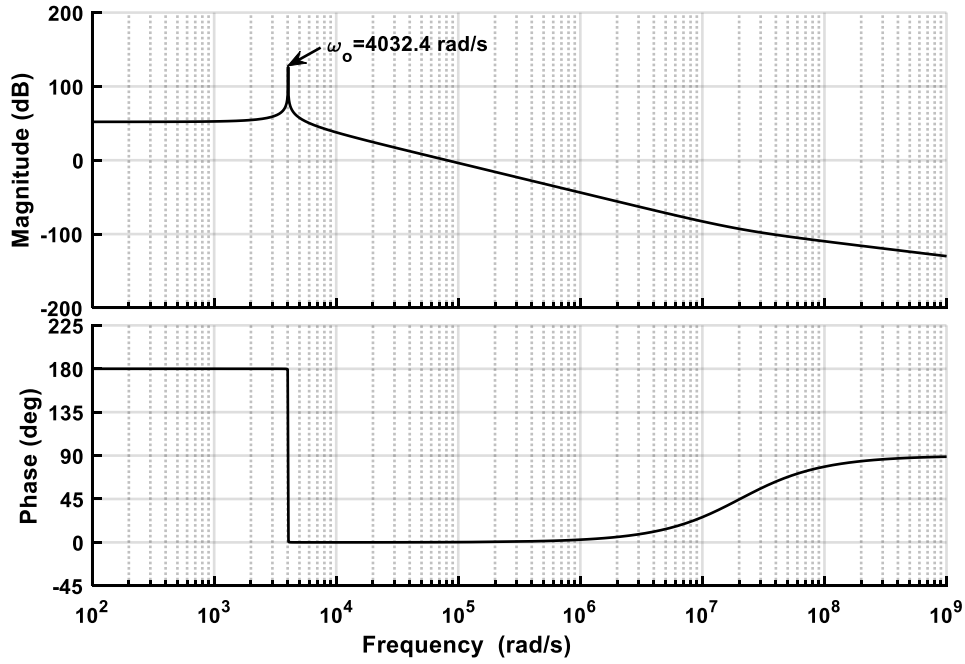
Figure 74: Bode diagram of $H_{v_{dc}d_2}(s)$ given in (5.1) with the following parameters $C_{dc}=41\mu F, L_2=1.5mH, r_{C_{dc}}=1.2m\Omega$ and $r_{l_2}=0.01\ m\Omega..$

It is known that a single integrator compensation such as PI controller force the loop gain of the system to start its phase at -90° and as discussed above at ω_0 an additional -180° phase delay is expected. So, it is expected the phase of the control loop gain to fall below -180° after ω_0 depending of the other system roots that lower than ω_0. To ensure wide attenuation of the closed loop transfer function, it is required that the control loop gain cut-off frequency (ω_c) is higher than the second-stage double pole frequency ($\omega_o = 1/\sqrt{C_{dc}L_2}$) [74, 83]. Having $\omega_c > \omega_o$ and with the phase in this frequency range below -180°, this makes the control loop most likely to be unstable. To demonstrate that the control toolbox in MATLAB Simulink is used for tuning the PI controller as given in (5.2) at a cut-off frequency higher than ω_o ($\omega_0 \approx 4 \times 10^3$ rad/s) and as an example ω_c is chosen to be 14.87×10^3 rad/s. The control loop gain (T) of the system is given in (5.3).

$$H_c(s) = k_v \frac{1+\dfrac{s}{\omega_z}}{s} = -11\frac{1+\dfrac{s}{325}}{s} \tag{5.2}$$

$$T = H_c(s).H_{v_{dc}d_2}(s).H_{pwm}(s) \tag{5.3}$$

Where $H_c(s)$ is the controller transfer function, $H_{v_{dc}d_2}(s)$ is given in (5.1), and $H_{pwm}(s) = \frac{1}{V_m}$, V_m is the amplitude of the PWM voltage carrier.

The control loop gain of the system with an ideal current source (T_IS) is shown in Figure 75. The linear analysis tool in MATLAB is used to measure the control loop gain. Basically the simulation measurement is based on injecting small perturbations signal at the input point of the plant and measure the response at output point as shown in Figure 76. As it can be seen in Figure 75, and as expected, the control loop gain phase starts at -90° due to the integral part of the controller. Then and due to the zero at 325 rad/s the phase changes from -90° to 0°. Finally, at ω_0 the loop gain phase changes from 0° to -180°. This makes the system unstable for any cut-off frequency higher than ω_0.
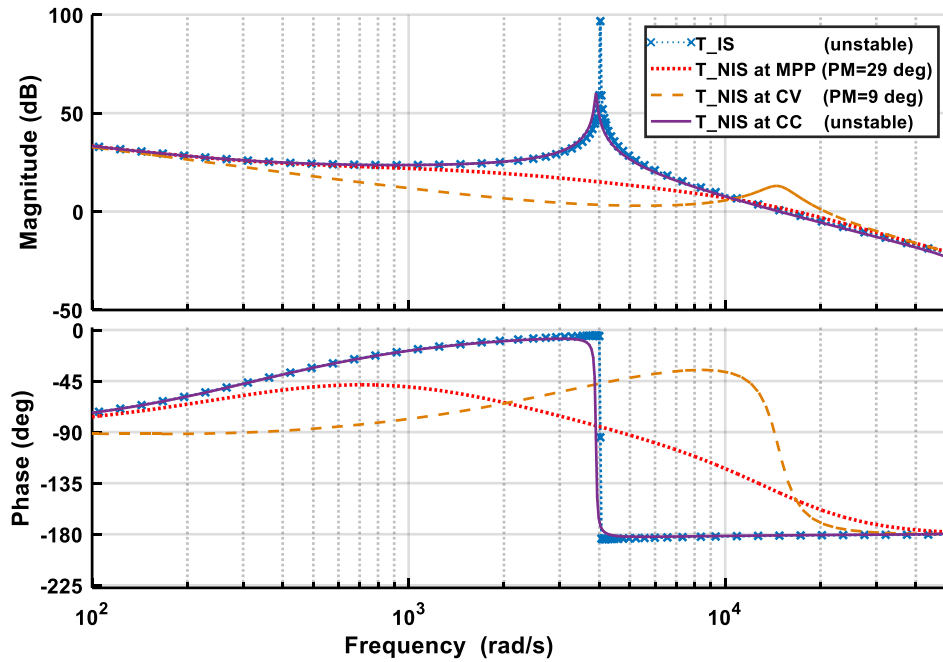

Figure 75: Simulation results of the control loop with ideal source (T_IS) and non-ideal source (T_NIS). PV operates at CV ($V_{pv}=35V$), MPP ($V_{pv}=29V$) and CC ($V_{pv}=19V$) regions. $K_v=11$, $C_{dc}=41\mu F$, $L_2=1.5$ mH, $f_{sw1}= f_{sw2}=100$ kHz and $G = 1000\ W/m^2$.
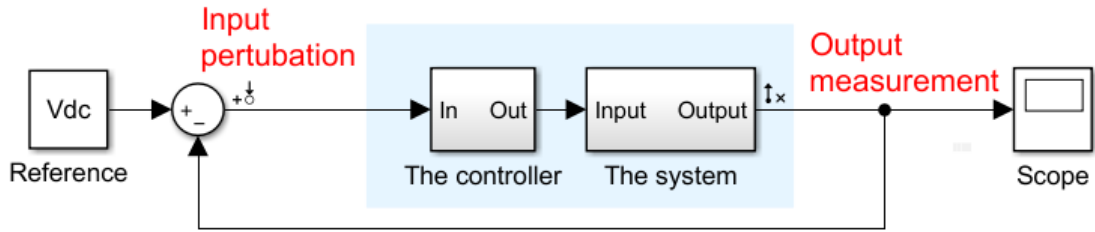
Figure 76: The control loop gain simulation measurement points (see Appindex C.4 for full block diagram and explaination of linear analysis tool in MATLAB)

Despite the above analysis which eliminates the single integrator compensator as a possible choice for controlling the input-side of a boost converter, it was used in the literature to control the input side of a boost converter in PV applications such as in [71, 82, 95]. In these studies [71, 82, 95] the stability problem due to the power stage double pole is not discussed and it seems that it was not affecting their system stability because the control loop gain cut-off frequency was designed lower than ω_o. As an example in [82] the control loop gain is tuned at 60 Hz while the boost converter double pole is at 890 Hz and in [71] the control loop gain cut-off frequency is kept below 10 Hz. However, the expense of designing ω_c lower than ω_o is poor close loop performance [74, 83].

It has been discussed earlier in Section 2.5.3 that the PV operating regions; constant current (CC), constant voltage (CV), and MPP source regions (refer to Figure 23 page 40 for PV operating regions), affect the dynamic performance of the control-to-input-voltage controller. To investigate the effect of the non-ideal SCPVM source on the control loop gain in (5.3), the ideal current source is replaced by the non-ideal SCPVM source then the control loop gain is measured again. The controller in (5.2) is kept the same despite having the control loop gain unstable. However, under the condition of $\omega_c > \omega_o$ is not possible to stabilise it.

Figure 75 shows the control loop gain of the second-stage converter with non-ideal source (T_NIS). The three operating regions are considered: CC, MPP, and CV regions. From Figure 75 it can be clearly seen that the NIS affects the designed control loop depending on the operating region. With SCPVM at CC region (See T_NIS as CC in Figure 75) the system behaves exactly as in case of the ideal source (the phase after ω_o fall to -180°). Therefore, any value of ω_c (under the condition of $\omega_c > \omega_o$) will results in an unstable control loop due to the insufficient phase margin.

In case of SCPVM operating at MPP and CV regions (see T_NIS at MPP and T_NIS at CV in Figure 75, respectively) the system is stable as it has not violate the stability criteria as the control loop gain is not -180° or below it. Although the system is stable, at CV region the phase margin (PM) is very small (9°) and that is not acceptable in real life applications.

For further investigations and to verify the findings which is based on analysing the control loop gain, a time domain simulation is carried out for the system in Figure 72.a with a SCPVM unit (NIS) operates at CV and CC regions for $G = 1000 \, W/m^2$. The results are depicted in Figure 77. At the beginning the system operates at CV region and at t=30 ms it changes to CC region. The operating region of the SCPVM unit is varied by changing the duty cycle of the first stage converter so that the PV voltage changes from 35V (CV region) to 19V (CC region). The results show that the system is stable at the CV region and unstable at the CC region as expected from the control loop gain in Figure 75. Still at CV region the system shows continuous oscillations at the steady state (see Figure 77) and that's due to the small PM at this region which is 9°. Even though operating at MPP and in CV region has a positive effect on the control loop gain as the PM margin has improved, the PM is insufficient to be accepted for real life application especially at CV region.
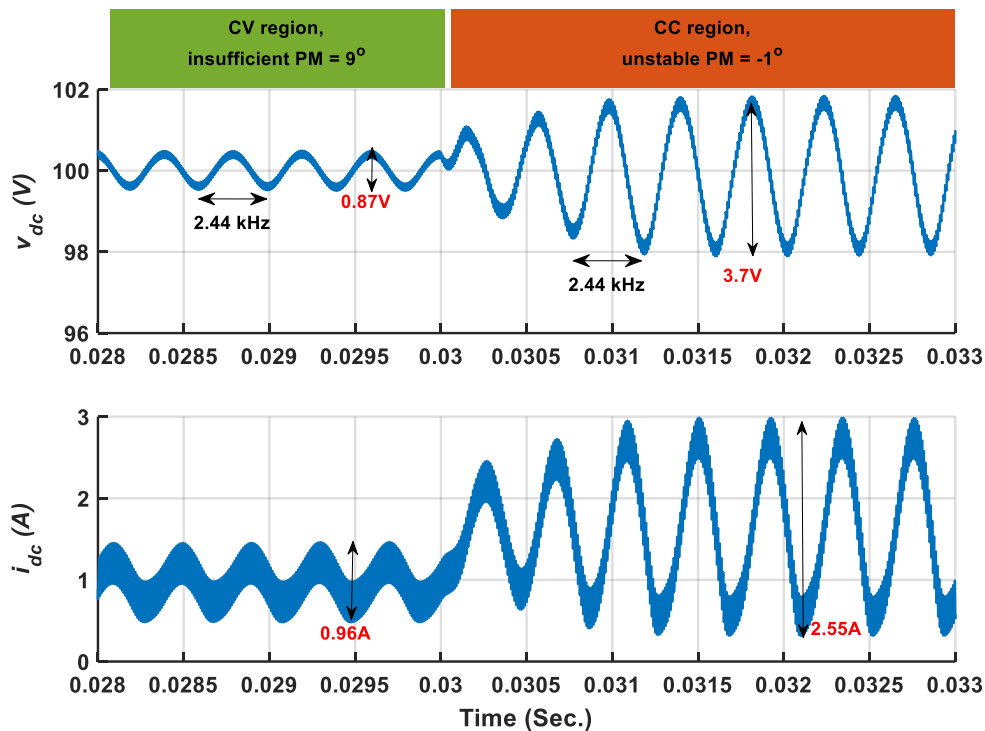

Figure 77: Simulation results of double-stage PV system with PI controller as PV moves from CV region (V_{pv}=35V) to CC region (V_{pv}=19V). K_v=11, C_{dc}=41μF, L_2=1.5mH, C_{in}=1.5 μF, f_{sw1}= f_{sw2}=100 kHz, G=1000 W/m².

To sum it all, the PI controller is not suitable to control a second order power stage converter due to the phase delay incurred by the power stage double pole. A higher order controller is required to overcome this problem as will be discussed in the next section.

5.3.2 Three-pole two-zero (3P2Z) compensation

The three-pole two-zero compensation method (structure is shown in (5.4)) include two zeros placed in the neighbourhood of the power stage double pole ($\omega_{z1} < \omega_o < \omega_{z2}$) to compensate for the -180° phase delay incurred by the power stage double pole. This will ensure a good phase for the frequencies beyond ω_o and allow sufficient PM at the designed ω_c. The two high-frequency poles ω_{p1} and ω_{p2} are necessary to provide good attenuation at the high frequencies to make sure that the high-frequency switching noises are fairly filtered [74, 83]. The control block diagram was shown in Figure 73. The voltage sensor $H_v(s)$ is assumed to operate as unity gain.

$$H_c(s) = \frac{k_v}{s} \frac{(1+\dfrac{s}{\omega_{z1}})(1+\dfrac{s}{\omega_{z2}})}{(1+\dfrac{s}{\omega_{p1}})(1+\dfrac{s}{\omega_{p2}})} \tag{5.4}$$

5.3.2.1 Control performance with 3P2Z and an ideal current source

Assuming an ideal input current source at the input of the second-stage converter the control toolbox in MATLAB Simulink is used for tuning of the three-pole two-zero controller as given in (5.5). Root Locus and the bode diagram of the designed control loop gain viewing the locations of the designed zeros and poles are shown in Figure 78 and Figure 79, respectively.
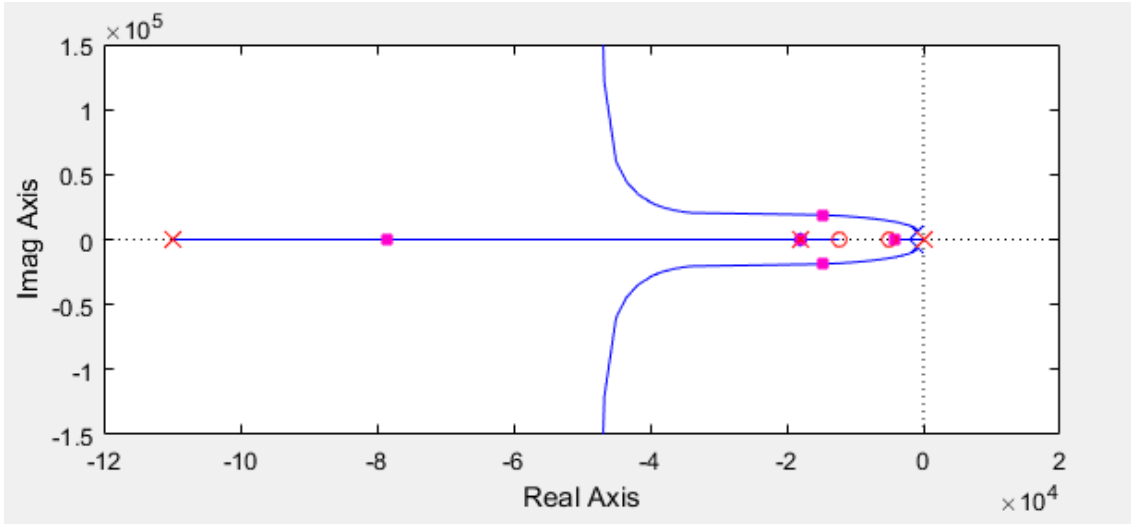
*Figure 78: Root locus of the 3P2Z control loop gain*
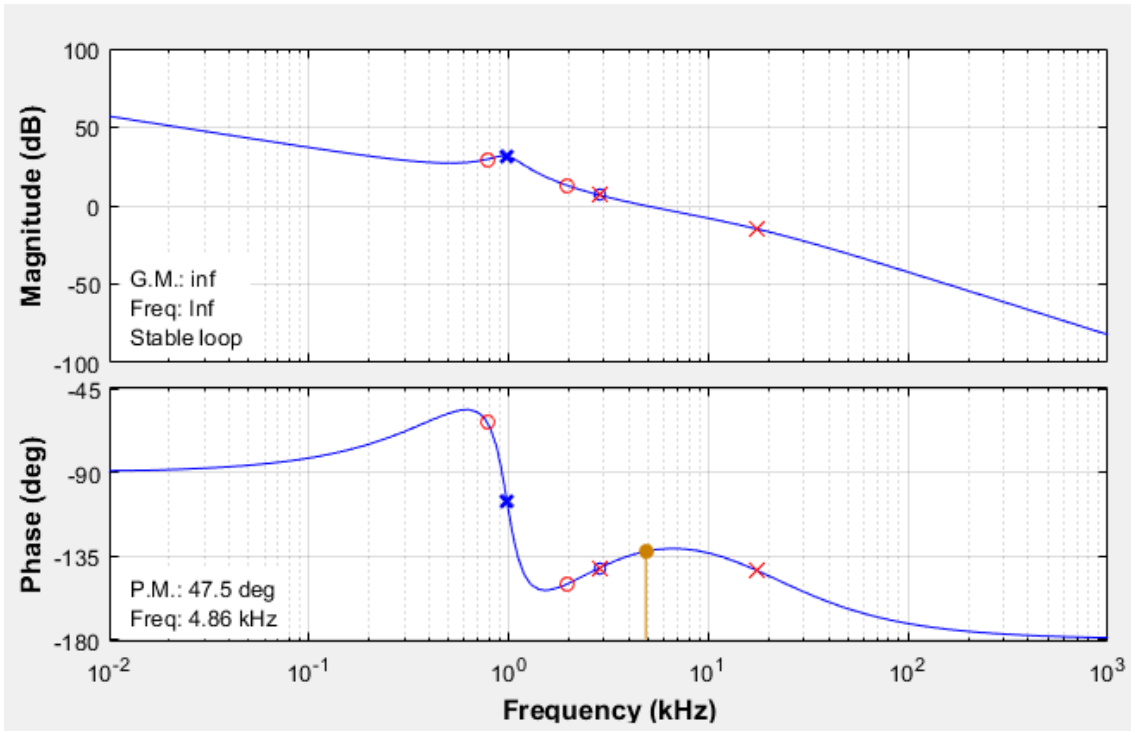
Figure 79: Bode Diagram of the designed control loop showing the locations of the designed zeros and poles

The analytical and simulation results of the control loop gain $T = H_c(s).H_{v_{dc}d_2}(s).H_{pwm}(s)$ are shown in Figure 80. The simulation results is obtained as described earlier by using the linear analysis tool in MATLAB (see Figure 76)

$$H_c(s) = \frac{k_v}{s} \frac{(1+\frac{s}{\omega_{z1}})(1+\frac{s}{\omega_{z2}})}{(1+\frac{s}{\omega_{p1}})(1+\frac{s}{\omega_{p2}})} = \frac{-222}{s} \frac{(1+\frac{s}{4.9\times10^3})(1+\frac{s}{1.2308\times10^4})}{(1+\frac{s}{1.79\times10^4})(1+\frac{s}{1.0996\times10^5})} \qquad (5.5)$$
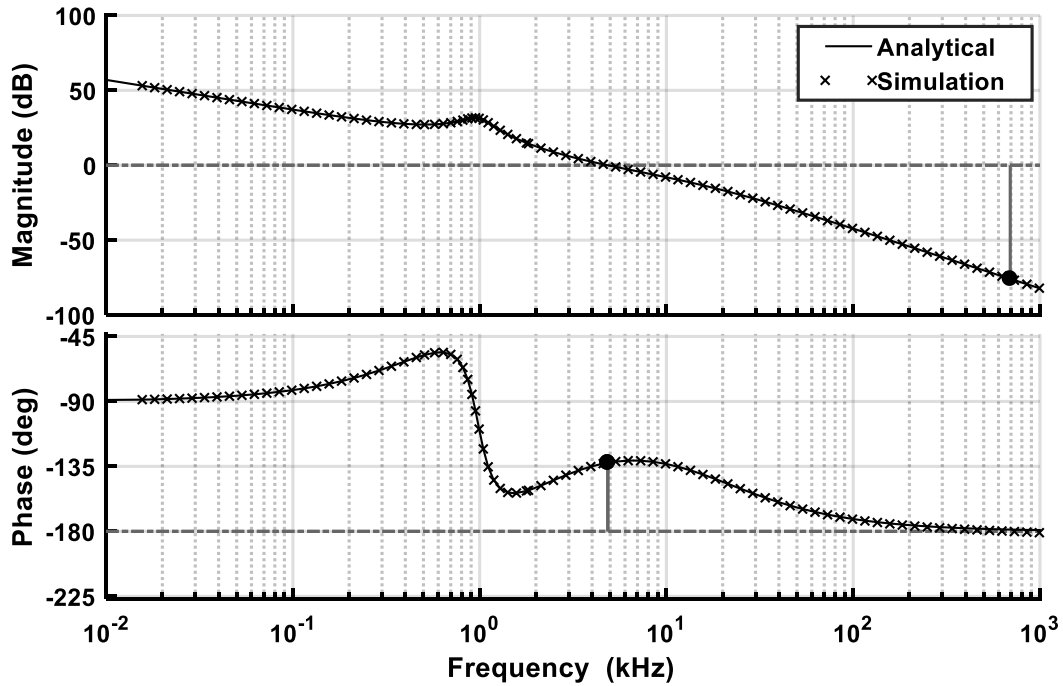
Figure 80: Analytical and simulation results of the control loop gain with 3P2Z controller and ideal input current source of 4.7A (f_c =4.86 kHz, PM=47.5°, $T_{settle} =$ 0.3 ms). System parameters: C_{dc}=44μF, L_2=0.6mH, r_{cdc}=1.26Ω, r_{l2}=6.4mΩ, and f_{sw2}=60 kHz. (Analytical optained by (5.3) and the simulation is measured using MATLAB linear analysis tool as describe in Appendix C.4 and shown in Figure 145)

Table 10: 3P2Z controller specifications

Controller Type	Specifications		
	f_c	PM	Settling time
3P2Z	4.86 kHz	47.5º	0.30 ms

5.3.2.1.1 Effect of changes in dc-link capacitance C_{dc}

A small dc-link capacitance is desirable for reducing system cost and improving system reliability. However, the second-stage control loop is normally designed for a specific value of C_{dc}. Changing C_{dc} value will affect the performance of the designed controller, because the second-stage double pole frequency depends on the value of C_{dc} as can be seen from (5.6). In order to achieve the same initial designed performance, after changing C_{dc} it will require re-designing the controller. However, the aim from changing C_{dc} without re-tuning the controller is to compare the system performance in case an ideal current source with the case of having SCPVM unit as non-ideal source. Keeping the controller parameters unchanged will show how tolerant is the controller in case of ideal current source and SCPVM source under different C_{dc} values. That will give an insight to the level of the dynamic interaction between system's stages that is

110

imposed by the non-ideal SCPVM source which will add additional constraints on re-tuning the designed controller as will be discussed later in the next sections.

Therefore, this section investigates the acceptable limit of C_{dc} to ensure harmless effect on the already designed control loop based on having ideal current source. Within this acceptable limit it is expected that the value of C_{dc} is sufficient to keep the system stable without the need to re-design the controller.

From the transfer function of the duty-cycle-to-dc-link voltage $H_{v_{dc}d_2}$ in (5.1) the second-stage double pole frequency (ω_o) is:

$$\omega_o = \frac{1}{\sqrt{L_2.C_{dc}}} \tag{5.6}$$

It depends on C_{dc} and L_2 values and based on the 3P2Z controller design rules to ensure good dynamic performance ω_o has to be in between the controllers zeros. Therefore, the designed zeros in (5.5) allow frequency range for ω_o as follow:

$$\omega_{z1} < \omega_o < \omega_{z2}$$
$$4.9 \times 10^3 \, rad/\sec < \omega_o < 1.230810^4 \, rad/\sec \tag{5.7}$$
$$780 \, Hz < f_o < 1959 \, Hz$$

The relation in (5.7) provides the design limitation for C_{dc} and L_2. The resulting frequency from any combination of C_{dc} and L_2 values has to be within the limit in (5.7). For a given second-stage inductance that designed for specific current ripple suppression (in this research L_2=600µH) the limits of C_{dc} can be found as follow:

$$4.9 \times 10^3 \, rad/\sec < \omega_o < 1.2308 \times 10^4 \, rad/\sec$$
$$4.9 \times 10^3 \, rad/\sec < \frac{1}{\sqrt{L_2.C_{dc}}} < 1.2308 \times 10^4 \, rad/\sec$$
$$4.9 \times 10^3 \, rad/\sec < \frac{1}{\sqrt{600\mu H.C_{dc}}} < 1.2308 \times 10^4 \, rad/\sec \tag{5.8}$$
$$11 \, \mu F < C_{dc} < 69 \, \mu F$$

Figure 81 and Figure 82 show the effect of C_{dc} on the control loop as the value gets smaller or higher than the allowed limit, respectively. When C_{dc} value is lower than the minimum limit, ω_o is pushed to a frequency higher than ω_{z2}. That initiates the problem

of the -180° phase delay resulting in unacceptable PM as shown in Figure 81. The case is different with large value of C_{dc} (higher than the limit in (5.8)) as the PM of the control loop gain increases as shown in Figure 82. However, higher PM results in larger ζ which might lead to an overdamped system with undesirable long settling time and very slow input response.
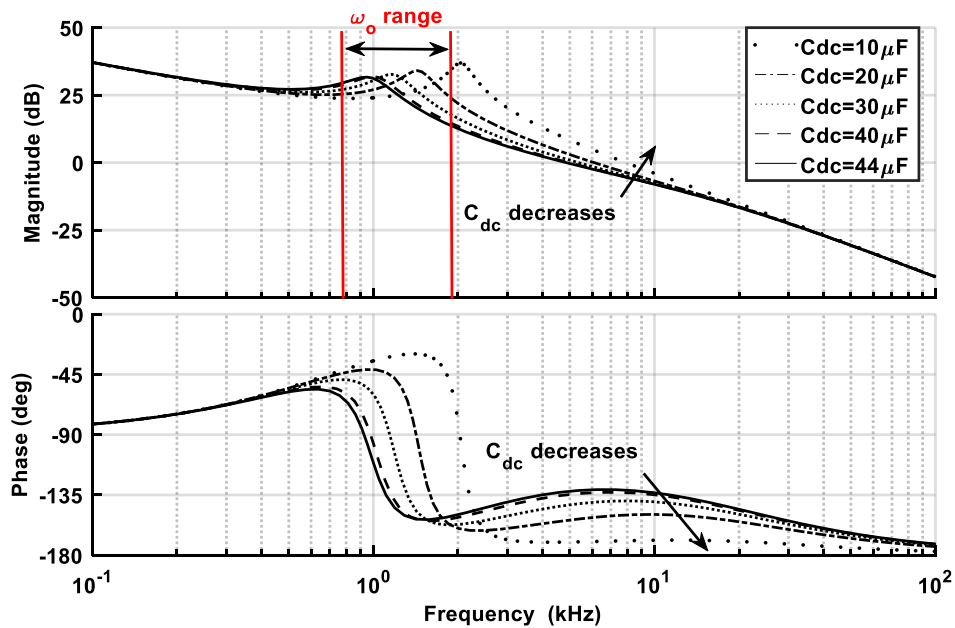

Figure 81: Effect of small C_{dc} on the control loop gain with ideal current source (4.7A) and 3P2Z controller in (5.5). $L_2=0.6mH$, $r_{cdc}=1.26\Omega$, $r_{l2}=6.4m\Omega$, and $f_{sw2}=60\ kHz$. (control loop gain measured using the model shown in Figure 145 in Appendix C.4)
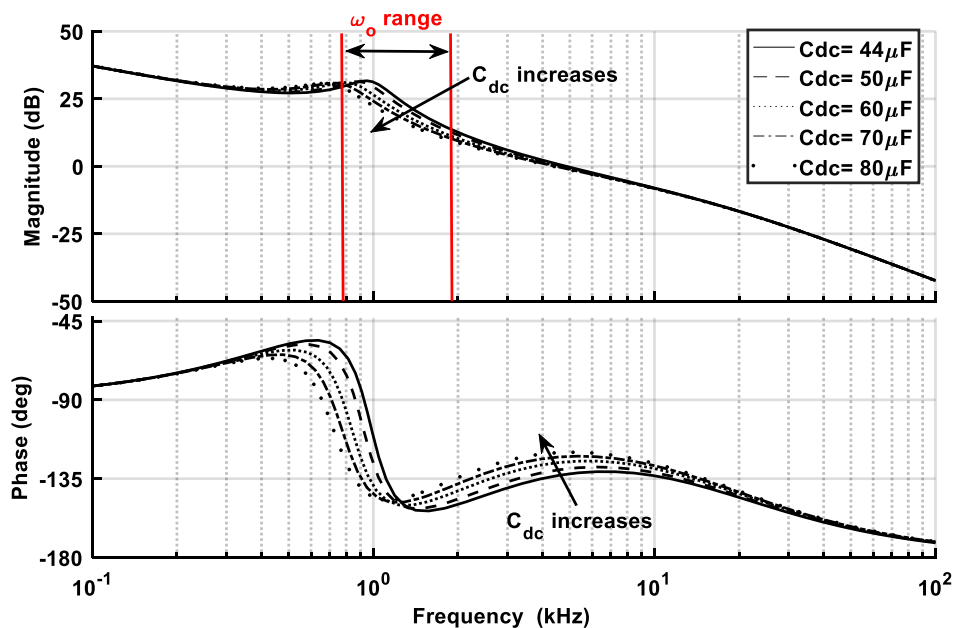

Figure 82: Effect of large C_{dc} on the control loop gain with ideal current source (4.7A) and 3P2Z controller in (5.5). $L_2=0.6mH$, $r_{cdc}=1.26\Omega$, $r_{l2}=6.4m\Omega$, and $f_{sw2}=60\ kHz$. (control loop gain measured using the model shown in Figure 145 in Appendix C.4)

The simulation result of the system with an ideal current source under different values of C_{dc} is shown in Figure 83 and Figure 84. The system is stable when sufficient C_{dc} value is used as in Figure 83.a. While in Figure 83.b the insufficient value of 10µF results in unstable system due to the small PM of the control loop.
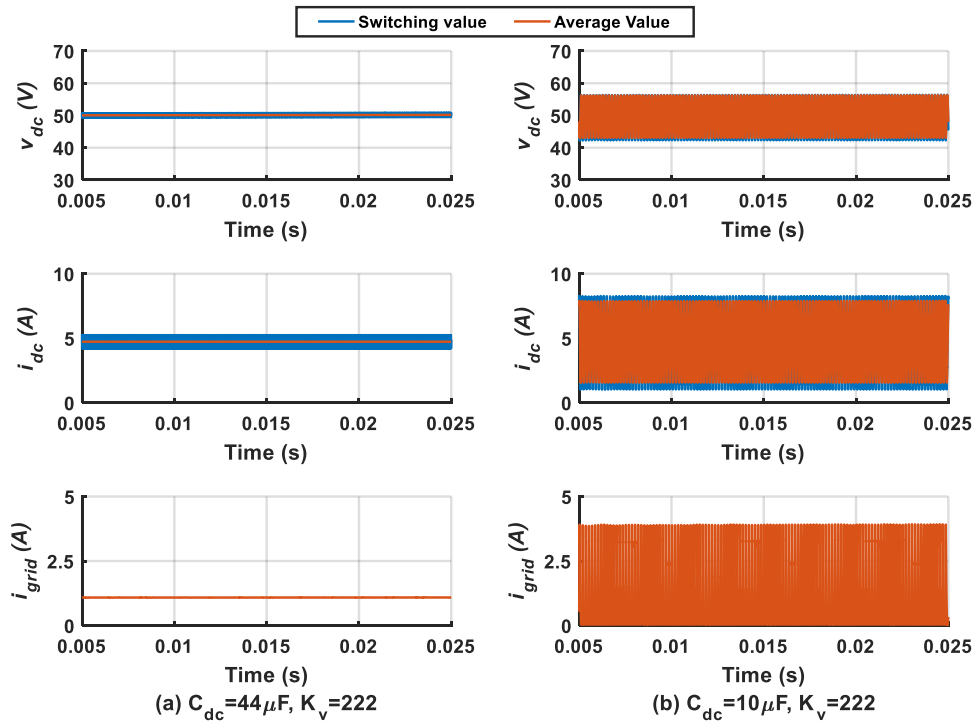
*Figure 83: Controller performance with ideal current source (4.7A); (a) stable operation with sufficient capacitance of 44µF (b) unstable operation due to insufficient capacitance of 10µF. L_2=0.6mH, r_{cdc}=1.26Ω, r_{l2}=6.4mΩ, 3P2Z controller in (5.5), and f_{sw2}=60 kHz. (the average value is the mean value of the input signal over one cycle of the 60 kHz switching frequency).*
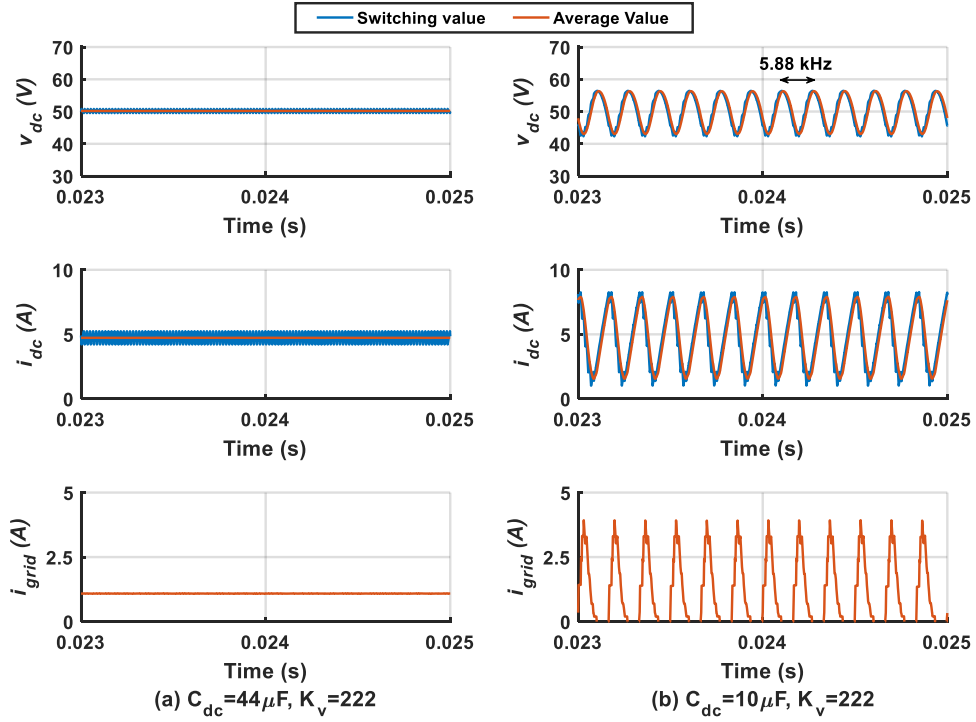
Figure 84: Zoom in of Figure 83.

5.3.2.2 Control performance with 3P2Z and a SCPVM unit as a non-ideal source

In this section the dynamic performance of the control loop is checked when the ideal current source is replaced with the original SCPVM source. The 3P2Z control is kept the same as in (5.5) which is designed based on an ideal current source. Figure 85 shows simulation results when one SCPVM unit is connected to the second-stage converter with $C_{dc} = 44\mu F$ and $G = 1000\,W/m^2$.

As discussed in Chapter 4, in steady-state (under constant solar irradiation) the P&O operating point varies every T_{mppt} and that induce periodic low-order frequency and transient oscillations in the dc-link bus. These periodic oscillations in the dc-link due to the non-ideal SCPVM source will be seen as disturbances by the control loop of the second-stage converter forcing it to interact to regulate the dc-link voltage as required every T_{mppt}. It was revealed in Chapter 4 that the dynamics and the level of the oscillations in the dc-link bus depend on the P&O parameters, solar irradiation level, and PV operating region. So, it is expected that the second-stage control loop will interact differently depending on the operating condition of the SCPVM unit. Therefore, in this section the effect of the SCPVM unit when operates under different solar irradiation levels (G) and different PV operating regions (different value of V_{pv})

on the designed control loop is explored. Then, the effect of the P&O parameters (Δd and T_{mppt}) are discussed.
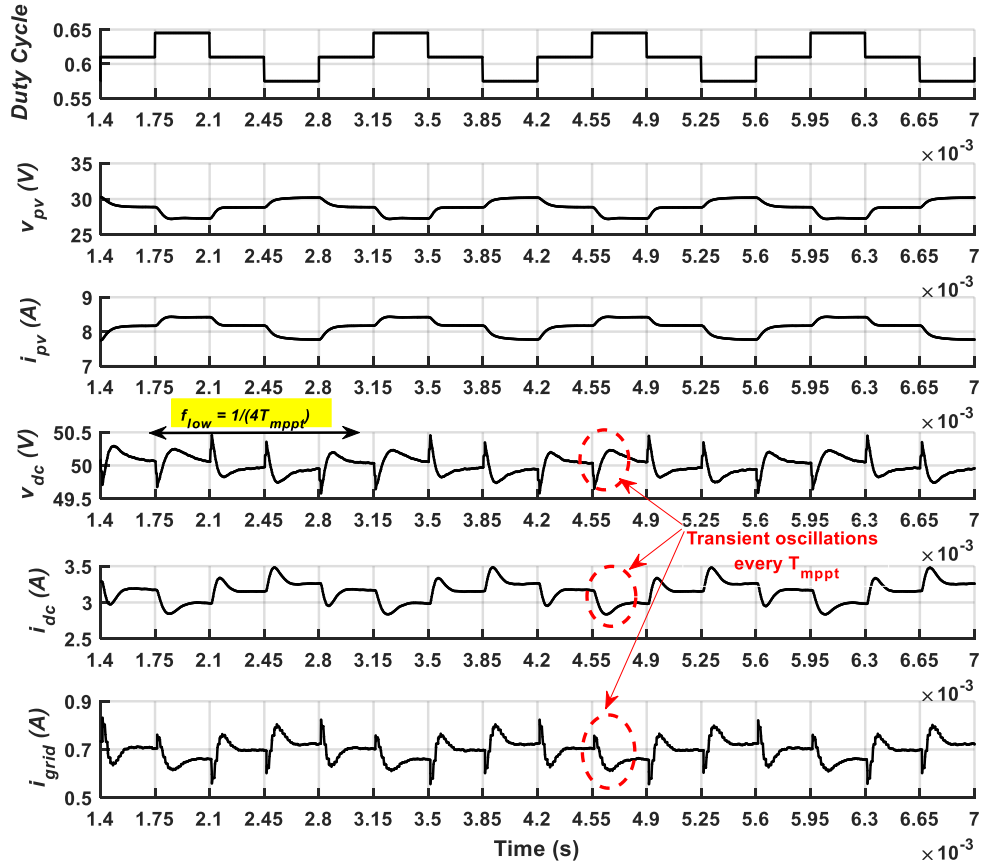

Figure 85: Simulation results of one SCPVM unit connected to the second-stage converter with 3P2Z controller in (5.5). $G = 1000W/m^2$, Δd=0.035, T_{mppt}=0.35ms, C_{dc}=44µF, and V_{grid}=200V.

5.3.2.2.1 Effect of different solar irradiation levels on the performance of the second-stage converter

The simulation results of the control loop for the system with non-ideal SCPVM source at different solar irradiation level is shown in Figure 86. The results show that with the non-ideal source (i.e. SCPVM unit) the system is more damped than the case with ideal current source. The higher the solar irradiation is, the more damped the system becomes. Also, the cut-off frequency of the system is slightly reduced. The result in Figure 86 is verified by time domain simulations as shown in Figure 87 and Figure 88. Figure 87 compares the transient behaviour of IS and NIS at high solar irradiation and show that the dc-link voltage is more damped with NIS. Figure 88 shows the transient behaviour under different solar irradiation levels (e.g. for 1000 W/m^2, 800 W/m^2, 600

W/m^2, and 400 W/m^2) which becomes more damped as the solar irradiation level increases.
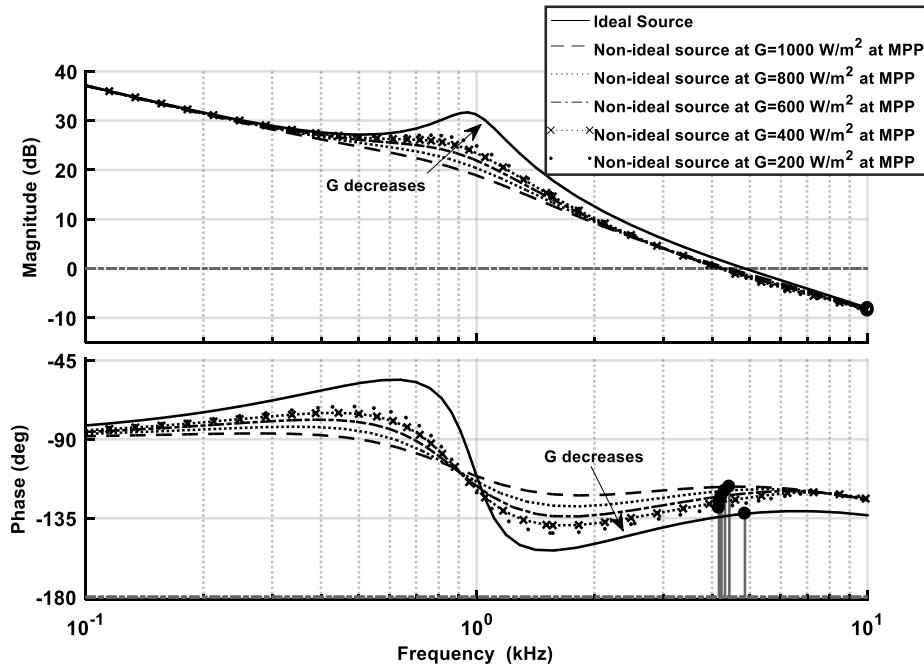
Figure 86: Effect of the non-ideal current source 'SCPVM unit' on the control loop gain under different solar irradiation level. C_{dc}=44μF and K_v=222. (control loop gain measured using the model shown in Figure 146Figure 145 in Appendix C.4)
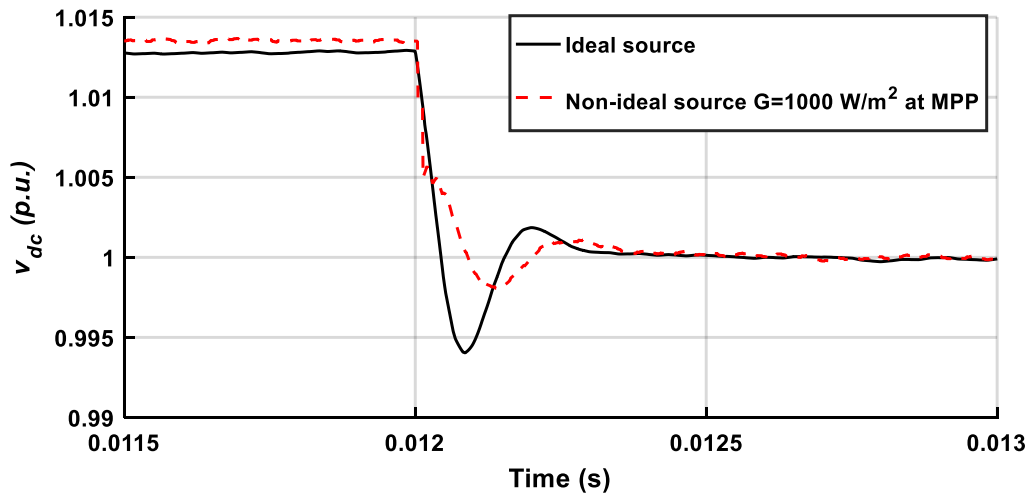

Figure 87:Time domain simulation of the dc-link voltage when the first-stage duty cycle changes from D $_{mppt}$ to D $_{mppt}$+Δd. C_{dc}=44μF and V_{dc_rated} =44V.
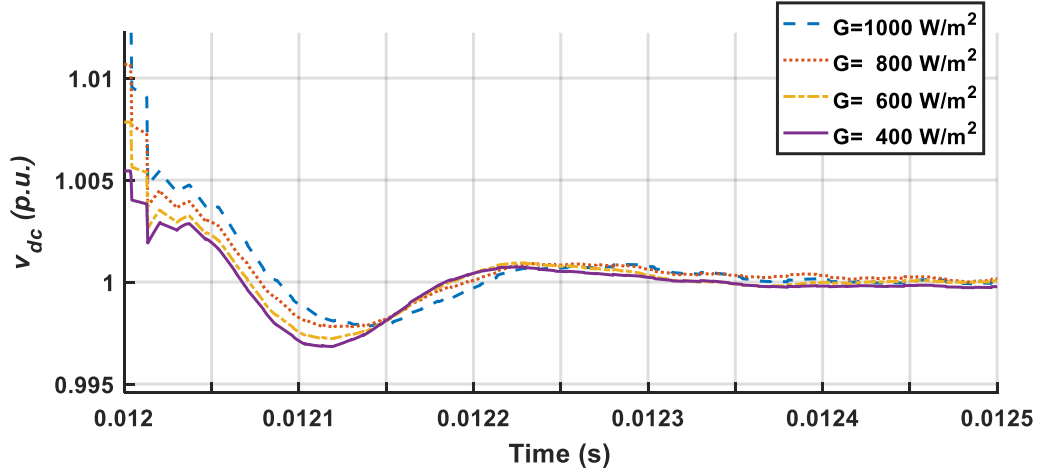
Figure 88: The dc-link transient behaviour when SCPVM unit operates under different solar irradiation levels. V_{dc_rated} =44V. C_{dc}=44µF.

5.3.2.2.2 Effect of PV operating regions

In this case the solar irradiation is kept constant at 1000 W/m^2 and the voltage across the PV is varied to different values to check the effect of the PV operating region on the dynamic performance of the control loop. The simulation results of the control loop are shown in Figure 89. The lower the PV voltage (such as v_{pv}=25V in Figure 89), the more the system behaves as an ideal current source with the least effect on the control loop gain. When the PV voltage increases toward MPP ($V_{pv} = V_{mpp}$) and to the constant voltage region (e.g. 33V in Figure 89) the system becomes more damped with higher PM. Also, the cut-off frequency of the system is influenced slightly. The time domain simulation of the dc-link voltage transient behaviour in Figure 90 verifies the simulation results of the control loop in Figure 89. The higher the PV module voltage the more damped is the control loop gain.

5.3.2.2.3 Effect of P&O parameters Δd and T_{mppt}

The perturbation step size *Δd* affects the three steady-state values of the PV module voltage V_{pv} including $V_{pv-left}$, V_{pv-mpp} and $V_{pv-right}$ (see Figure 55, page 83). These values can be found by using (4.4). In grid connected mode the output voltage V_{dc} is controlled at constant value and in this case and based on (4.4) for a specific PV module voltage at MPP (i.e. V_{pv-mpp}) D_{mppt} will be constant and the adopted value *Δd* decides the values of $V_{pv-left}$ and $V_{pv-right}$. It was discussed earlier in section 5.3.2.2.2 that the transient dynamic of the control loop depends on the value of V_{pv} (see Figure 89 and Figure 90). Therefore, a different value of Δd changes $V_{pv-left}$

117

and $V_{pv-right}$ that leads to different transient dynamics of the control loop. The smaller Δd is, the slightest the dynamic of the control loop is affected as the difference between $V_{pv-left}$ and $V_{pv-right}$ will be very small. However, the minimum value of Δd is constrained by the SCPVM dynamic and the average rate of change in the solar irradiation as given in equation (2.10).
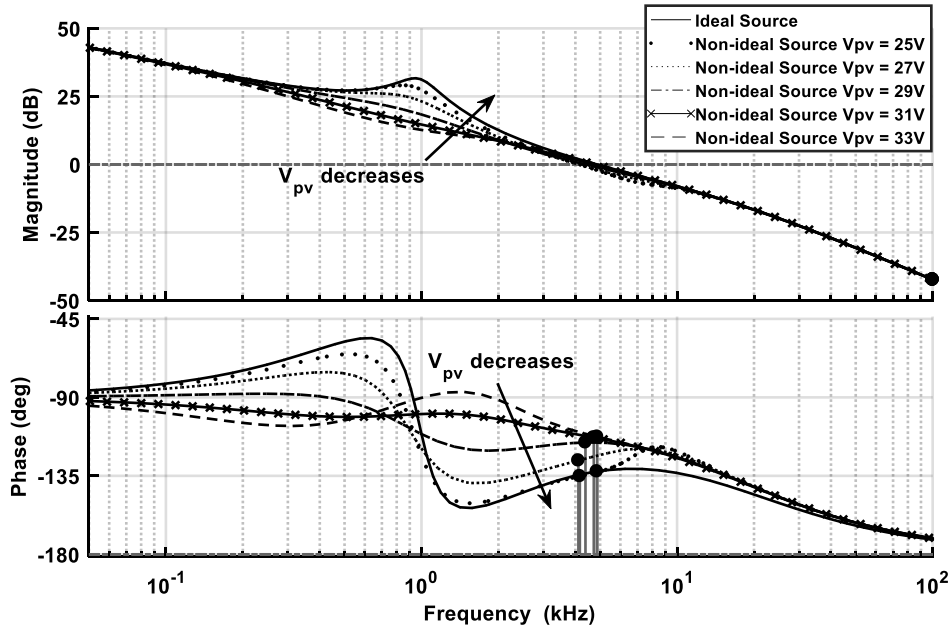
Figure 89: Effect of different PV operating regions on the control loop gain.
$C_{dc}=44\mu F$, $K_v=222$, and $G=1000W/m2$. (control loop gain measured using the model shown in Figure 146 Figure 145in Appendix C.4).
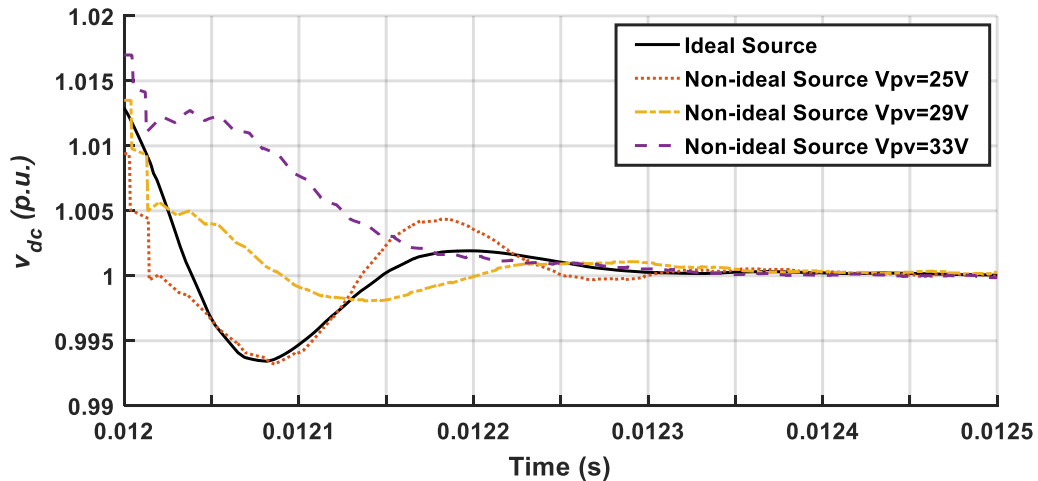
Figure 90: The dc-link transient behaviour when SCPVM unit operates at different operating region. $V_{dc\_rated}=44V$. $C_{dc}=44\mu F$, and $G=1000$ $W/m2$.

As has been discussed in chapter 2, section 2.3.1.2, the time interval between two adjacent perturbations T_{mppt} is optimised based on the transient behaviour of the PV

118

module voltage and current (v_{pv} and i_{pv}) of the SCPVM unit. However, the P&O perturbations also affect the dc-link voltage and current (v_{dc} and i_{dc}) and that forces the controller to enter a transient mode every T_{mppt} as seen in Figure 85. The given time for v_{dc} and i_{dc} to settle to their new steady state value after each perturbation is limited by T_{mppt}. Therefore, it is expected that a control loop characterised by a settling time longer than T_{mppt} will result in unsettled transient periods in the dc-link which will certainly affect the system power quality. In contrast, when the control loop gain is characterised by a settling time shorter than T_{mppt}, the current transient period in the dc-link will settle down before a new transient period start. As discussed in Section 3.3.3 $T_{mppt}$is chosen to be 0.35 ms for the first-stage converter. This has been taken into account when designing the second-stage controller and control loop gain in (5.5) is designed with a settling time (T_{settle}) of 0.3 ms.

To demonstrate the effect of different values of T_{mppt} on the settling of the transient in the dc-link and grid sides due to the P&O perturbation the original designed P&O sampling period ($T_{mppt} = 0.35\ ms$) is changed first to a longer period of 0.7 ms then to a shorter period of 0.2 ms as shown in Figure 91 and Figure 92, respectively. The longer sampling period of 0.7 ms is providing longer time for the v_{dc} , i_{dc} and i_{grid} to be settled and damped before the next P&O perturbation occurs as shown in Figure 91. In case of shorter sampling period of 0.2 ms which is the minimum limit for the studied system based on (3.12) (see Section 3.3.3) the new transient period starts before the previous transient oscillations finish. The result is frequent unsettled transient periods in the dc-link and grid sides.

In order to make sure that the transients of v_{dc} and i_{dc} are settled, the settling time of the dc-link control loop has to be shorter than T_{mppt}. That can be achieved either by considering this from the beginning when designing the control loop gain of the second-stage or by readjusting the P&O sampling time to be longer than the designed control loop gain settling time. However, the second option is not desirable as it degrades the P&O performance. It is important to highlight that as for voltage-mode controller the transient characteristics (e.g. the settling time) of the control loop gain are influenced by solar irradiation level and the PV operating region as was shown in Figure 86 and Figure 89. Therefore, the worst case which leads to the longest dc-link control loop settling time has to be considered when comparing with T_{mppt}. According

to Figure 86 and Figure 89 the worst case is when the irradiation and PV voltage are at their highest operating values (where ζ and PM increase).
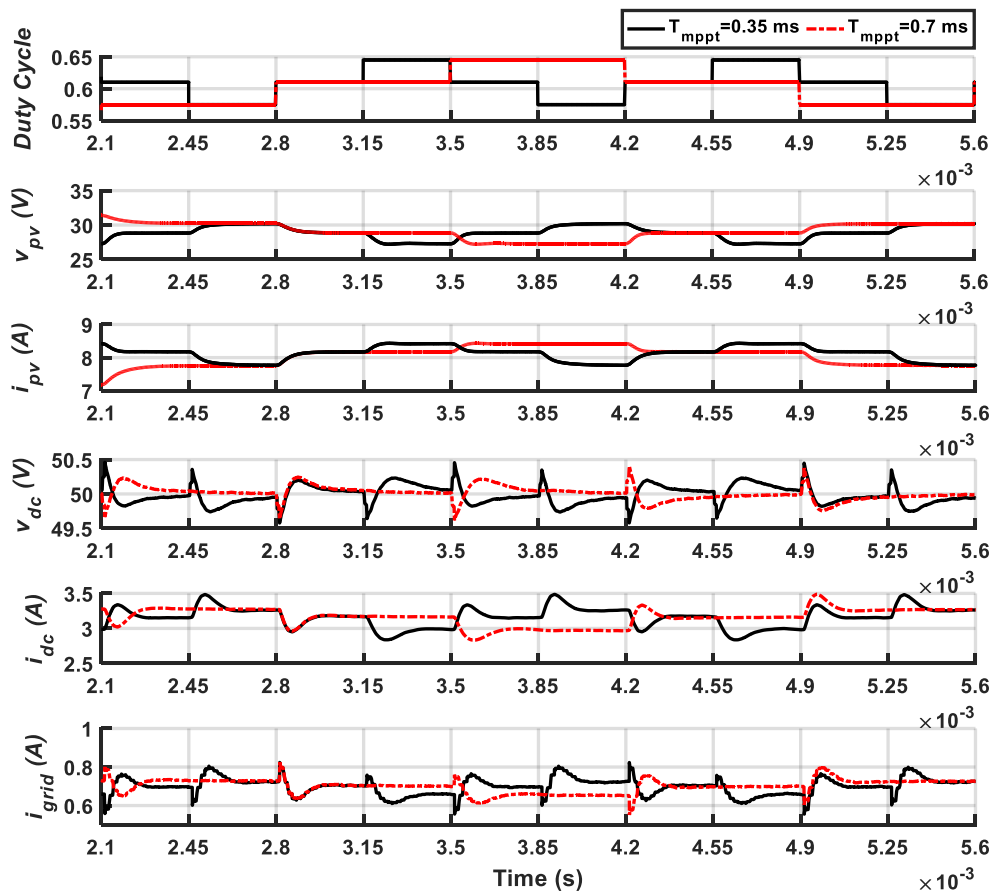
Figure 91: Effect of increasing T_{mppt} on settling of the transient oscillations in the dc-link and grid sides (V_{dc}, I_{dc} and I_{grid}). $G = 1000\ W/m^2$, C_{dc}=44µF, L_2=600 µH, 3P2Z controller in (5.5).
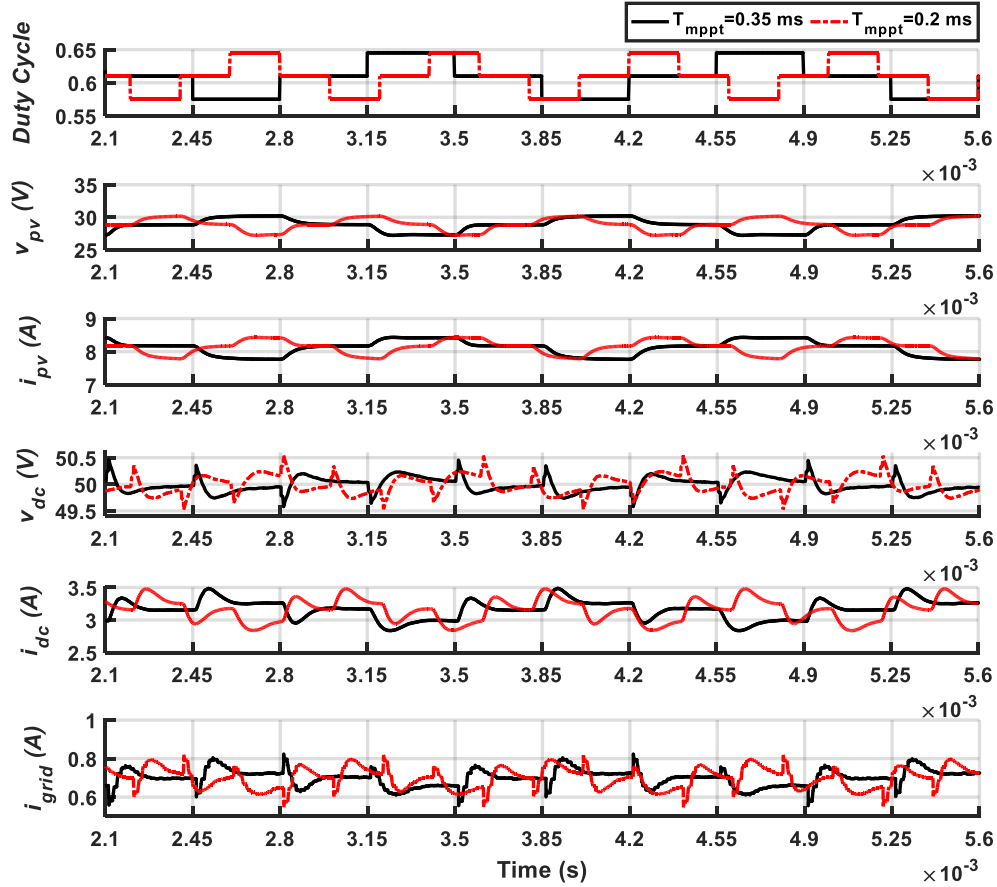
Figure 92: Effect of reducing T_{mppt} on settling of the transient oscillations in the dc-link and grid sides (V_{dc}, I_{dc} and I_{grid}). $G = 1000 \ W/m^2$, C_{dc}=44µF, L_2=600 µH, 3P2Z controller in (5.5).

5.3.2.2.4 Effect of changes in dc-link capacitance C_{dc}

As has been shown in Figure 86 - Figure 91 the control loop gain is stable under different solar irradiation levels and different PV operating regions for the nominal dc-link capacitance value (C_{dc}=44µF). In this section the PV voltage and the solar irradiation are kept constant and C_{dc} is varied to different values to check its effect on the control loop gain as shown in Figure 93. One can see that the control loop gain becomes less damped with lower PM when C_{dc} decreases. In other words the transient behaviour of the dc-link voltage V_{dc} will be more oscillatory and take longer time to settle when C_{dc} decreases.
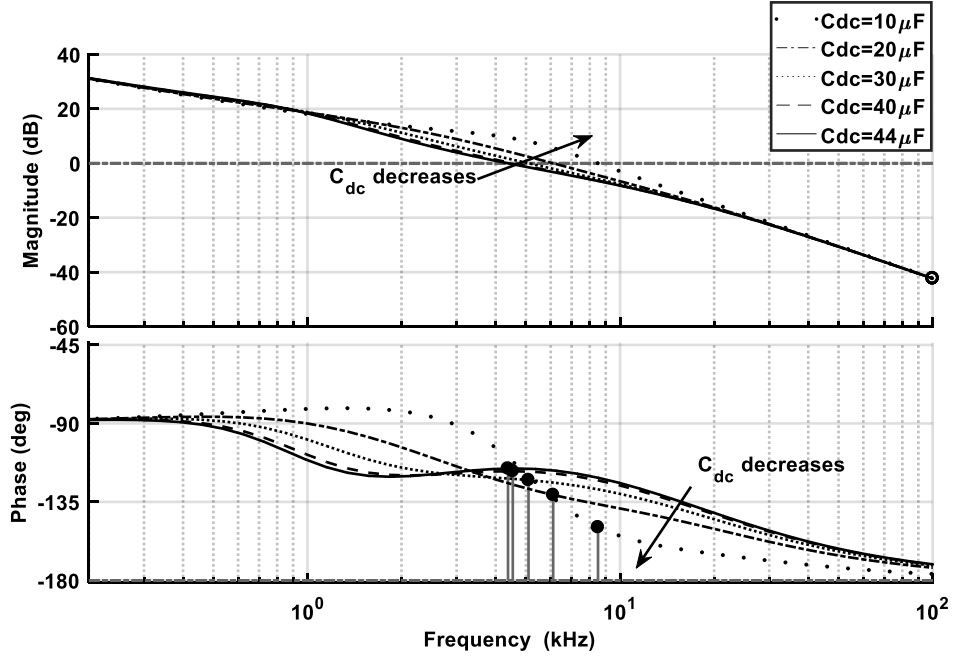
Figure 93: Effect of C_{dc} on the control loop gain. G=1000 W/m² and 3P2Z controller in (5.5). (control loop gain measured using the model shown in Figure 146Figure 145 in Appendix C.4)

Time domain simulations of the v_{dc} and i_{dc} for different values of C_{dc} is shown in Figure 94. It shows that at decreased value of C_{dc}, the v_{dc} transient during T_{mppt} becomes more oscillatory and it takes longer time to settle. Also, C_{dc} affects the transient performance of the uncontrolled i_{dc}. The transient behaviours of v_{dc} and i_{dc} are very important as with the employed P&O controller the system enters transient mode every T_{mppt}. That makes the transient dynamics of v_{dc} and i_{dc} a critical factor in deciding the minimum required capacitance in the system and re-tuning the controller after changing C_{dc} to ensure high power quality and stability. Obviously, the value of C_{dc} should not result in a high transient oscillations or long settling time that violate the condition of $T_{settle} < T_{mppt}$ as was discussed earlier in Section 5.3.2.2.3. Figure 94 shows poor transient performance of v_{dc} and i_{dc} at low capacitance value of 14.2µF and that affect the dc-link power quality significantly.

In the previous analysis considering ideal current source, the limiting range of C_{dc} is decided based on the condition of having $\omega_{z1} < \omega_o < \omega_{z2}$ to avoid the -180° phase delay caused by the power stage double pole. Higher constraints are applied on the C_{dc} in case of non-ideal SCPVM source which is associated with the dynamic performance of the dc-link voltage and current. In addition to that, the P&O sampling time is another constraint as it limits the transient time of v_{dc} and i_{dc} after each P&O perturbation. As

discussed above and previously in Chapter 4 the dc-link transient performance is a function of C_{dc}, G, v_{pv}, and of course it is a function of the controller parameters (e.g. K_v). As the system operates in MPP mode and P&O step size is typically very small the variations in v_{pv} is steady state will be small and thus its effect on the transient behaviour can be ignored. Therefore, the next section provides some simulation examples that explore the effect of C_{dc}, G, and K_v on system power quality.
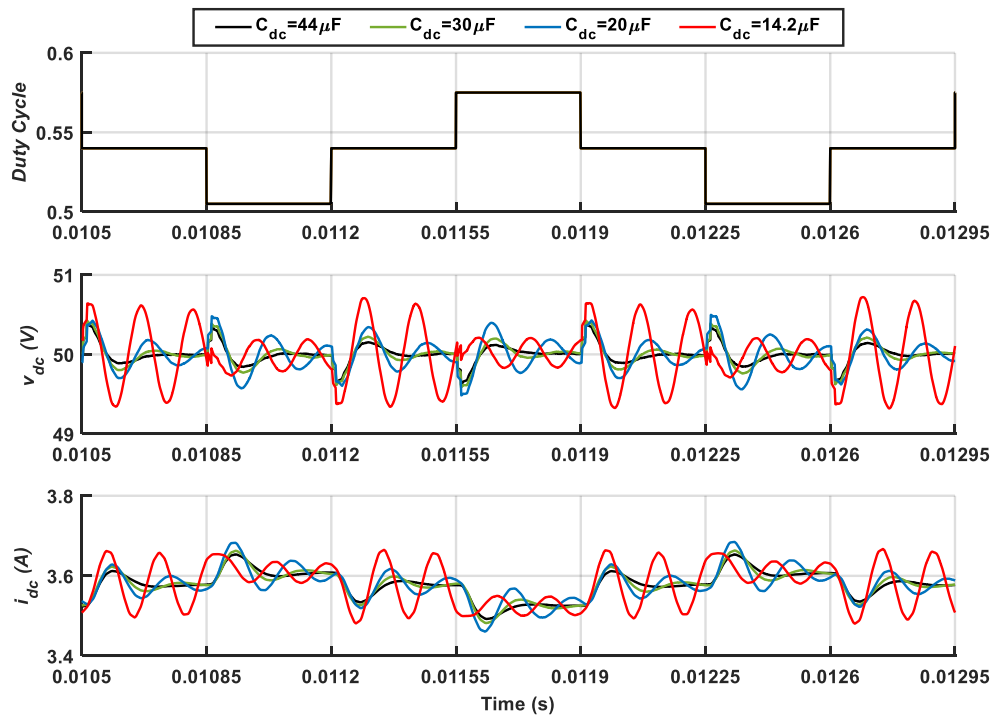
Figure 94: Effect of C_{dc} on the dc-link voltage and current transients. G=1000W/m^2.

5.3.2.2.5 Time domain simulation

Figure 95 show simulation results of the system operating with two different values of C_{dc}. In case of sufficient C_{dc} of 30 µF as shown in Figure 95.a good transient performance and power quality are achieved at the dc-link and grid sides. When C_{dc} is reduced to 14.2 µF as shown in Figure 95.b the power quality has degraded significantly (see the dc-link and grid current waveforms in Figure 95.b). The poor power quality is associated with the poor transient performance in the dc-link side. Depending on how small C_{dc} is a worse situation might occur (i.e. poorer power quality and chaotic like behaviour) especially if C_{dc} value results in transient settling time that longer than the P&O sampling time.

The small value of C_{dc} in Figure 95.b has affected the transient performance. The transient became more oscillatory and required longer settling time which violates the

123

condition of having $T_{settle} < T_{mppt}$. So frequent unsettled transient oscillations occur in the dc-link and grid sides and that affect the system power quality. Considering longer P&O sampling period to allow the transient of v_{dc} and i_{dc} to settle down is one of the options that can help to avoid the chaotic like behaviour in the dc-link bus. However, as shown in Figure 96 the P&O sampling period has to be increased to ten times the original designed T_{mppt} (from 0.35 ms to 3.5 ms) to allow enough time for the dc-link voltage and current to settle when C_{dc} is reduced to 14.2 µF. However, this solution is not desirable as it degrades the P&O performance. As shown in Figure 95 the poor power quality in the dc-link has not affected the three step operation of the P&O controller, so increasing T_{mppt} is not necessary and it will only reduce the P&O efficiency without solving the problem of the poor power quality at the dc-link and grid sides.
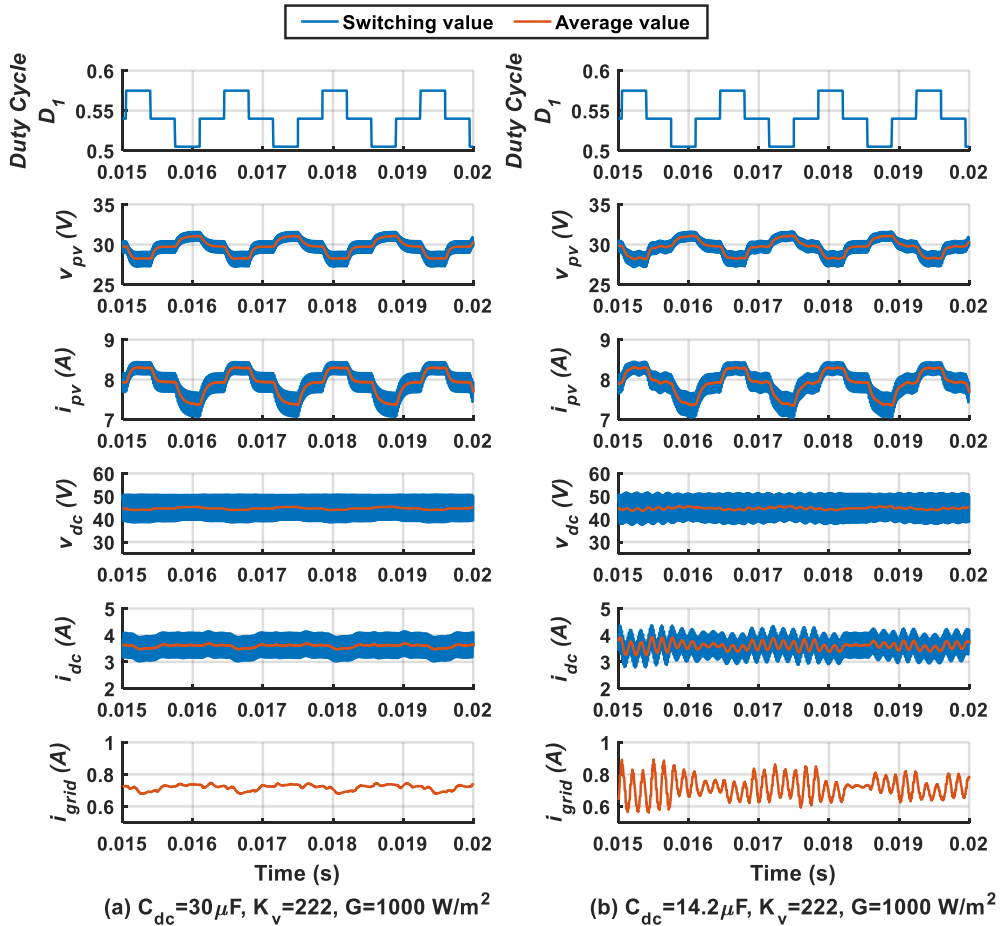

Figure 95: Effect of C_{dc} on the dc-link and grid power quality with 3P2Z controller in (5.5); (a) sufficient capacitance of 30µF, (b) insufficient capacitance of 14.2µF. (the average value is mean value of the input signal over a one cycle of the 60 kHz switching frequency).

124

The first 25 ms of the simulation results in Figure 97 is for same T_{mppt}, G and K_v used in Figure 95 but with C_{dc} reduced slightly more to 14.1 µF. It can be seen that the situation is getting worse and now the system is unstable.

It has been discussed earlier that the transient performance of i_{dc} (see Figure 59, page 89) and the controlled v_{dc} (Figure 86, page 116) depends on the solar irradiation level and as the instability in Figure 97 is due to the poor transient performance (that was caused by the reduced capacitance value of 14.1µF under G=1000 W/m^2), it is expected that changing the solar irradiation level can be a factor that affect the system stability depending on the effect of G on the transient behaviour. As an example, at t=25ms in Figure 97 the solar irradiation has changed from 1000 W/m^2 to 800 W/m^2 and both K_v and C_{dc} are kept the same. The result shows that reducing the irradiation level has stabilised the system. That might be associated with the fact that at lower solar irradiation the transient dynamics of v_{dc} and i_{dc} become faster and in this case the dc-link voltage and current have a better chance to settle down within the given time period of T_{mppt}.
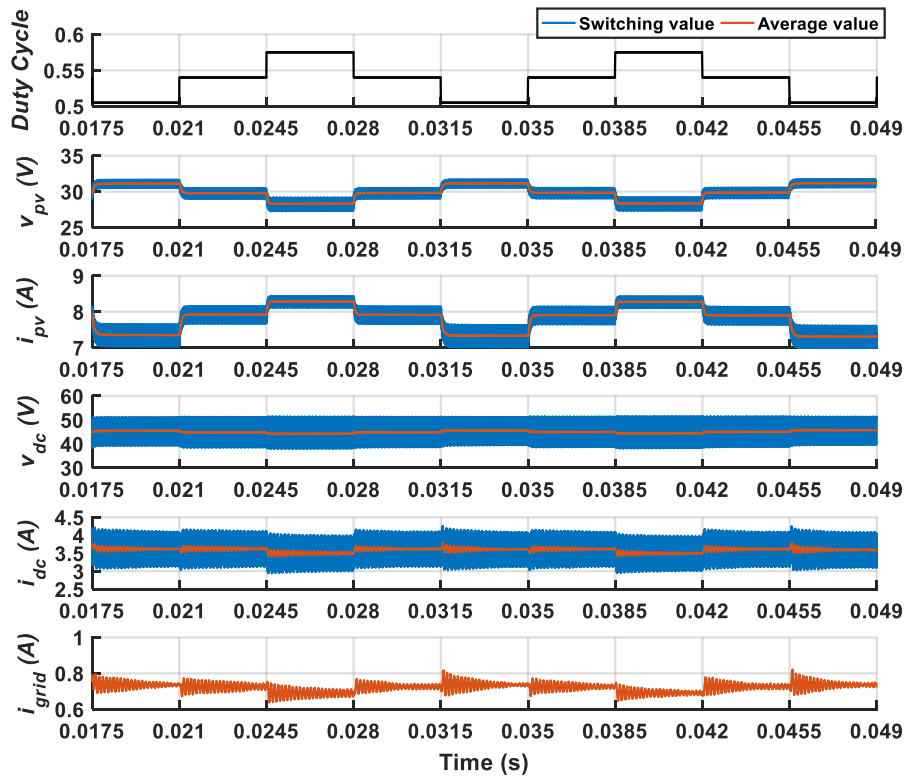
Figure 96: Effect of T_{mppt} on settling time of the transient oscillations in the dc-link and grid sides with small C_{dc}=14.2 µF, $G = 1000$ W/m^2,3P2Z controller in (5.5). and T_{mppt}=3.5ms. (the average value is mean value of the input signal over a one cycle of the 60 kHz switching frequency).

125
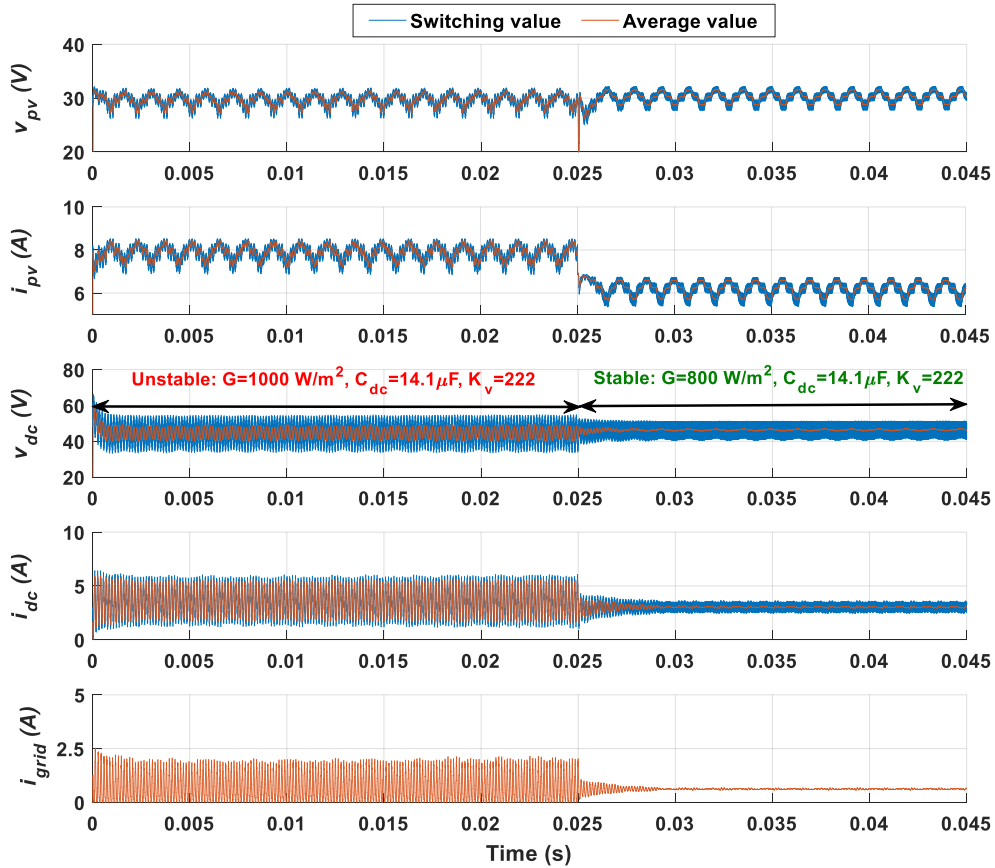
Figure 97: Effect of solar irradiation level on the dc-link and grid stability.
C_{dc}=14.1µF, 3P2Z controller in (5.5), at t<25ms $G = 1000 \, W/m^2$, and at t>25ms
$G = 800 \, W/m^2$. *(the average value is mean value of the input signal over a running*
window of one cycle of the 60 kHz switching frequency).

Another option to stabilise the system can be by re-tuning the controller. It was seen in Figure 93 that when the capacitance size reduces, the PM of the control loop gain decreases and f_c increases. These two values; the PM and f_c can be readjusted by re-tuning the voltage gain of the 3P2Z controller K_v. Based on Figure 93, reducing K_v will readjust the control loop gain characteristic by increasing the PM and reducing f_c and in that reversing the effect of reduced C_{dc}. Figure 98 shows the effect of changing K_v on stabilising the system. The unstable system with $G = 1000$ W/m^2, C_{dc}=14.1 µF, and K_v=222 became stable after K_v has been reduced to 215 at t=25 ms.
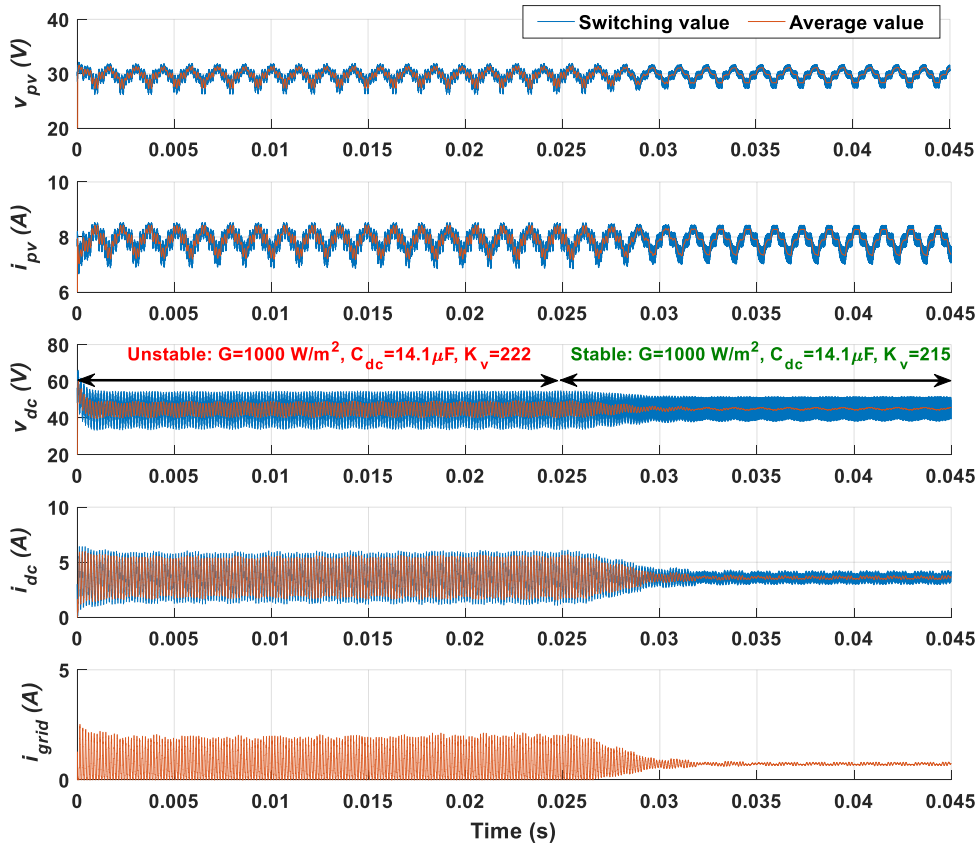
Figure 98: Effect of the voltage gain K_v on the dc-link and grid stability. C_{dc}=14.1μF, G=1000 W/m², at t<25ms K_v=222, at t>25ms K_v=215. (the average value is mean value of the input signal over a running window of one cycle of the 60 kHz switching frequency).

5.3.2.3 Stability region with 3P2Z compensation for ideal current source and for SCPVM as non-ideal current source

Based on the discussion in the previous section, at specific values of C_{dc}, K_v and G a poor dynamic performance might occur in the dc-link and that can cause chaotic like behaviour and even loss of system stability. The critical values of C_{dc} for different K_v and G values for the double-stage boost converter in MPP mode are identified in this section through simulations. First, for different solar irradiation levels (G) and under specific voltage gain (K_v) the dc link capacitance C_{dc} is reduced in small steps until the system become unstable (at critical value $C_{dc\_\min\_G}$). Then, for this critical capacitance value the cut-off frequency of the control loop, $\omega_{c\_unstable\_G}$, is measured from the simulation result of the control loop gain. Of note is that the value of $C_{dc\_\min\_G}$ changes as K_v changes. Therefore, the minimum $C_{dc\_\min\_G}$, for different irradiation and voltage gain levels, is found to be defined by (5.12) which is derived from the control loop gain T (see Figure 99) as follow:

$$T = H_c(s).H_{v_{dc}d_2}(s).H_{pwm}(s) \tag{5.9}$$

Substituting (5.1), (5.4), and $H_{pwm}(s) = \frac{1}{V_m}$ in (5.9):

$$T = \frac{K_v V_{grid}}{V_m} \cdot \frac{1 + r_{C_{dc}} C_{dc} s}{L_2 C_{dc} s^2 + C_{dc}(r_{l2} + r_{C_{dc}})s + 1} \cdot \frac{\left(1 + \dfrac{s}{\omega_{z1}}\right)\left(1 + \dfrac{s}{\omega_{z2}}\right)}{\left(1 + \dfrac{s}{\omega_{p1}}\right)\left(1 + \dfrac{s}{\omega_{p2}}\right)} \tag{5.10}$$

ω_o at $\omega_{c\_unstable\_G}$ is $\dfrac{1}{\sqrt{L_2 C_{dc\_min\_G}}}$. From Figure 99 and equation (5.10), the following relation is derived:

$$20\log\left(\frac{K_v V_{grid}/V_m}{\omega_{z1}}\right) - 40\log\left(\frac{\omega_{z2}}{1/\sqrt{L_2 C_{dc\_min\_G}}}\right) - 20\log\left(\frac{\omega_{c\_unstable\_G}}{\omega_{z2}}\right) = 0 \; dB \tag{5.11}$$
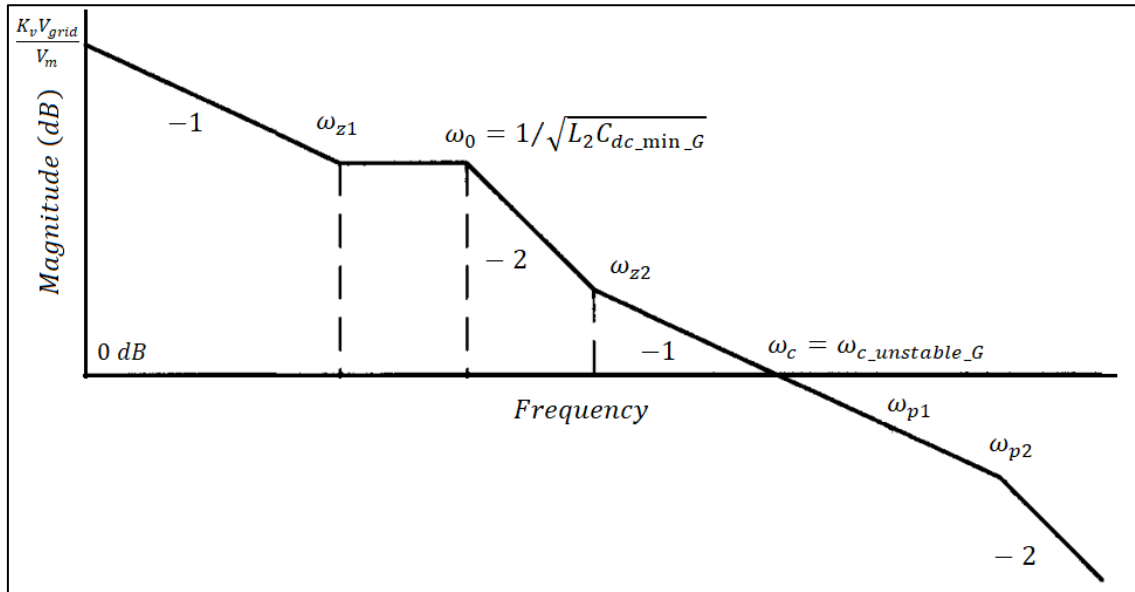

Figure 99: Graphical construction of the asymptotes of the control loop gain magnitude.

Solving and re-arranging equation (5.11) for $C_{dc\_min\_G}$ gives:

$$C_{dc\_min\_G} = \frac{K_v \; V_{grid}}{L_2 V_m \, \omega_{z1} \, \omega_{z2} \, \omega_{c\_unstable\_G}} \tag{5.12}$$

128

where K_v is the dc gain of the 3P2Z voltage mode controller, V_{grid} is the dc grid voltage, $\omega_{c\_unstable\_G}$ is the cut-off frequency where the system becomes unstable at irradiation G, L_2 is the inductance of the second stage converter, ω_{z1} and ω_{z2} are the 3P2Z controller zeros.

Therefore, based on (5.12) with SCPVM unit the minimum required dc-link capacitance C_{dc} in MPP mode with a 3P2Z voltage-mode-controller *(5.5)* with different K_v values for double-stage boost converter is depicted in Figure 100. The same equation in (5.12) can be used to find the minimum dc-link capacitance in case of having an ideal current source at the input of the second-stage converter which is also shown in Figure 100. The value of the ideal current is considered to be equivalent to the case of the SCPVM unit operating at MPP of the highest solar irradiation ($ideal\ current = I_{pv}^{1000}(1 - D_{mppt})$). So, in Figure 100 the minimum dc-link capacitance with SCPVM source is compared with the minimum dc-link capacitance in case of an ideal current source and as it can be seen the SCPVM source at the highest solar irradiation present the worst case scenario. At specific K_v the SCPVM source required higher dc-link capacitance value than the ideal current source case to ensure stable operation. The SCPVM source adds another constraint on the second-stage controller design and in this case changing the capacitance size and re-tuning the controller parameter K_v based on ideal current source might be not sufficient.
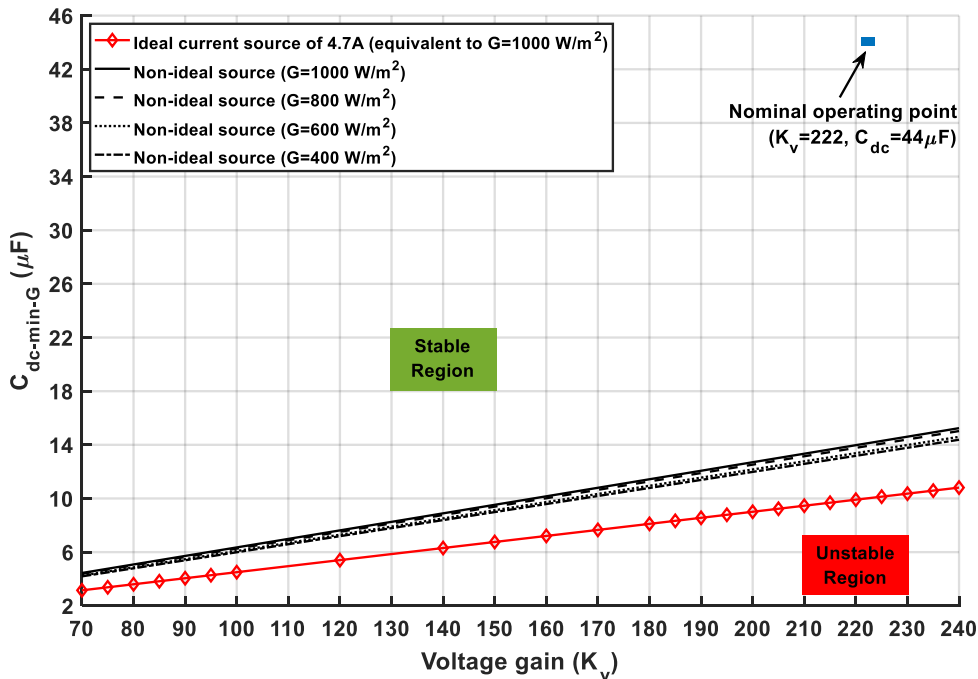
Figure 100: Minimum dc-link capacitance for ideal current source and SCPVM source with 3P2Z controller (5.5) and different K_v values.

Another simulation example for the system with SCPVM source is shown in Figure 101. At the beginning the system is stable at $G=1000\ W/m^2$, $K_v=150$, and $C_{dc}=13$ μF, then the voltage gain has increased to 225 and that destabilised the system. The stable and unstable operating points of the previous simulations results in Figure 97, Figure 98 and Figure 101 are shown on Figure 102 which verifies the accuracy of the given stability margin.
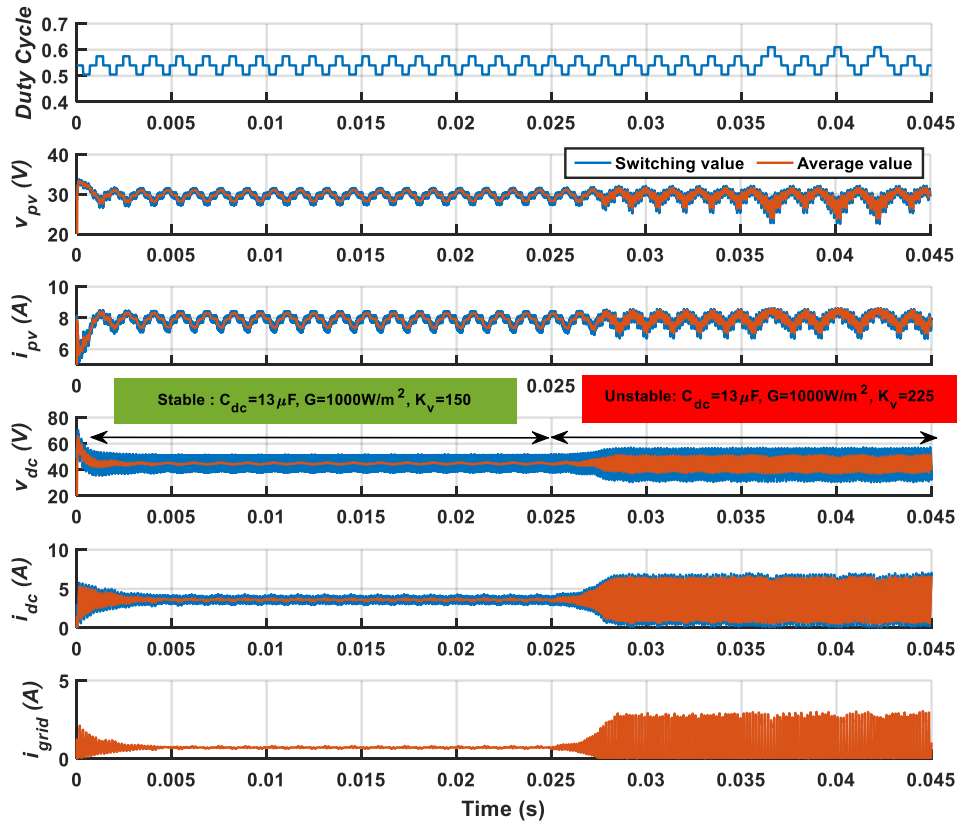
Figure 101: Destabilise the system when K_v is increased from 150 to 225 with $C_{dc}=13μF$ and $G=1000W/m^2$. (the average value is mean value of the input signal over a running window of one cycle of the 60 kHz switching frequency).
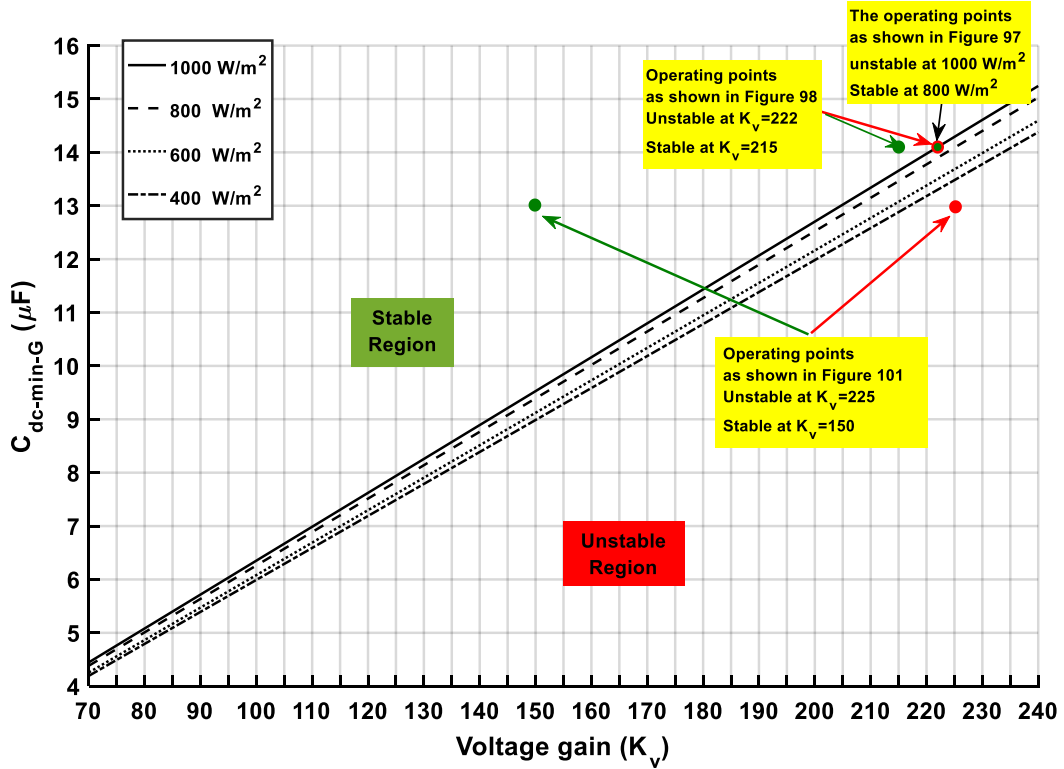
Figure 102: Showing the operating points in Figure 97, Figure 98 and Figure 101 on the curves of the minimum dc-link capacitance for SCPVM source.

5.4 Cascaded Current-Voltage Controller for Second Stage DC/DC Boost Converter

Usually a PV system that is over 1 kW capacity is controlled by cascaded current-voltage controller to control the current transient and avoid failure due to high transient peaks. In this section a cascaded current-voltage controller is designed for the system under study. The dynamic performance of the designed controller is checked through simulating the system for the two cases of having ideal current source and non-ideal SCPVM source. Effect of C_{dc}, G, and the proportional voltage gain K_{pv} on the stability of the system is investigated through simulation examples.

5.4.1 Control performance with cascaded current-voltage controller and an ideal current source

For designing the cascaded current-voltage controller it is assumed that the first-stage converter is an ideal current source, as it was the case in designing the voltage-mode controller. Accordingly, the transfer functions of the reference current-to-dc-link voltage ($H_{v_{dc}i_{l2\_ref}}$) and duty-cycle-to-current ($H_{i_{l2}d_2}$)of the second stage are:

$$H_{v_{dc}i_{l2\_ref}}(s) = \frac{-1}{C_{dc}s} \qquad (5.13)$$

$$H_{i_{l2}d_2}(s) = \frac{1}{L_2 s} \qquad (5.14)$$

The control block diagram is shown in Figure 103. The voltage and current sensors are assumed to operate as unity gain. The control toolbox on MATLAB Simulink is used for tuning the PI controllers of the voltage and current as given in (5.15) and (5.16), respectively. The specifications of the controllers are given in Table 11.

$$H_{cv}(S) = K_{pv} + \frac{K_{iv}}{s} = -1 + \frac{-10^4}{s} \qquad (5.15)$$

$$H_{ci}(S) = K_{pi} + \frac{K_{ii}}{s} = 38 + \frac{1.33 \times 10^6}{s} \qquad (5.16)$$
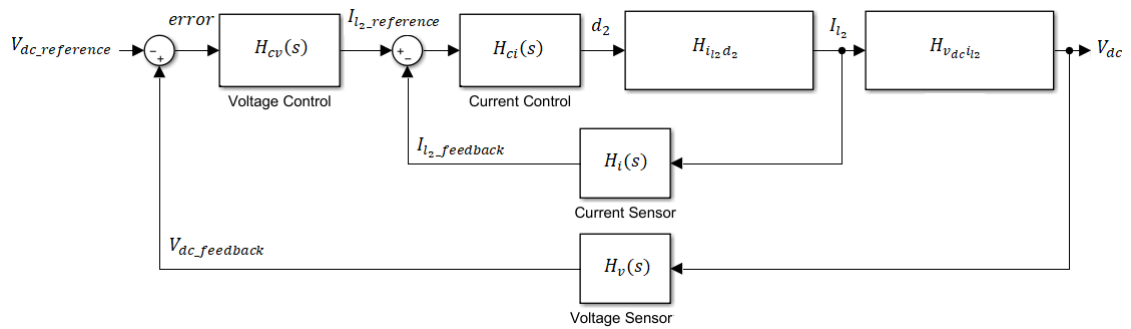
Figure 103: Block diagram of the cascaded current-voltage controller

Table 11: Cascaded current-voltage controller specifications

Controller Type	Specifications		
	f_c	PM	Settling time
PI voltage controller	3.91 kHz	67.8º	0.33 ms
PI current controller	11.2 kHz	63.7º	0.1 ms

The simulation result of the system with an ideal current source under different values of C_{dc} is shown in Figure 104. The system is stable when sufficient C_{dc} value is used as in Figure 104.a. The value of C_{dc} has decreased in small steps until the system became unstable at 20.5μF as shown in Figure 104.b.
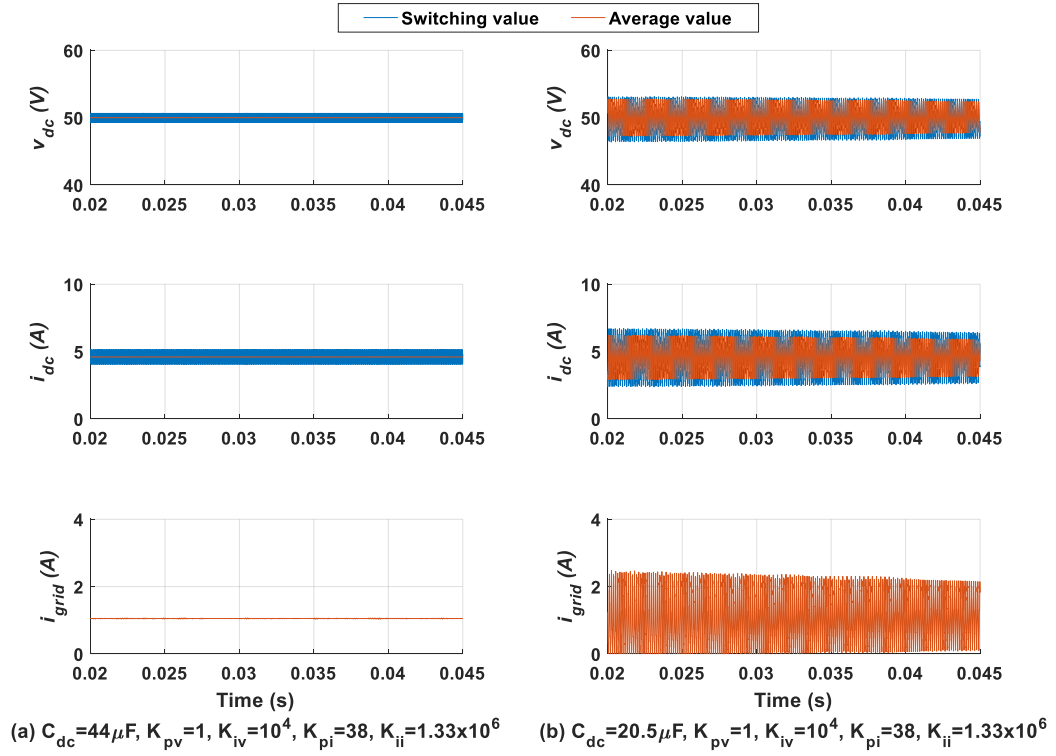
Figure 104: Cascaded controller with ideal current source (4.7A) (a) stable operation with sufficient capacitance size of 44μF (b) unstable operation due to insufficient capacitance size of 20.5μF. (the average value is mean value of the input signal over a one cycle of the 60 kHz switching frequency).

5.4.2 Control performance with cascaded current-voltage controller and a SCPVM unit as a non-ideal source

In this section the performance of the designed cascaded controller is checked when the ideal current source is replaced with the original non-ideal SCPVM source. As shown in Figure 105 the periodic oscillations in the dc-link power due to the P&O controller of the non-ideal SCPVM source are seen as disturbances by the controller and forcing it to enter transient mode every T_{mppt}. Similar to the case of the 3P2Z controller the effect of C_{dc}, G, and the proportional voltage gain K_{pv} on system stability is checked.

133
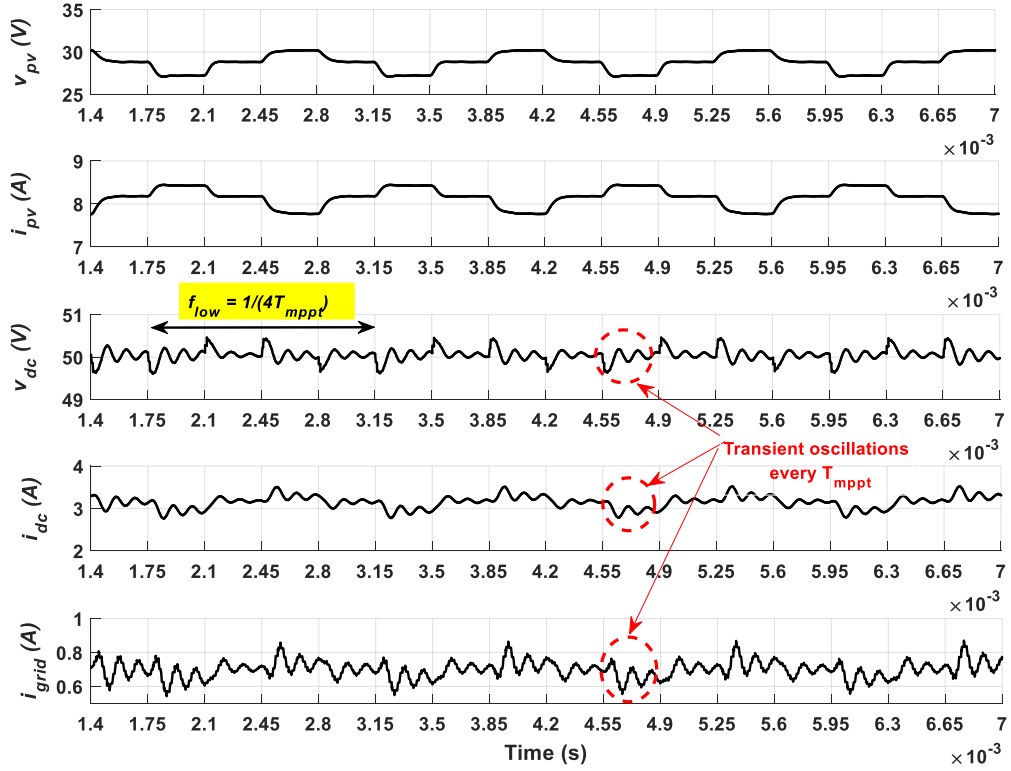
Figure 105: Simulation results of one SCPVM unit connected to the second-stage converter with cascaded current-voltage controller. $G = 1000W/m^2$, $\Delta d=0.035$, $T_{mppt}=0.35$ ms, $C_{dc}=44\mu F$, $K_{pv}=1$, $K_{iv}=1\times10^4$, $K_{pi}=38$, $K_{ii}=1.33\times10^6$, $V_{grid}=200V$.

5.4.2.1   Effect of C_{dc} size

In this test as shown in Figure 106 solar irradiation level and K_{pv} are kept constant at $1000\ W/m^2$ and 1, respectively, while the value of the C_{dc} has changed from 44 µF to 22 µF. Figure 106 shows that in case of sufficient C_{dc} size of 44 µF, as shown in Figure 106.a, good transient performance and power quality are achieved. When C_{dc} is reduced to 22 µF, as shown in Figure 106.b, the power quality at both the dc-link and grid sides has degraded significantly. This emphasises that also with the cascaded controller the dc-link transient becomes more oscillatory and required longer time to settle with small capacitance size which might results in chaotic like behaviour.
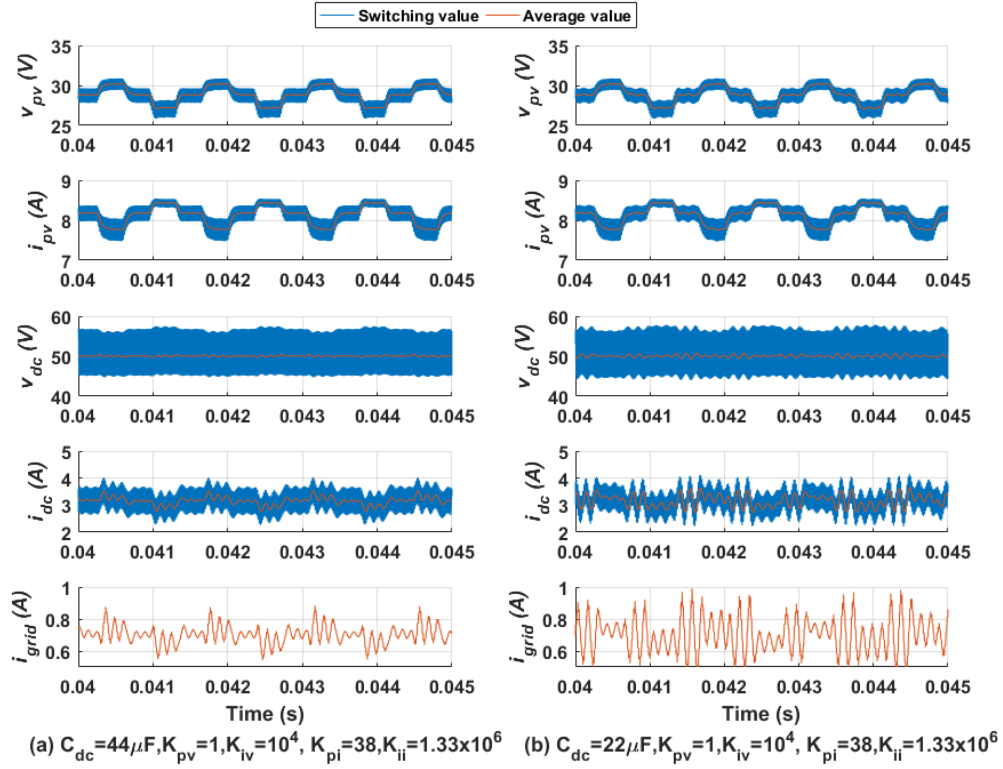
Figure 106: Effect of C_{dc} value on the power quality in the dc-link and grid sides at G=1000W/m² and $k_{pv} = 1$: (a) sufficient capacitance size 44μF (b) insufficient capacitance size 22μF. (the average value is mean value of the input signal over a one cycle of the 60 kHz switching frequency).

5.4.2.2 Effect of solar irradiation level

In this test as shown in Figure 107 C_{dc} value and K_{pv} are kept constant at 21.5 μF and 1, respectively. The solar irradiation level has changed from 600 W/m^2 to 1000 W/m^2. Figure 107 shows that with cascaded controller the solar irradiation level also affect the power quality of the dc-link and grid sides. Same as 3P2Z voltage mode controller the high solar irradiation level presents the worst case scenario which drive system to a chaotic like behaviour and instability under specific operating point (C_{dc} and k_v) as shown in Figure 107.
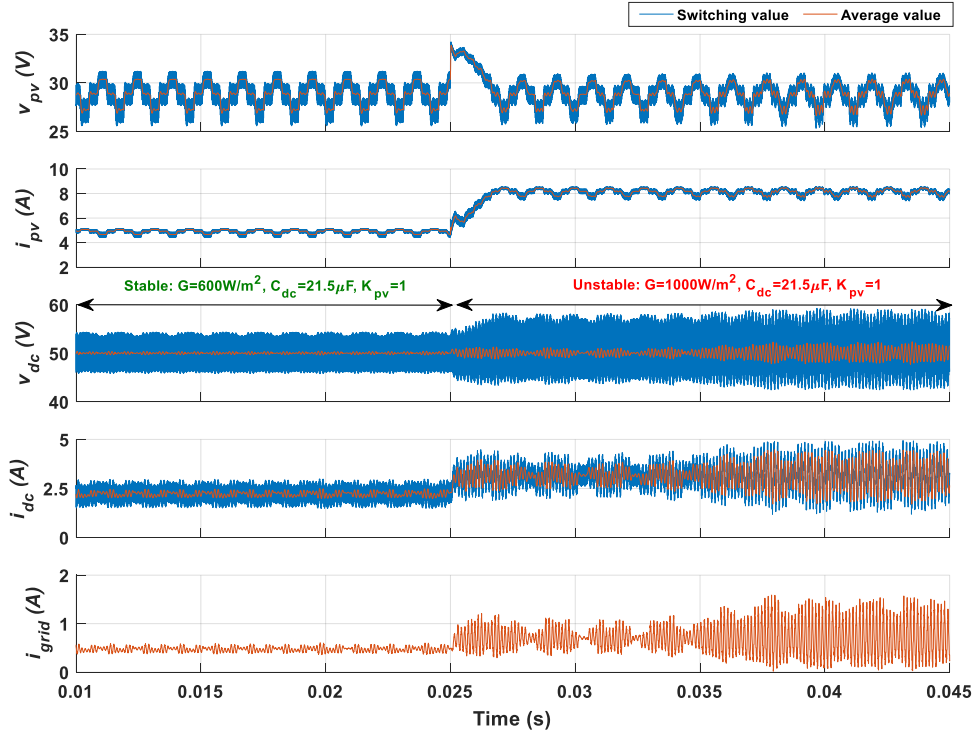
Figure 107: Effect of solar irradiation level on the dc-link and grid stability. C_{dc} and k_{pv} are kept constant at 21.5 µF and 1, respectively. (the average value is mean value of the input signal over a one cycle of the 60 kHz switching frequency).

5.4.2.3 Effect of the proportional voltage gain

Another factor that affects system stability is the controller gain parameters. In case cascaded controller re-tuning the proportional voltage gain (K_{pv}) will adjust the control loop cut-off frequency and the PM. In this test, as shown in Figure 108, C_{dc} value and G are kept constant at 21.5 µF and 1000 W/m^2, respectively. The value of K_{pv} has changed from 0.8 to 1. Based on Figure 108, increasing K_{pv} from 0.8 to 1 degrades the cascaded controller performance and drives system to instability.
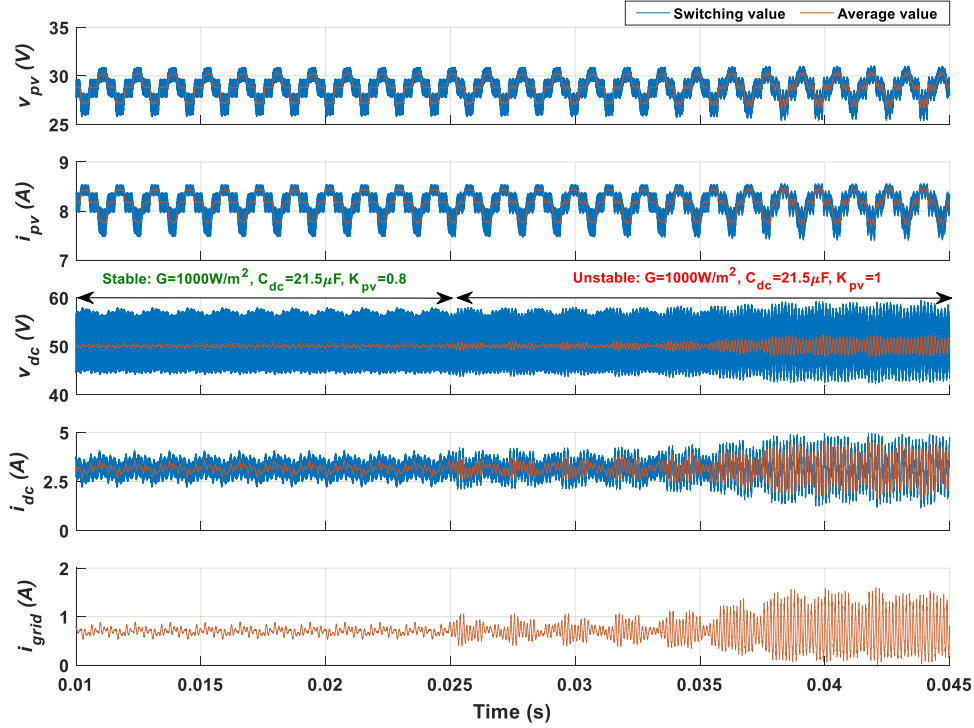
Figure 108: Effect of the proportional gain of the voltage controller (k_{pv}) on the dc-link and grid stability. C_{dc} and G are kept constant at 21.5 µF and 1000 W/m², respectively. (the average value is mean value of the input signal over a one cycle of the 60 kHz switching frequency).

5.5 Design Recommendations for the DC-link Voltage Controller

In order to control the dc-link voltage in grid-connected PV system with double-stage DC/DC boost converter, the following is recommended:

- For low power rating system where voltage-mode controller is suitable, the single integrator controllers such as PI controller are not suitable to control the input-side of DC/DC boost converter due to the -180º phase delay incurred by the power stage double pole at $\omega_c > \omega_o$ which results in insufficient phase margin or even unstable control loop gain when PV operates in CC region. A higher order controller is recommended to overcome this problem such as 3P2Z controllers.

- Modelling the SCPVM units as an ideal current source can simplify designing the controller of the second-stage converter. However, the original SCPVM unit under different operating conditions has to be considered when evaluating the performance of the controller and re-tuning the controller in case of changing

the value of C_{dc} to ensure stable operation under different operating conditions such as solar irradiation level, PV voltage, and P&O sampling time.

- To reduce the dynamic interaction between the first-stage and the second-stage converters and avoid chaotic like behaviour, the second-stage control loop settling time T_{settle} has to be shorter than the first-stage P&O controller sampling period T_{mppt}.

- To ensure $T_{settle} < T_{mppt}$, the worst case which leads to the longest T_{settle} has to be considered which occurs when the solar irradiation and the PV voltage are at their highest operating values.

5.6 Conclusion

The dynamic interactions between the system stages in the double-stage DC/DC boost converter are analysed through simulation. The dynamic interaction is explored in case of having an ideal current source (the SCPVM is modelled as a current source) connected to the second-stage converter and in case of having SCPVM unit connected to the second-stage converter. The results from the two aforementioned cases are compared and it reveals that: (I) the assumption that SCPVM units can be lumped together and modelled as an ideal current source might be insufficient and misleading, especially, if small dc-link capacitance is used, which is normally very desirable, (II) the SCPVM unit increases the dynamic interaction between the system stages due the induced low-order frequency and transient oscillations by the P&O controller. It was shown through simulation that the effect of the P&O controller on the control loop of the second-stage converter at MPPT mode depend on the P&O sampling time (T_{mppt}), the solar irradiation level, the size of C_{dc}, controller specifications (e.g. settling time and voltage gain), and system cut-off frequency.

Simulation examples are provided to show that under specific operating conditions the dynamic interaction between the system stages increases and may leads to undesirable operating behaviour (chaotic like behaviour). It was shown that at MPPT mode and for specific P&O parameters the dynamic interaction increases as solar irradiation increases, C_{dc} decreases, or system cut-off frequency increases (e.g. controller voltage gain increases). Accordingly, design recommendations and guidelines are provided in order to avoid undesirable operating behaviour.

Although the output impedance of the SCPVM unit is not discussed in this work, it affects the interaction between the system stages as the output impedance is not the same as when an ideal current source is assumed at the input of the second-stage converter. Also, the output impedance of the SCPVM units depends on the solar irradiation and the number of the parallel connected units and that will affect the interaction between the system stages differently.

6 ACTIVE SUPPRESSION OF P&O RELATED HARMONICS

6.1 Abstract

In this chapter a novel system-level controller named as "active filter" is proposed to reduce the progression of the P&O related harmonics into the dc-link bus and as a consequence improve the efficiency and power quality of the overall system. The level of the harmonics suppression was shown analytically and through simulation. First, the proposed active filter is described for multiple parallel connected and synchronised SCPVM units. Secondly, the effect of the active filter on improving the dc-link power quality by suppressing the P&O related harmonics is explored analytically by comparing the dc-link current variation in case the system operating with and without active filter. Finally, the effect of the active filter on the dynamic interaction between the system stages of the double-stage parallel SCPVM system consisting of two parallel SCPVM units (see Figure 39) and operating with small dc-link capacitance value is explored through simulation examples.

6.2 Introduction

As has been discussed in chapter 4, the conventional widely used Perturbation and Observation (P&O) maximum power point tracker introduces harmonics in the common dc-link bus and grid. Also, it was shown that in a PV system which consists of multiple parallel connected and synchronised SCPVM units, the level of the harmonics become more critical. Furthermore, in Chapter 5 it was shown that the P&O related harmonics increase the dynamic interactions between the SCPVM units and the second-stage control system and that affects the minimum required capacitance size for stable operation in double-stage boost converter.

In this chapter a novel system-level controller named as "active filter" is proposed to reduce the progression of the P&O related harmonics into the dc-link bus and as a consequence improve the efficiency and power quality of the overall system. For this analysis multiple parallel connected SCPVM units connected to a stiff dc-link voltage as shown in Figure 51 is considered. Then, the effect of the active filter on reducing the dynamic interaction between system stages with small dc-link capacitance value is explored through simulation for the double-stage parallel SCPVM system (see Figure 39) consisting of two parallel SCPVM units connected to a second-stage DC/DC boost converter.

In this work as a quantitative measure for power quality (PQ) of the system the following relation is used:

$$PQ = \frac{\sqrt{\sum_{h=1}^{n} I_h^2}}{I_{dc}} \times 100\% \qquad (6.1)$$

Where I_h is the current of h harmonic and I_{dc} is the DC component of the current.

6.3 Proposed Active Filtering Method

The outline of the proposed active filtering approach considering *n* SCPVM units connected in parallel is shown in Figure 109 and the m-file code is provided in Appendix E. The new system-level controller can suppress the harmonics levels by synchronising and aligning the harmonics in i_{scpvmk_out}, which are generated by SCPVM$_k$, to be out of phase with an identical or closely identical harmonics generated by another SCPVM unit in the system (e.g. SCPVM$_m$, $1 \leq m \leq n$, and $m \neq k$). As a result the harmonics levels are suppressed at their total output (i_{dc}).

The SCPVM units generate identical harmonics levels if they operate under the same solar irradiation and the same P&O duty-cycle operating point (see Figure 56, Figure 58, Figure 59, and Figure 60). Accordingly, each two SCPVM units under the same solar irradiation can form a pair to be controlled as one unit.

The first step of the proposed algorithm is to group the *n*-parallel SCPVM units in the system into *j* pairs where the generated harmonics levels by the units in each pair *i* (*SCPVM$_{1\_pair\_i}$* and *SCPVM$_{2\_pair\_i}$*) are identical or closely identical. The pair units can be formed as a fixed pair or flexible pair. In the case of fixed pair the SCPVM units of a pair are chosen in advance and the formed pairs will not change during the system operation. The fixed pair can be chosen based on the distance between the SCPVM units as very near modules are most likely to have the same solar irradiation level and generate identical harmonics levels. However, under shading conditions the fixed pairs might not be the optimal solution for greater harmonics suppression. Flexible pairs give the possibility to re-arrange the units of pairs in case of shading to ensure high degree of harmonics suppression. For this purpose, as shown in Figure 109, the PV module current (i_{pvk}) is used to identify the SCPVM units which work under similar solar irradiation level and to decide on the units of each pair. So, the system-level controller

141

compare the PV output currents (i.e. $i_{pv1}, i_{pv2}, ..., i_{pvn}$) every T_{mppt} and rearrange the units into the appropriate pairs if required as shown in Figure 109.
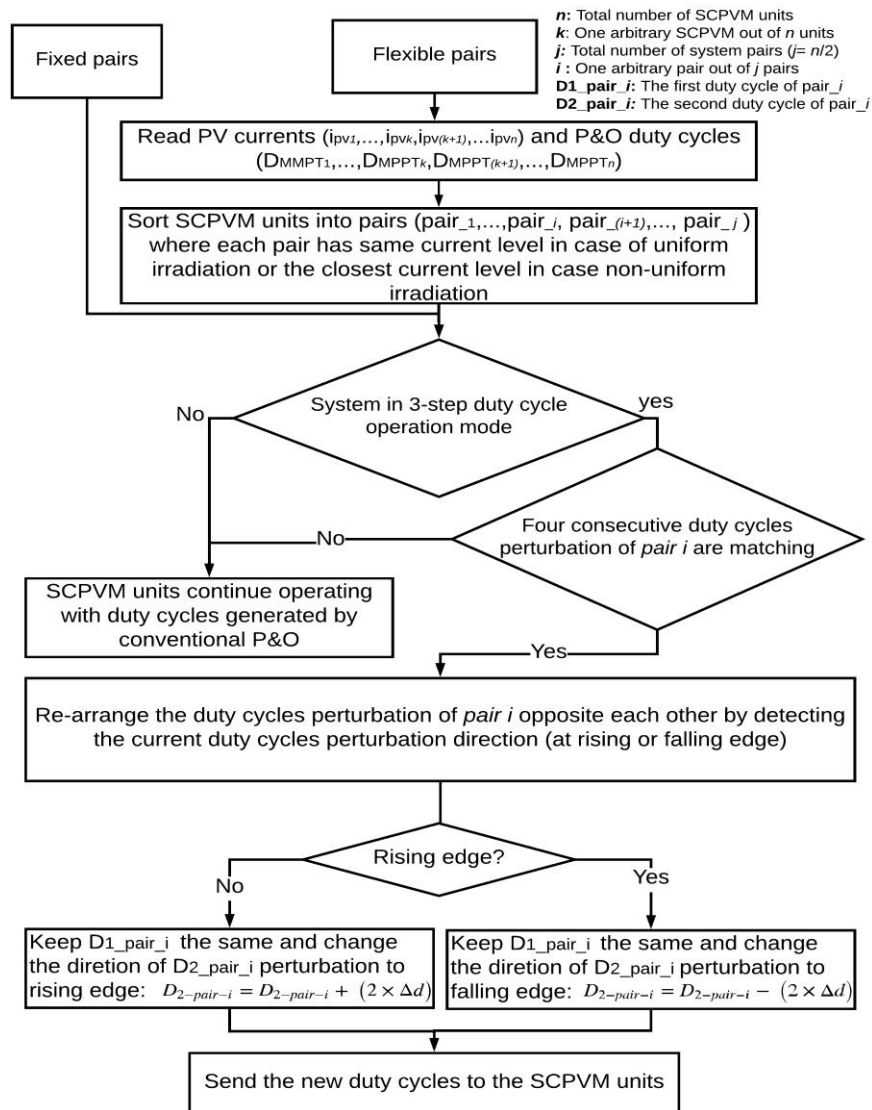
Figure 109: Outline of the proposed system-level controller ''active filter'' (interrupt routine at every T_{mppt}).

As shown in Figure 109 the second step in the proposed algorithm is to make sure that the SCPVM units in each pair are in the three-step mode (i.e. in steady state operation) by checking four consecutive duty cycles perturbations of each unit in a pair. This is required to avoid interrupting the transients following a sudden and big change in irradiation. Then, the duty cycles perturbations of the SCPVM units in a pair are checked if their perturbations are in phase (i.e. perturbations every T_{mppt} are in the same direction) or out of phase (i.e perturbations every T_{mppt} are in opposite direction). If the units of a pair are in the three-step mode and their waveforms are aligned in

phase, the system level controller (i.e the active filter) aligns them out of phase by controlling the perturbation direction of the Synchronised P&O controllers. The perturbation direction is adjusted in order to have the three-step duty cycles of a pair ($D_{1\_pair\_i}$ and $D_{2\_pair\_i}$) out of phase by detecting the present duty cycles perturbation direction (at rising or falling edge) as shown in Figure 109. In each pair the duty cycle of one SCPVM unit is kept unchanged while the duty cycle of the other SCPVM unit is modified by adding or deducting two times Δd (i.e. the duty cycle step) from the current value of the duty cycle, depending on the value of the duty cycle of the other SCPVM unit in a pair. The control diagram of the proposed controller is shown in Figure 110.
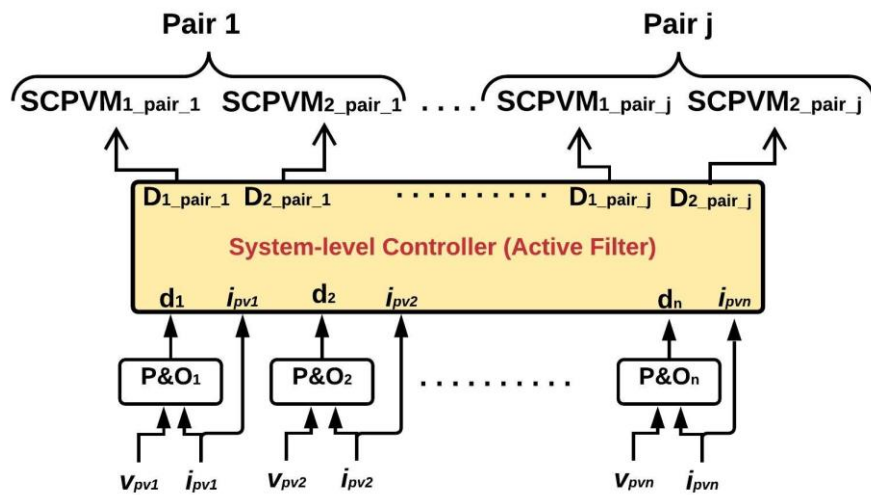
Figure 110: Control diagram of the proposed active filter controller

For further demonstration of how the system-level controller operates, MATLAB Simulink model is used for testing the proposed active filtering method. The SCPVM units are connected to stiff 50V dc-link bus (the second-stage converter is modelled as a stiff voltage source). The simulation test in Figure 111 consists of a system with only two SCPVM units (SCPVM$_1$ and SCPVM$_2$) operating under uniform solar irradiation of 1000 W/m^2. The simulation results before applying the active filter are shown in Figure 111.a. The rising (↑) and falling (↓) edges of D$_1$ and D$_2$ occur at the same time producing in phase low-frequency oscillation and in phase transient response peaks in i_{scpvm1_out} and i_{scpvm2_out}. In this case and based on (4.8) and (4.9) the peak-peak variation in i_{dc} is two times the peak-peak variation in i_{scpvm1_out} and i_{scpvm2_out} as can be seen in Figure 111.a. On the contrary, after applying the active filter as shown in Figure 111.b the low-frequency oscillation and the transient peaks in i_{scpvm1_out} and

i_{scpvm2_out} are aligned out of phase and they are significantly suppressed in the dc-link current i_{dc}. This is achieved by the active filter that rearranges the rising and falling edges of D$_1$ and D$_2$ opposite each other.

The simulation results of the dc-link current i_{dc} with and without active filter as shown in Figure 111, demonstrate that the proposed active filter has suppressed the harmonics levels in the dc-link which improves the power quality injected to the grid. The overall current variation in i_{dc} has been decreased by 75% after applying the active filter (from 1.2A to 0.3A without and with active filter, respectively as shown in Figure 111) and PQ has improved and it is less than 1% with active filter.
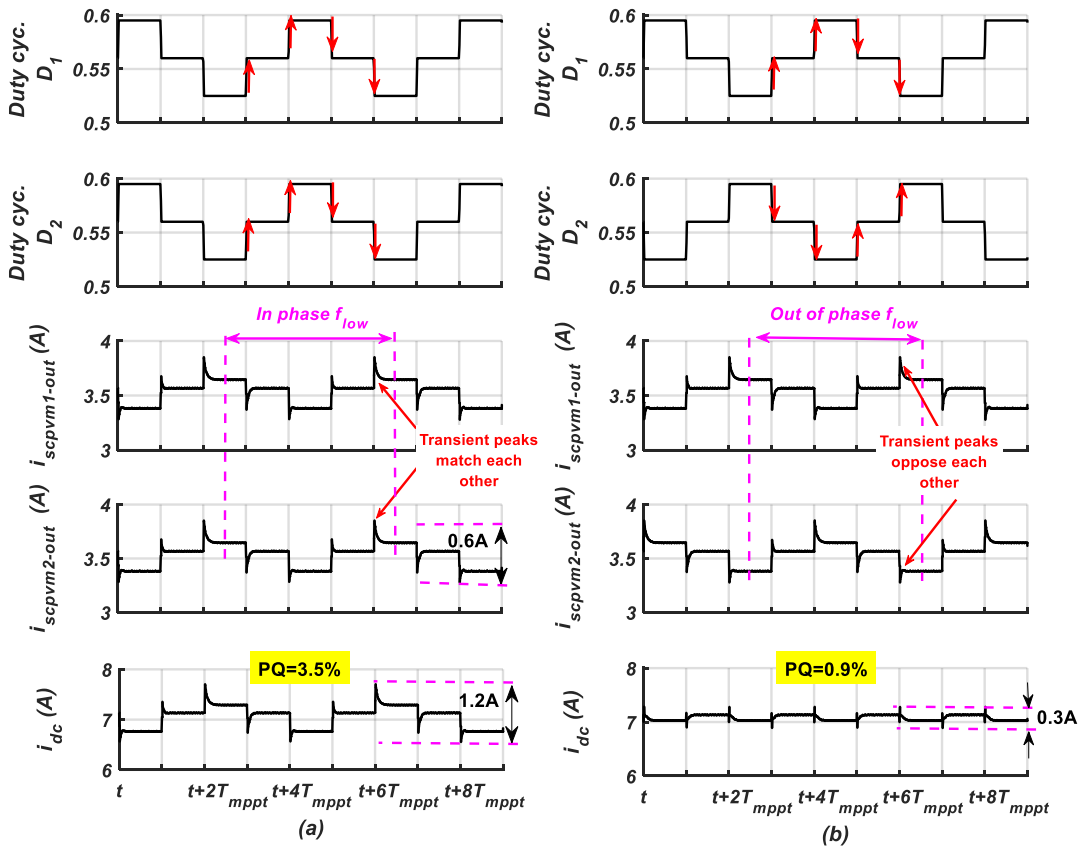
Figure 111: Simulation result of two parallel-connected SCPVM units under uniform irradiation of $1000\ W/m^2$. (a) Without active filter, (b) with active filter. $C_{dc} = 2 \times 22\mu F$ and $V_{dc}=50V$.

The capability of the proposed active filter working under transient in solar irradiation for both fixed and flexible pair approach is demonstrated in Figure 112. In this test four SCPVM units are considered; at the beginning the units work under uniform solar irradiation (800 W/m^2) and in the following pairs: the first pair includes (SCPVM$_1$,

SCPVM$_2$) and the second pair includes (SCPVM$_3$, SCPVM$_4$). Then after 19.8 ms SCPVM$_2$ and SCPVM$_4$ work under reduced solar irradiation, for example shading. In case of fixed pair approach as shown in Figure 112.a, the units of each pair are kept the same. While when flexible pair approach is employed as shown in Figure 112.b, the algorithm rearranged the system pairs based on their generated current level. Consequently, SCPVM$_3$ is switched to work with SCPVM$_1$. SCPVM$_2$ and SCPVM$_4$ form the second pair. The switching process between the pairs can be clearly seen from i_{pvk} in the first row of Figure 112.b.

Comparing the power quality in Figure 112.a and Figure 112.b, it can be seen that a higher degree of suppression in the peak-peak variation is gained with flexible pair approach. The steady-state peak-peak (transient peaks are not included) dc-link power variation (ΔP_{dc}) decreased by more than 13% with flexible pair approach compared with fixed pair approach (from 19.4 W with fixed pair approach to 16.7 W with flexible pair approach) as shown in the last row of Figure 112.a and Figure 112.b. When taking the transient peaks into account, the overall peak-peak power variation decreased by 50% with flexible pair approach compared with the fixed pair approach (from 40 W with fixed pair to 20 W with the flexible pair approach).

In addition to improving system power quality, the advantages of the proposed active filter are: it does not require any additional measurements as it uses the same signals which are already measured for the distributed P&O controllers, does not require adding any extra switching power electronic circuits, low cost implementation and simple software.

The proposed active filter can suppress the harmonics levels imposed by the P&O controller. However, the system still contains some oscillations as can be observed in last row of Figure 111.b and Figure 112. These oscillations are associated with the non-linear characteristics of the PV source which result in asymmetrical variation of i_{pv} about MPP as will be discussed in the next section.
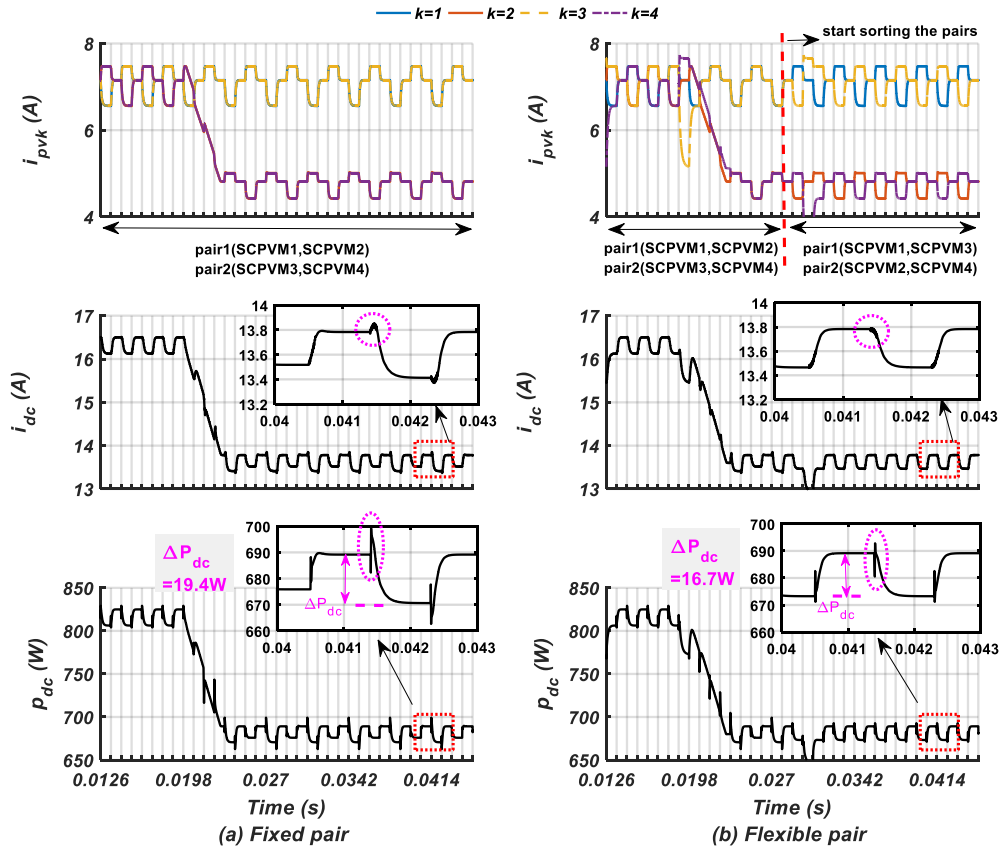
Figure 112: Simulation results of four SCPVM units (a) Fixed pair approach (b) Flexible pair approach. At t<19.8 ms, $G_1 = G_2 = G_3 = G_4 = 800W/m^2$, and at t≥19.8 ms the solar irradiation on $SCPVM_2$ and $SCPVM_4$ dcreased from $800W/m^2$ to $600W/m^2$ ($G_1 = G_3 = 800W/m^2$, $G_2 = G_4 = 600W/m^2$).

6.4 P&O Related Harmonics Suppression Level in the DC-link Bus of Multi-parallel SCPVM Units

An example of the waveforms of the periodic oscillations due to the P&O controller in the output current of two arbitrary SCPVM units connected to a stiff voltage source under uniform and non-uniform solar irradiation are shown in Figure 113 and Figure 114, respectively. It worth paying attention to that the final steady-state values and the transient behaviour of these figures can be different depending on the solar irradiation level.

The maximum and minimum values of the output current of one arbitrary SCPVM unit k under solar irradiation G and including the transient oscillations can be defined as follows:

$$I^G_{scpvmk\_out\_max} = I^G_{scpvmk\_out\_mpp} + \Delta i^G_{k\_ss\_mpp\_to\_right} + \Delta i^G_{k\_trans\_right\_to\_max}$$
$$I^G_{scpvmk\_out\_min} = I^G_{scpvmk\_out\_mpp} - \Delta i^G_{k\_ss\_mpp\_to\_left} - \Delta i^G_{k\_trans\_left\_to\_min}$$

(6.2)

where $\Delta i^G_{k\_ss\_mpp\_to\_right}$ and $\Delta i^G_{k\_ss\_mpp\_to\_left}$ are given in (6.3) and they are the right and left steady-state peak amplitudes measured with respect to the desired operating point MPP, respectively. $\Delta i^G_{k\_trans\_right\_to\_max}$ and $\Delta i^G_{k\_trans\_left\_to\_min}$ are also given in (6.3) and they are the right and left transient peak amplitudes measured with respect to the right and left steady-state values of i_{scpvmk_out}, respectively.

$$\Delta i^G_{k\_ss\_mpp\_to\_left} = I^G_{scpvmk\_out\_mpp} - I^G_{scpvmk\_out\_left}$$
$$\Delta i^G_{k\_ss\_mpp\_to\_right} = I^G_{scpvmk\_out\_right} - I^G_{scpvmk\_out\_mpp}$$
$$\Delta i^G_{k\_trans\_left\_to\_min} = I^G_{scpvmk\_out\_left} - I^G_{scpvmk\_out\_min}$$
$$\Delta i^G_{k\_trans\_right\_to\_max} = I^G_{scpvmk\_out\_max} - I^G_{scpvmk\_out\_right}$$

(6.3)

where $I^G_{scpvm\_out\_mpp}$ is the SCPVM output current at MPP and irradiation G, $I^G_{scpvm\_out\_right}$ is the SCPVM output current at Right MPP and irradiation G, $I^G_{scpvm\_out\_left}$ is the SCPVM output current at Left MPP and irradiation G. $I^G_{scpvmk\_out\_left}$, $I^G_{scpvmk\_out\_mpp}$, $I^G_{scpvmk\_out\_right}$ are given in (4.2).

Figure 113: The output current of two SCPVM units $i^G_{scpvmk\_out}$ under uniform solar irradiation.

147
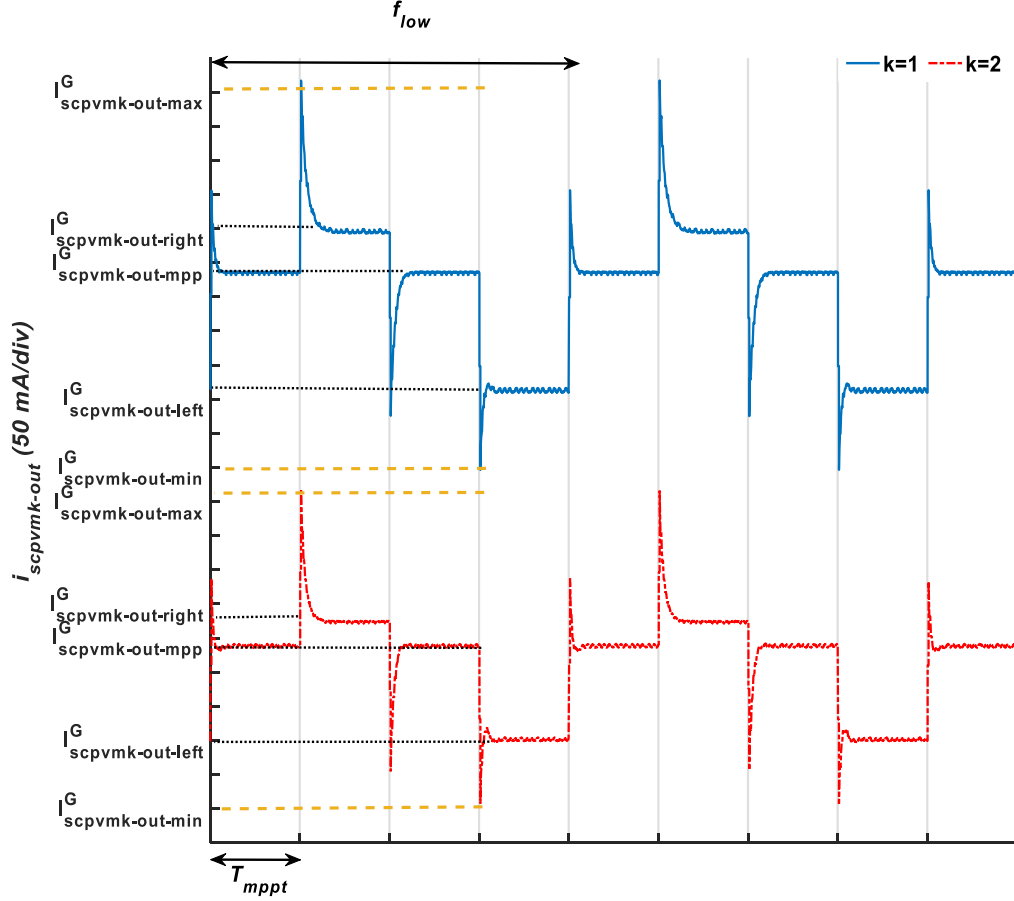
Figure 114: The output current of two SCPVM units $i^G_{scpvmk\_out}$ under non-uniform solar irradiation.

One can see from Figure 113 and Figure 114 that $\Delta i^G_{k\_ss\_mpp\_to\_left}$ is greater than $\Delta i^G_{k\_ss\_mpp\_to\_right}$; both are measured with respect to the desired operating point MPP as given in (6.3), that is associated with the non-linear characteristic of the PV source. The slope of the PV current-voltage characteristic curve increases when the operating point moves to the right resulting in an asymmetric variation around the desired MPP. $\Delta i^G_{k\_ss\_mpp\_to\_left}$ and $\Delta i^G_{k\_ss\_mpp\_to\_right}$ can be found analytically by inserting (4.2) in (6.3) and the results for three different solar irradiation levels is shown in Figure 115. In general Δd is chosen as small as possible and for the adopted value in this work $\Delta d = 0.035$ we have:

$$\Delta i^G_{k\_ss\_mpp\_to\_left} > \Delta i^G_{k\_ss\_mpp\_to\_right}$$
$$I^G_{scpvmk\_out\_mpp} - I^G_{scpvmk\_out\_left} > I^G_{scpvmk\_out\_right} - I^G_{scpvmk\_out\_mpp} \tag{6.4}$$

148
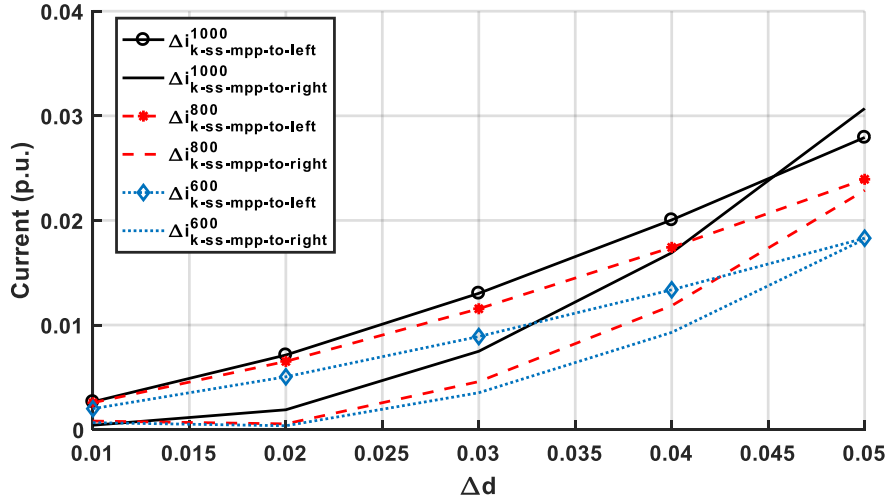
Figure 115: The left and right steady-state peak amplitudes of $i_{scpvmk\_out}^{G}$ for different Δd values and solar irradiation levels (obtained analytically by (6.3) and (4.2)).

6.4.1 DC-link current variation without active filter

The dc-link current for multi-parallel connected SCPVM units is:

$$i_{dc} = \sum_{k=1}^{n} i_{scpvmk\_out}^{G} \tag{6.5}$$

In case of synchronised P&O controllers of n-parallel SCPVM units the overall variation of dc-link current is:

$$\Delta i_{dc\_overall} = \sum_{k=1}^{n} \Delta i_{scpvmk\_out}^{G} \tag{6.6}$$

General waveforms of the periodic oscillations due to the P&O controller in the dc-link current of two arbitrary SCPVM units connected to a stiff voltage source under uniform and non-uniform solar irradiation are shown in second row of Figure 116 and Figure 117, respectively. With reference to (6.2); before applying the proposed active filtering approach, the overall peak-to-peak variation of the dc-link current for n-parallel connected SCPVM units under uniform (see Figure 116) and non-uniform (see Figure 117) solar irradiation can be given as follow:

$$\Delta i_{dc\_overall} = \sum_{k=1}^{n} \Delta i_{k\_ss\_mpp\_to\_right}^{G} + \Delta i_{k\_trans\_right\_to\_max}^{G} + \Delta i_{k\_ss\_mpp\_to\_left}^{G} + \Delta i_{k\_trans\_left\_to\_min}^{G}$$

$$\tag{6.7}$$
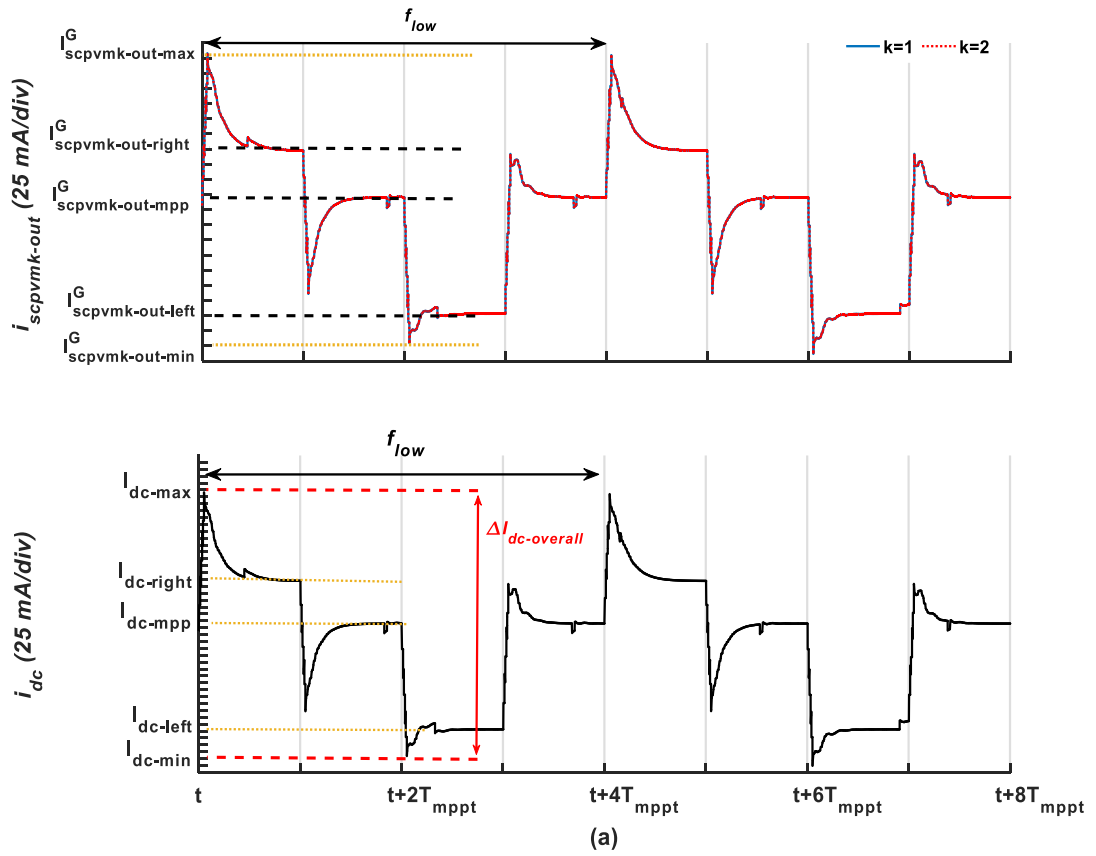
Figure 116: The output current of two SCPVM units $i^{G}_{scpvmk\_out}$ and their total current i_{dc} under uniform irradiation without active filter.
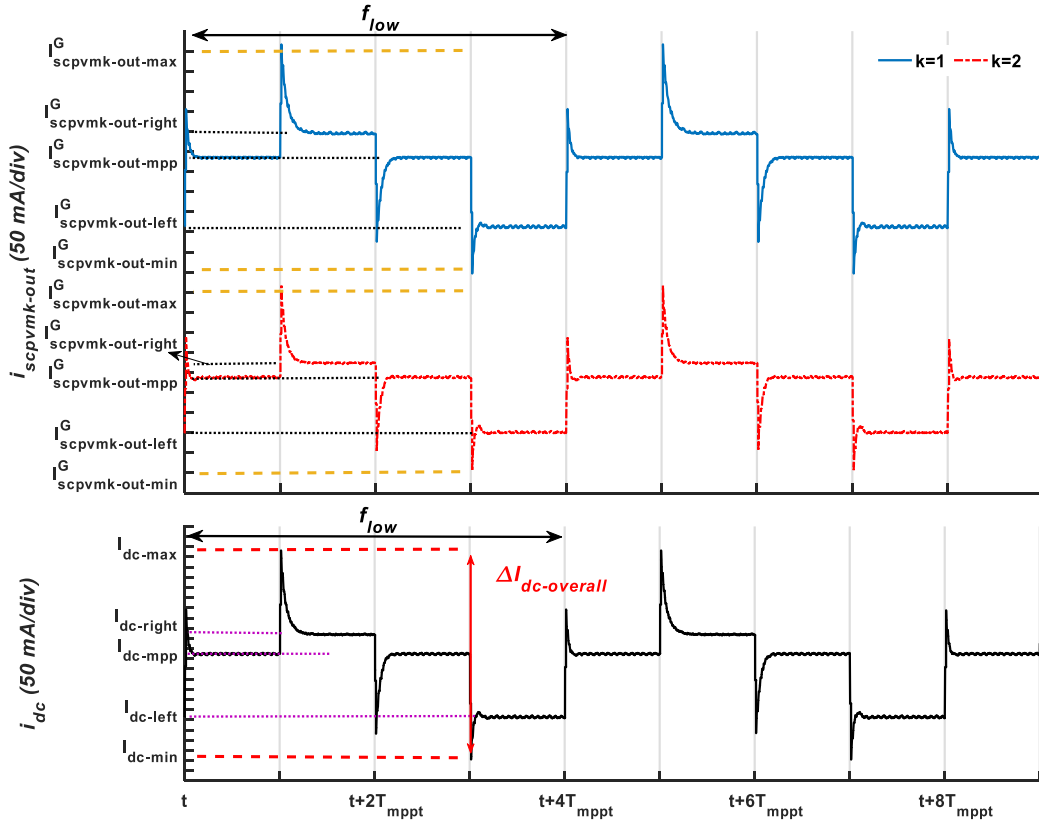
Figure 117: The output current of two SCPVM units $i^G_{scpvmk\_out}$ and their total current i_{dc} under non-uniform irradiation without active filter.

Under uniform solar irradiation on all *n* SCPVM units, it can be assumed that:

$$\Delta i^{\cdot G}_{k\_ss\_mpp\_to\_right} = \Delta i^{\cdot G}_{(k+1)\_ss\_mpp\_to\_right} = \ldots = \Delta i^{\cdot G}_{n\_ss\_mpp\_to\_right} = \Delta i_{ss\_mpp\_to\_right}$$

$$\Delta i^{\cdot G}_{k\_ss\_mpp\_to\_left} = \Delta i^{\cdot G}_{(k+1)\_ss\_mpp\_to\_left} = \ldots = \Delta i^{\cdot G}_{n\_ss\_mpp\_to\_left} = \Delta i_{ss\_mpp\_to\_left}$$

$$\Delta i^{\cdot G}_{k\_trans\_right\_to\_\max} = \Delta i^{\cdot G}_{(k+1)\_trans\_right\_to\_\max} = \ldots = \Delta i^{\cdot G}_{n\_trans\_right\_to\_\max} = \Delta i_{trans\_right\_to\_\max}$$

$$\Delta i^{\cdot G}_{k\_trans\_left\_to\_\min} = \Delta i^{\cdot G}_{(k+1)\_trans\_left\_to\_\min} = \ldots = \Delta i^{\cdot G}_{n\_trans\_left\_to\_\min} = \Delta i_{trans\_left\_to\_\min}$$

(6.8)

Thus, the overall peak-peak variation of the DC-link current (i_{dc}) is:

$$\Delta i^{\cdot uniform}_{dc\_overall} = n \times \left(\Delta i_{ss\_mpp\_to\_right} + \Delta i_{trans\_right\_to\_\max} + \Delta i_{ss\_mpp\_to\_left} + \Delta i_{trans\_left\_to\_\min} \right)$$ (6.9)

Without active filter the frequency of the dc-link current variation is the same as in i_{scpvmk_out} which is f_{low} as given in (4.1).

6.4.2   DC-link current variation with active filter

Assuming $SCPVM_k$ is the first unit and $SCPVM_m$ is the second unit of a *pair i* ($(1 \leq k \leq n) \,\&\, (1 \leq m \leq n)$ and $k \neq m$). The output current of the first SCPVM unit of *pair i* ($i^G_{1\_pair\_i}$) and the output current of the second SCPVM unit of *pair i* ($i^G_{2\_pair\_i}$) are as follow:

$$i^G_{1\_pair\_i} = i^G_{scpvmk\_out}$$
$$i^G_{2\_pair\_i} = i^G_{scpvmm\_out} \tag{6.10}$$

And at the three P&O operating points we have:

$$I^G_{1\_pair\_i\_mpp} = I^G_{scpvmk\_out\_mpp}$$
$$I^G_{1\_pair\_i\_right} = I^G_{scpvmk\_out\_right} \tag{6.11}$$
$$I^G_{1\_pair\_i\_left} = I^G_{scpvmk\_out\_left}$$

$$I^G_{2\_pair\_i\_mpp} = I^G_{scpvmm\_out\_mpp}$$
$$I^G_{2\_pair\_i\_right} = I^G_{scpvmm\_out\_right} \tag{6.12}$$
$$I^G_{2\_pair\_i\_left} = I^G_{scpvmm\_out\_left}$$

And the right and the left peaks are:

$$\Delta i^G_{1\_pair\_i\_ss\_mpp\_to\_left} = I^G_{1\_pair\_i\_mpp} - I^G_{1\_pair\_i\_left}$$
$$\Delta i^G_{1\_pair\_i\_ss\_mpp\_to\_right} = I^G_{1\_pair\_i\_right} - I^G_{1\_pair\_i\_mpp}$$
$$\Delta i^G_{2\_pair\_i\_ss\_mpp\_to\_left} = I^G_{2\_pair\_i\_mpp} - I^G_{2\_pair\_i\_left} \tag{6.13}$$
$$\Delta i^G_{2\_pair\_i\_ss\_mpp\_to\_right} = I^G_{2\_pair\_i\_right} - I^G_{2\_pair\_i\_mpp}$$

When the active filtering approach is applied, two SCPVM units work as a pair as shown in Figure 118 under uniform solar irradiation and in Figure 119 under non-uniform solar irradiation. If one unit in a pair operates at the Right MPP, the other unit in the pair operates at the Left MPP. With reference to Figure 118 and Figure 119, the peaks of the transient response and the low-frequency variation of the units' output currents are aligned opposite each other and they are effectively suppressed in the total output current of the pair. A small transient variation still can be observed in the output current due to the difference in the transient dynamics of the aligned operating points (the left MPP and the right MPP have different transient dynamics as was shown in Figure 60) and a low-order frequency oscillation still can be observed due to the asymmetric variations around the desired MPP ($\Delta i^G_{1\_pair\_i\_ss\_mpp\_to\_left} \neq \Delta i^G_{2\_pair\_i\_ss\_mpp\_to\_right}$) and ($\Delta i^G_{1\_pair\_i\_ss\_mpp\_to\_right} \neq \Delta i^G_{2\_pair\_i\_ss\_mpp\_to\_left}$). As shown in Figure 118 and Figure 119 the influence of the non-suppressed transient

oscillations on the overall peak-peak variation in the total dc-link current of the pair is significantly small compared to the variation caused by the final steady-state values. Therefore and to simplify the analysis, the transients are neglected and only the steady-state values are considered in the following analysis to find the peak-peak variation in the dc-link current.
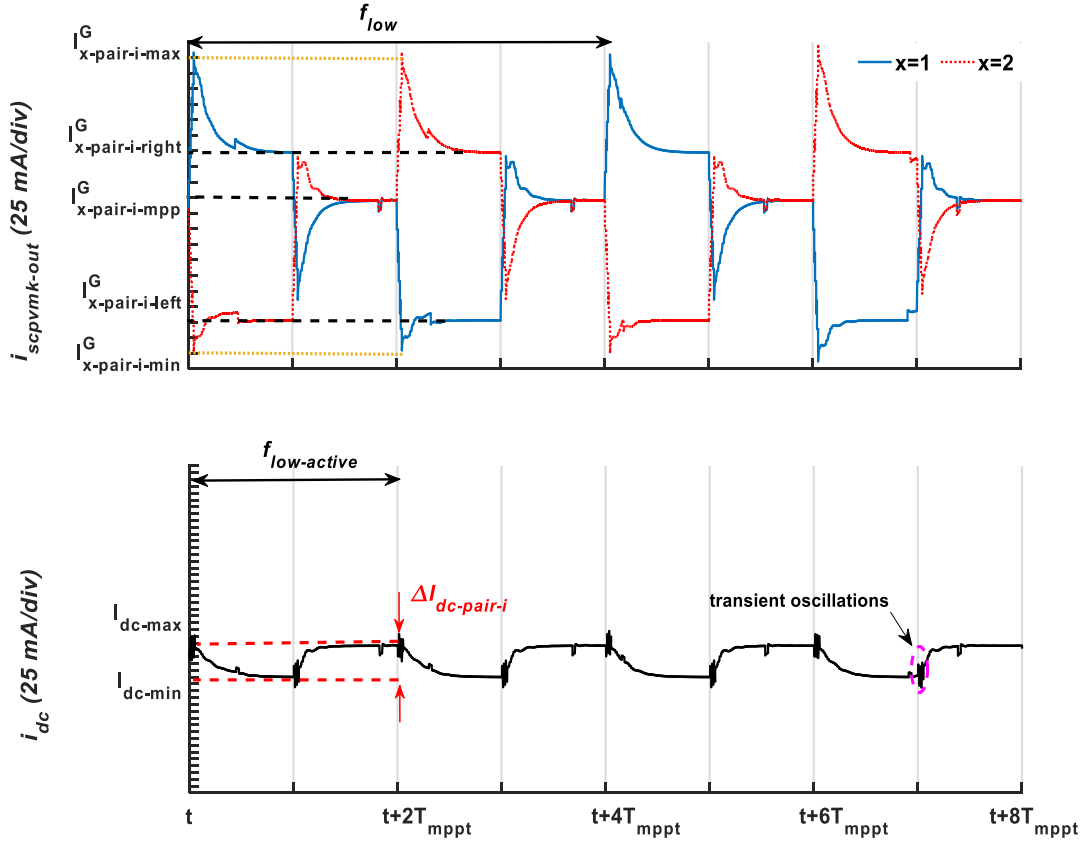
Figure 118: The output current of two SCPVM units $i^G_{scpvmk\_out}$ and their total current i_{dc} under uniform irradiation with active filter.

With reference to Figure 118 and Figure 119, for the active filtering approach:

$$\Delta i^G_{1\_pair\_i\_ss\_mpp\_to\_left} \neq \Delta i^G_{2\_pair\_i\_ss\_mpp\_to\_right}$$
$$\Delta i^G_{1\_pair\_i\_ss\_mpp\_to\_right} \neq \Delta i^G_{2\_pair\_i\_ss\_mpp\_to\_left}$$

(6.14)

153
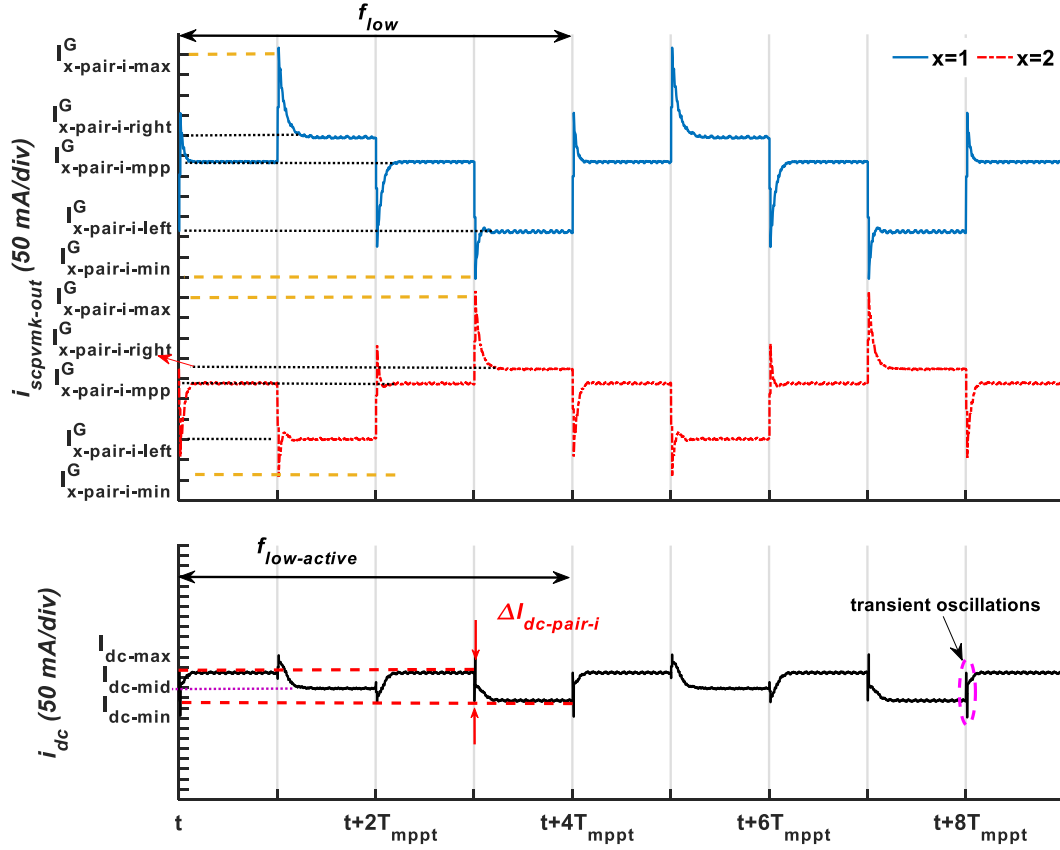
Figure 119: The output current of two SCPVM units $i^G_{scpvmk\_out}$ and their total current i_{dc} under non-uniform irradiation with active filter.

And based on (6.4) the following relations are valid:

$$I^G_{1\_pair\_i\_mpp} - I^G_{1\_pair\_i\_left} > I^G_{2\_pair\_i\_right} - I^G_{2\_pair\_i\_mpp} \tag{6.15}$$

$$I^G_{2\_pair\_i\_mpp} - I^G_{2\_pair\_i\_left} > I^G_{1\_pair\_i\_right} - I^G_{1\_pair\_i\_mpp} \tag{6.16}$$

Rearranging (6.15) and (6.16) gives:

$$\underbrace{I^G_{1\_pair\_i\_mpp} + I^G_{2\_pair\_i\_mpp}}_{\text{Maximum value}} > \underbrace{I^G_{1\_pair\_i\_right} + I^G_{2\_pair\_i\_left}}_{\text{First minimum value}} \tag{6.17}$$

$$\underbrace{I^G_{1\_pair\_i\_mpp} + I^G_{2\_pair\_i\_mpp}}_{\text{Maximum value}} > \underbrace{I^G_{1\_pair\_i\_left} + I^G_{2\_pair\_i\_right}}_{\text{Second minimum value}} \tag{6.18}$$

154

The left sides of (6.17) and (6.18) are equal and present the maximum steady-state value of the total output current of *pair i* (I_{dc_max}) as shown in the second row of Figure 118 and Figure 119.

$$I_{dc\_\max} = I^G_{1\_pair\_i\_mpp} + I^G_{2\_pair\_i\_mpp} \tag{6.19}$$

The right-sides of (6.17) and (6.18) present two minimum steady-state values. The global minimum value (I_{dc_min}) depends on the operating condition of a pair; if it is operating under uniform or non-uniform irradiation. Accordingly the overall peak-peak variation of the dc-link current of each case is discussed separately

6.4.2.1   Uniform solar irradiation

In the case of uniform solar irradiation on *pair i* ($G_1=G_2$) as shown in Figure 118:

$$
\begin{aligned}
I^G_{1\_pair\_i\_right} &= I^G_{2\_pair\_i\_right} \\
I^G_{1\_pair\_i\_left} &= I^G_{2\_pair\_i\_left}
\end{aligned}
\tag{6.20}
$$

Consequently, the right-side values of (6.17) and (6.18) are equal and the total output current of *pair i* has one minimum value (I_{min}) as shown in the second row of Figure 118. Thus, under uniform solar irradiation the peak-to-peak variation of the total output current of one pair is given by:

$$
\begin{aligned}
\Delta i^{uniform}_{dc\_pair\_i} &= (I^G_{1\_pair\_i\_mpp} + I^G_{2\_pair\_i\_mpp}) - (I^G_{1\_pair\_i\_left} + I^G_{2\_pair\_i\_right}) \\
&= (I^G_{1\_pair\_i\_mpp} - I^G_{1\_pair\_i\_left}) - (I^G_{2\_pair\_i\_right} - I^G_{2\_pair\_i\_mpp}) \\
&= \quad \Delta i^G_{1\_pair\_i\_ss\_mpp\_to\_left} - \Delta i^G_{2\_pair\_i\_ss\_mpp\_to\_right}
\end{aligned}
\tag{6.21}
$$

And for *j* pairs and under uniform irradiation on each pair (solar irradiation levels on a pair are equal) the peak-peak variation of the dc-link current is:

$$\Delta i^{uniform}_{dc\_overall\_active} = \sum_{i=1}^{j=n/2} \left(\Delta i^G_{1\_pair\_i\_ss\_mpp\_to\_left} - \Delta i^G_{2\_pair\_i\_ss\_mpp\_to\_right} \right) \tag{6.22}$$

Under uniform irradiation on all *j* pairs of SCPVMs we have:

$$
\begin{pmatrix}
\Delta i^{G}_{1\_pair\_i\_ss\_mpp\_to\_right} = \Delta i^{G}_{2\_pair\_i\_ss\_mpp\_to\_right} = \\
\Delta i^{G}_{1\_pair\_(i+1)\_ss\_mpp\_to\_right} = \Delta i^{G}_{2\_pair\_(i+1)\_ss\_mpp\_to\_right} = ... \\
.... = \Delta i^{G}_{1\_pair\_j\_ss\_mpp\_to\_right} = \Delta i^{G}_{2\_pair\_j\_ss\_mpp\_to\_right}
\end{pmatrix} = \Delta i_{ss\_mpp\_to\_right}
$$
$$
\begin{pmatrix}
\Delta i^{G}_{1\_pair\_i\_ss\_mpp\_to\_left} = \Delta i^{G}_{2\_pair\_i\_ss\_mpp\_to\_left} = \\
\Delta i^{G}_{1\_pair\_(i+1)\_ss\_mpp\_to\_left} = \Delta i^{G}_{2\_pair\_(i+1)\_ss\_mpp\_to\_left} = ... \\
.... = \Delta i^{G}_{1\_pair\_j\_ss\_mpp\_to\_left} = \Delta i^{G}_{2\_pair\_j\_ss\_mpp\_to\_left}
\end{pmatrix} = \Delta i_{ss\_mpp\_to\_left}
$$
(6.23)

Thus the peak-peak ripple of the dc-link current under global uniform irradiation is:

$$
\begin{aligned}
\Delta i^{uniform}_{dc\_overall\_active} &= j \times \left(\Delta i_{ss\_mpp\_to\_left} - \Delta i_{ss\_mpp\_to\_right} \right) \\
&= \frac{n}{2} \times \left(\Delta i_{ss\_mpp\_to\_left} - \Delta i_{ss\_mpp\_to\_right} \right)
\end{aligned}
$$
(6.24)

6.4.2.2 Non-uniform solar irradiation

In the case of non-uniform local solar irradiation on *pair i* (for example $G_1 > G_2$) as shown in Figure 119:

$$
\begin{aligned}
I^{G}_{1\_pair\_i\_right} &\neq I^{G}_{2\_pair\_i\_right} \\
I^{G}_{1\_pair\_i\_left} &\neq I^{G}_{2\_pair\_i\_left}
\end{aligned}
$$
(6.25)

Thus, the right-sides values of (6.17) and (6.18) are not equal and for $G_1 > G_2$:

$$
\Delta i^{G}_{1\_pair\_i\_ss\_mpp\_to\_left} > \Delta i^{G}_{2\_pair\_i\_ss\_mpp\_to\_left}
$$
(6.26)

$$
-\Delta i^{G}_{2\_pair\_i\_ss\_mpp\_to\_right} > -\Delta i^{G}_{1\_pair\_i\_ss\_mpp\_to\_right}
$$
(6.27)

From (6.26) and (6.27) we have:

$$
\Delta i^{G}_{1\_pair\_i\_ss\_mpp\_to\_left} - \Delta i^{G}_{2\_pair\_i\_ss\_mpp\_to\_right} > \Delta i^{G}_{2\_pair\_i\_ss\_mpp\_to\_left} - \Delta i^{G}_{1\_pair\_i\_ss\_mpp\_to\_right}
$$
(6.28)

Inserting (6.13) in (6.28):

$$
I^{G}_{1\_pair\_i\_left} + I^{G}_{2\_pair\_i\_right} < I^{G}_{1\_pair\_i\_right} + I^{G}_{2\_pair\_i\_left}
$$
$$
I_{dc\_min} < I_{dc\_mid}
$$
(6.29)

Therefore, from (6.19) and (6.29) the overall peak-peak dc-link current variation with non-uniform local solar irradiation on *pair i* can be found as follow:

$$
\begin{aligned}
\Delta i_{dc\_pair\_i}^{non-uniform} &= I_{dc\_\max} - I_{dc\_\min} \\
&= (I_{1\_pair\_i\_mpp}^{G} + I_{2\_pair\_i\_mpp}^{G}) - (I_{1\_pair\_i\_left}^{G} + I_{2\_pair\_i\_right}^{G}) \\
&= (I_{1\_pair\_i\_mpp}^{G} - I_{1\_pair\_i\_left}^{G}) - (I_{2\_pair\_i\_right}^{G} - I_{2\_pair\_i\_mpp}^{G}) \\
&= \qquad \Delta i_{1\_pair\_i\_ss\_mpp\_to\_left}^{G} - \Delta i_{2\_pair\_i\_ss\_mpp\_to\_right}^{G}
\end{aligned}
\tag{6.30}
$$

6.4.3 The decreased percentage in the dc-link current variation after applying the active filter

6.4.3.1 Uniform solar irradiation

Comparing (6.24) with (6.9) it can be shown that under global uniform solar irradiation the peak-peak variation can be decreased by more than 50% as follows:

$$
\begin{aligned}
Decreased\ \% &= \left(1 - \frac{\Delta i_{dc\_overall\_active}^{uniform}}{\Delta i_{dc\_overall}^{uniform}}\right) \times 100\% \\
&= \left(1 - \frac{n/2}{n} \frac{\Delta i_{ss\_mpp\_to\_left} - \Delta i_{ss\_mpp\_to\_right}}{\left(\begin{array}{c}\Delta i_{ss\_mpp\_to\_left} + \Delta i_{ss\_mpp\_to\_right} + \\ \Delta i_{trans\_right\_to\_\max} + \Delta i_{trans\_left\_to\_\min}\end{array}\right)}\right) \times 100\% \\
&= 100\% - \frac{\Delta i_{ss\_mpp\_to\_left} - \Delta i_{ss\_mpp\_to\_right}}{\left(\begin{array}{c}\Delta i_{ss\_mpp\_to\_left} + \Delta i_{ss\_mpp\_to\_right} + \\ \Delta i_{trans\_right\_to\_\max} + \Delta i_{trans\_left\_to\_\min}\end{array}\right)} \times 50\%
\end{aligned}
\tag{6.31}
$$

As shown in Figure 118, under uniform solar irradiation on a pair *i* the frequency of the dc-link current ripple is:

$$
f_{low\_active} = 2 \times f_{low}
\tag{6.32}
$$

And for *j pairs* the frequency of the dc-link will be the same as (6.32).

6.4.3.2 Non-uniform solar irradiation

Assuming a system operating with two units (SCPVM$_k$ and SCPVM$_m$) k=1 and m=2, with active filter and with reference to (6.3), (6.11), (6.12), (6.13) we have:

$$\Delta i^{\cdot G}_{1\_pair\_1\_ss\_mpp\_to\_left} = \Delta i^{\cdot G}_{1\_ss\_mpp\_to\_left}$$
$$\Delta i^{\cdot G}_{2\_pair\_1\_ss\_mpp\_to\_right} = \Delta i^{\cdot G}_{2\_ss\_mpp\_to\_right}$$

(6.33)

Thus, the dc-link current variation in (6.30) can be written as follow:

$$\Delta i^{\cdot non-uniform}_{dc\_pair\_i} = \Delta i^{\cdot G}_{1\_ss\_mpp\_to\_left} - \Delta i^{\cdot G}_{2\_ss\_mpp\_to\_right}$$

(6.34)

Without active filter the dc-link current variation for two SCPVM units can be found using (6.7):

$$\Delta i_{dc\_overall} = \begin{pmatrix} \Delta i^{\cdot G}_{1\_ss\_mpp\_to\_right} + \Delta i^{\cdot G}_{1\_trans\_right\_to\_max} + \Delta i^{\cdot G}_{1\_ss\_mpp\_to\_left} + \\ \Delta i^{\cdot G}_{1\_trans\_left\_to\_min} + \Delta i^{\cdot G}_{2\_ss\_mpp\_to\_right} + \Delta i^{\cdot G}_{2\_trans\_right\_to\_max} + \\ \Delta i^{\cdot G}_{2\_ss\_mpp\_to\_left} + \Delta i^{\cdot G}_{2\_trans\_left\_to\_min} \end{pmatrix}$$

(6.35)

Equation (6.35) can be re-formatted as follow:

$$\begin{pmatrix} \Delta i_{dc\_overall} - \Delta i^{\cdot G}_{1\_ss\_mpp\_to\_right} - \Delta i^{\cdot G}_{1\_trans\_right\_to\_max} - \\ \Delta i^{\cdot G}_{1\_trans\_left\_to\_min} - \Delta i^{\cdot G}_{2\_trans\_right\_to\_max} - \Delta i^{\cdot G}_{2\_ss\_mpp\_to\_left} - \\ \Delta i^{\cdot G}_{2\_trans\_left\_to\_min} - 2\Delta i^{\cdot G}_{2\_ss\_mpp\_to\_right} \end{pmatrix} = \begin{pmatrix} \Delta i^{\cdot G}_{1\_ss\_mpp\_to\_left} + \\ \Delta i^{\cdot G}_{2\_ss\_mpp\_to\_right} - \\ 2\Delta i^{\cdot G}_{2\_ss\_mpp\_to\_right} \end{pmatrix}$$

$$\Delta i_{dc\_overall} - \underbrace{\begin{pmatrix} \Delta i^{\cdot G}_{1\_ss\_mpp\_to\_right} + \Delta i^{\cdot G}_{1\_trans\_right\_to\_max} + \Delta i^{\cdot G}_{1\_trans\_left\_to\_min} + \\ \Delta i^{\cdot G}_{2\_trans\_right\_to\_max} + \Delta i^{\cdot G}_{2\_ss\_mpp\_to\_left} + \Delta i^{\cdot G}_{2\_trans\_left\_to\_min} + \\ 2\Delta i^{\cdot G}_{2\_ss\_mpp\_to\_right} \end{pmatrix}}_{z} = \begin{pmatrix} \Delta i^{\cdot G}_{1\_ss\_mpp\_to\_left} - \\ \Delta i^{\cdot G}_{2\_ss\_mpp\_to\_right} \end{pmatrix}$$

$$\Delta i_{dc\_overall} \quad - \quad z \quad = \Delta i^{\cdot G}_{1\_ss\_mpp\_to\_left} - \Delta i^{\cdot G}_{2\_ss\_mpp\_to\_right}$$

(6.36)

Thus, from (6.34) and (6.36):

$$\Delta i^{\cdot non-unifrom}_{dc\_pair\_i} = \Delta i_{dc\_overall} - z$$

(6.37)

From (6.37) one can conclude that with active filter the peak to peak current variation of a pair will be less than the case without active filter by a value equal to z. The decreased percentage for one pair can be calculated as follow:

$$Decreased \; \% = \left(1 - \frac{\Delta i_{dc\_pair\_i}^{\cdot non-uniform}}{\Delta i_{dc\_overall}}\right) \times 100\%$$

$$= 100\% - \left(\frac{\Delta i_{dc\_overall} - z}{\Delta i_{dc\_overall}}\right) \times 100\%$$

$$= 100\% - \left(\frac{\Delta i_{1\_ss\_mpp\_to\_left}^{G} - \Delta i_{2\_ss\_mpp\_to\_right}^{G}}{\begin{array}{l}\Delta i_{1\_ss\_mpp\_to\_right}^{G} + \Delta i_{1\_trans\_right\_to\_max}^{G} + \Delta i_{1\_ss\_mpp\_to\_left}^{G} + \\ \Delta i_{1\_trans\_left\_to\_min}^{G} + \Delta i_{2\_ss\_mpp\_to\_right}^{G} + \Delta i_{2\_trans\_right\_to\_max}^{G} + \\ \Delta i_{2\_ss\_mpp\_to\_left}^{G} + \Delta i_{2\_trans\_left\_to\_min}^{G}\end{array}}\right) \times 100\%$$

(6.38)

And as

$$\Delta i_{1\_ss\_mpp\_to\_left}^{G} - \Delta i_{2\_ss\_mpp\_to\_right}^{G} \ll \left(\begin{array}{l}\Delta i_{1\_ss\_mpp\_to\_right}^{G} + \Delta i_{1\_trans\_right\_to\_max}^{G} + \Delta i_{1\_ss\_mpp\_to\_left}^{G} + \\ \Delta i_{1\_trans\_left\_to\_min}^{G} + \Delta i_{2\_ss\_mpp\_to\_right}^{G} + \Delta i_{2\_trans\_right\_to\_max}^{G} + \\ \Delta i_{2\_ss\_mpp\_to\_left}^{G} + \Delta i_{2\_trans\_left\_to\_min}^{G}\end{array}\right)$$

Consequently, even under non-uniform irradiation on a pair a significant suppression level is expected in dc-link current variation of the two SCPVM units when they operate as a pair.

If one or more of the *j* pairs operates under non-uniform irradiation, the more identical the level of generated harmonics from the units in a pair (e.g. their solar irradiation is as close as possible to each other) the greater harmonic suppression is achieved.

As shown in Figure 119, under non-uniform solar irradiation on a pair a low order-frequency variation at f_{low} is still observed in the total output current after applying the active filter. For *j* pairs it is expected to be the same under Synchronised SCPVM units.

6.5 Minimum DC-link Capacitance with Active Filter

In this section, a system consists of two SCPVM units connected to the second-stage DC/DC boost converter via a common dc-link bus as shown in Figure 39, page 58 is considered. It has been discussed in Chapter 5 that under specific operating condition the interaction between system stages increases and can lead to chaotic like behaviour and even loss of system stability. The aim of this section is to show the effect of the proposed active filter on the minimum required dc-link capacitance. Therefore, before

applying the active filter to the system the dc-link capacitance C_{dc} is reduced until undesirable operating behaviour at the dc-link bus is observed. While the system operating with this insufficient C_{dc} value the proposed active filter is enabled to explore its effect on the minimum required dc-link capacitance for stable operation by suppressing the harmonics in the dc-link bus. The system is tested considering two different controllers for the second-stage converter; voltage mode 3P2Z controller and cascaded current-voltage controller.

6.5.1 Voltage mode 3P2Z controller

In this test the dc-link voltage is controlled by 3P2Z controller. The total dc-link capacitor is reduced to 24μF until the chaotic like behaviour is observed in the dc-link bus and grid as shown in Figure 120 for the time period less than 15 ms. Then, the active filter is enabled at t=15 ms as shown in Figure 120. It can be seen that the active filter has helped to stabilise the system by suppressing the P&O related harmonics (i.e. reducing the dc-link current variation). With the active filter the dc-link power variations are suppressed and that reduces the disturbances seen by the second-stage controller.
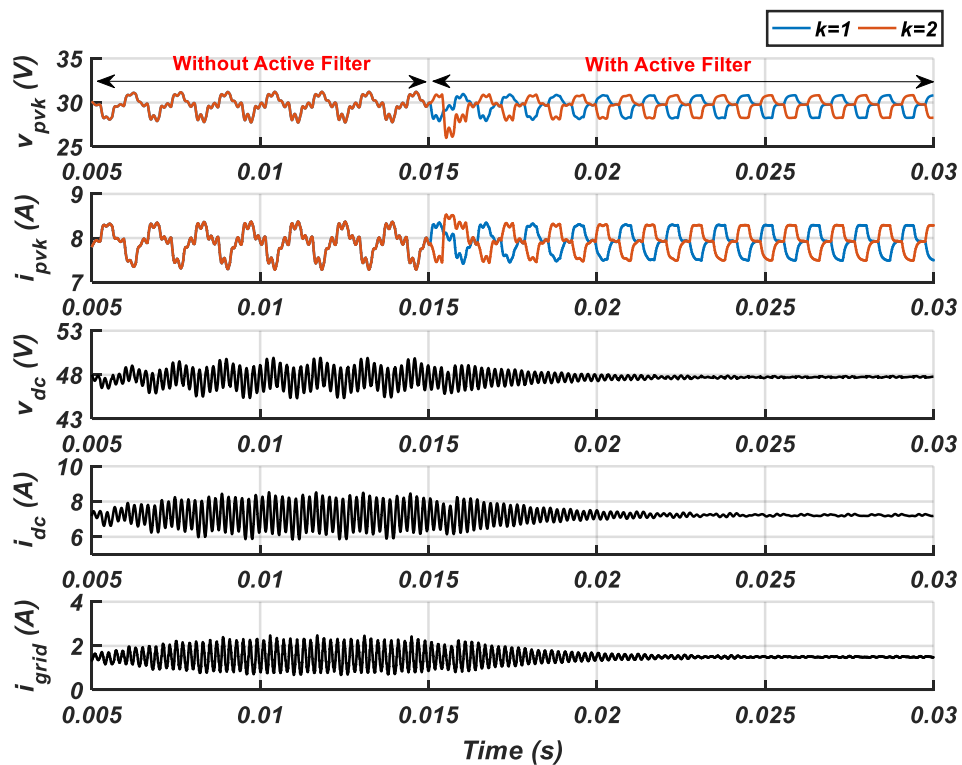
Figure 120: Simulation results show the effect of the active filter on stabilising the system when operating under insufficient C_{dc} size with 3P2Z controller (5.5). n=2, C_{dc}=24μF, K_v=222,V_{dc}=48V and G=1000 W/m². (Only average values are shown).

6.5.2 Cascaded current-voltage controller

In this test the dc-link voltage is controlled by cascaded current-voltage controller. The total dc-link capacitor is reduced until the chaotic like behaviour is observed in the dc-link bus and grid as shown in Figure 121 for the time period less than 15 ms. Then, the active filter is enabled at t=15 ms as shown in Figure 121. The active filter stabilise the system and allow the system to operate with smaller capacitance size than the case without active filter.
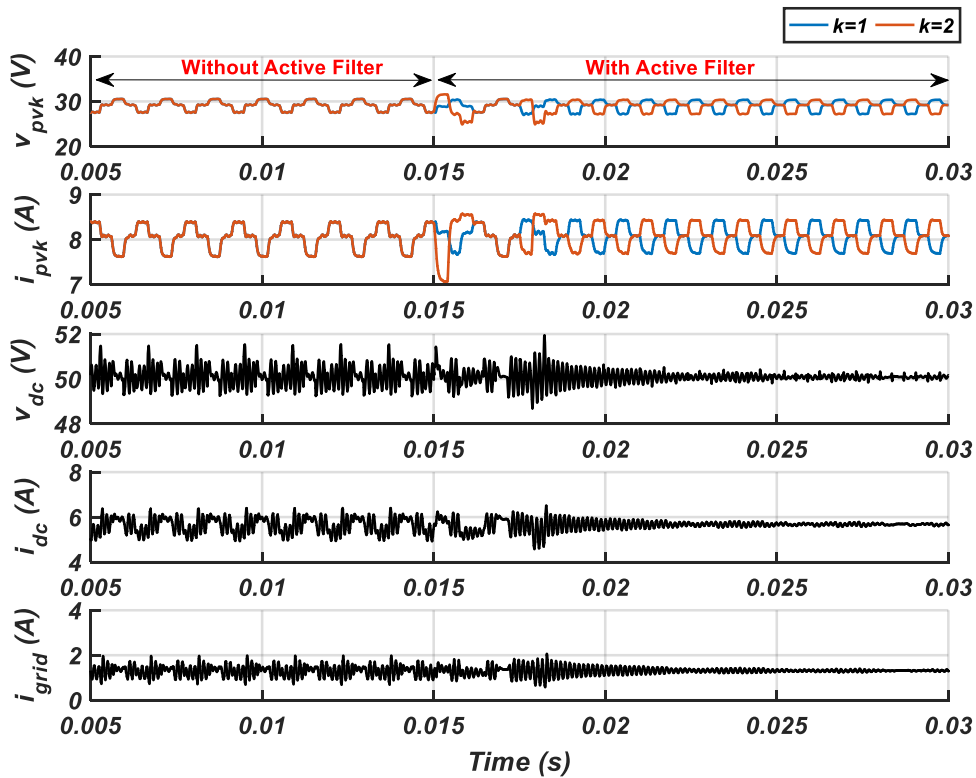

Figure 121: Simulation results show the effect of the active filter on stabilising the system when operating under insufficient C_{dc} size with cascaded controller. n=2, C_{dc}=22μF, K_{pv}=1, K_{iv}=10^4, K_{pi}=38, $K_{ii} = 1.33 \times 10^6$ and G=1000 W/m². (Only average values are shown).

6.6 Conclusion

A novel system-level controller named as "active filter" is proposed to reduce the progression of the P&O related harmonics into the dc-link bus, reduce the dynamic interaction between system stages, and improve the efficiency and power quality of a PV system that consists multiple parallel connected SCPVM units. The concept of the active filter is based on synchronising the P&O controllers of n-parallel connected SCPVM units, sorting the units into pairs, and aligning the generated harmonics by the units in each pair to be out of phase. As a result the harmonics levels are supressed at

the total output of the parallel units. An analytical analysis is provided to proof the effectiveness of the proposed active filter by comparing the dc-link harmonics level before and after employing the active filter. The analysis show more than 50% decrease in the harmonics can be achieved with the proposed active filter. Moreover, with the proposed active filter the dc-link current ripple of the double-stage DC/DC boost converter is notably reduced (i.e. dc-link power quality has improved) and in that a smaller DC-link capacitor can be used. Also, improved control dynamics for both converter stages can be achieved.

7 EXPERIMENTAL VERIFICATIONS

7.1 Abstract

This chapter includes full description of the developed experimental prototype in the lab as shown in Figure 122. The method of emulating the PV module in the lab using programmable power supply is provided. The designed inductors and the selected components for the first-stage and the second-stage converters are provided. The procedure to optimise the P&O controller is described. Finally, experimental results are provided to validate: (I) the P&O related harmonics at the PV and dc-link sides, (II) the effectiveness of the proposed active filter, and (III) the dynamic interaction between the system stages and the effect of the proposed active filter to reduce it.

7.2 Experimental Setup

For experimental verifications, a prototype of double-stage parallel SCPVM units connected to a main dc bus is developed in the lab as shown in Figure 122. Two programmable power supplies are used to emulate the PV modules. The first-stage converters are rated at 250W each and the second-stage converter is rated at 500W. A dSPACE controller board (DS1103) is used to implement the distributed P&O controllers, the proposed system-level controller, and manages information exchange between SCPVM units. The dc-link bus voltage is controlled by the second-stage converter via cascaded current-voltage controller. The total dc-link capacitance is 44µF which is split into halves at the output of the first-stage boost converters. The main DC bus is controlled by a programmable electronic load at a constant voltage of 200V.

(a) Programmable power supplies
(b) First stage DC/DC boost converters
(c) Measurement boards
(d) DC-link bus
(e) Second stage DC/DC boost converter
(f) Programmable electronic load
(g) dSPACE expansion box DS1103
(h) dSPACE input/output connector board
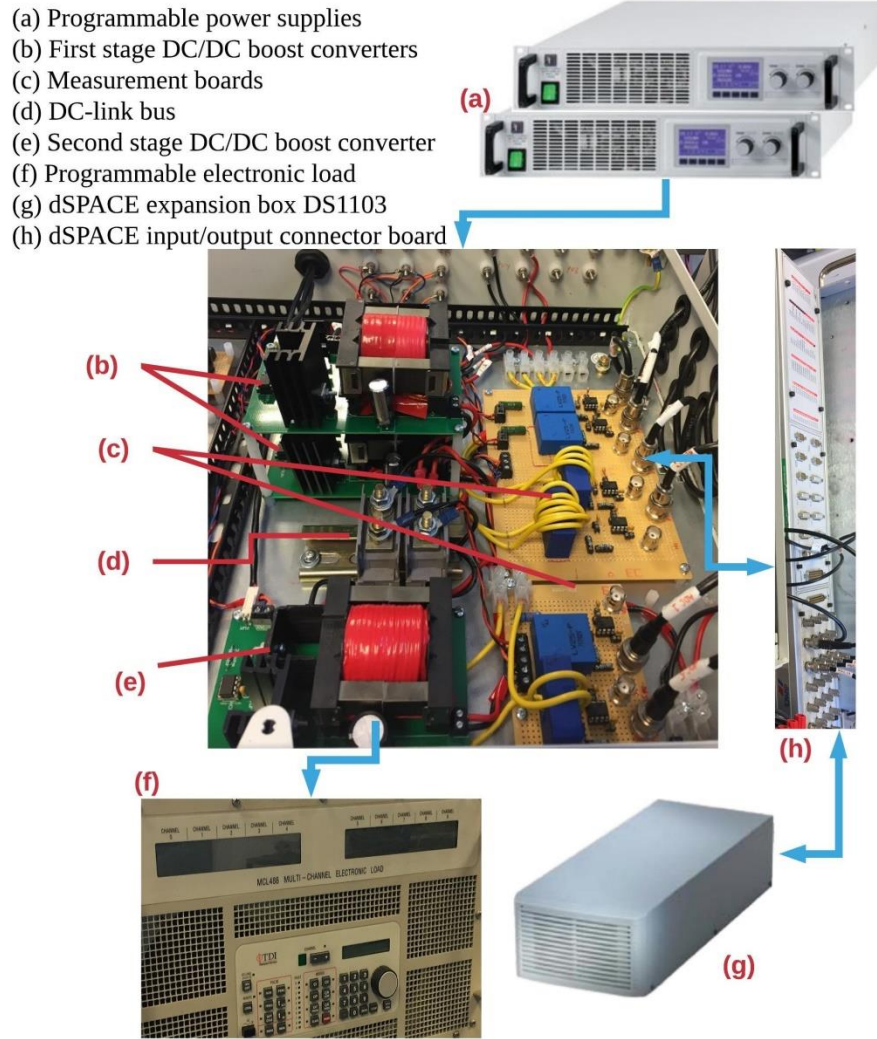
Figure 122: Experimental prototype of double-stage parallel SCPVM configuration connected to a main DC bus.

7.2.1 PV emulator

In this work a programmable DC power supply, Matlab/simulink and dSPACE are used to implement the PV module. A mathematical model of the PV module based on equation (2.6) is implemented using Matlab Simulink (the hardware implementation is done using dSPACE DS1103 controller board). The m-file for the PV model is provided in Appendix C. The model is capable to emulate actual PV module under different environmental conditions. The PV Simulink model is then used to control the programmable power supply via dSPACE. The operation depends on reading the value of the output voltage across the programmable power supply (i.e. the PV module voltage v_{pv}). This reading is inserted to the PV Simulink model through the Analog to Digital connection port of the dSPACE. Then, the Simulink model of the PV gives a reference current to that certain voltage. Finally, the reference current signal is sent to

the Analog port of the programmable power supply via Digital to Analog connection port of the dSPACE to set its output current (i.e. i_{pv}) at the value of the reference signal.

The PV lab model is verified by comparing its characteristic curve with the PV simulation model. The PV lab characteristic curve is obtained by connecting variable dc voltage load to the PV emulator. Then, V_{pv} and I_{pv} are recorded while changing the load voltage in small steps from zero to the open circuit voltage of the PV module under different solar irradiation levels. Figure 123 compares the experimental and simulation results of the PV model. Both the experimental and the simulation results are matching and show similar behaviour under different solar irradiation levels. Furthermore, the model is compared with the manufacturer characteristics curve in the datasheet available in [42] and the model results are highly matching the manufacturer's curves with less than 3% error.

7.2.2 SCPVM and second-stage converters components

The circuits of the boost converters are implemented on PCB boards. The capacitance and inductor are selected based on the designed values in Chapter 3, sections 3.3 and 3.4. The inductors are built in the lab using the core geometrical method [74]. For the SCPVM converters ferrite core, ETD54 is used with 26 turn of 0.4 mm diameter of Litz wire. LCR analyser is used to measure the inductance of the SCPVM converters designed inductors and the results are 0.212 mH and 0.199 mH at 60 kHz switching frequency. Rest of the components are selected off shelf and are the same for both converters as given in Table 12. For the second-stage converter ferrite core, PM 62/49 is used with 22 turn of 0.4 mm diameter of Litz wire. The result of the second stage inductance at 60kHz is measured by the LCR analyser and it is 0.519 mH at 60 kHz. The rest of the components for the second stage converter are given in Table 13.
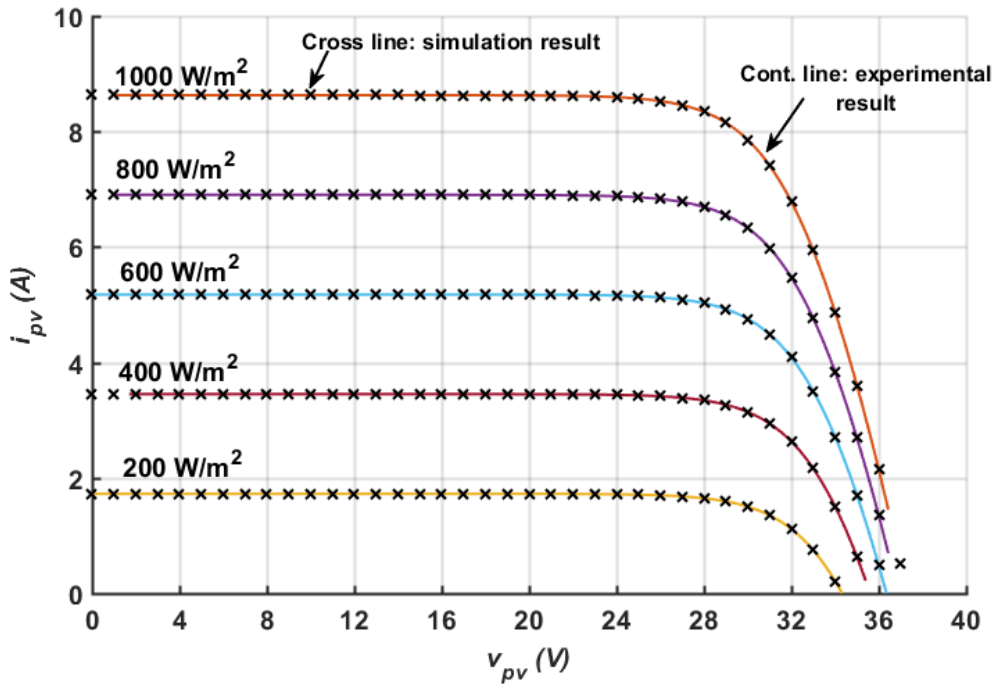
Figure 123: Current-voltage characteristic curve of the PV module: (continuous line) Experimental results, and (cross line) Simulation results.

Table 12: SCPVM Converter Components

Element	Converter component
Capacitor of C_{in}	Aluminium Electrolytic Capacitor, 50V dc, 2.2 µF
Switch	N-channel MOSFET, 26 A, 200V
Diode	High Voltage SiC Schottky Diode, 1200V 20A
Capacitor of C_o	Aluminium Electrolytic Capacitor, 400V dc, 22 µF

Table 13: Second-stage Converter Components

Element	Converter component
Switch	N-Channel MOSFET, 23 A, 900 V
Diode	High Voltage SiC Schottky Diode, 1200V 20A
Capacitor of C_{out_2}	Aluminium Electrolytic Capacitor, 450V dc, 47 µF

7.2.3 P&O optimisation

In order to optimise the P&O sampling time, the transients dynamic of v_{pv} and i_{pv} are measured when the PV emulator (i.e. the programmable power supply) is connected to the first-stage converter. For this test the second-stage converter is disconnected and at the dc-link bus a constant voltage load of 50V is connected. First, a current demand of 3.5A is sent to the Analog port of the PV emulator via the dSPACE. Then, a small unit step change in the duty-cycle is applied (0.035 step change which is equal to the P&O controller step size in the simulation work). It was found that 50 ms is required for v_{pv} and i_{pv} to settle as shown in Figure 124. Therefore, 50 ms sampling time is considered for P&O controller. Due to the slow dynamic behaviour of the PV emulator, the P&O sampling period in the experimental work of $T_{mppt} = 50\ ms$ is much longer than the

sampling period of $T_{mppt} = 0.35\ ms$ that considered in the simulation analysis. However, this is will not affect the main findings of this work. Based on (4.1) in the experimental work the generated low frequency oscillation in the dc-link bus will be related to T_{mppt} of 50 ms, so the expected low frequency ripple is 5 Hz for three-step operation of the P&O controller. The perturbation step size Δd is chosen to be 0.035; the same as the simulation parameter.
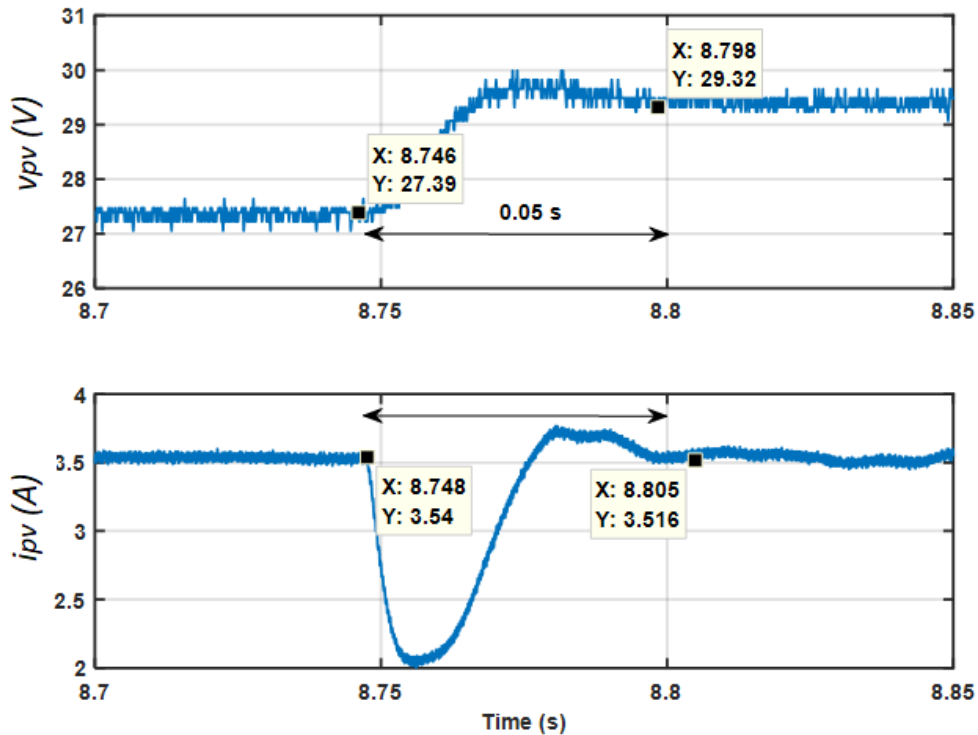

Figure 124: Experimental results: the transients dynamic of v_{pv} and i_{pv}. $G = 1000\ W/m^2$

7.3 Experimental Results of Two SCPVM Units Connected to a Constant Voltage Bus

In this section the experimental tests are carried out for SCPVM units connected to a dc-link bus that controlled at constant voltage by the programmable electronic load as shown in Figure 125 (the second-stage converter is not included in the results of this section). First, one SCPVM unit is tested to show the P&O related harmonics at the PV and dc-link sides. Then, two SCPVM units are used to verify the proposed active filter approach.

(a) Programmable power supplies
(b) First stage DC/DC boost converters
(c) Measurement boards
(d) DC-link bus
(e) Programmable electronic load
(f) dSPACE expansion box DS1103
(g) dSPACE input/output connector board
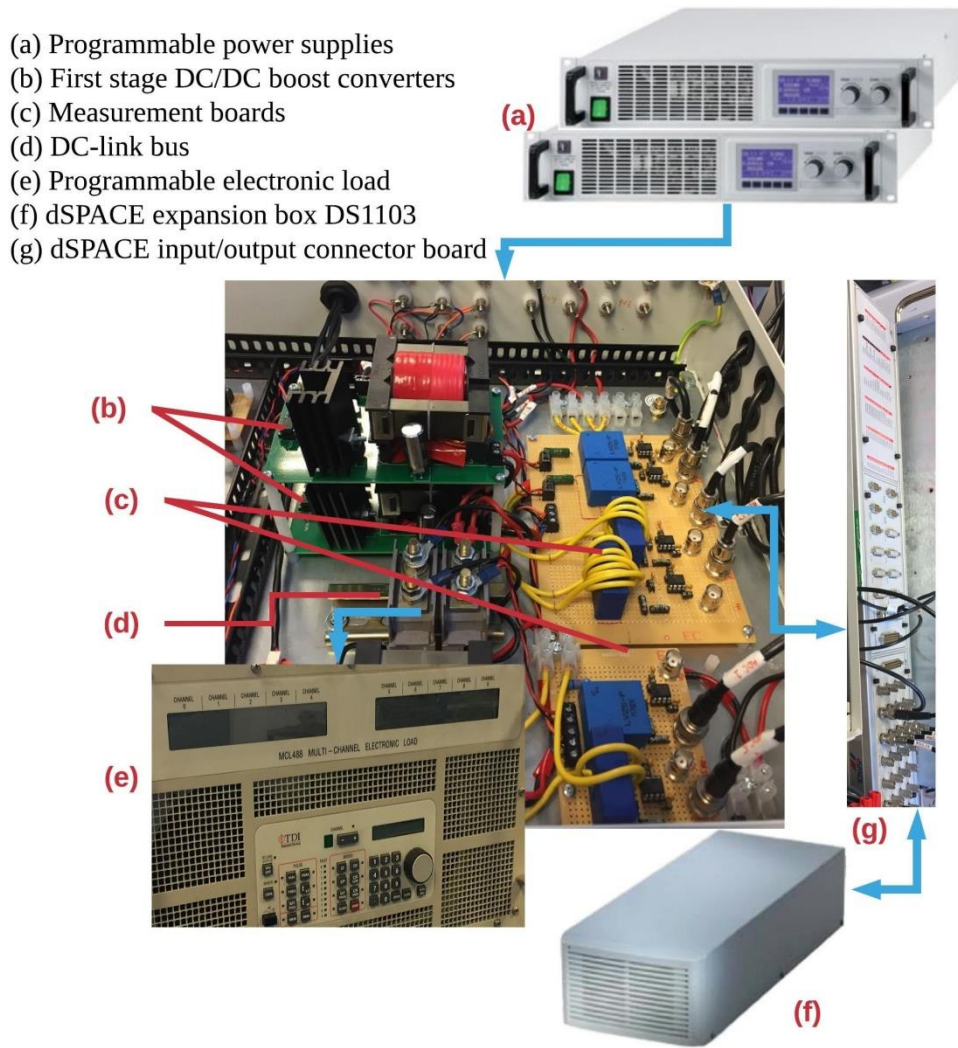
Figure 125: Experimental prototype of two parallel SCPVM units connected to dc-link bus controlled by programmable electronic load.

7.3.1 Single SCPVM unit

In this test only one SCPVM unit is connected to the dc-link bus which is controlled by the programmable electronic load at a constant voltage of 50V. Figure 126 shows the effect of solar irradiation level on steady-state variation of i_{pv} due P&O controller. It shows the 5 Hz low frequency variation as expected from (4.1). Also, it can be seen that the peak-peak steady-state variation (denoted in Figure 126 as Δi_{pv}) increases as the solar irradiation increases (e.g. $\Delta i_{pv}^{200} = 0.24 \ A \ and \ \Delta i_{pv}^{1000} = 1A$) as was expected in the analytical analysis (see Figure 57, page 86). Also, transient oscillations are observed every T_{mppt} as the PV module current changes at every time P&O perturbs.

The output current of the SCPVM unit (i_{scpvm_out}) is shown in Figure 127.a when the unit operate under two different solar irradiation levels (800 W/m^2 and 400 W/m^2). The

frequency of the low order variation is 5 Hz which is associated with the 50 ms P&O sampling time as expected form (4.1). Figure 127.b and Figure 127.c show the change in the transient dynamic due to solar irradiation variation and P&O operating point changes from MPP → Left MPP → MPP → Right MPP, respectively. In Figure 127.b and Figure 127.c the original waveforms are divided by their final values to make is easier to compare the settling behaviour. The system still show similar behaviour as expected analytically (see Figure 59 and Figure 60, Page 89) with more damped dynamic at higher solar irradiation (see Figure 127.b) and show different transient behaviour under the three P&O operating points (see Figure 127.c).
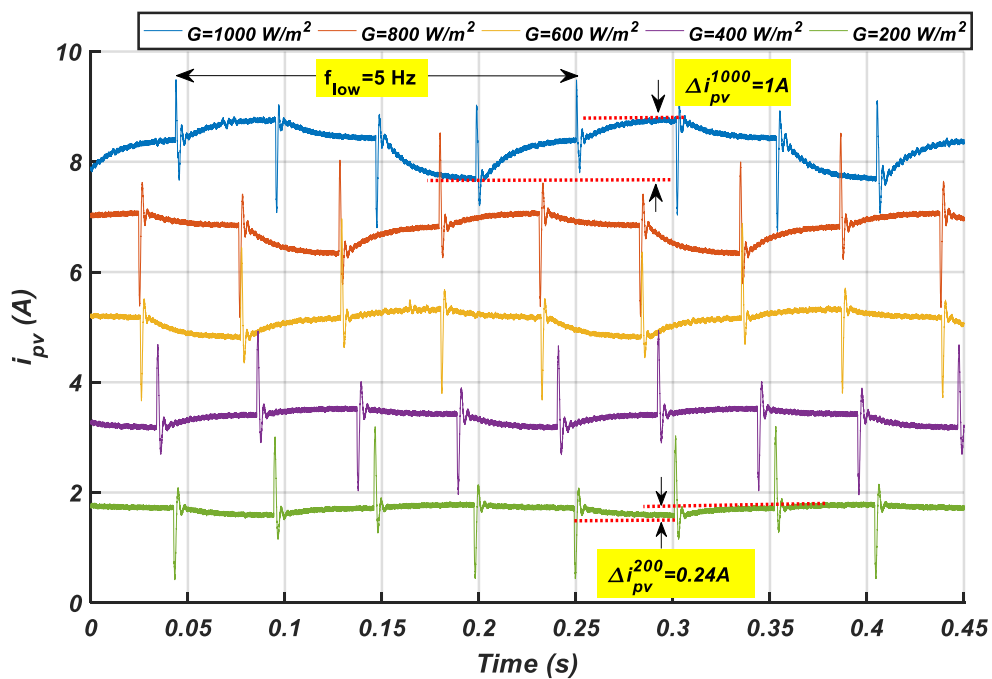

Figure 126: Experimental results of i_{pv} under different solar irradiation level. T_{mppt}=50 ms, Δd=0.035.
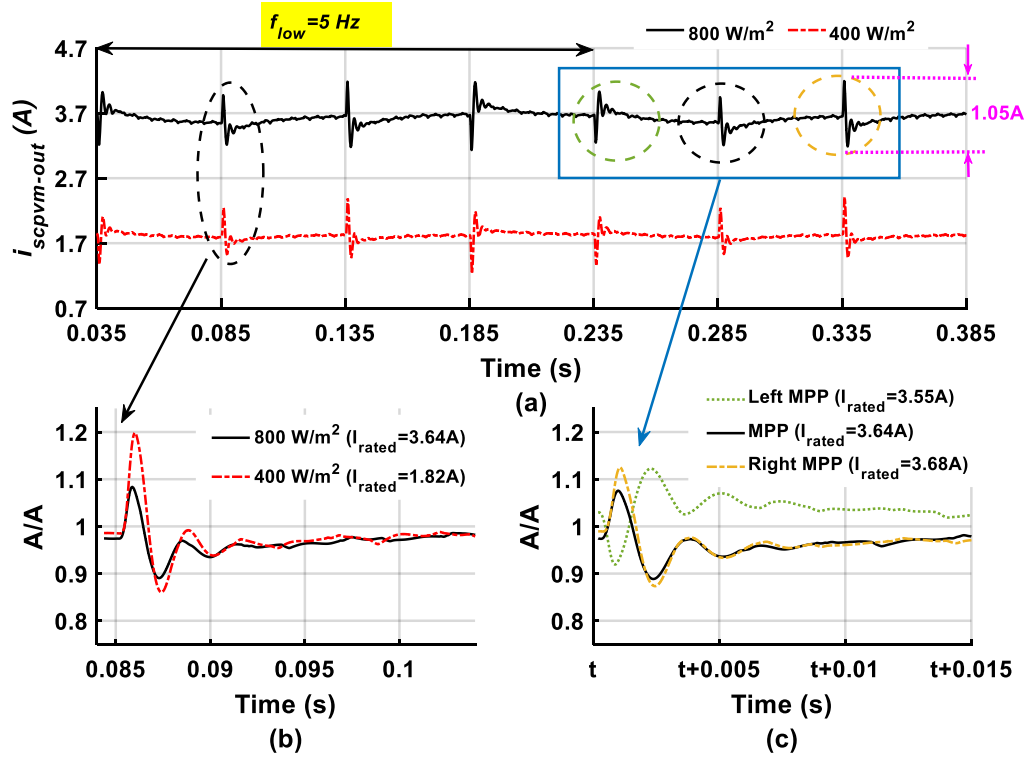
Figure 127: Experimental results of the output current of one SCPVM unit ($T_{mppt}=50$ ms, $\Delta d=0.035$).

7.3.2 Two SCPVM units

In this test two SCPVM units are connected to the dc-link bus. Figure 128 and Figure 129 show two SCPVM units operating with non-synchronised and synchronised P&O controllers, respectively. The non-synchronised case (Figure 128) shows inconsistent dc-link variation which is not easy to be presented as a function of the variation of one SCPVM unit. That is because in this case the dc-link variation is not only a function of T_{mppt}, but also a function of the time delay between the P&O perturbations of SCPVM1 and SCPVM2 and this delay is unknown before units are operating and it can change if units stopped working and restarted again. In the synchronised case (Figure 129) the v_{dc} and i_{dc} variations occur at the same times as if the system operate with one SCPVM unit as defined in (4.1), but in this case the dc-link variation is two times larger than the non-synchronised case.

The effect of increasing the number of the synchronised parallel-connected SCPVM units under uniform solar irradiation can be verified by comparing the overall variation of the one unit in Figure 127.a with the two units in Figure 129.As expected from (4.9) the overall variation in i_{dc} of the Synchronised SCPVM units in Figure 129 is

approximately twice the overall variation of one SCPVM unit (see Figure 127.a for 800W/m^2) with that to be 2.2 A and 1.05 A, respectively.
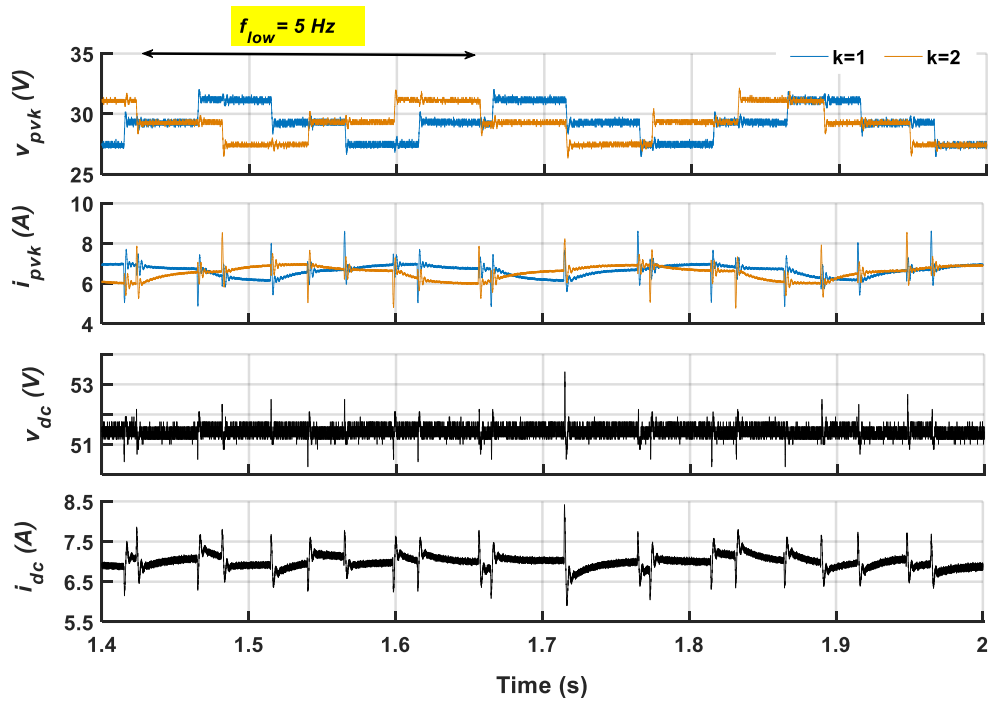

Figure 128: Experimental results for uniform non-synchronised case: n=2, $T_{mppt}=50$ ms, $\Delta d=0.035$, $G_1=G_2=800W/m^2$.
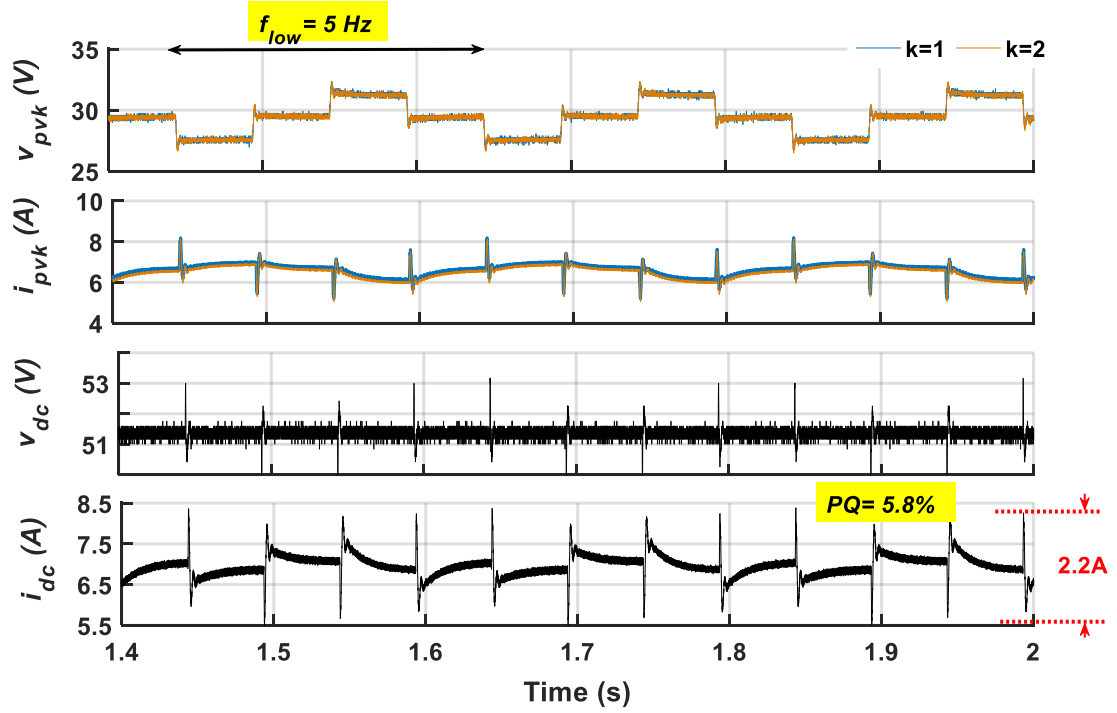
Figure 129: Experimental results for uniform synchronised case without active filter: n=2, T_{mppt}=50 ms, Δd=0.035, G_1=G_2=800W/m^2.

The proposed active filter is tested under different operating conditions such as uniform, non-uniform and transient in solar irradiation. In case uniform irradiation of 800 W/m^2, the results before and after applying the active filter are shown in Figure 129 and Figure 130, respectively. With the active filter the overall variation in i_{dc} is effectively suppressed by more than 77% (from 2.2A to 0.5A as shown in Figure 129 and Figure 130, respectively).

The FFT of i_{dc} in Figure 131 is comparing the harmonics of i_{dc} waveform in Figure 129 (without active filter) with i_{dc} waveform in Figure 130 (with active filter). It shows that with the active filter all harmonics above 30 Hz are cancelled completely and harmonics below 30Hz are effectively suppressed except at *2f$_{low}$* (10 Hz) as expected from (6.32).
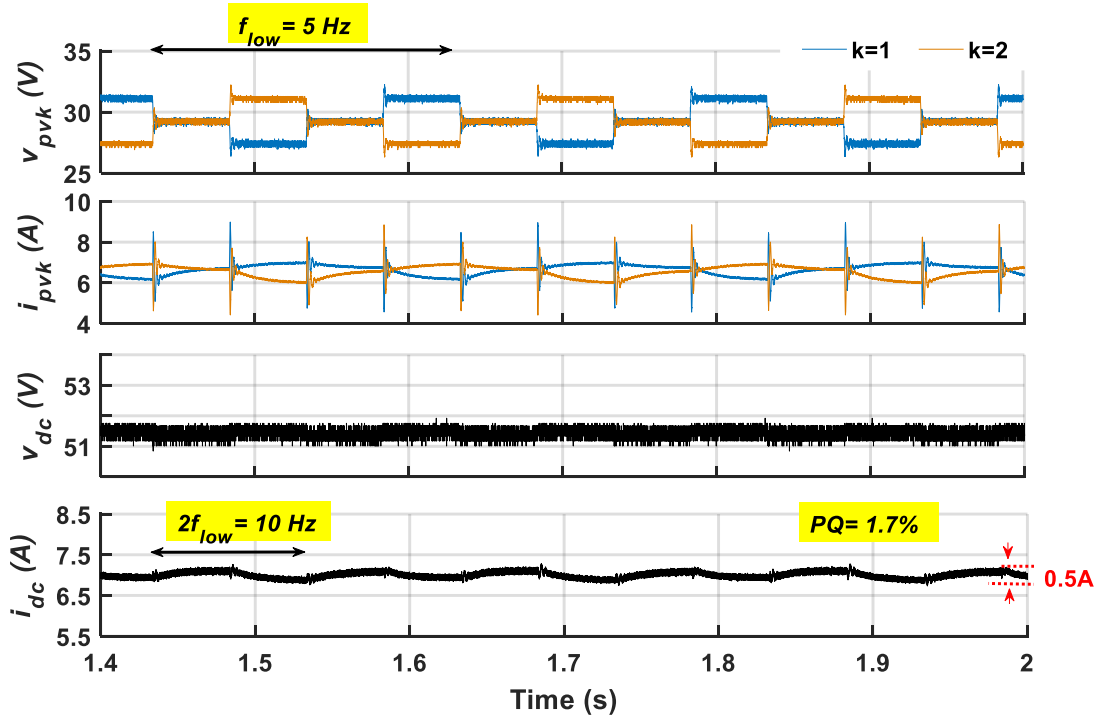
Figure 130: Experimental results for uniform synchronised case with active filter: n=2, T_{mppt}=50 ms, Δd=0.035, G_1=G_2=800W/m².

(a) FFT of the dc-link current
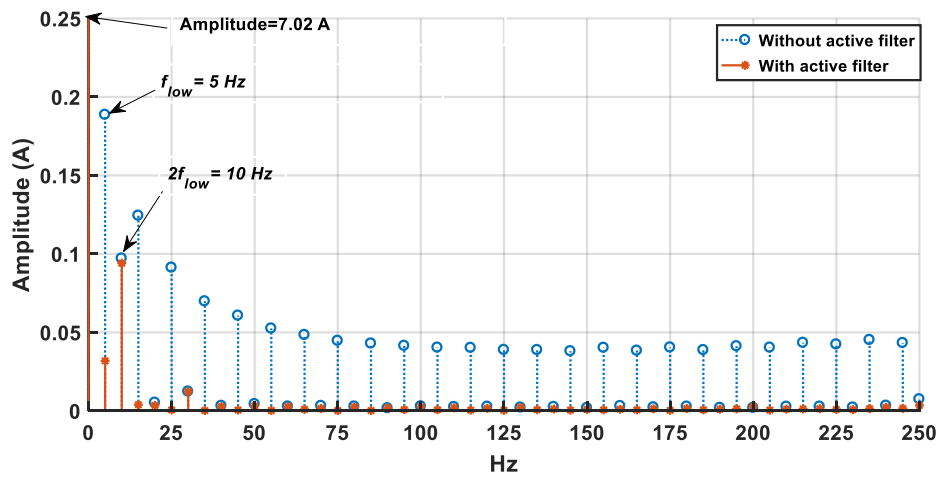

(b) Zoom in of the FFT results in a

Figure 131: FFT of the dc-link current i_{dc} shown in Figure 129 and Figure 130.

The non-uniform irradiation case before and after applying the active filter is shown in Figure 132. After applying the active filter (Figure 132.b), the overall variation of i_{dc} has improved by more than 71% (decreased from 2A without active filter to 0.57A with active filter). That verifies the effectiveness of the active filter in improving dc-link power quality even under non-uniform solar irradiation levels. The suppression level is not as effective as the previous case with uniform solar irradiation. It is only 6% less than the uniform case (77% for uniform case and 71% for non-uniform case) and that when the difference between the solar irradiation levels on the SCPVM units is ±50%. It will be less effective if the difference between the solar irradiation levels is bigger. This is because the harmonics level generated by a pair operating under non-uniform solar irradiation are not identical. The FFT results of i_{dc} without and with active filter for the non-uniform case is shown in Figure 132.c. It shows that the harmonics levels are effectively suppressed.

174
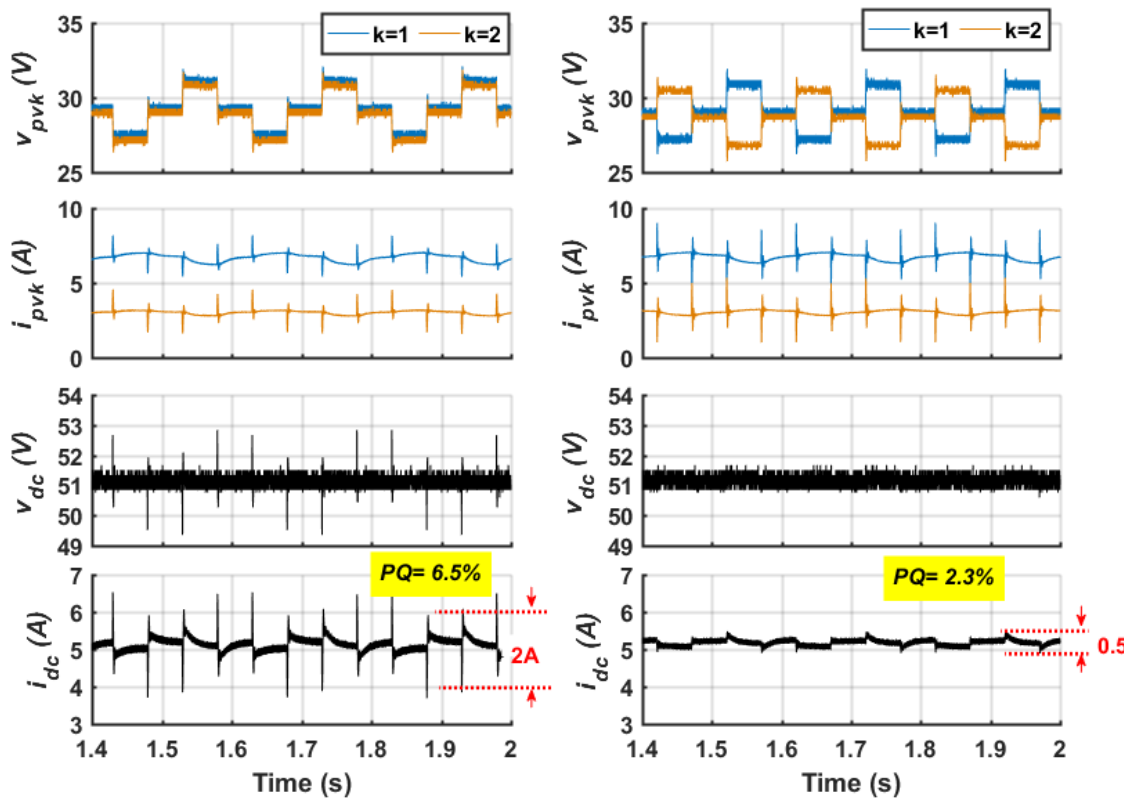
Figure 132: Experimental results for non-uniform solar irradiation: $n=2$, $T_{mppt}=50ms$, $\Delta d=0.035$, $G_1=800W/m^2$ and $G_2=400W/m^2$; (a) synchronised P&O without active filter (b) synchronised P&O with active filter (c) FFT of i_{dc} waveforms shown in a and b

Finally, the capability of the proposed active filter under transient in solar irradiation is demonstrated without and with active filter in Figure 133 and Figure 134, respectively. Three cases of slow, medium and fast average change rate in solar irradiation are

considered. The active filter maintains high power quality before, during and after the transient in case of slow ($50 \, W/(m^2.s)$) and medium ($100 \, W/(m^2.s)$) change rate of solar irradiation as shown in Figure 134.a and Figure 134.b, respectively. In case of the fast change rate ($300 \, W/(m^2.s)$) as shown in Figure 134.c, the active filter maintains high power quality before and after the transient period. During the transient period the active filter is disabled automatically as it continuously checks three duty-cycle steps mode and at this change rate ($300 \, W/(m^2.s)$) in solar irradiation and based on the adopted P&O parameters in this work, the P&O algorithm does not operate with three duty-cycle steps. That's happen when the variation of the output power caused by the solar irradiation is larger than the one caused by the P&O duty-cycle step size Δd. The relation in (2.9) is not satisfied (see Chapter 2, Section 2.3.1.2). In this case the best is that the active filter waits until the system is in three-step-duty-cycle operation.

For the tested system the maximum solar irradiation change rate before P&O get confused can be found from (2.10). The tested system has the following parameters (T_{mppt}=50 ms, Δd=0.035, V_{mpp}=29V, I_{mpp}=8.15A, the PV cell material constant K=6.895×10^{-3} A.m^2/W, r_{pv_mpp}=4.244Ω (calculated from (2.7)), H=0.0105A/V (calculated from (2.10)). Substituting these values in (2.10), that result in $\dot{G} = 162 \, W/(m^2.s)$. Accordingly, for slow change rate of $50 \, W/(m^2.s)$ and medium change rate $100 \, W/(m^2.s)$ which are less than $162 \, W/(m^2.s)$ the system operate in three step duty-cycle mode all time. While for the fast change rate of $300 \, W/(m^2.s)$ which is higher than $162 \, W/(m^2.s)$ the three step duty-cycle mode can be lost and that is clearly seen in Figure 134.c

Figure 133: Experimental results without active filter and under transient of solar irradiation at (a) $50 \, W/(m^2.s)$*, (b)* $100 \, W/(m^2.s)$ *and (c)* $300 \, W/(m^2.s)$ *change rate.*

Figure 134: Experimental results with active filter and under transient of solar irradiation at (a) $50\ W/(m^2.s)$*, (b)* $100\ W/(m^2.s)$ *and (c)* $300\ W/(m^2.s)$ *change rate.*

7.4 Experimental Results of Double-stage Parallel SCPVM Units Connected to a Main DC Bus

In this section the double-stage parallel SCPVM units connected to a main DC bus as shown in Figure 122 is considered to show the effectiveness of the proposed active filter approach when the SCPVM units are connected to the second-stage converter and to show the dynamic interaction between the SCPVM units with the second-stage controller.

Cascaded current-voltage controller is used to control the dc-link voltage. The controller parameters are tuned in the lab as given in (7.1) for the case when the SCPVM units operate under 400 W/m^2 solar irradiation level.

$$G_{cv}(S) = K_{pv} + \frac{K_{iv}}{s} = -0.24 + \frac{-10}{s}$$

$$G_{ci}(S) = K_{pi} + \frac{K_{ii}}{s} = 50 + \frac{50 \times 10^2}{s}$$

(7.1)

Figure 135 shows the system operating under uniform solar irradiation of 400 W/m^2. At the beginning the system operates without active filter then at $t \cong 0.75\ s$ the active filter is enabled. It can be seen that after applying the active filter the overall variation in i_{dc} is effectively suppressed by 70% (from 2A to 0.6A as shown in Figure 135).
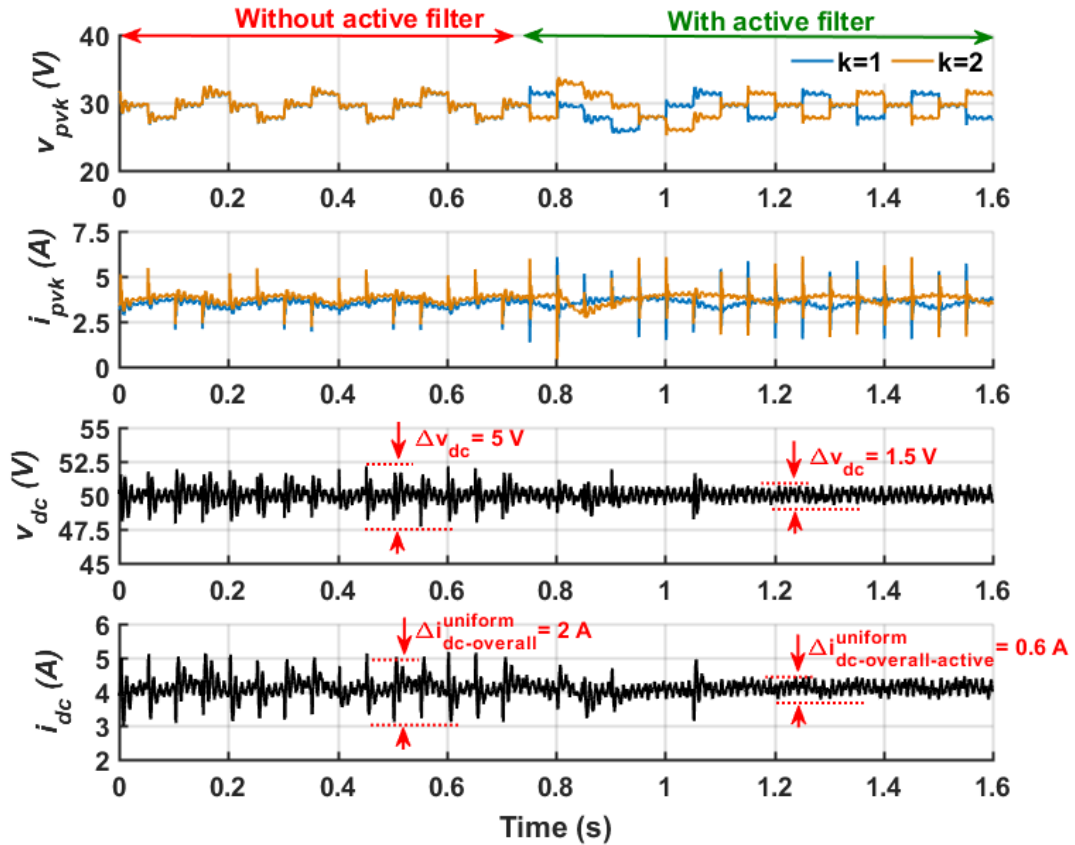
Figure 135: Experimental results for uniform synchronised case without and with active filter and cascaded current-voltage controller (7.1): n=2, T$_{mppt}$=50ms, Δd=0.035, G$_1$=G$_2$=400W/m², C$_{dc}$=44μF.

The interaction between the SCPVM converters and the second-stage converter due to the P&O related harmonics can be shown either by reducing the dc-link capacitance,

increasing the proportional voltage gain (k_{pv}) of the cascaded controller or increasing the solar irradiation level. First, the dc-link capacitance value is reduced to 22μF as shown in Figure 136. As can be seen with small capacitance value and without the active filter it becomes harder to control the dc-link voltage especially with the dc-link current changing continuously due to the P&O perturbations. After applying the active filter at $t \cong 0.95\ s$, the active filter suppress the changing in the dc-link current (improve the dc-link current quality) and that make is easier to control the dc-link voltage with the low capacitance value.
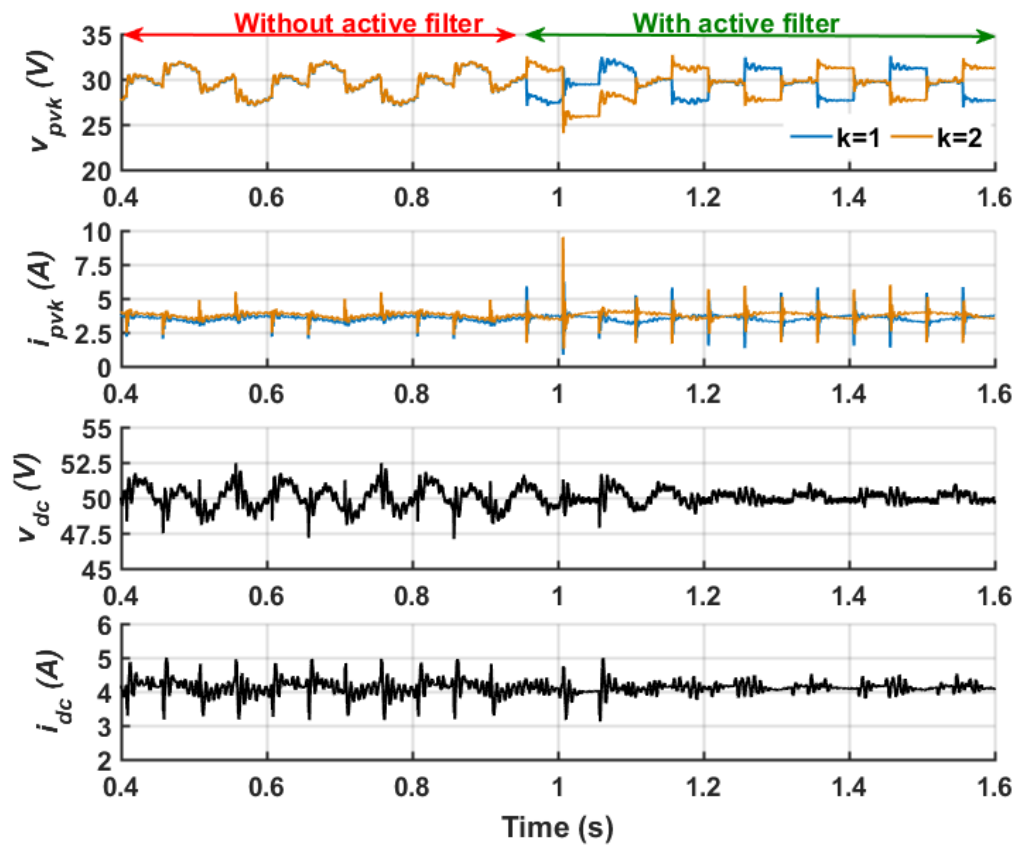
Figure 136: Experimental results show the effect of the active filter on controlling v_{dc} when operating with reduced capacitance size with cascaded current-voltage controller (7.1): n=2, T_{mppt}=50ms, Δd=0.035, G_1=G_2=400 W/m², C_{dc}=22μF.

Figure 137 shows the effect of the active filter on reducing the dynamic interaction between the system stages when the voltage gain is increased. At the beginning and as the system is operating with active filter as k_{pv} increasing from 0.24 to 1.05. As shown in Figure 137 the active filter maintain stable operation even at high value of k_{pv}. Then at the large value of k_{pv} of 1.05 the active filter is disabled at $t \cong 1.55\ s$. As it can be seen in Figure 137 the dc-link voltage and current enter chaotic like behaviour because at this high voltage gain $T_{settle} > T_{mppt}$.

180
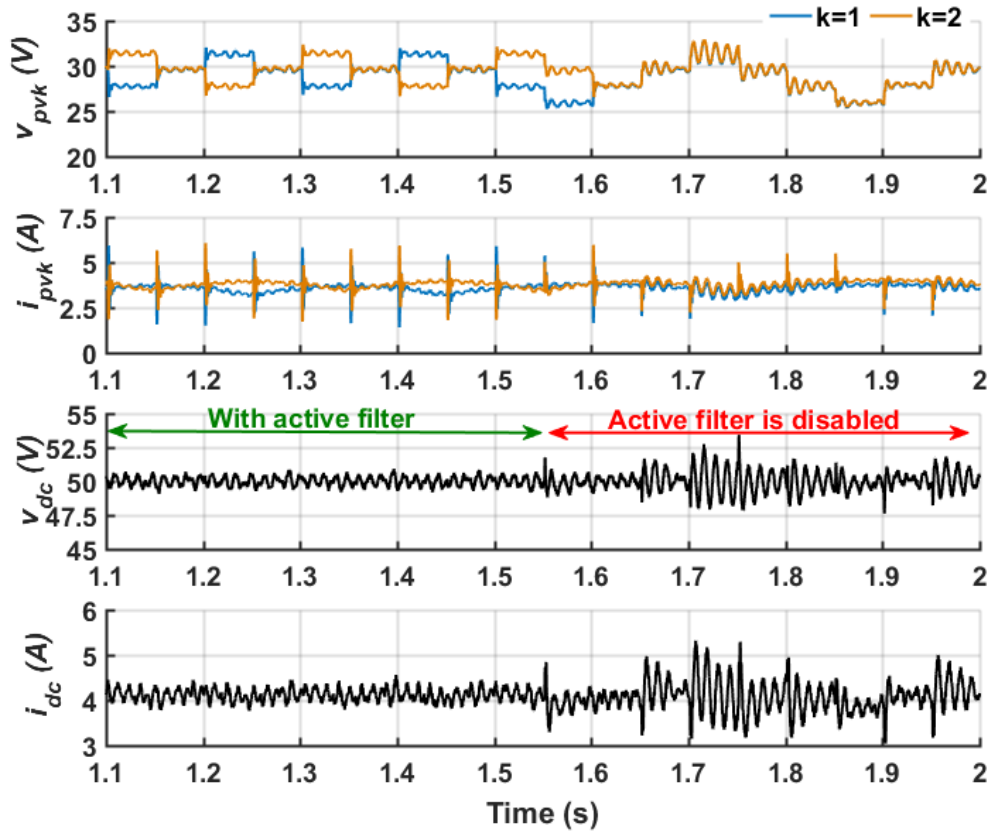
Figure 137: Experimental results show the effect of the active filter on system stability when operating with high voltage gain with cascaded current-voltage controller: n=2, T_{mppt}=50ms, Δd=0.035, G_1=G_2=400 W/m^2, C_{dc}=44μF, k_{pv}=1.05.

Finally, the increased interaction between the system stages due to the solar irradiation level and the effect of the active filter to reduce the dynamic interactions is shown in Figure 138. At the beginning, the system is stable when operating at $G = 400 \, W/m^2$ then at $t \cong 3.7 \, s$ the irradiation level changed to $500 \, W/m^2$. As can be seen, the interaction between the system stages had increased and that affected the power quality at the dc-link. While the system still operating under high solar irradiation of $500 \, W/m^2$ the active filter is enabled at $t \cong 7.25 \, s$. The active filter reduced the harmonics injected to the dc-link bus from the SCPVM units. This minimised the dynamic interaction between the stages and improved the dc-link power quality significantly.
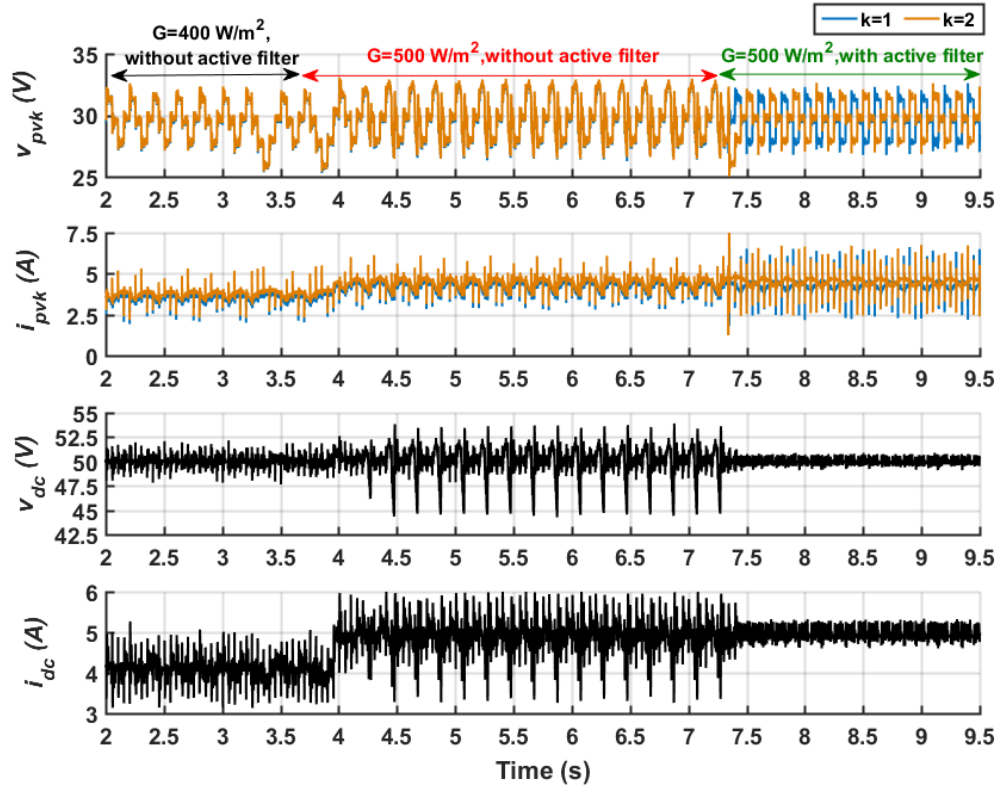
Figure 138: Experimental results show the effect of the active filter on system stability when solar irradiation level changes with cascaded current-voltage controller: n=2, $T_{mppt}=50ms$, $\Delta d=0.035$, $C_{dc}=44\mu F$, $k_{pv}=0.24$.

7.5 Conclusion

A prototype of double-stage parallel SCPVM system consists of two SCPVM units is developed in the lab in order to validate the analysis of the P&O related harmonics, to test the proposed active filter and to show the dynamic interactions between system stages. The experimental results confirm the analysis of the P&O related harmonics and show the effect of the solar irradiation level, the P&O operating point, and the total number of the parallel connected SCPVM units on the level of the overall dc-link power variation. Also, the experimental results validate the effectiveness of the proposed active filter approach under uniform irradiation, non-uniform irradiation, transient in solar irradiation and in the case of high dynamic interaction between the system stages. The dynamic interaction between the system stages is shown for small capacitance value, high control-voltage gain and high solar irradiation level.

8   CONCLUSIONS AND FUTURE WORK

In this chapter the outcomes of this research are summarised. Then, the main contributions are highlighted. Finally, research prospective is discussed.

8.1   Summary

PV is considered one of the promising renewable sources to produce clean energy and be part of the electricity generation. Therefore, the characteristics of the non-linear PV source, MPPT techniques, configurations and topologies of grid-connected PV systems, and controller structures for different operating modes (i.e. grid-connected and islanded modes) have been discussed in Chapter 2. In addition to that, two concerns for a grid-connected PV system have been discussed in Chapter 2. The first concern is related to the effect of the non-linear PV source on the dynamic performance of the system such as system damping factor, phase margin, and cut-off frequency. The impact of the non-linear PV source depends on the system controller structure in terms of controlling the input side or the output side of the PV interface converter. In the case of controlling the input side of the system, the damping factor and cut-off frequency are the ones most affected. In the case of controlling the output side (this is applied in the case of islanded mode operation) the non-linear PV source changes the system dynamic and may generate right half plane roots which affect system stability depending on the converter topology and the PV operating region. The second concern is related to the poor power quality from grid-connected PV systems. It has been reported that grid-connected PV systems is one of the sources which deliver harmonics to the grid due to many reasons such as large populations of PV inverters, resonance between the grid and the PV inverter, or large amounts of fluctuation in PV power. In addition to the aforementioned sources of harmonics in PV systems, during the work on this research it was observed that there is possible impact of the P&O controller on increasing the harmonics in PV grid-connected systems, which leads to a poor power quality. In parallel, recent studies have reported the same observations based on experimental results. The P&O technique is widely used in commercial converters for PV applications, especially for low-cost implementations which make the newly reported P&O related harmonics problem a subject undergoing intense study until researchers find a solution.

As discussed in Chapter 2 there are several configurations to connect a PV system to the grid and each configuration leads to different converter topologies and P&O architectures (centralised or distributed P&O). Therefore, it is difficult to generalise the

effect of the PV system on the power quality in the grid. In this work, the main focus is on double-stage parallel SCPVM configuration connected to a DC bus. A DC/DC boost converter is considered for both system stages. In Chapter 3, the design considerations of the double-stage DC/DC boost converter, P&O parameters optimisation and dc-link voltage control structures have been discussed. First, the available range of the dc-link voltage for successful tracking of MPP has been identified. Then, the effect of that voltage range on the first-stage converter parameters under different weather conditions is analysed. The converter parameters are chosen based on the highest solar irradiation condition to ensure high performance of the MPPT and small inductance core size. Regarding P&O parameters (T_{mppt} and Δd), they are designed based on the dynamic behaviour of the first-stage converter and the adopted PV module to ensure an optimal efficiency of the three-step operation. In addition to that, Chapter 3 provides a brief discussion of the different controller types that can be used to control the common DC-link bus in grid-connected mode such as the voltage mode and cascaded current-voltage controllers. Finally, time domain simulation and FFT results for the designed system are provided. The results show that the P&O controller is one of the sources that produce harmonics in the common DC-link bus and grid.

In Chapter 4, an analytical model of the DC-link current variation due to the P&O controller is provided as a function of P&O parameters (Δd and T_{mppt}), solar irradiation level, and the number of the parallel SCPVM units in the system (from a single SCPVM unit to n-parallel-connected units). In addition to that, the harmonics analysis considers the dynamic behaviour of the non-linear PV source under different operating points and the synchronisation between the P&O controllers of the parallel-connected SCPVM units. The analytical model can be used to predict the harmonics frequency and explore the factors which affect the harmonics level induced by the P&O controller. In addition to that, the analytical model helps to understand the power quality degradation behaviour due to P&O related harmonics and that will help to find the most efficient method to eliminate it.

In Chapter 5, the dynamic interaction between a SCPVM unit and the second-stage DC-link controller is analysed through simulations. It is important to understand the possible interactions between a SCPVM unit and the rest of the system as that can help to set system design recommendations and guidelines. The impacts of the P&O controller on increasing the dynamic interaction between system stages and on

designing the second-stage controller are highlighted. Three different types of DC-link controllers are considered: PI, 3P2Z, and cascaded current-voltage controllers. For each controller the dynamic interaction is explored in case of having an ideal current source (the SCPVM is modelled as a current source) connected to the second-stage converter and in case of having SCPVM unit connected to the second-stage converter. The results from the two aforementioned cases are compared and it reveals that the SCPVM unit increases the dynamic interaction between the system stages due to the P&O controller. As discussed in Chapter 4, the P&O operating point varies every T_{mppt} and that induces periodic low-order frequency and transient oscillations in the DC-link bus. The effect of these oscillations on the control loop of the second-stage converter at MPPT mode depend on the P&O parameters (Δd and T_{mppt}), the solar irradiation level, the size of C_{dc}, controller structure, and system cut-off frequency. It was shown through simulation examples that under specific operating conditions the dynamic interaction between the system stages increases and may lead to undesirable operating behaviour (chaotic like behaviour). It was shown that at MPP and for specific P&O parameters the dynamic interaction increases as solar irradiation increases, C_{dc} decreases, or system cut-off frequency increases (e.g. controller voltage gain increases). Accordingly, design recommendations and guidelines are provided in order to avoid any undesirable operating behaviour.

In Chapter 6, a novel system-level controller named as "active filter" is proposed to reduce the progression of the P&O related harmonics into the DC-link bus, reduce the dynamic interaction between system stages, and improve the efficiency and power quality of the PV system that consists of multi-parallel SCPVM units. The concept of the active filter is based on synchronising the P&O controllers of n-parallel connected SCPVM units, sorting the units into pairs, and aligning the generated harmonics by the units in each pair to be out of phase. As a result the harmonics levels are suppressed at the total output of the parallel units. An analysis is provided to prove the effectiveness of the proposed active filter by comparing the DC-link variations level before and after employing the active filter. The analysis shows more than 50% decrease in the current variations can be achieved with the proposed active filter. Moreover, as the DC-link current ripple of the double-stage DC/DC boost converter is notably reduced with the active filter (i.e. DC-link power quality has improved) that allows a smaller DC-link capacitor to be used. Also, improved control dynamics for both converter stages can be achieved.

In Chapter 7, a prototype of double-stage parallel SCPVM system consists of two SCPVM units is developed in the lab in order to validate the analytical analysis of the P&O related harmonics, to test the proposed active filter and to show the dynamic interactions between system stages. The experimental results confirm the analytical analysis of the P&O related harmonics and show the effect of the solar irradiation level, the P&O operating point, and the total number of the parallel connected SCPVM units on the level of the overall DC-link power variation. Also, the experimental results validate the effectiveness of the proposed active filter approach under uniform irradiation, non-uniform irradiation, transient in solar irradiation and in the case of high dynamic interaction between the system stages. The dynamic interaction between the system stages is shown for small capacitance value, high control-voltage gain and high solar irradiation level.

8.2 Main Contributions

- Analysis and modelling of P&O related harmonics

  A detailed analysis of the P&O related harmonics generated by the grid-connected double-stage SCPVM configuration has been carried out in this work. The frequency of the harmonics is provided as a function of the P&O parameters. Regarding the amplitudes of the harmonics it has been shown that they are function of the P&O parameters, solar irradiation level, and number of the parallel connected SCPVM units.

- Dynamic interaction in double-stage parallel SCPVM system

  The impact of the SCPVM unit on the second-stage DC-link controller is investigated through simulation. The analysis considered different types of DC-link controllers, P&O parameters, solar irradiation levels, PV operating regions, and DC-link capacitance sizes. The obtained results can help to set system design recommendations and guidelines such as sizing the DC-link capacitance and designing the DC-link voltage controller.

- Active suppression of PV related harmonics

A cost-effective system level controller is proposed as a solution to minimise the harmonics injected to the DC-link bus and grid due to the employed parallel distributed P&O controllers in the grid-connected PV system. With the proposed controller: (I) more than 50% decrease in the harmonics level can be achieved, (II) DC-link power quality is improved by eliminating the harmonics injected by the P&O controllers, (III) dynamic interaction between system stages is reduced, (IV) smaller DC-link capacitance size can be used, and (V) improved control dynamics for both converter stages can be achieved.

8.3 Future Work

Although significant progress has been made in this work regarding investigating P&O related harmonics and their effect on increasing the dynamic interactions between system stages in double-stage PV system, a number of areas still deserve further investigations.

- In this research the analysis of the PV related harmonics only considers a SCPVM unit based on a DC/DC boost converter. It could be interesting to apply the modelling approach on other topologies in order to study the impact of different converter topologies on the PV related harmonics.

- In this work the impact of a SCPVM unit on the rest of the system and the critical dynamic interaction point due to distributed P&O controllers have been analysed through simulation. Future work could be focused on providing analytical model that identify the critical dynamic interaction point between system stages for one SCPVM unit and multiple SCPVM units and determining the minimum system conditions to avoid any undesirable operating behaviour.

- This work covered the dynamic interactions between the first-stage and the second-stage of the double-stage parallel SCPVM system due to the induced low-order frequency and transient oscillations by the distributed P&O controllers. Future work could be focused on investigating the interaction between the first-stage converters and the second-stage converter due to the output impedance of the first-stage converters which depends on the solar irradiation level and the number of the connected SCPVM units. The investigation could include a comparison between three cases: first-stage

converters modelled as ideal current sources, first-stage converters without the active filter, and first-stage converters with the active filter.

- In this work the effectiveness of the proposed system level controller is compared only with the conventional P&O controller. It could be interesting to have a study that compares the proposed system level controller with other more advanced MPPT algorithms in terms of effect on grid power quality, cost, complexity and efficiency.

- In this work the proposed active filter is suitable to be implemented for PV system configurations that are based on distributed P&O architecture such as double-stage parallel SCPVM, single-stage parallel SCPVM and series string configurations. These configurations allow implementing the proposed active filter at the system level where system parameters are closely identical and communication between converters is not a problem as they are so close to each other. It could be interesting to explore the possibility of implementing the active filter in the case of other PV system configurations that are based on a centralised P&O controller such as series centralised configuration. In this case two PV systems such as two roof-top residential PV systems have to communicate with each other in order to synchronise their P&O controllers and suppress the related harmonics. The challenges in this case would be the distance between the PV systems and proposing an algorithm that can provide optimal harmonics suppression for two systems that have been designed with different parameters.

REFERENCES

[1]   R. H. Lasseter and P. Paigi, "Microgrid: a conceptual solution," in *Power Electronics Specialists Conference. IEEE 35th Annual*, 2004, vol. 6, pp. 4285-4290 Vol.6.

[2]   B. Lasseter, "Microgrids," in *Power Engineering Society Winter Meeting. IEEE*, 2001, vol. 1, pp. 146-149 Vol.1.

[3]   J. A. Peas Lopes, C. L. Moreira, and A. G. Madureira, "Defining control strategies for MicroGrids islanded operation," *IEEE Transactions on Power Systems,* vol. 21, no. 2, pp. 916-924, 2006.

[4]   K. De Brabandere, B. Bolsens, J. Van den Keybus, A. Woyte, J. Driesen, and R. Belmans, "A Voltage and Frequency Droop Control Method for Parallel Inverters," *IEEE Transactions on Power Electronics,* vol. 22, no. 4, pp. 1107-1115, 2007.

[5]   L. Yun Wei and K. Ching-Nan, "An Accurate Power Control Strategy for Power-Electronics-Interfaced Distributed Generation Units Operating in a Low-Voltage Multibus Microgrid," *IEEE Transactions on Power Electronics,* vol. 24, no. 12, pp. 2977-2988, 2009.

[6]   J. Rocabert, A. Luna, F. Blaabjerg, and P. Rodriguez, "Control of Power Converters in AC Microgrids," *IEEE Transactions on Power Electronics,* vol. 27, no. 11, pp. 4734-4749, 2012.

[7]   Z. Qing-Chang, "Robust Droop Controller for Accurate Proportional Load Sharing Among Inverters Operated in Parallel," *IEEE Transactions on Industrial Electronics,* vol. 60, no. 4, pp. 1281-1290, 2013.

[8]   E. Romero-Cadaval, G. Spagnuolo, L. Garcia Franquelo, C. A. Ramos-Paja, T. Suntio, and W. M. Xiao, "Grid-connected photovoltaic generation plants: components and operation," *IEEE Industrial Electronics Magazine,* vol. 7, no. 3, pp. 6-20, 2013.

[9]   D. F. R. Fu, R. Margolis, M. Woodhouse, K. Ardani, "Solar Photovoltaic System Cost Benchmark: Q1 2017," USANREL/TP-6A20-68925, 2017, Available: https://www.nrel.gov/docs/fy17osti/68925.pdf, Accessed on: April 2019.

[10]   J. H. R. Enslin and P. J. M. Heskes, "Harmonic interaction between a large number of distributed power inverters and the distribution network," *IEEE Transactions on Power Electronics,* vol. 19, no. 6, pp. 1586-1593, 2004.

[11]   D. G. Infield, P. Onions, A. D. Simmons, and G. A. Smith, "Power quality from multiple grid-connected single-phase inverters," *IEEE Transactions on Power Delivery,* vol. 19, no. 4, pp. 1983-1989, 2004.

[12]   Y. Yang, K. Zhou, and F. Blaabjerg, "Current Harmonics From Single-Phase Grid-Connected Inverters -Examination and Suppression," *IEEE Journal of Emerging and Selected Topics in Power Electronics,* vol. 4, no. 1, pp. 221-233, 2016.

[13]   D. Gallo *et al.*, "Case studies on large PV plants: Harmonic distortion, unbalance and their effects," in *2013 IEEE Power & Energy Society General Meeting*, 2013, pp. 1-5.

[14]   T. Messo, J. Jokipii, A. Aapro, and T. Suntio, "Time and frequency-domain evidence on power quality issues caused by grid-connected three-phase photovoltaic inverters," in *2014 16th European Conference on Power Electronics and Applications*, 2014, pp. 1-9.

[15]   R. K. Varma, S. A. Rahman, T. Vanderheide, and M. D. N. Dang, "Harmonic Impact of a 20-MW PV Solar Farm on a Utility Distribution Network," *IEEE Power and Energy Technology Systems Journal,* vol. 3, no. 3, pp. 89-98, 2016.

[16] R. Langella, A. Testa, J. Meyer, F. Möller, R. Stiegler, and S. Z. Djokic, "Experimental-based evaluation of PV inverter harmonic and interharmonic distortion due to different operating conditions," *IEEE Transactions on Instrumentation and Measurement,* vol. 65, no. 10, pp. 2221-2233, 2016.

[17] P. Pakonen, A. Hilden, T. Suntio, and P. Verho, "Grid-connected PV power plant induced power quality problems - experimental evidence," in *2016 18th European Conference on Power Electronics and Applications*, 2016, pp. 1-10.

[18] R. Langella, A. Testa, S. Z. Djokic, J. Meyer, and M. Klatt, "On the interharmonic emission of PV inverters under different operating conditions," in *2016 17th International Conference on Harmonics and Quality of Power*, 2016, pp. 733-738.

[19] T. Ise, "Functions and Configurations of Quality Control Center on FRIENDS," in *Transmission and Distribution Conference and Exhibition: Asia Pacific. IEEE/PES*, 2002, vol. 1, pp. 590-595 vol.1.

[20] T. Dragicevic, J. C. Vasquez, J. M. Guerrero, and D. Skrlec, "Advanced LVDC electrical power architectures and microgrids: a step toward a new generation of power distribution networks," *Electrification Magazine, IEEE,* vol. 2, no. 1, pp. 54-65, 2014.

[21] S. Kai, Z. Li, X. Yan, and J. M. Guerrero, "A Distributed Control Strategy Based on DC Bus Signaling for Modular Photovoltaic Generation Systems With Battery Energy Storage," *IEEE Transactions on Power Electronics,* vol. 26, no. 10, pp. 3032-3045, 2011.

[22] R. S. Balog and P. T. Krein, "Bus Selection in Multibus DC Microgrids," *IEEE Transactions on Power Electronics,* vol. 26, no. 3, pp. 860-867, 2011.

[23] D. Salomonsson, L. Soder, and A. Sannino, "An Adaptive Control System for a DC Microgrid for Data Centers," *IEEE Transactions on Industry Applications,* vol. 44, no. 6, pp. 1910-1917, 2008.

[24] H. Kakigano, Y. Miura, T. Ise, and R. Uchida, "DC Micro-grid for Super High Quality Distribution - System Configuration and Control of Distributed Generations and Energy Storage Devices -," in *Power Electronics Specialists Conference. PESC. 37th IEEE*, 2006, pp. 1-7.

[25] P. Karlsson and J. Svensson, "DC bus voltage control for a distributed power system," *IEEE Transactions on Power Electronics,* vol. 18, no. 6, pp. 1405-1412, 2003.

[26] H. Kakigano, Y. Miura, T. Ise, and R. Uchida, "DC Voltage Control of the DC Micro-grid for Super High Quality Distribution," in *Power Conversion Conference - Nagoya*, 2007, pp. 518-525.

[27] H. Kakigano, Y. Miura, and T. Ise, "Low-Voltage Bipolar-Type DC Microgrid for Super High Quality Distribution," *IEEE Transactions on Power Electronics,* vol. 25, no. 12, pp. 3066-3075, 2010.

[28] R. Alsharif and M. Odavic, "Photovoltaic generators interfacing a DC micro-grid: design considerations for a double-stage boost power converter system," in *2016 18th European Conference on Power Electronics and Applications (EPE'16 ECCE Europe)*, 2016, pp. 1-10.

[29] R. Alsharif, M. Odavic, and K. Atallah, "Active suppression of photovoltaic system related harmonics in a DC microgrid," in *2017 IEEE Energy Conversion Congress and Exposition (ECCE)*, 2017, pp. 1594-1601.

[30] A. Sangwongwanich, Y. Yang, D. Sera, and F. Blaabjerg, "Interharmonics from grid-connected PV systems: Mechanism and mitigation," in *2017 IEEE 3rd International Future Energy Electronics Conference and ECCE Asia (IFEEC 2017 - ECCE Asia)*, 2017, pp. 722-727.

[31]   A. Sangwongwanich, Y. Yang, D. Sera, H. Soltani, and F. Blaabjerg, "Analysis and Modeling of Interharmonics from Grid-Connected Photovoltaic Systems," *IEEE Transactions on Power Electronics,* pp. 8353-8364, 2018.

[32]   *Your Guide to Renewable Energy*. Available: http://www.renewable-energysources.com/

[33]   J. A. Gow and C. D. Manning, "Development of a photovoltaic array model for use in power-electronics simulation studies," *IEE Proceedings -Electric Power Applications,* vol. 146, no. 2, pp. 193-200, 1999.

[34]   M. G. Villalva, J. R. Gazoli, and E. R. Filho, "Comprehensive Approach to Modeling and Simulation of Photovoltaic Arrays," *IEEE Transactions on Power Electronics,* vol. 24, no. 5, pp. 1198-1208, 2009.

[35]   A. Chatterjee, A. Keyhani, and D. Kapoor, "Identification of Photovoltaic Source Models," *IEEE Transactions on Energy Conversion,* vol. 26, no. 3, pp. 883-889, 2011.

[36]   R. F. Coelho, F. Concer, and D. C. Martins, "A proposed photovoltaic module and array mathematical modeling destined to simulation," in *IEEE International Symposium on Industrial Electronics*, 2009, pp. 1624-1629.

[37]   G. Walker, "Evaluating MPPT Converter Topologies Using a MATLAB PV Model," *Australia Journal of Electrical & Electronics Engineering,* vol. 21, no. 2001, pp. 49-56.

[38]   N. Femia, G. Petrone, G. Spagnuolo, and M. Vitelli, *Power electronics and control techniques for maximum energy harvesting in photovoltaic systems* (Industrial Electronics Series). U.S.: Taylor & Francis Group, 2013.

[39]   N. Femia, G. Petrone, G. Spagnuolo, and M. Vitelli, "Optimization of perturb and observe maximum power point tracking method," *IEEE Transactions on Power Electronics,* vol. 20, no. 4, pp. 963-973, 2005.

[40]   W. Xiao, W. G. Dunford, P. R. Palmer, and A. Capel, "Regulation of Photovoltaic Voltage," *IEEE Transactions on Industrial Electronics,* vol. 54, no. 3, pp. 1365-1374, 2007.

[41]   M. G. Villalva, T. G. de Siqueira, and E. Ruppert, "Voltage regulation of photovoltaic arrays: small-signal analysis and control design," *IET Power Electronics,* vol. 3, no. 6, pp. 869-880, 2010.

[42]   www.sharp.co.uk. SHARP NU Series 245W, 240W and 235W [Online]. Available: http://www.sharp.co.uk/cps/rde/xchg/gb/hs.xsl/-/html/product-details.htm?product=NUE240J5&cat=46000

[43]   T. Esram and P. L. Chapman, "Comparison of photovoltaic array maximum power point tracking techniques," *IEEE Transactions on Energy Conversion,* vol. 22, no. 2, pp. 439-449, 2007.

[44]   W. Xiao and W. G. Dunford, "A modified adaptive hill climbing MPPT method for photovoltaic power systems," in *2004 IEEE 35th Annual Power Electronics Specialists Conference*, 2004, vol. 3, pp. 1957-1963.

[45]   R. Haroun, A. El Aroudi, A. Cid-Pastor, G. Garica, C. Olalla, and L. Martinez-Salamero, "Impedance Matching in Photovoltaic Systems Using Cascaded Boost Converters and Sliding-Mode Control," *IEEE Transactions on Power Electronics,* vol. 30, no. 6, pp. 3185-3199, 2015.

[46]   D. P. Hohm and M. E. Ropp, "Comparative study of maximum power point tracking algorithms using an experimental, programmable, maximum power point tracking test bed," in *2000 Conference Record of the Twenty-Eighth IEEE Photovoltaic Specialists Conference*, 2000, pp. 1699-1702.

[47]   K. Ishaque, Z. Salam, M. Amjad, and S. Mekhilef, "An improved particle swarm optimization (PSO)-based MPPT for PV with reduced steady-state

oscillation," *IEEE Transactions on Power Electronics,* vol. 27, no. 8, pp. 3627-3638, 2012.

[48] K. H. Hussein, I. Muta, T. Hoshino, and M. Osakada, "Maximum photovoltaic power tracking: an algorithm for rapidly changing atmospheric conditions," *IEE Proceedings - Transmission and Distribution Generation,* vol. 142, no. 1, pp. 59-64, 1995.

[49] A. M. Bazzi and P. T. Krein, "Concerning "maximum power point tracking for photovoltaic optimization using ripple-based extremum seeking control"," *IEEE Transactions on Power Electronics,* vol. 26, no. 6, pp. 1611-1612, 2011.

[50] P. Verma, P. Mahajan, and R. Garg, "Comparison of intelligent and conventional MPPT algorithms for PhotoVoltaic system under partially shaded conditions," in *2017 Recent Developments in Control, Automation & Power Engineering (RDCAPE)*, 2017, pp. 505-510.

[51] D. Roche, H. Outhred, and R. J. Kaye, "Analysis and control of mismatch power loss in photovoltaic arrays," *Progress in Photovoltaics: Research and Applications,* vol. 3, no. 2, pp. 115-127, 1995.

[52] Y. H. Ji, D. Y. Jung, C. Y. Won, B. K. Lee, and J. W. Kim, "Maximum power point tracking method for PV array under partially shaded condition," in *2009 IEEE Energy Conversion Congress and Exposition*, 2009, pp. 307-312.

[53] S. B. Kjaer, J. K. Pedersen, and F. Blaabjerg, "A review of single-phase grid-connected inverters for photovoltaic modules," *IEEE Transactions on Industry Applications,* vol. 41, no. 5, pp. 1292-1306, 2005.

[54] Q. Li and P. Wolfs, "A Review of the Single Phase Photovoltaic Module Integrated Converter Topologies With Three Different DC Link Configurations," *IEEE Transactions on Power Electronics,* vol. 23, no. 3, pp. 1320-1333, 2008.

[55] N. Femia, G. Lisi, G. Petrone, G. Spagnuolo, and M. Vitelli, "Distributed Maximum Power Point Tracking of Photovoltaic Arrays: Novel Approach and System Analysis," *IEEE Transactions on Industrial Electronics,* vol. 55, no. 7, pp. 2610-2621, 2008.

[56] E. Roman, R. Alonso, P. Ibanez, S. Elorduizapatarietxe, and D. Goitia, "Intelligent PV Module for Grid-Connected PV Systems," *IEEE Transactions on Industrial Electronics,* vol. 53, no. 4, pp. 1066-1073, 2006.

[57] G. R. Walker and P. C. Sernia, "Cascaded DC-DC converter connection of photovoltaic modules," *IEEE Transactions on Power Electronics,* vol. 19, no. 4, pp. 1130-1139, 2004.

[58] B. Burge, B. Goeldi, S. Rogalla, and H. Schmidt, "Module Integrated Electronics – An Overview," in *25th European Photovoltaic Solar Energy Conference and Exhibition*, 2010, pp. 3700–3707.

[59] W. Li and X. He, "Review of nonisolated high-step-up DC/DC converters in photovoltaic grid-connected applications," *IEEE Transactions on Industrial Electronics,* vol. 58, no. 4, pp. 1239-1250, 2011.

[60] R. Haroun, A. El Aroudi, A. Cid-Pastor, and L. Martinez-Salamero, "Stability issues in cascade connected switching converters for DC microgrid applications," in *IEEE International Symposium on Circuits and Systems (ISCAS)*, 2013, pp. 1324-1327.

[61] G. R. Walker and J. C. Pierce, "Photovoltaic DC-DC module integrated converter for novel cascaded and bypass grid connection topologies - Design and optimization," in *2006 37th IEEE Power Electronics Specialists Conference*, 2006, pp. 1-7.

[62] F. Mocci and M. Tosi, "Comparison of power converter technologies in photovoltaic applications," in *Electrotechnical Conference*, 1989, pp. 11-15.

[63] G. R. Walker and P. C. Sernia, "Cascaded DC-DC converter connection of photovoltaic modules," in *IEEE 33rd Annual Power Electronics Specialists Conference*, 2002, vol. 1, pp. 24-29 vol.1.

[64] X. Weidong, N. Ozog, and W. G. Dunford, "Topology study of photovoltaic interface for maximum power point tracking," *IEEE Transactions on Industrial Electronics,* vol. 54, no. 3, pp. 1696-1704, 2007.

[65] T. Dragicevic, X. Lu, J. Vasquez, and J. Guerrero, "DC Microgrids - Part I: A Review of Control Strategies and Stabilization Techniques," *IEEE Transactions on Power Electronics,* vol. PP, no. 99, pp. 1-1, 2015.

[66] A. Alfergani, K. A. Alfaitori, A. Khalil, and N. Buaossa, "Control strategies in AC microgrid: A brief review," in *2018 9th International Renewable Energy Congress (IREC)*, 2018, pp. 1-6.

[67] S. K. Sahoo, A. K. Sinha, and N. K. Kishore, "Control Techniques in AC, DC, and Hybrid AC-DC Microgrid: A Review," *IEEE Journal of Emerging and Selected Topics in Power Electronics,* vol. 6, no. 2, pp. 738-759, 2018.

[68] X. Hui Guang, H. Jun Ping, Q. Yi, and L. Yang Hua, "Energy management and control strategy for DC micro-grid in data center," in *China International Conference on Electricity Distribution (CICED)*, 2012, pp. 1-6.

[69] Z. H. Jian, Z. Y. He, J. Jia, and Y. Xie, "A review of control strategies for DC micro-grid," in *Fourth International Conference on Intelligent Control and Information Processing (ICICIP)*, 2013, pp. 666-671.

[70] K. Sun, L. Zhang, Y. Xing, and J. M. Guerrero, "A Distributed Control Strategy Based on DC Bus Signaling for Modular Photovoltaic Generation Systems With Battery Energy Storage," *IEEE Transactions on Power Electronics,* vol. 26, no. 10, pp. 3032-3045, 2011.

[71] T. Messo, J. Jokipii, J. Puukko, and T. Suntio, "Determining the Value of DC-Link Capacitance to Ensure Stable Operation of a Three-Phase Photovoltaic Inverter," *IEEE Transactions on Power Electronics,* vol. 29, no. 2, pp. 665-673, 2014.

[72] N. Femia, G. Petrone, G. Spagnuolo, and M. Vitelli, "A Technique for Improving P&O MPPT Performances of Double-Stage Grid-Connected Photovoltaic Systems," *IEEE Transactions on Industrial Electronics,* vol. 56, no. 11, pp. 4473-4482, 2009.

[73] A. Urtasun, P. Sanchis, and L. Marroyo, "Adaptive Voltage Control of the DC/DC Boost Stage in PV Converters With Small Input Capacitor," *IEEE Transactions on Power Electronics,* vol. 28, no. 11, pp. 5038-5048, 2013.

[74] R. W. Erickson and D. Maksimović, *Fundamentals of Power Electronics*, 2nd ed. Boston, Mass., 2001.

[75] M. K. Kazimierczuk, *Pulse-Width Modulated DC-DC Power Converters*, 2nd ed. Chichester, UK: John Wiley & Sons, 2016.

[76] H. Sira-Ramírez and R. Silva-Ortigoza, *Control Design Techniques in Power Electronics Devices* (Power Systems). London: Springer, 2006.

[77] G. Petrone, G. Spagnuolo, R. Teodorescu, M. Veerachary, and M. Vitelli, "Reliability Issues in Photovoltaic Power Processing Systems," *IEEE Transactions on Industrial Electronics,* vol. 55, no. 7, pp. 2569-2580, 2008.

[78] A. Capel, J. C. Marpinard, J. Jalade, and M. Valentin, "Current Fed and Voltage Fed Switching DC/DC Converters - Steady State and Dynamic Models their Applications in Space Technology," in *Fifth International Telecommunications Energy Conference*, 1983, pp. 421-430.

[79] K. Siri, "Study of system instability in solar-array-based power systems," *Aerospace and Electronic Systems, IEEE Transactions on,* vol. 36, no. 3, pp. 957-964, 2000.

[80] J. Leppaaho and T. Suntio, "Characterizing the Dynamics of the Peak-Current-Mode-Controlled Buck-Power-Stage Converter in Photovoltaic Applications," *IEEE Transactions on Power Electronics,* vol. 29, no. 7, pp. 3840-3847, 2014.

[81] M. Sitbon, J. Leppaaho, T. Suntio, and A. Kuperman, "Dynamics of Photovoltaic-Generator-Interfacing Voltage-Controlled Buck Power Stage," *IEEE Journal of Photovoltaics,* vol. 5, no. 2, pp. 633-640, 2015.

[82] J. Viinamaki, J. Jokipii, T. Messo, T. Suntio, M. Sitbon, and A. Kuperman, "Comprehensive dynamic analysis of photovoltaic generator interfacing DC-DC boost power stage," *IET Renewable Power Generation,* vol. 9, no. 4, pp. 306-314, 2015.

[83] K. Ogata, *Modern Control Engineering*, 5th ed. London: Pearson, 2010.

[84] X. Zhu, Y. Zhang, and J. Yang, "A voltage ripple suppression method of DC microgrid under unbalanced load," in *2017 20th International Conference on Electrical Machines and Systems (ICEMS)*, 2017, pp. 1-5.

[85] X. Cao, Q. C. Zhong, and W. L. Ming, "Ripple eliminator to smooth DC-bus voltage and reduce the total capacitance required," *IEEE Transactions on Industrial Electronics,* vol. 62, no. 4, pp. 2224-2235, 2015.

[86] H. Li, K. Zhang, and H. Zhao, "Active DC-link power filter for single phase PWM rectifiers," in *8th International Conference on Power Electronics - ECCE Asia*, 2011, pp. 2920-2926.

[87] D. Chen and L. Xu, "Autonomous DC voltage control of a DC microgrid with multiple slack terminals," *IEEE Transactions on Power Systems,* vol. 27, no. 4, pp. 1897-1905, 2012.

[88] E. Jamshidpour, B. Nahid-Mobarakeh, P. Poure, S. Pierfederici, F. Meibody-Tabar, and S. Saadate, "Distributed active resonance suppression in hybrid DC power systems under unbalanced load conditions," *IEEE Transactions on Power Electronics,* vol. 28, no. 4, pp. 1833-1842, 2013.

[89] L. Guo, S. Zhang, X. Li, Y. W. Li, C. Wang, and Y. Feng, "Stability analysis and damping enhancement based on frequency-dependent virtual impedance for DC microgrids," *IEEE Journal of Emerging and Selected Topics in Power Electronics,* vol. 5, no. 1, pp. 338-350, 2017.

[90] Z. Zhao, P. Yang, Y. Wang, Z. Xu, and J. M. Guerrero, "Dynamic characteristics analysis and stabilization of PV-based multiple microgrid clusters," *IEEE Transactions on Smart Grid,* vol. PP, no. 99, pp. 1-1, 2017.

[91] D. Boroyevich, I. Cvetkovic, D. Dong, R. Burgos, W. Fei, and F. Lee, "Future Electronic Power Distribution Systems - a Contemplative View -," in *12th International Conference on Optimization of Electrical and Electronic Equipment*, 2010, pp. 1369-1380.

[92] (2012). *Gide to the installation of photovoltaic system*. Available: https://www.microgenerationcertification.org/images/PV%20Book%20ELECTRONIC.pdf

[93] M. A. Farahat, H. M. B. Metwally, and A. A. Mohamed, "Optimal Choice and Design of Different Topologies of DC–DC Converter Used in PV Systems, at Different Climatic Conditions in Egypt," *Renewable Energy,* vol. 43, pp. 393-402, 2012.

[94] N. D. Benavides and P. L. Chapman, "Boost Converter with a Reconfigurable Inductor," in *IEEE Power Electronics Specialists Conference (PESC)*, 2007, pp. 1695-1700.

[95] T. Messo, J. Jokipii, and T. Suntio, "Steady-state and dynamic properties of boost-power-stage converter in photovoltaic applications," in *Power Electronics for Distributed Generation Systems (PEDG), 2012 3rd IEEE International Symposium on*, 2012, pp. 34-40.

APPENDIX A: Photovoltaic Generators Interfacing a DC Micro-Grid: Design Considerations for a Double-Stage Boost Power Converter System

Photovoltaic Generators Interfacing a DC Micro-Grid: Design Considerations for a Double-Stage Boost Power Converter System

R. Alsharif, Student Member, IEEE, M. Odavic, Fellow Member, IEEE

The University of Sheffield
Department of Electronic and Electrical Engineering
Sir Fredrick Mappin Building, Mappin Street,
Sheffield S1 3JD, UK
ryaalsharif1@sheffield.ac.uk , m.odavic@sheffield.ac.uk

Keywords: «Double-stage dc-dc converter», «Photovoltaic», «Stability», «DC micro-grid».

Abstract: A photovoltaic generator (PVG) is usually connected to a DC micro-grid via a multi-stage-step-up power converter to improve system modularity, minimise shading effects and boost PVG voltage. Under varying operating conditions, the nonlinear characteristics of a PVG may affect performance of the entire PVG system. Further, if these issues are not properly taken into account at the design stage, significant changes in system dynamics may risk stability of the system. Therefore, it is important to understand interactions between a PVG and the rest of the system. A clear understanding of these interactions can help to set system design recommendations and guidelines. In particular, this paper explores the effects of a nonlinear PVG source interfacing a double-stage conventional boost converter connected to a DC bus. It addresses the impact of these effects on the design of both the power circuit and the control loops. Finally, this paper provides system design recommendations to ensure stability under varying operating conditions.

1. Introduction

Burning fossil fuels has been identified as a primary cause of global warming which has led to a number of environmental and socio-economic problems. To address these issues, governments around the world have set targets in generating electricity from clean resources such as wind, solar, geothermal, hydroelectric and fuel cells. Among these resources, over the last few years the installed capacity of solar PV generators have experienced huge growth due to their improved efficiency and reduced cost per watt [1].These improvements make solar energy one of the most promising renewable sources in electricity generation. Of note is that the main challenges in connecting distributed generators (DGs) to the main grid are: synchronization, harmonics, voltage rise, circulating current and instability caused mainly by an increased number of connected DGs. That being the case, an AC micro-grid has been proposed as a new paradigm for connecting DGs to the main power network [2, 3] and significant work has been made to improve their performance [4, 5]. However, power quality is still an ongoing issue in AC micro-grids, especially for very sensitive power loads. The author in [6] proposed a DC micro-grid as a possible configuration to meet the needs of customers' power quality, since when DC micro-grids have received more attention in the research community. Many studies have been devoted to DC micro-grids where they have been recognized not only for providing high power quality but also for many other advantages such as a smaller system, higher efficiency and a simple control structure [6].

This paper focuses on the generation side of the DC micro-grid, and in particular when using the PVG as a primary DG. The standardization of the DC micro-grid goes towards adopting 380-400 V as the nominal voltage for the main DC bus where all DG sources are connected to it. Low PVG voltage (30-48V) can be boosted by one of three ways: I) connecting many PVG modules in series; II) connecting PVG modules in parallel through single-stage high-step-up converter type; III) connecting PVG modules in parallel through a double-stage step-up converter. These different system configurations for interfacing a PVG system to a DC micro-grid are discussed in Section 2 below.

Conventionally, PVG converters are chosen based on 70% of the rated power of the PVG system. The rationale behind the downsizing of the converter is to reduce its cost. However, this approach results

in reduced efficiency of energy harvesting at the high solar irradiations. In this case, the design procedure for optimal selection of converter parameters (i.e. inductance L and capacitance C) is based on considering only 70% of the nominal power of the PVG under the maximum current ripple condition [7, 8]. In [8] for the boost converter design a duty cycle of 0.5 is selected, because the maximum current ripple condition occurs when the output voltage is twice the input voltage. This conventional design procedure does not report on the limitation of the output voltage due to the maximum power point tracking (MPPT) controller, or the effect of different weather conditions on choosing optimal values for L and C. The authors in [9] has considered the MPPT limitation and the effect of weather conditions on choosing the converter parameters, but the analysis is restricted only to stand-alone applications (i.e. resistive load at the output). In grid-connected mode applications, the PVG system is connected to a regulated DC bus which implies a fixed level of voltage at the output to be considered for converter design. Moreover, connecting a PVG to a DC micro-grid requires a high conversion ratio which has to be taken into account when designing the power-stage. The design considerations of PV-interfaced power converters when connected to a DC micro-grid are not well documented in the literature, and therefore discussed in this paper.

For PVG systems interfacing a DC micro-grid, the literature focuses on improving MPP tracking algorithms [10], proposing new topologies to increase system efficiency or to reduce the cost [11], suggesting different controllers arrangements to ensure high performance at both grid-connected and islanded modes [12] and highlighting stability issues that occur in DC micro-grids due to constant power loads. However, the interactions between the non-linear PVG sources and the rest of the system, which may affect the system performance and stability, are not well documented. A clear understanding of these interactions can help to set system design recommendations and guidelines for the PVG power-stage interfacing a DC micro-grid, and for this reason these issues are investigated in this paper.

2. System Configuration

It is generally agreed that a future DC system should be formed as multiple buses with different voltage levels. The main bus with most of DGs connected to it, is suggested as having a regulated voltage level in the range of 380-400V, since this voltage level can meet the industry standard for consumer electronics with the power factor correction circuit at the input [12, 13]. Also, this voltage level offers good efficiency when supplying high-demanding loads (e.g. hybrid electric vehicle chargers, washing machines) [12]. The PVG low voltage output (around 30-48V) is usually connected to the high voltage DC bus (~400V). The most common configuration connects multiple PVG modules in series to a centralized MPPT power converter [1]. The main disadvantage of this configuration is very sensitive to mismatching phenomena which increase the system losses. Also, the centralized MPPT may induce increased power losses resulting in poor overall system efficiency. To overcome the drawbacks of mismatching and MPPT low efficiency, nowadays an alternative PVG system structure called Distributed MPPT (DMPPT) is widely adopted [10]. It is based on dedicating an MPPT DC/DC converter for each PVG module. In the rest of this paper, a PVG module with its dedicated MPPT converter will be referred to as a Self-Controlled Photovoltaic Module (SCPVM). A series connection of multiple SCPVMs can be directly connected to the DC micro-grid. The drawback of this configuration is that under a mismatching condition there is difficulty in achieving the desired output voltage of some SCPVMs. This is because voltage across each SCPVM depends on the ratio of its output power with respect to the total output power of the whole string [10]. To solve this problem an advanced and more complex control structure is necessary, or a parallel configuration adopted instead.

In the parallel configuration, the SCPVMs are connected in parallel to the main DC bus. The main disadvantage of this topology is the requirements set on a DC/DC converter to fulfil two contrasting requirements: a high-step-up voltage conversion ratio (about 10-15) and a high conversion efficiency [10]. That being the case, a significant number of research papers have been focused on achieving these requirements for a single-stage-power conversion system, with different solutions proposed in [11]. Another approach to boost the voltage is by using a double-stage-power conversion [11]. In this configuration, the conventional boost converter can be used for each stage. Choosing between the

2

single-stage and the double-stage power conversion is normally based on its capability to provide high-step-up voltage, high efficiency, low cost, simplicity, high MPPT efficiency and high MPP tracking speed. The single-stage conversion topology is superior in its efficiency but the dynamic performance of the MPPT with the new proposed single-stage topologies has not been proven so far. However, in the case of double-stage based on using conventional boost converter, a high MPPT efficiency has been proven [10] and achieving high tracking speed is easy due to the simple structure of the boost converter.

The parallel configuration with double-stage boost converter is adopted in this paper as it offers advantages in boosting the voltage, minimizing shading effects, improving system modularity, improving MPPT performance and efficiency, and providing the same voltage level at the output of each SCPVM under mismatching conditions. The full system configuration is shown in Figure 1. The system consists of many SCPVMs connected in parallel. Each SCPVM consists of a DC/DC boost converter, a PV generator (i.e. PVG NU-E240) and a MPPT digital controller. In this paper, the controllers' implementation is based on the assumption that the DC micro-grid is in grid-connected mode or in islanded mode where the storage system is large enough to allow MPP tracking all the time. The first-stage converter's controller is responsible for MPP tracking (i.e. direct duty cycle perturbation and observation P&O method is adopted) and the second-stage converter's controller controls the DC-link voltage V_{dc}. The DC micro-grid voltage (V_{grid}=400V) is controlled either by the bidirectional AC/DC inverter which connects the DC micro-grid to the main AC network, or by the storage system converter. The second stage DC/DC converter is responsible for boosting the V_{dc} voltage to the DC micro-grid voltage (V_{grid}=400V).

The technical specifications of the PVG

NU-E240 (J5)	
Quantity and wiring cells in series	60
Maximum Power	240 Wp
Open Circuit Voltage	37.3 V
Short Circuit Current	8.63 A
Standard Operation Condition	25 °C
Voltage Maximum Power (V_{MPP})	30.2 V
Current Maximum Power (I_{MPP})	7.95 A
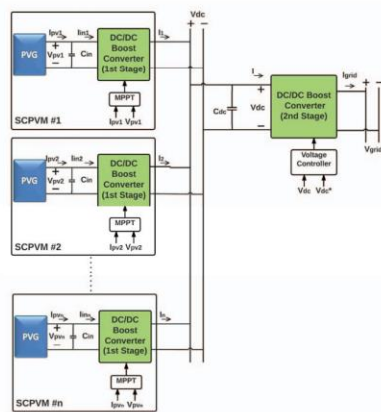
Figure 1: System Configuration, PVG interfaced DC micro-grid

The data and the simulation results in this paper are obtained from a simplified system; the case when the system has only one SCPVM. However, the system can be scaled up for a higher power rating simply by increasing the number of parallel SCPVMs, and increasing the power rating of the second stage converter. The first-stage converter of the SCPVM does not need to be re-designed if identical PVG panels are used.

3. Design Considerations of double-stage DC-DC Boost Converter

There are two key points to be considered when designing the first-stage converter, namely the limitation on the output voltage to ensure the MPPT is functioning under all weather conditions and the effect of changes in weather conditions and output voltage on the converter parameters.

The first-stage boost DC/DC converter is controlled by an MPPT algorithm to track the maximum power available, and to adjust the duty cycle of the converter accordingly. The required duty cycle

(D_{MPP}) for the boost converter to obtain the maximum power from the PV array can be found from the basic boost voltage gain equation in [14].

$$\frac{V_{out}}{V_{in}} = \frac{1}{1-D} \tag{1}$$

If the system operates at MPP, the PVG voltage will be $V_{in} = V_{mpp}^{STC}$ and if the output voltage is regulated, then the output voltage V_{out} will be constant. Assuming a converter efficiency of 100% (*i.e.* $P_{in} = P_{mpp} = P_{out}$), the duty cycle is given by:

$$D_{mpp} = 1 - \frac{V_{mpp}^{STC}}{V_{out}} \tag{2}$$

Under different solar irradiation and constant temperature conditions, V_{mpp} changes very slightly and can be assumed to be constant (equal to V_{mpp}^{STC}). This means that both the input voltage and the output voltage of the boost converter are constant, thus the duty cycle will not change as the irradiation changes. This makes the design of the converter easier. The situation will be different if the effect of changing the cell temperature is included because V_{mpp} will not be constant in this case. Figure 2(a) shows the required duty cycle for the highest and lowest irradiation to achieve the maximum power
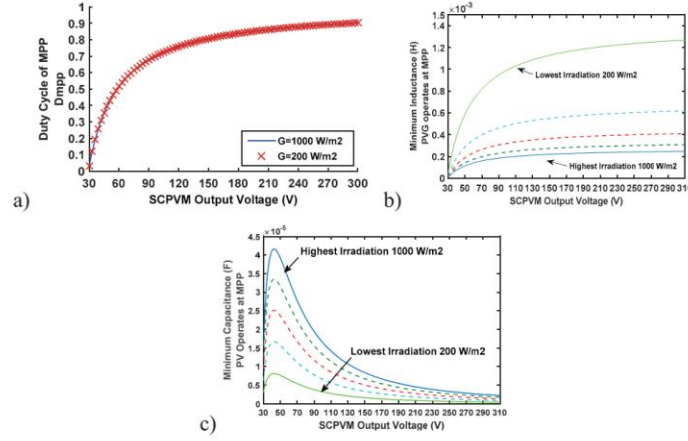

Figure 2: Effect of SCPVM voltage and solar irradiation (1000 W/m²-200 W/m²) on the first stage converter design: (a) Duty cycle (b) Inductance size for 13% current ripple (c) Capacitance size for 1% voltage ripple.

point for a given constant output voltage. It shows that the duty cycle is the same for different irradiation conditions and it hits its maximum defined limit of $D_{max} = 0.9$ at 290V. Therefore, for the tested system under constant temperature conditions, the output voltage limit is given by:

$$V_{mpp}^{STC} < V_{out} < \frac{V_{mpp}^{STC}}{1-D_{max}} \tag{3}$$

and

$$29\,V < V_{out} < 290\,V \tag{4}$$

First-stage converter design and its parameters (i.e. inductance L and capacitance C) selection will be analysed considering the output voltage range in (4). The minimum inductance L_{min} of the first stage converter can be found from the following equation [14]:

$$L_{min} = \frac{V_{in} \cdot D_{MPP}}{\Delta I_{p-p} \cdot f_{sw}} \tag{5}$$

4

In general, the current ripple ΔI_{p-p} in (5) can be selected based on the minimum current ripple requirement for the highest PV input current (i.e. the highest irradiation) or for the lowest input current (i.e. the lowest irradiation). Figure 2(b) shows the effect of changing the solar irradiation and SCPVM output voltage on L_{min}. Low solar irradiation conditions present the worse-case design requirement. However, other factors have to be considered such as the inductance core size, power production, and its effect on the speed of the MPPT controller in deciding which operating point to use for the design. If L is designed based on the highest irradiation, the result is smaller inductance than for the lowest irradiation as shown in Figure 2(b). In this case the core size will be smaller [15] and the MPP tracking is faster [10]. However, two key drawbacks can be identified. First, at lower solar irradiation the current ripple amplitude accounts for the higher percentage of the total current and thus the power production of the PV panel will be lower than in the case if the higher inductance were used [15]. Second, under the conditions of low input current (i.e. low solar irradiation) the converter might operate in discontinuous conduction mode (DCM). If L is designed based on the lowest irradiation the higher inductance is needed and more power will be extracted at the low irradiation levels [15]. However, for this case the core size has to be designed for the highest current to avoid magnetic saturation.

The inductance is one of the factors that affects the MPPT sampling rate. A smaller inductance will result in the faster MPPT for the same input capacitance [10]. Aiming for the faster MPPT and small inductance core, high irradiation is used for designing L. DCM can be avoided by opting for the current ripple to be less than twice the minimum current at the lowest irradiation.

The capacitance can be found from equation (6) [14]. The effect of the irradiation level and the SCPVM output voltage on the capacitance size is shown in Figure 2(c) for peak to peak voltage ripple requirements v_r of 1%. The highest irradiation level presents the worst case scenario.

$$C_{min} = \frac{I_{out}\, D_{MPP}}{v_r \cdot f_{sw}} \tag{6}$$

Figure 2(c) shows that increasing the output voltage will reduce the required capacitance; however, this will increase the duty cycle which affects the inductor copper losses and the semiconductor conduction losses [14]. Also, going back to the inductance design, increasing the output voltage will increase the inductance size. Another point that has to be considered when choosing the capacitance is the chosen PVG configuration. As example, in case of series connection of SCPVM, the voltage across each SCPVM will vary randomly due to the non-uniform solar irradiation [10]. Therefore, in order to meet the minimum voltage ripple requirement the worst case operating condition has to be considered in the design of C_{dc}. This limitation is not applied in the case of parallel connections which give more flexibility in choosing C_{dc} depending on the regulated DC-link voltage.

The proposed double-stage boost converter requires a conversion ration to be not less than 14 to boost the voltage from 29V to 400V. Splitting this conversion ratio between the two converter stages will guarantee better performance and avoid that one of the converters operating at a very high conversion ratio. The converter of the SCPVM has been designed with a conversion ratio of 3.5 and output voltage of 100V. Therefore, the inductance (L_1) and the capacitance (C_{dc}) are chosen as 200 µH and 41 µF, respectively. The second-stage converter is designed for a conversion ratio of 4 and its parameters (L_2 & C_o) are selected so that the peak-peak output voltage (V_{grid}) ripple is less than 1.5V and the peak-peak current ripple is 20% of the input current, in the case when the SCPVM operates under the highest solar irradiation.

4. The Effect of PVG on the Controller Performance

The controller structure of the system operating at MPP mode is shown in Figure 3(a). MPPT's parameters (sampling period T_{mpp} and the amplitude of the duty-cycle perturbation Δd) has been optimized based on [16]. A PID controller (7) is used for controlling the dc-link voltage.

$$G_c(s) = \frac{K_v}{s} \frac{\left(1+\frac{s}{\omega_{z1}}\right)\left(1+\frac{s}{\omega_{z2}}\right)}{\left(1+\frac{s}{\omega_{p1}}\right)\left(1+\frac{s}{\omega_{p2}}\right)} \tag{7}$$

5

The controller is designed by considering an ideal current source at the input of the second-stage converter as shown in Figure 3(b). The transfer function of the duty-cycle-to-dc-link voltage $G_{v_{dc}d_2}$ of the second-stage is:

$$G_{v_{dc}d_2}(s) = \frac{\bar{v}_{dc}}{\bar{d}_2} = -\frac{V_{grid}}{L_2 C_{dc}} \frac{1 + r_{C_{dc}} C_{dc} s}{s^2 + \frac{r_{l2} + r_{C_{dc}}}{L_2}s + \frac{1}{L_2 C_{dc}}} \tag{8}$$
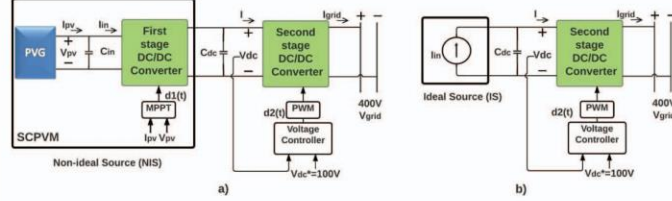
Figure 3: Controller structure of the simplified system. (a) non-ideal source configuration, (b) ideal source configuration.

A switching model of the double-stage boost converter connected to a 400V grid is implemented in MATLAB Simulink. The PVG NU-E240 is modelled using the single diode model. The simulation parameters for the P&O controller and the first-stage and second-stage converters are listed in Table I. The designed PID controller is shown in (9). The cut-off frequency ω_c is tuned to 118k rad/s which gives a phase margin of PM$\cong$66° and a gain margin of GM=105dB.

$$G_c(s) = \frac{-197}{s} \frac{\left(1 + \frac{s}{1904}\right)\left(1 + \frac{s}{5338.6}\right)}{\left(1 + \frac{s}{2e+07}\right)\left(1 + \frac{s}{3.142e+05}\right)} \tag{9}$$

Table I: Simulation Parameters

Parameter	First-stage converter							P&O		Second-stage conv.			
	C_{in}	r_{cin}	L_1	r_{l1}	C_{dc}	r_{cdc}	f_{sw}	T_{mpp}	Δd	L_2	C_o	r_{co}	f_{sw2}
Value	1.5	8	200	6.4	41	1.2	100	60	0.02	1.5	4	12	100
Unit	μF	$m\Omega$	μH	$m\Omega$	μF	$m\Omega$	kHz	μs	-	mH	μF	$m\Omega$	kHz

Figure 4 shows the analytical and simulation results for the control loop $T = G_c(s) \cdot G_{v_{dc}d_2}(s) \cdot G_{PWM}(s)$ for the system with ideal-source IS (Figure 3(b)) and with non-ideal source NIS (i.e. with SCPVM) under the conditions of solar irradiation changes. The figure shows that with the NIS as an input, the system is well damped at high solar irradiation, while the cut-off frequency and the PM are not affected.

Figure 5 shows the effect of the NIS when the PVG operating regions (i.e. constant voltage CV, constant current CC and MPP as shown in Figure 6) vary. In can be noted that the phase of the system is greatly affected at the low and medium frequencies. However, the phase is the same for all regions at high frequencies.

As seen in Figure 4 and 5 the high cut-off frequency has ensured the same system performance (the same phase and gain margins) under different operating conditions. However, this cut-off frequency is very high and might not be reasonable for real practical applications with higher power ratings. The switching frequency of the second-stage is chosen to be 100 kHz which allows very high cut-off frequency, though normally lower switching frequency is preferable to avoid high switching losses.

6
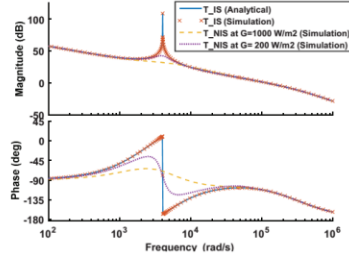
Figure 4: Effect of non-ideal source on the control loop. T_IS is the control loop gain with ideal current source. T_NIS is the control loop gain with non-ideal source. C_{dc}=41uF, V_{dc}=100V, V_{grid}=400V, and K_v=197. SCPVM operates at MPP.
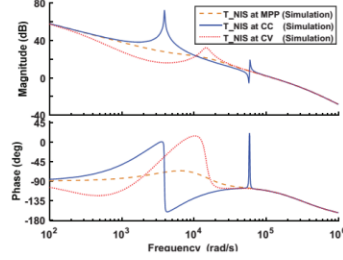
Figure 5: Effect of non-ideal source on the control loop when operating region changes. T_NIS is the control loop with non-ideal source. C_{dc}=41uF, V_{dc}=100V, V_{grid}=400V, K_v=197 and G=1000 W/m2.

For these reasons ω_c is decreased by reducing the voltage gain K_v. Then the effect of the NIS source on the control loop gain at different operating regions is again examined. The control loop gain results after reducing ω_c to 12.7k rad/s are depicted in Figure 7. It shows that the system cut-off frequency and PM are affected as the operating region changes. In this paper the area of particular interest is the MPP region. It can be observed that in MPP mode, the system PM improves as K_v decreases which in return enhances system stability. The PM of the system in MPP mode has been measured from simulations for three different values of K_v as listed in Table II.

Table II: Simulation results for the phase margin PM as ω_c reduced. The system operates at MPP mode and C_{dc} is 41 µF.

| K_v	ω_c(k.rad/se	PM
197	118	66°
15	12.7	103°
6	2.6	106°
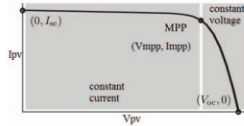
Figure 6: The three operating regions of PVG
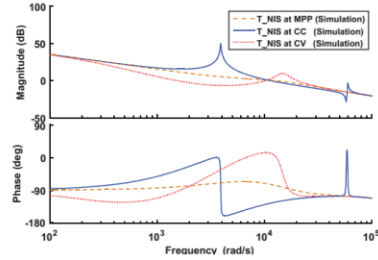
Figure 7: Effect of non-ideal source on the control loop gain when ω_c is reduced. C_{dc}=41uF, Vdc=100V, V_{grid}=400V and K_v=15. At MPP (V_{pv}=29V), CV (V_{pv}=35V), and CC (V_{pv}=19V).

5. The Minimum DC-link Capacitance

Figure 8 shows the DC-link and grid currents for two different values of C_{dc} (i.e. for 70 µF and 20 µF). From the results it can be observed that the harmonic currents injected into the DC link were increased as the size of C_{dc} was reduced. These harmonics are produced from the increased interactions between the two converters as the DC-link capacitance is reduced and under these conditions the P&O duty cycle perturbations of the SCPVM are seen as disturbances by the second-stage. In addition, Figure 9 shows the effect of different irradiation levels on the harmonic currents injected into the DC link.

7

Based on the above discussion, at specific values of C_{dc}, K_v and DC-link current the high-order harmonics might occur in the DC-link and that can cause chaotic behaviour and even loss of system stability. The critical values of C_{dc} for different Kv and irradiation values for the double-stage boost converter in MPP mode were identified from the simulations. Firstly, for different solar irradiations (G) and under specific voltage gain (K_v) the dc link capacitance C_{dc} is reduced in small steps until the system became unstable (at critical value $C_{dc\_min\_G}$). For this critical capacitance value the cut-off frequency of the control loop, $\omega_{c\_unstable\_G}$, was measured from the simulation. Of note is that the value of $C_{dc\_min\_G}$ changes as K_v changes. The minimum $C_{dc\_min\_G}$, for different irradiation and voltage gain levels, to ensure stable operation of the system was found to be defined by (10) which can be derived from the control loop gain T shown in Figure 10 and the steps provided in Appendix A.

$$C_{dc\_min\_G} = \frac{V_m K_v K_G}{L_2\, \omega_{z1}\, \omega_{z2}\, \omega_{c\_unstable\_G}} \tag{10}$$

where K_v is the dc gain of the voltage controller, K_G is the dc gain of $G_{v_{dc}d_2}$, $\omega_{c\_unstable\_G}$ is the cut-off frequency where the system becomes unstable at irradiation G, L_2 is the inductance of the second stage, ω_{z1} and ω_{z2} are the PID controller's zeros. The minimum required DC-link capacitance C_{dc} at MPP of a input-voltage-mode-controlled double-stage boost converter is depicted in Figure 11.
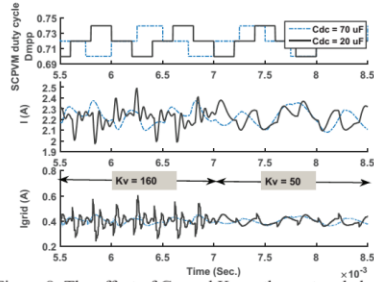

Figure 8: The effect of C_{dc} and K_v on the system behaviour: G=1000 W/m2, C_{dc}=20uF and 70uF, V_{dc}*=100 V, V_{grid}=400V, T_{mpp}=0.2ms, and K_v is changing from 160 to 50 at t=7ms
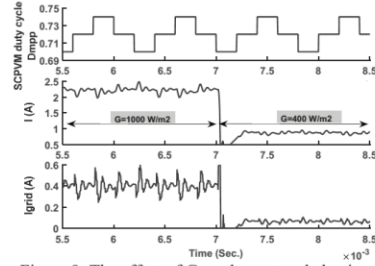

Figure 9: The effect of G on the system behaviour: G changes from1000 to 400 W/m2 at t=7ms, C_{dc}=20 uF, V_{dc}*=100 V, V_{grid}=400V, T_{mpp}=0.2ms, and K_v=160.
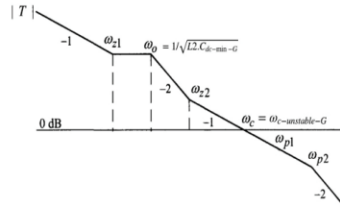

Figure 10: Asymptotic plot of the control loop gain magnitude.
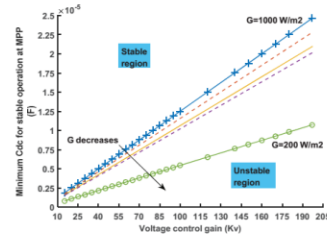
Figure 11: Stable operating regions of the double-stage boost converter

The unstable case, when SCPVM operates at MPP and insufficient value of C_{dc} (e.g. 20uF) is used with high solar irradiation (1000 W/m2) and K_v=197, is shown in Figure 12 and Figure 13. In Figure 12 it can be seen that after reducing K_v from 197 to 150 at t=7ms, the system stabilises. Figure 13 shows the effect on stability due to changes in irradiation; the system becomes stable by reducing the irradiation from 1000 W/m^2 to 400 W/m^2.

8
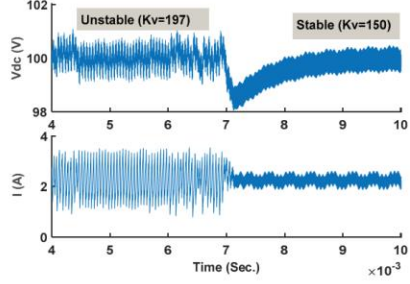
Figure 12: Stabilising the system by reducing Kv from 197 to 150 under the same solar irradiation. (HG=1000W/m2, Vdc=100V, Cdc=20 uF)
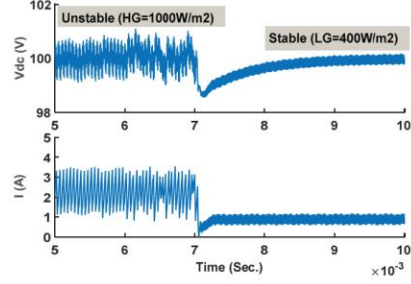
Figure 13: Effect of solar irradiation changes from HG=1000W/m2 to LG=400W/m2, Vdc=100V, Cdc=20uF, Kv=197

6. Conclusions

The design considerations of the double-stage boost converter for connecting a PVG to a DC micro-grid have been discussed. The available range of the DC-link voltage for successful tracking of MPP has been identified. The effect of that voltage range on the first-stage converter parameters under different weather condition is analysed. The converter parameters are chosen based on the highest solar irradiation condition to ensure high performance of the MPPT, small inductance core size and the required DC-link voltage ripple under different weather conditions.

Regarding the controller design, designers have to bear in mind that when operating at low or medium system bandwidth the cut-off frequency and PM are affected by the non-linear PVG source as the operating region changes due to weather conditions or load variations.

Minimizing the DC-link capacitance is preferable for system reliability, however it was shown in this paper that insufficient dc-link capacitance can lead to chaotic behaviour and even loss of system stability. To avoid this problem the minimum dc-link capacitance for stable operation of the double-stage boost-converter was identified under different solar irradiation levels and with different voltage gain of the second-stage converter.

Appendix A

The control loop gain (T) is

$$T = G_c(s).G_{v_{dc}d_2}(s).G_{PWM}(s) \tag{A1}$$

$G_{PWM}(s) = \frac{1}{V_m}$. Defining $K_G = -V_{grid}$ equation (A1) gives (A2):

$$T = \frac{K_v K_G}{V_m} \cdot \frac{1 + r_{C_{dc}} C_{dc} s}{L_2 C_{dc} s^2 + C_{dc}(r_{l2} + r_{C_{dc}})s + 1} \cdot \frac{\left(1 + \frac{s}{\omega_{z1}}\right)\left(1 + \frac{s}{\omega_{z2}}\right)}{\left(1 + \frac{s}{\omega_{p1}}\right)\left(1 + \frac{s}{\omega_{p2}}\right)} \tag{A2}$$

The resonance frequency ω_o at $\omega_{c\_unstable\_G}$ is $\frac{1}{\sqrt{L_2 C_{dc\_min\_G}}}$. From Figure 11 and equation (A2), the following relation is derived:

$$20 \log\left(\frac{K_v K_G / V_m}{\omega_{z1}}\right) - 40 \log\left(\frac{\omega_{z2}}{1/\sqrt{L_2 C_{dc\_min\_G}}}\right) - 20 \log\left(\frac{\omega_{c\_unstable\_G}}{\omega_{z2}}\right) = 0 \, dB \tag{A3}$$

Solving and re-arranging equation (A3) for $C_{dc\_min\_G}$ gives:

$$C_{dc\_min\_G} = \frac{V_m K_v K_G}{L_2 \, \omega_{z1} \, \omega_{z2} \, \omega_{c\_unstable\_G}} \tag{A4}$$

9

203

References

[1] E. Romero-Cadaval, G. Spagnuolo, L. Garcia Franquelo, C. A. Ramos-Paja, T. Suntio, and W. M. Xiao, "Grid-Connected Photovoltaic Generation Plants: Components and Operation," *IEEE Industrial Electronics Magazine,* vol. 7, pp. 6-20, 2013.

[2] R. H. Lasseter and P. Paigi, "Microgrid: a conceptual solution," in *Power Electronics Specialists Conference. IEEE 35th Annual,* 2004, pp. 4285-4290 Vol.6.

[3] B. Lasseter, "Microgrids," in *Power Engineering Society Winter Meeting. IEEE,* 2001, pp. 146-149 Vol.1.

[4] Z. Qing-Chang, "Robust Droop Controller for Accurate Proportional Load Sharing Among Inverters Operated in Parallel," *IEEE Transactions on Industrial Electronics,* vol. 60, pp. 1281-1290, 2013.

[5] J. Rocabert, A. Luna, F. Blaabjerg, and P. Rodriguez, "Control of Power Converters in AC Microgrids," *IEEE Transactions on Power Electronics,* vol. 27, pp. 4734-4749, 2012.

[6] T. Ise, "Functions and Configurations of Quality Control Center on FRIENDS," in *Transmission and Distribution Conference and Exhibition: Asia Pacific. IEEE/PES,* 2002, pp. 590-595 vol.1.

[7] X. Weidong, N. Ozog, and W. G. Dunford, "Topology Study of Photovoltaic Interface for Maximum Power Point Tracking," *IEEE Transactions on Industrial Electronics,* vol. 54, pp. 1696-1704, 2007.

[8] J. Viinamaki, J. Kivimaki, T. Suntio, and L. Hietalahti, "Design of Boost-power-stage Converter for PV Generator Interfacing," in *16th European Conference on Power Electronics and Applications,* 2014, pp. 1-10.

[9] M. A. Farahat, H. M. B. Metwally, and A. A. Mohamed, "Optimal Choice and Design of Different Topologies of DC–DC Converter Used in PV Systems, at Different Climatic Conditions in Egypt," *Renewable Energy,* vol. 43, pp. 393-402, 2012.

[10] N. Femia, G. Petrone, G. Spagnuolo, and M. Vitelli, *Power Electronics and Control Techniques for Maximum Energy Harvesting in Photovoltaic Systems.* U.S.: Taylor & Francis Group, 2013.

[11] W. Li and X. He, "Review of Nonisolated High-Step-Up DC/DC Converters in Photovoltaic Grid-Connected Applications," *IEEE Transactions on Industrial Electronics,* vol. 58, pp. 1239-1250, 2011.

[12] T. Dragicevic, J. C. Vasquez, J. M. Guerrero, and D. Skrlec, "Advanced LVDC Electrical Power Architectures and Microgrids: A step toward a new generation of power distribution networks," *Electrification Magazine, IEEE,* vol. 2, pp. 54-65, 2014.

[13] D. Boroyevich, I. Cvetkovic, D. Dong, R. Burgos, W. Fei, and F. Lee, "Future Electronic Power Distribution Systems - a Contemplative View -," in *12th International Conference on Optimization of Electrical and Electronic Equipment,* 2010, pp. 1369-1380.

[14] R. W. Erickson, *Fundamentals of Power Electronics,* 2nd ed. Boston, Mass., 2001.

[15] N. D. Benavides and P. L. Chapman, "Boost Converter with a Reconfigurable Inductor," in *IEEE Power Electronics Specialists Conference (PESC),* 2007, pp. 1695-1700.

[16] N. Femia, G. Petrone, G. Spagnuolo, and M. Vitelli, "Optimization of Perturb and Observe Maximum Power Point Tracking Method," *IEEE Transactions on Power Electronics,* vol. 20, pp. 963-973, 2005.

10

APPENDIX B: Active Suppression of Photovaltaic System Related Harmonics in a DC Microgrid

Active Suppression of Photovoltaic System Related Harmonics in a DC Microgrid

R. Alsharif , M. Odavic, K. Atallah
Department of Electronic and Electrical Engineering
The University of Sheffield
Sheffield, United Kingdom
ryaalsharif1@sheffield.ac.uk , m.odavic@sheffield.ac.uk

Abstract— **A photovoltaic (PV) generator is one of the primary power sources in a DC micro-grid (MG). The power generated by PV systems may inject high-order transient harmonics and low frequency ripple into the DC MG, especially if a conventional widely used Perturbation and Observation (P&O) maximum power point tracker is employed. In this paper a novel active filtering approach is proposed to improve the power quality of a parallel-connected double-stage PV system with dedicated decentralized P&O controllers, by eliminating or reducing the progression of the P&O related harmonics into the grid. The proposed active filtering approach is based on implementing a system-level controller that can control the operation of multiple decentralized P&O controllers and as a consequence can improve the efficiency of the overall system. The proposed solution is tested on a system consisting of multiple parallel-connected self-controlled PV modules which are connected to a DC MG through a common DC/DC boost converter. The simulation results demonstrate that the quality of the power injected to the DC MG can be significantly improved. Further, the DC-link current ripple of the double-stage converter is also notably reduced so that a smaller DC-link capacitor can be used. Improved control dynamics for the first and second converter stages can also be achieved.**

Keywords—photovoltaic; power quality; micro-grid; harmonics

I. INTRODUCTION

The fast growth of modern electronic loads and renewable energy sources make DC micro-grids (MGs) more attractive with many potential advantages, especially for high power quality [1]. A photovoltaic (PV) generator has been recognized as promising renewable source for electricity generation [2]. Nowadays the double-stage PV systems are widely adopted in order to overcome the drawbacks of the single-stage systems; this mainly being the poor system efficiency under mismatching phenomena [3].

The maximum power point tracking (MPPT) algorithm is essential in PV systems for extracting maximum available power from the PV module under different operating conditions. Many different MPPT algorithms have been proposed [4, 5]. The most commonly used algorithm is perturb and observe (P&O) due to its simplicity and low cost. P&O tracks the maximum power point (MPP) by injecting a small perturbation into the system. In this approach, after the system has approached the MPP, it continues oscillating about the MPP. The characteristics of the oscillations depend on the P&O parameters such as the perturbation step size and sampling period [6]. The optimal three-step P&O duty cycle maximizes the average power extracted from a PV module and ensures periodic and stable oscillation about the MPP [6]. However, the literature reports on the MPPT related harmonics [3], [6]-[9] present in the grid. Also, these harmonics can affect system stability and drive the system into a chaotic behaviour, as reported in[10].

This paper first gives a brief overview of the conventional approaches to filtering the PV related harmonics. It then proposes a novel filtering method to actively suppress the P&O related high-order transient and low order harmonics. The proposed active filtering method is based on implementing a system-level controller that can control the operation of multiple decentralized P&O controllers.

II. SYSTEM CONFIGURATION

A self-controlled photovoltaic module (SCPVM) is based on dedicating a maximum power point tracking (MPPT) DC/DC converter to each PV module [3]. Nowadays the SCPVMs are widely adopted in order to overcome some drawbacks of the centralized MPPT; mainly the high sensitivity to mismatching phenomena and the poor system efficiency. The most common approach for connecting SCPVM units to a DC MG is the series configuration [3, 11]. However, the major drawback of this approach occurs under mismatching conditions when it is difficult to achieve the desired output voltage for some SCPVMs [3]. To overcome this problem the new trend of connecting PV systems to a DC MG goes towards adopting parallel connected SCPVM units through a common second-stage step-up converter [3].

In this work the circuit configuration with parallel connected SCPVMs is adopted. The system under study consists of four parallel SCPVMs (of 240W each) which are connected to the DC MG through the DC/DC boost converter, as shown in Fig. 1. The control strategy is based on the assumption that the DC MG is in grid-connected mode or in islanded mode where the storage system is large enough to allow MPP tracking all the time. The first-stage controller is responsible for MPPT (i.e. direct duty cycle P&O method is adopted) and the second-stage controller controls dc-link voltage V_{dc} (i.e. the peak current controller is adopted). In

1594
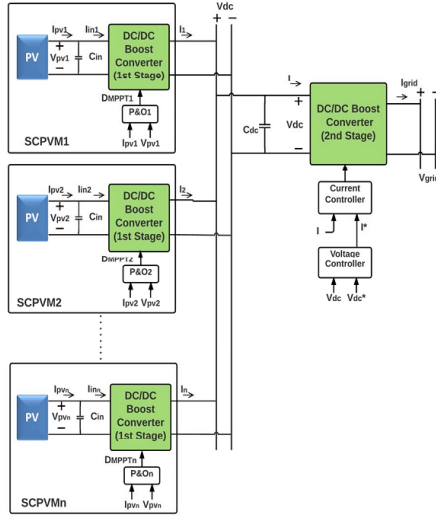
Fig. 1.   Multiple parallel connected SCPVMs through a DC/DC converter to the DC MG

general, the DC MG voltage V_{grid} can be controlled either by the bidirectional ac/dc inverter which connects a DC MG to the main grid, or by the storage system converter. In this work voltage V_{grid} is modelled as an ideal voltage source. The second stage dc/dc converter is responsible for boosting the voltage V_{dc} to the level of V_{grid} of 400V. The system parameters and the PV specifications are listed in Table I and Table II, respectively.

III.   THE EFFECT OF P&O CONTROLLER

A. Low Frequency Harmonics

The low frequency harmonics observed in the dc-link bus in the double-stage PV system are caused by the perturbation nature of the P&O algorithm. These harmonics dependent on the P&O sampling period T_{MPP} and the number of P&O duty cycle steps in the steady state. The frequency of these harmonics can be obtained from (1) and for the optimal three-step operation (1) simplifies to $f_{low} = 1/(4T_{MPP})$. The three-step operation is shown in Fig. 2.

$$f_{low} = \frac{1}{(2 \times number\ of\ the\ P\&O\ duty\ cycle\ steps - 2) \times T_{MPP T}} \quad (1)$$

B. High Order Transient Harmonics

High order transient harmonics are also induced by the P&O MPPT controller which introduces continuous small perturbations into the P&O duty cycle in order to track the MPP. In the double-stage PV system, the optimal three-step P&O duty cycle perturbations generated by the first-stage converter are seen as constant disturbances by the second-stage

converter. The endless duty cycle perturbations force the second-stage converter to enter the transient modes at every P&O sampling instant, which needs to be taken into account in the design of the second stage converter. Fig. 2 shows the four main transient intervals, which are marked as 1, 2, 3 and 4, where each interval starts at the instant when the P&O duty cycle is perturbed. These four main transient intervals are then repeated in sequence every $1/f_{low}$. Of note is that the experimental results presented in [8, 9] show the existence of the PV related high-order transient harmonics in the grid.

TABLE I.   GLOSSARY OF TERMS AND PARAMETERS OF DOUBLE-STAGE PV SYSTEM

Symbol & Glossary		Value
SCPVMn	Self-control PV module of unit number n	4 units
Δd	P&O duty cycle step size	0.02
T_{MPPT}	P&O sampling period	200 µs
f_{sw1}, f_{sw2}	Switching frequency of 1st stage and 2nd stage converters, respectively	f_{sw1}=100kHz f_{sw2}=25kHz
P_1, P_2	Rated power of the 1st stage and 2nd stage converters, respectively	P_1=240W P_2=1000W
C_{in}	Capacitance of the input capacitor of the 1st stage converter	1.5 µF
L_1, L_2	Inductances of the input inductors of the 1st stage and 2nd stage converters, respectively	L_1= 0.2mH L_2= 3.0mH
C_{dc}	Total DC-link Capacitance	13 µF
C_o	Capacitance of the output capacitor of the 2nd stage converter	75 µF
V_{dc}	DC-link voltage	100V
V_{grid}	DC micro-grid voltage	400V
K_{pv}, K_{iv}	Propotional and integral gain of the 2nd stage outer loop voltage contoller	K_{pv}=0.113 K_{iv}=155.4
K_{pc}, K_{ic}	Propotional and integral gain of the 2nd stage inner loop current contoller	K_{pc}=135 K_{ic}=3025e3
ω_{cv}, PM_v	Voltage loop cut-off frequency and phase margine	4.8 kHz, 65.5°
ω_{cc}, PM_c	Current loop cut-off frequency and phase margine	9 kHz, 65.6°
G	Solar irradiation	Vary
I	DC-link current	Vary
I_{grid}	Average DC micro-grid current	Vary
I_{pvn}	PV output current of unit number n	Vary
V_{pvn}	PV output voltage of unit number n	Vary

TABLE II.   PV MODULE SPECIFICATIONS

NU-E240 (J5)	
Number of cells in series	60
Maximum Power	240 Wp
Open Circuit Voltage	37.3 V
Short Circuit Current	8.62 A
Standard Operation Condition Temperature	25 °C
Maximum Power Point Voltage (V_{MPP})	30.2 V
Maximum Power Pont Current (I_{MPP})	7.9 A

1595

IV. CLASSICAL APPROACHES TO SUPPRESS PV RELATED HARMONICS

For the system analysed in this work, Fig. 3 shows the simulation results of the DC link voltage and current after increasing DC link capacitance C_{dc} from 13µF to 41µF. It can be seen that the high order transient harmonics and the low frequency harmonics have been suppressed with respect to the case when C_{dc}=13µF, as is presented in Fig.2. This is the most common approach to reduce the PV related harmonics, however, this solution is not desirable as it reduces system reliability and increases losses and cost.

Another common approach is to reduce the bandwidth of the second-stage converter well below the frequency of the low-order P&O harmonics. However, this approach will lead to the decreased dynamic response of the second-stage converter and consequently the reduced efficiency. Moreover, the system cut-off frequency has to be greater than the system resonant frequency $\omega_0 = 1/\sqrt{L_2 C_{dc}}$ [12] and for the system parameters given in Table I, the cut-off frequency cannot be set sufficiently low to filter out the low order harmonics with a frequency of f_{low} =1.25 kHz.

Fig. 4 shows the simulation results for the case when the P&O sampling period is increased from T_{MPPT}=0.2ms to T_{MPPT}=0.6ms. For this case it is even harder to suppress the low-order harmonics as their frequency decreases from f_{low}=1.25kHz to f_{low}=417Hz.

V. PROPOSED ACTIVE SUPPRESSION OF PV HARMONCIS

The outline of the proposed active filtering approach considering n SCPVM units connected in parallel is shown in Fig. 5. In order to demonstrate how the proposed active filtering approach works, a system of only two SCPVM units operating under uniform solar irradiation is firstly considered. Also, P&O sampling period T_{MPPT} is set to a value of 0.3ms to better illustrate the transient harmonics. The simulations results are shown in Fig. 6.a, where the high order transient and low order harmonics in I_1 and I_2 can be clearly observed. The DC-link current I is actually the sum of the output currents of the SCPVM units (i.e. $I=I_1+I_2$) and thus it also contains the significant high order transient and low order harmonics, as can be seen in Fig. 6.a.

The behaviour of the high-order transient oscillations depends on the directions of the perturbations in the MPPT duty cycle $_t$ (i.e. rising ↑ or falling ↓). At the rising edge of D_{mppt1}, the oscillation in the current I_1 starts by a downswing and oscillates until the steady state is reached or the next perturbation occurs, depending on the P&O sampling period and the system dynamics. On the contrary, at the falling edge of D_{mppt1}, the oscillation in the current I_1 starts by an upswing and oscillates until the steady state is reached or the next perturbation occurs. The same behaviour can be observed in the current I_2.

If the rising and falling edges of D_{mppt1} and D_{mppt2} occur at the same time, as is shown in Fig. 6.a, the high order transient and low order harmonics in I_1 and I_2 are in phase and the amplitude of these harmonics in the dc link current I is exactly
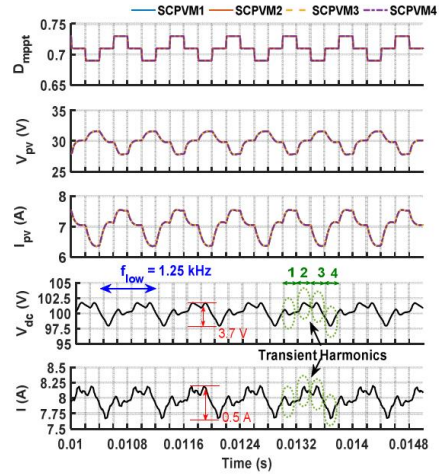

Fig. 2. Low frequency and high transient harmonics injected into DC link bus by four SCPVMs. G=900W/m², C_{dc}=13µF, V_{dc}^*=100V, V_{grid}=400V, and T_{MPPT}=0.2ms.
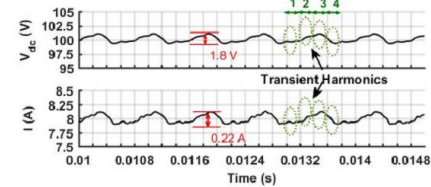

Fig. 3. Filtering the high order harmonics and low frequency ripple by increasing C_{dc}. Four SCPVMs, G=900W/m², C_{dc}=41µF, V_{dc}^*=100V, V_{grid}=400V, and T_{MPPT}=0.2ms.
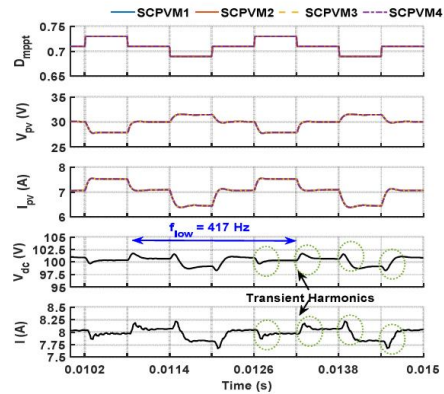

Fig. 4. The effect of the P&O sampling period on the low frequency ripple and transient oscillations injected the DC link bus. Four SCPVMs, G=900W/m², C_{dc}=13µF, V_{dc}^*=100V, V_{grid}=400V, and T_{MPPT}=0.6ms.

two times the amplitude of the harmonics in I_1 and I_2. It can be then readily concluded that by increasing the number of parallel connected SCPVM units, the harmonics in the DC-link current are expected to increase substantially. On the contrary, if the harmonics in I_1 and I_2 are out of phase, they will be completely eliminated in the dc link current I. This can be achieved when D_{mppt1} and D_{mppt2} are out of phase, as is shown in Fig. 6.b. The simulation results of the dc link current I and dc link voltage V_{dc}, shown in Fig. 6.b, demonstrate that the high
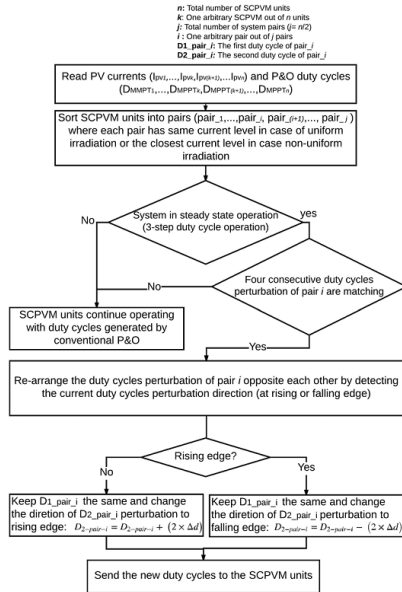
Fig. 5. Outline of the proposed system-level controller
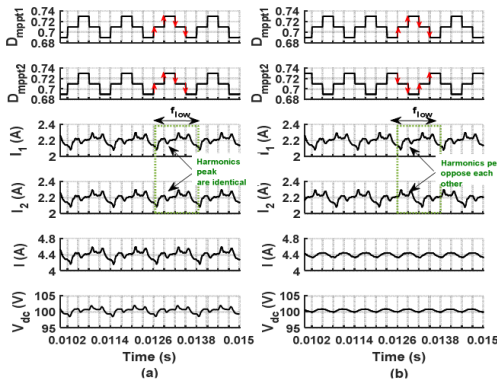
Fig. 6. Two parallel-connected SCPVM units under uniform irradiation of 1000 W/m². (a) Results without active filtering, (b) Results with active filtering. C_{dc}=13µF, V_{dc}*=100V, V_{grid}=400V, and T_{MPPT}=0.3ms

order transient harmonics are completely eliminated and the low order harmonics are significantly suppressed in the dc link. This will be further discussed in section VI.

In order to force the P&O perturbations of different SCPVM units to oscillate in opposite directions, a system-level controller to synchronise the operation of all SCPVM units is proposed in this work. The successful implementation of this controller requires that the electrical characteristics of all PV units are similar and the three-step P&O operation in steady state is achieved. The outline of the proposed active filtering approach considering n SCPVM units connected in parallel is shown in Fig. 5.

As can be seen from the diagram in Fig. 5 the SCPVM units have to be firstly sorted into the appropriate pairs. The pairs are chosen based on the closest irradiation requirement and this is obtained by comparing the PV output currents (i.e. Ipv_1, Ipv_2, ..., Ipv_n). In the case of the uniform solar irradiation the output currents of all PV modules are the same (or slightly different) and SCPVM pairs can be arbitrary decided.

The second step in the proposed algorithm is to make sure that the SCPVM units in each pair are in the optimal three-step mode (i.e. in steady state operation), before the active filtering is enabled. This is required to avoid interrupting the transients following a sudden and big change in irradiation. This is achieved by checking four consecutive duty cycle perturbations of each unit in a pair.

The last step in the proposed method is to control the duty cycle perturbations of two SCPVM units in each pair to work in opposite directions. In each pair the duty cycle of one SCPVM unit is kept unchanged while the duty cycle of the other SCPVM unit is modified by adding or deducting two times Δd (i.e. the duty cycle step) from the current value of the duty cycle, depending on the value of the duty cycle of the other SCPVM unit in a pair.

VI. LOW FREQUENCY RIPPLE SUPPRESSION

The proposed active filter can suppress the high order transient and low order harmonics imposed by the P&O controller. However, the system will still contain some low order harmonics as can been observed in Fig. 6.b. These harmonics are associated with the non-linear characteristics of the PV source, as discussed below in this section.

Fig. 7 shows a general current-voltage characteristic curve of a PV module. The three-step P&O operation is characterized by the following three points: MPP, Left MPP and Right MPP, as shown in red, green and yellow in Fig. 7, respectively.

These periodic oscillations can be also observed at the output of an SCPVM, as shown in Fig. 8. The results in Fig. 8 are generated analytically for illustration purposes and don't include the high order transient harmonics which are normally present in the output of a SCPVM, as was demonstrated before.

The maximum and minimum values of the output current of an arbitrary SCVPM unit (SCPVMk) under solar irradiation G can be defined as follows:

$$I_{k\_max}^{G} = I_{k\_mpp}^{G} + U_{k\_l}^{G} \qquad (2)$$

$$I_{k\_min}^{G} = I_{k\_mpp}^{G} - U_{k\_r}^{G}$$

where $I_{k\_mpp}^{G}$ is the output current of SCPVMk when the PV

operates at the MPP under G irradiation level, $U_{k\_l}{}^G$ is the change in the output current when the PV operates at the Left MPP with respect to $I_{k\_mpp}{}^G$, and $U_{k\_r}{}^G$ is the change in the output current when the PV operates at the Right MPP with respect to $I_{k\_mpp}{}^G$. The slope of the PV current-voltage characteristic curve, as can be seen in Fig. 7, increases as the operating point moves to the right, resulting in:

$$U_{k\_r}^G > U_{k\_l}^G \tag{3}$$

A. Without the active filter

Before applying the proposed active filtering approach, the peak-to-peak ripple of the dc link current, when n SCPVM units are connected in parallel, is given by:

$$U_{p-p} = \sum_{k=1}^{n}\left(U_{k\_r}^G + U_{k\_l}^G\right) \tag{4}$$

Under uniform solar irradiation, it can be written:

$$U_{k\_r}^G = U_{(k+1)\_r}^G = \ldots = U_{n\_r}^G = U_r \tag{5}$$
$$U_{k\_l}^G = U_{(k+1)\_l}^G = \ldots = U_{n\_l}^G = U_l$$

Thus, the peak-to-peak ripple of the dc link output current I under uniform irradiation is given by:

$$U_{p-p} = n \times \left(U_l + U_r\right) \tag{6}$$

B. With the active filter

When the active filtering approach is applied, two SCPVM units work as a pair, i.e. if one unit in a pair operates at the Right MPP, the other unit in the pair operates at the Left MPP. With reference to Fig. 8b, for the active filtering approach it can be written:



Fig. 7. Current-voltage characteritic curve of a PV moduel

Fig. 8. Low frequency ripple in the outptut current of the two SCPVM units I_k and their total current (I) (a) without active filter (b) with active filter.

$$U_{x\_r}^{1\_pair-i} > U_{y\_l}^{2\_pair-i}$$
$$I_{x\_mpp}^{1\_pair\_i} - I_{x\_min}^{1\_pair\_i} > I_{y\_max}^{2\_pair\_i} - I_{y\_mpp}^{2\_pair\_i} \tag{7}$$
$$I_{x\_mpp}^{1\_pair\_i} + I_{y\_mpp}^{2\_pair\_i} > I_{y\_max}^{2\_pair\_i} + I_{x\_min}^{1\_pair\_i}$$

where x and y are any arbitrary SCPVM units out of n units and $U_{x\_r}^{1\_pair\_i}$ and $U_{y\_l}^{2\_pair\_i}$ are defined in Fig. 8b. The peak-to-peak ripple of the output current of one pair is given by:

$$U_{p-p}^{pair\_i} = (I_{x\_mpp}^{1\_pair\_i} + I_{y\_mpp}^{2\_pair\_i}) - (I_{y\_max}^{2\_pair\_i} + I_{x\_min}^{1\_pair\_i})$$
$$U_{p-p}^{pair\_i} = (I_{x\_mpp}^{1\_pair\_i} - I_{x\_min}^{1\_pair\_i}) - (I_{y\_max}^{2\_pair\_i} - I_{y\_mpp}^{2\_pair\_i}) \tag{8}$$
$$U_{p-p}^{pair\_i} = U_{x\_r}^{1\_pair-i} - U_{y\_l}^{2\_pair-i}$$

The peak-to-peak ripple of the dc link current is:

$$U_{p-p}^{active} = \sum_{i=1}^{j=n/2}\left(U_{x\_r}^{1\_pair-i} - U_{y\_l}^{2\_pair-i}\right) \tag{9}$$

Under uniform irradiation:

$$U_{x\_r}^{1\_pair\_i} = U_{y\_r}^{2\_pair\_i} = U_{x\_r}^{1\_pair\_(i+1)} = U_{y\_r}^{2\_pair\_(i+1)} = \ldots = U_{x\_r}^{1\_pair\_j} = U_{y\_r}^{2\_pair\_j} = U_r \tag{10}$$
$$U_{x\_l}^{1\_pair\_i} = U_{y\_l}^{2\_pair\_i} = U_{x\_l}^{1\_pair\_(i+1)} = U_{y\_l}^{2\_pair\_(i+1)} = \ldots = U_{x\_l}^{1\_pair\_j} = U_{y\_l}^{2\_pair\_j} = U_l$$

Thus the peak-to-peak ripple of the dc link current under uniform irradiation is:

$$U_{p-p}^{active} = j \times \left(U_r - U_l\right) = \frac{n}{2} \times \left(U_r - U_l\right) \tag{11}$$

Comparing (11) with (6) it can be shown that under uniform solar irradiation the peak-to-peak ripple can be decreased by more than 50% as follows:

$$Decreased\ \% = \left(1 - \frac{U_{p-p}^{active}}{U_{p-p}}\right) \times 100\% = \left(1 - \frac{n/2}{n}\frac{U_r - U_l}{U_r + U_l}\right) \times 100\% \tag{12}$$

$$Decreased\ \% = 100\% - \frac{U_r - U_L}{U_r + U_l} \times 50\%$$

The frequency of these harmonics is given by:

$$f_{low\_active} = 2 \times f_{low} \tag{13}$$

If one or more pairs working under non-uniform solar irradiation some other harmonics are expected in the system and this needs further analysis.

VII. SIMULATION RESULTS

The new proposed active filtering method is tested by simulating four SCPVM units connected to the DC MGs under three different cases: uniform irradiation, non-uniform irradiation, and high harmonics distortion. The first case is shown in Fig. 9 and it shows the system before and after applying the active filter. The high-order transient harmonics are filtered and the low frequency ripple is effectively suppressed as shown in Fig. 9.b. The amplitudes of the low order frequency harmonics in the voltage and current have been reduced by 83% and 82%, respectively, as expected according to (13) with more than 80% of decrease in the DC link power ripple, as shown in the last trace in Fig. 9.

The Fast Fourier Transform (FFT) analyses of the DC link voltage and current are shown in Fig. 10 and Fig. 11, respectively. The FFT results without active filter, shown in Fig. 10.a and Fig. 11.a, show the low order harmonics at f_{low}=1.25kHz, two times f_{low}, three times f_{low} and f_{MPPT}=5 kHz, and some other high order harmonics in both the voltage and
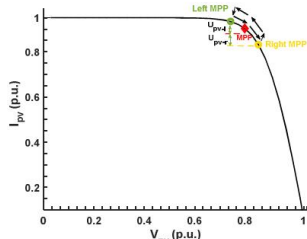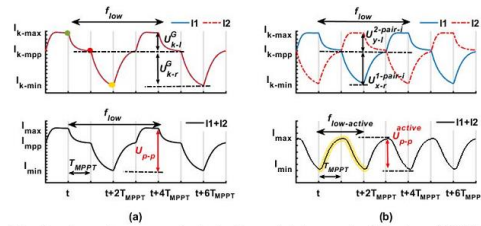
1598
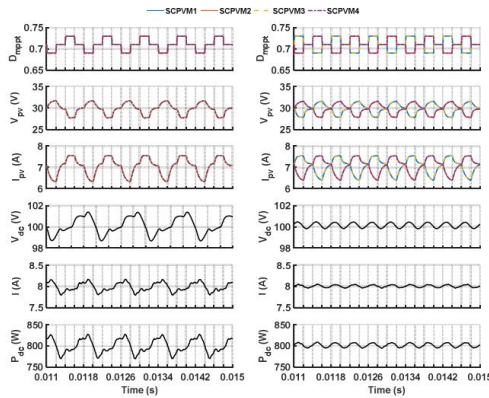
Fig. 9. Four SCPVM units under uniform solar irradiation of 900W/m²: (a) Without active filter (b) with active filter. V_{dc}^*=100V, C_{dc}=13μF, T_{MPPT}=200μs, V_{grid}=400V.
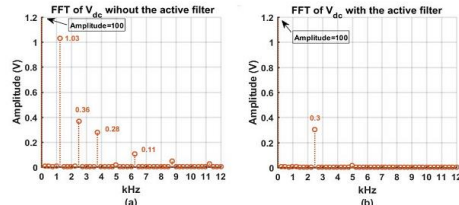

Fig. 10. FFT of the DC link voltage shown in Fig.9 (a) without active filter (b) with active filter
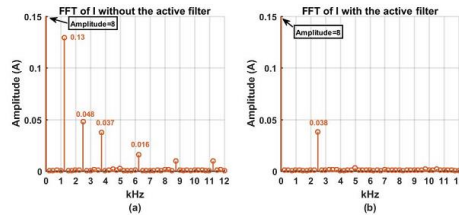
Fig. 11. FFT of the DC link current shown in Fig.9 (a) without active filter (b) with active filter

current. After applying the active filter, the FFT of the voltage and current are shown in Fig. 10.b and Fig. 11.b, respectively. The results show that the system contains harmonics at the two times f_{low} (2.5 kHz) as expected from (14) and at 5 kHz which is the frequency of the P&O controller f_{MPPT}.

In the second case, the capability of the proposed active filter under non-uniform irradiation is demonstrated. The results before and after the active filter is enabled are shown in Fig. 14.a and Fig. 14.b, respectively. In this test four SCPVM units first work under uniform solar irradiation (900 W/m²) and in the following pairs: the first pair includes (SCPVM1,

SCPVM2) and the second pair includes (SCPVM3, SCPVM4). Then after 0.02s SCPVM2 and SCPVM4 work under the reduced irradiation, for example under shading. After rearranging, the algorithm finds the new pairs; SCPVM3 is switched to work with SCPVM1 and SCPVM2 and SCPVM4 form the second pair. The switching process between the pairs can be clearly seen from I_{pv} in the second row of Fig. 14.b.

Next, the proposed active filter is tested when the system operating under reduced DC link capacitance C_{dc}. The results without and with the active filter are shown in Fig. 12. It can be observed that the power quality has been improved with no high order transient harmonics and significantly reduced low frequency ripple. The FFT result in Fig. 13 shows that with the active filter the only harmonics that exist in the system are 2.5 kHz and 5 kHz.

Finally, the capability of the proposed active filter to work with a very small value of C_{dc} is shown in Fig. 15. Without the active filter the system is in the chaotic mode as the second stage controller loses stability due to the high order transient harmonics in the dc link [10]. On the contrary, the system with the active filter is stable and in addition the high power quality is achieved. Fig. 16 shows the FFT of the system under chaotic behaviour (without active filter) and with the active filter.
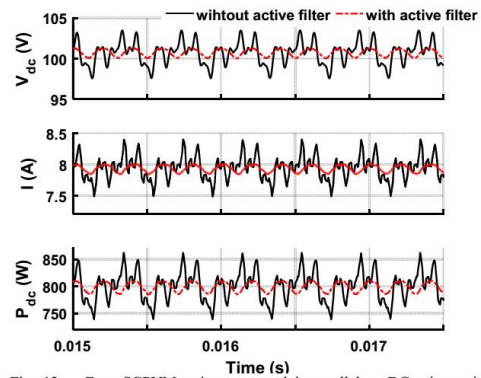

Fig. 12. Four SCPVM units connected in-parallel to DC micro-grid: (black continuous line) without active filter (red dashed line) with active filter. G=900W/m2, V_{dc}^*=100V, C_{dc}=5μF, T_{MPPT}=200μs, V_{grid}=400V
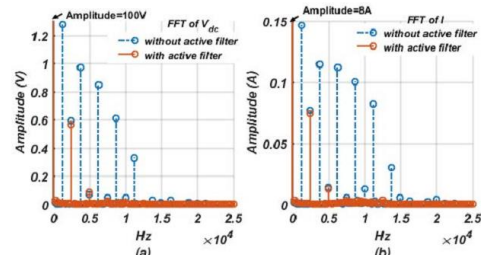

Fig. 13. FFT of the waveforms shown in Fig.13 (a) DC link voltage V_{dc} (b) DC link current I

1599

210
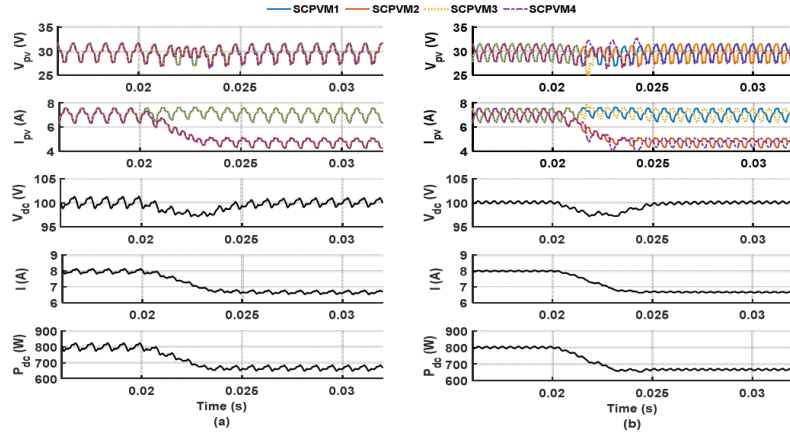
Fig. 14. Four SCPVM units under non-uniform solar irradiation. (a) without active filter (b) with active filter. Vdc*=100V, Cdc=29μF, TMPPT=200μs, Vgrid=400V.
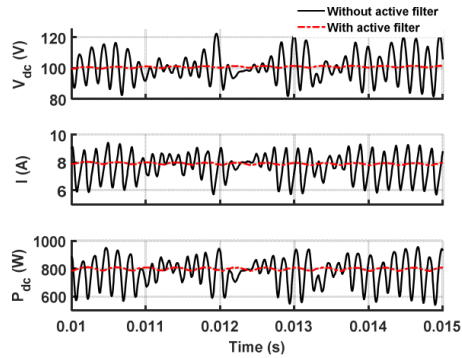
Fig. 15. Four SCPVM units connected in-parallel to DC micro-grid: (black continouse line) without active filter (red dashed line) with active filter. G=900W/m2, V_{dc}^*=100V, C_{dc}=3.4μF, T_{MPPT}=200μs, V_{grid}=400V
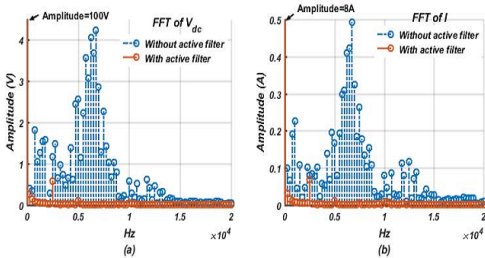

Fig. 16. FFT of the waveforms shown in Fig.15 (a) DC link voltage V_{dc} (b) DC link current I

CONCLUSION

A novel active filtering method has been proposed to improve the power quality of PV dominated DC MGs. It eliminates the high-order transient harmonics and suppresses the low frequency ripple caused by decentralized P&O controllers of multiple SCPVMs connected in parallel. It was shown that the proposed filter operates effectively under uniform and non-uniform solar irradiation. Moreover, with the proposed active filter the DC-link current ripple of the double-stage converter is also notably reduced and in that a smaller DC-link capacitor can be used. Also, improved control dynamics for both converter stages can be achieved.

REFERENCES

[1] T. Dragicevic, J. C. Vasquez, J. M. Guerrero, and D. Skrlec, "Advanced LVDC electrical power architectures and microgrids: a step toward a new generation of power distribution networks," *Electrification Magazine, IEEE,* vol. 2, pp. 54-65, 2014.

[2] E. Romero-Cadaval, G. Spagnuolo, L. Garcia Franquelo, C. A. Ramos-Paja, T. Suntio, and W. M. Xiao, "Grid-connected photovoltaic generation plants: components and operation," *IEEE Industrial Electronics Magazine,* vol. 7, pp. 6-20, 2013.

[3] N. Femia, G. Petrone, G. Spagnuolo, and M. Vitelli, *Power electronics and control techniques for maximum energy harvesting in photovoltaic systems.* U.S.: Taylor & Francis Group, 2013.

[4] N. Femia, D. Granozio, G. Petrone, G. Spagnuolo, and M. Vitelli, "Predictive & adaptive MPPT perturb and observe method," *IEEE Transactions on Aerospace and Electronic Systems,* vol. 43, pp. 934-950, 2007.

[5] A. Pandey, N. Dasgupta, and A. K. Mukerjee, "Design issues in implementing MPPT for improved tracking and dynamic performance," in *32nd Annual Conference on IEEE Industrial Electronics,* 2006, pp. 4387-4391.

[6] N. Femia, G. Petrone, G. Spagnuolo, and M. Vitelli, "Optimization of perturb and observe maximum power point tracking method," *IEEE Transactions on Power Electronics,* vol. 20, pp. 963-973, 2005.

[7] X. Weidong, N. Ozog, and W. G. Dunford, "Topology study of photovoltaic interface for maximum power point tracking," *IEEE Transactions on Industrial Electronics,* vol. 54, pp. 1696-1704, 2007.

1600

[8] P. Pakonen, A. Hilden, T. Suntio, and P. Verho, "Grid-connected PV power plant induced power quality problems - experimental evidence," in *2016 18th European Conference on Power Electronics and Applications*, 2016, pp. 1-10.

[9] R. Langella, A. Testa, J. Meyer, F. Möller, R. Stiegler, and S. Z. Djokic, "Experimental-based evaluation of PV inverter harmonic and interharmonic distortion due to different operating conditions," *IEEE Transactions on Instrumentation and Measurement,* vol. 65, pp. 2221-2233, 2016.

[10] R. Alsharif and M. Odavic, "Photovoltaic generators interfacing a DC micro-grid: design considerations for a double-stage boost power converter system," in *2016 18th European Conference on Power Electronics and Applications (EPE'16 ECCE Europe)*, 2016, pp. 1-10.

[11] W. Li and X. He, "Review of nonisolated high-step-up DC/DC converters in photovoltaic grid-connected applications," *IEEE Transactions on Industrial Electronics,* vol. 58, pp. 1239-1250, 2011.

[12] M. K. Kazimierczuk, *Pulse-Width Modulated DC-DC Power Converters*, 2nd ed. Chichester, UK: John Wiley & Sons, 2016.

1601

212

APPENDIX C: Simulink Models

C.1 Double-stage Parallel PV system

The Simulink model of the whole system "Double-stage DC/DC Boost Converter PV system" consists of four parallel SCPVM units is shown below in Figure 139. For more details each part of the model such as SCPVM, second-stage converter, SCPVM controllers and the controllers are shown separately in Figure 140, Figure 141, Figure 142 and Figure 143, respectively.
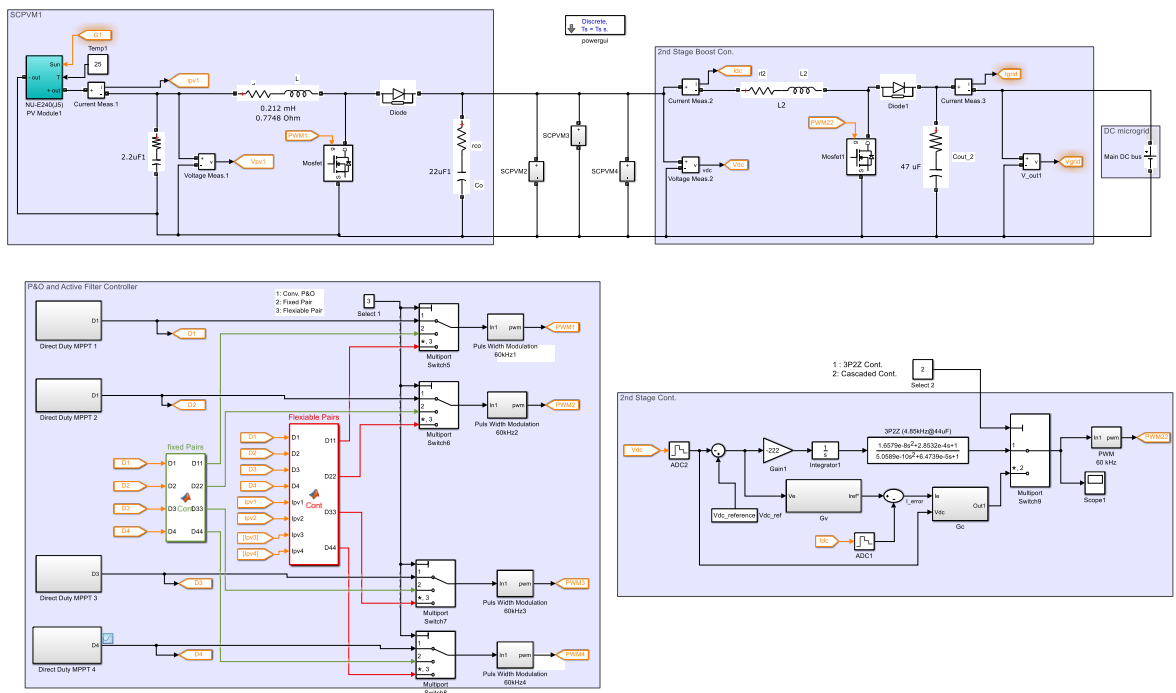

Figure 139: Simulink model of double-stage parallel SCPVM system consists of four SCPVM units.
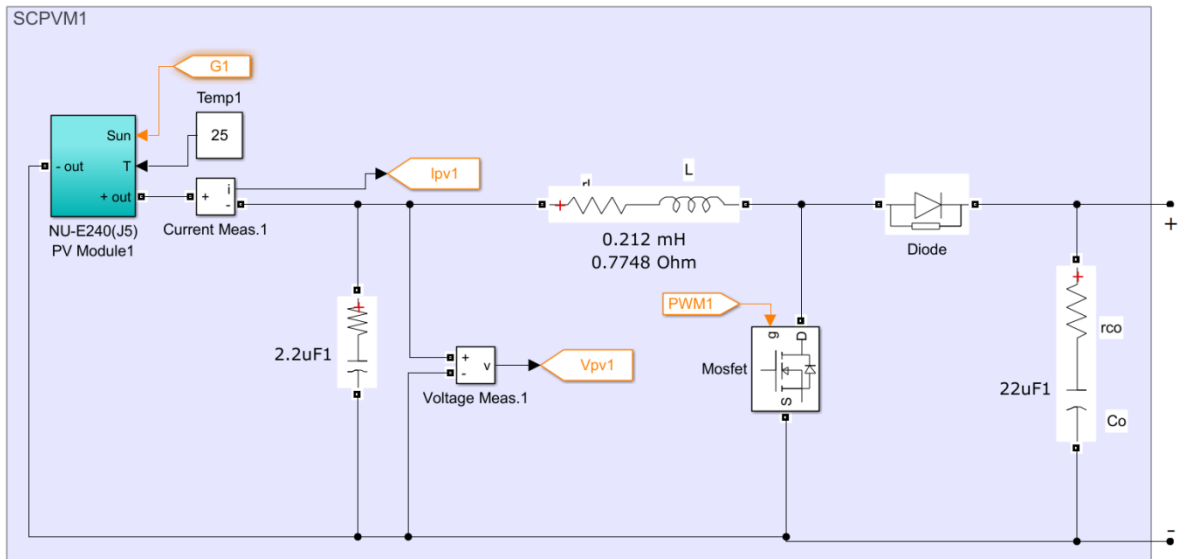
*Figure 140: Simulink model of the SCPVM unit. PV algorithm is given in Appendix C.2*
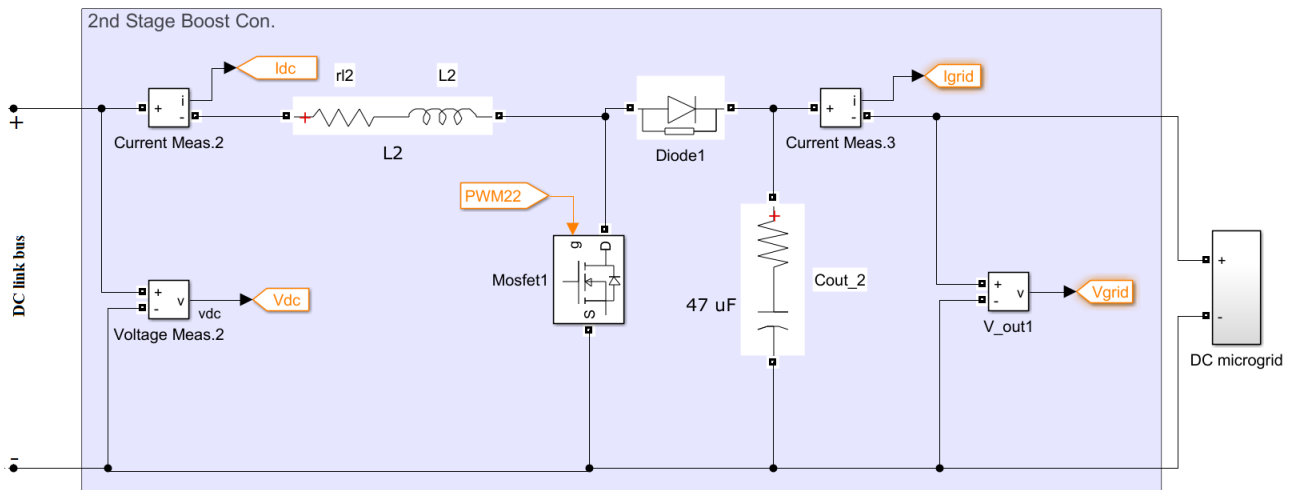

Figure 141: Simulink model of the second-stage boost converter
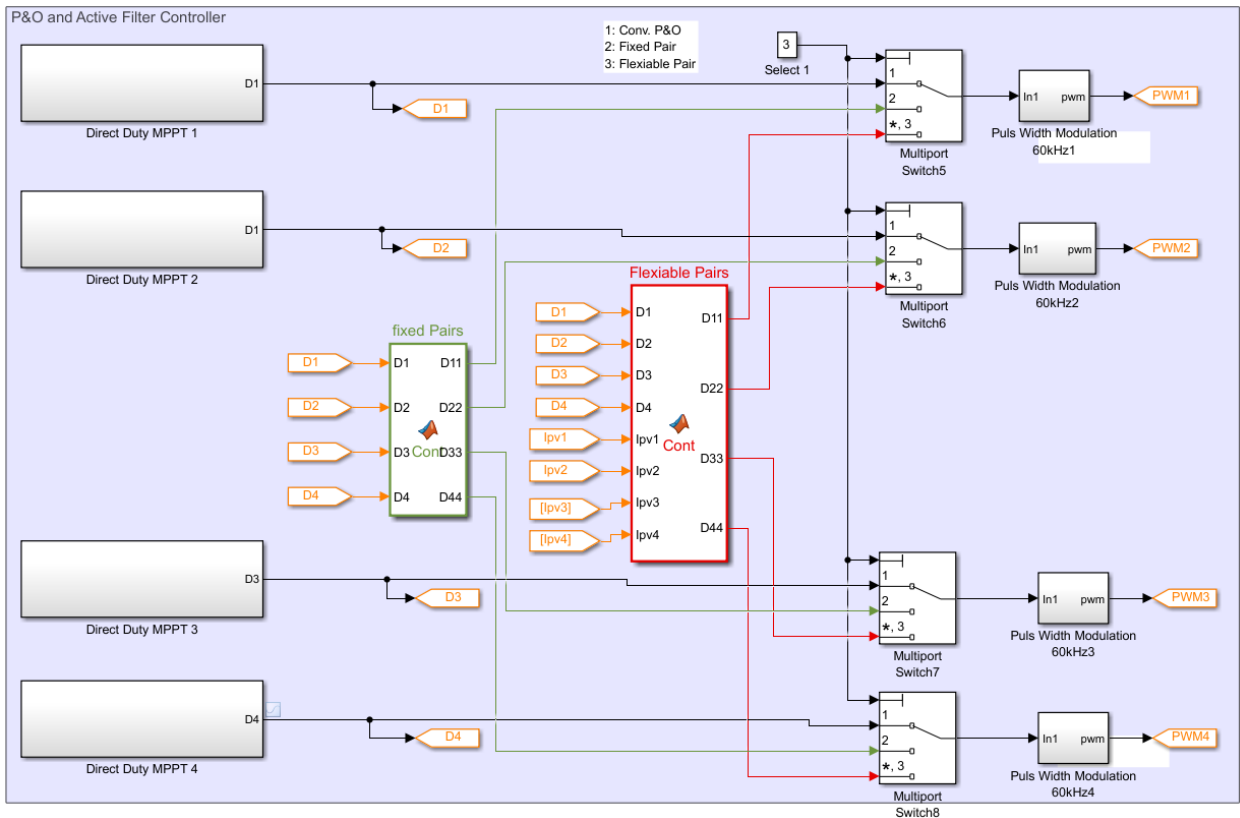
Figure 142: Simulink model of the SCPVM controllers of the first-stage boost converter (SCPVM unit). P&O algorithm is given in Appendix C.3 and Fixed pair and Flexible pair algorithms are given in Appendix E.
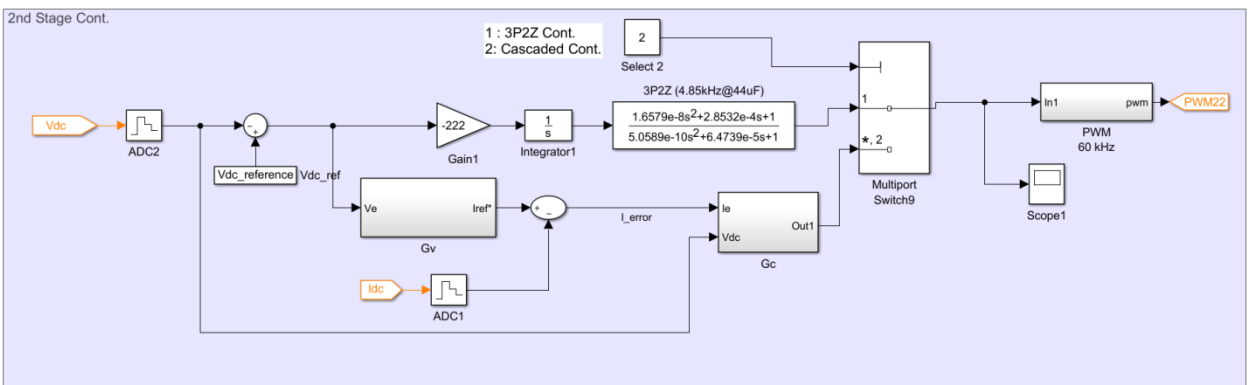
Figure 143: Simulink model of the 3P2Z and cascaded controllers of the second-stage boost converter

C.2 PV algorithm

```matlab
% PV model for the NU-E240 (J5)
% Given inputs PV voltage vpv, Solar irradiation G, and temperature Temp

function Ipv = pv(vpv,G,Temp)
% k is Boltzman constant, q is the charge of an electron,
%A is the diode quality factor, Vg is the band gap voltage,
%Ns is number of series cells
k=1.38e-23; q=1.6e-19; A=1.2; Vg=1.12; Ns=60;

T1=273+25;
Voc_T1=37.3/Ns; % open circuit voltage per cell at temperature T1
Isc_T1=8.63;    %short circuit current per cell at temp T1

T2=273+75;
Voc_T2=30.8/Ns; % open circuit voltage per cell at temperature T2
Isc_T2=8.65;    %short circuit current per cell at temp T2

TaK=273+Temp;  % array working temp
TrK=273+25;    % reference temp

Iph_T1=Isc_T1*G;    %light generated current at T1
a=(Isc_T2-Isc_T1)/Isc_T1*1/(T2-T1);
Iph=Iph_T1.*(1+a.*(TaK-T1));

Vt_T1=k*T1/q;
Ir_T1=Isc_T1/(exp(Voc_T1/(A*Vt_T1))-1);
Ir_T2=Isc_T2/(exp(Voc_T2/(A*Vt_T1))-1);

b=Vg*q/(A*k);
Ir=Ir_T1*(TaK/T1).^(3/A).*exp(-b.*(1./TaK-1/T1));

x2v=Ir_T1/(A*Vt_T1)*exp(Voc_T1/(A*Vt_T1));
dvdI_Voc=-1.15/Ns/2; % dV/dI at Voc per cell from manufacturers graph
Rs=-dvdI_Voc-1/x2v;  % series resistance per cell

vt_Ta=A*1.38e-23*TaK/(1.60e-19); % the thermal voltage

for j=1:5
    Ipv=Ipv-(Iph-Ipv-Ir.*(exp((Vc+Ipv.*Rs)./vt_Ta)-1))./ ...
    (-1-(Ir.*(exp((Vc+Ipv.*Rs)./vt_Ta)-1)).*Rs./vt_Ta);
end
```

216

C.3 P&O algorithm

```matlab
function D  = PandO(D_value, Vpv, Ipv)

Dinit = D_value(1);
Dmax = D_value(2);
Dmin = D_value(3);
deltaD = D_value(4);
% ( increasing D = decreasing V )

persistent Vold Pold Dold;

dataType = 'double';

if isempty(Vold)
    Vold=30;
    Pold=0;
    Dold=Dinit;
end
P= Vpv*Ipv;
dV= Vpv - Vold;
dP= P - Pold;

if dP ~= 0
    if dP < 0
        if dV < 0
            D = Dold - deltaD;
        else
            D = Dold + deltaD;
        end
    else
        if dV < 0
            D = Dold + deltaD;
        else
            D = Dold - deltaD;
        end
    end
else D=Dold;
end

if D >= Dmax || D<= Dmin
    D=Dold;
end

Dold=D;
Vold=Vpv;
Pold=P;
```

C.4 Simulink model for control loop gain measurements using MATLAB linear Analysis Tool

The Linear Analysis Tool (shown in Figure 144) lets you perform linear analysis of nonlinear Simulink models. Using this tool you can:

- Interactively linearize models at different operating points

- Interactively obtain operating points by trimming or simulating models

- Perform exact linearization of nonlinear models

- Perform frequency response estimation of nonlinear models

In this work the Linear Analysis Tool is used to measure the control loop gain by following these steps:

- Specify the initial state values in the model

- Open the linear analysis tool for the model, select Analysis > Control Design > Linear Analysis.

- Define the portion of the model to linearize:

  o To specify the linearization input, right-click the input signal of the controller block, and select Linear Analysis Points > ±⅄ Input Perturbation. The default perturbation size is $10^{-5}(1 + |x|)$, where x is the operating point value of the perturbed state or the input. The input point is not the input of the block; rather it is an additive input to the signal.

  o To specify the linearization output, right-click the output signal of the dc-link voltage, and select Linear Analysis Points > ⅄* Open-loop Output.

- Linearize the system at the operating points

Figure 145 shows the Simulink model and the input and output points for measuring the control loop gain with the ideal current source. Figure 146 shows the Simulink model that used when the SCPVM is used as a source for the second-stage converter.
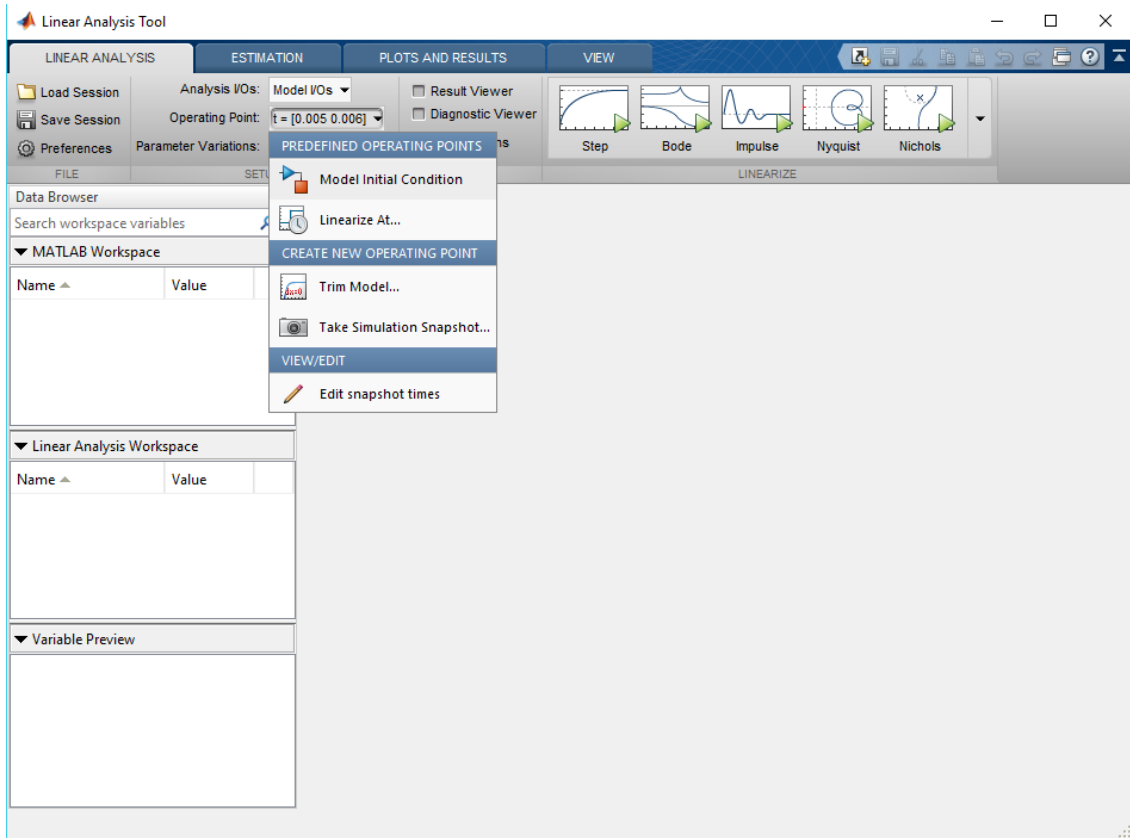
*Figure 144: Snapshot of the MATLAB Linear Analysis Tool*
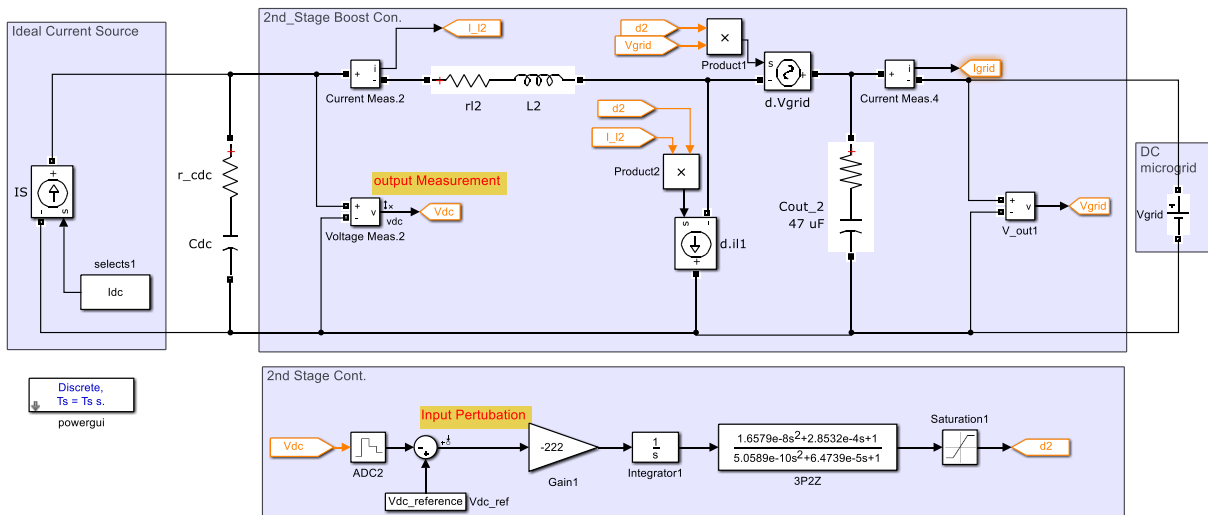
Figure 145: Simulink model of the system with ideal current as a source for the second-stage converter and control loop gain measurement points
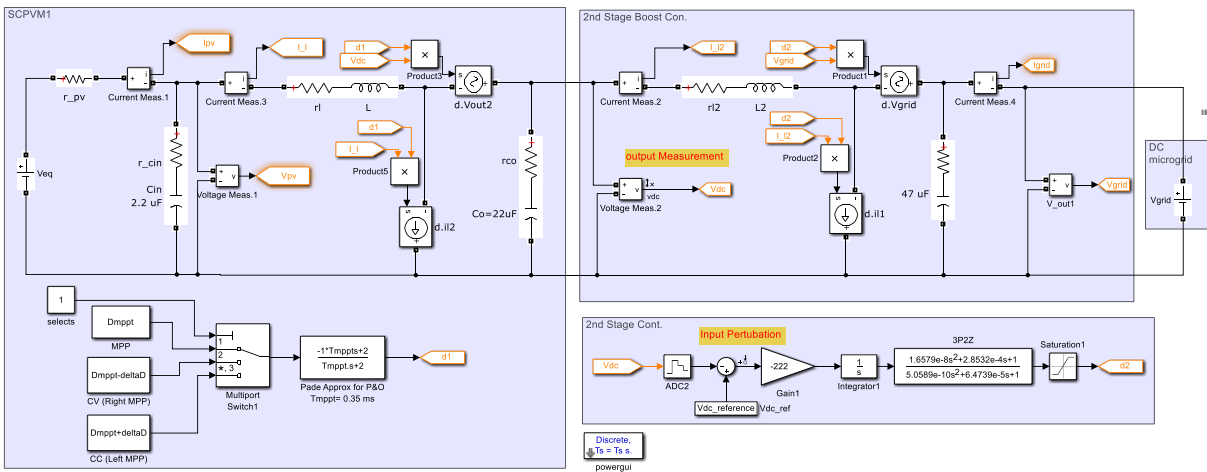
Figure 146: Simulink model of the system with SCPVM as a source for the second-stage converter and control loop gain measurement points

220

APPENDIX D: Steady-state Peak-peak Variation of the i_{pv}, i_{scpvm_out} and i_{dc}

```matlab
% Calculating the steady-state variation of the PV surrent, SCPVM output current, and
dc-link current
%Irated is the rated current, Vrated is the rated voltage, vdc is the dc-link voltage,
% deltaD is the P&O step size, n is the number of the SCPVM units
Irated=8.15; Vrated=37.3; vdc=50; deltaD=0.035; n=6;

for i=1:11
Dmppt=1-(Vpv_mpp/vdc1);
vpv_mpp=vdc*(1-Dmppt);
vpv_right=vdc*(1-(Dmppt-deltaD));
vpv_left=vdc*(1-(Dmppt+deltaD));
Ipv_mpp=pv(vpv_mpp,G,Temp);
Ipv_right=pv(vpv_right,G,Temp);
Ipv_left=pv(vpv_left,G,Temp);

% steady-state peak-peak variation in the pv current
delta_ipv_left(i,1)=(Ipv_left-Ipv_mpp)/Irated;
delta_ipv_right(i,1)=(Ipv_mpp-Ipv_right)/Irated;
delta_ipv(i,1)=(Ipv_left-Ipv_right)/Irated;

% steady state peak-peak variation at the SCPVM output current
I_scpvm_out_mpp(i,1)=(Ipv_mpp*(1-Dmppt))/Irated;
I_scpvm_out_right(i,1)=(Ipv_right*(1-(Dmppt-deltaD)))/Irated;
I_scpvm_out_left(i,1)=(Ipv_left*(1-(Dmppt+deltaD)))/Irated;
if (I_scpvm_out_right(i,1)>=I_scpvm_out_mpp(i,1))&&(I_scpvm_out_left(i,1)
<=I_scpvm_out_mpp(i,1))
    delta_I_scpvm_out_ss(i,1)=I_scpvm_out_right(i,1)-I_scpvm_out_left(i,1);
    delta_I_scpvm_out_right_to_mpp(i,1)=I_scpvm_out_right(i,1)-I_scpvm_out_mpp(i,1);
    delta_I_scpvm_out_left_to_mpp(i,1)=I_scpvm_out_mpp(i,1)-I_scpvm_out_left(i,1);
elseif(I_scpvm_out_right(i,1)<=I_scpvm_out_mpp(i,1))&&(I_scpvm_out_left(i,1)
<=I_scpvm_out_mpp(i,1))
    delta_I_scpvm_out_ss(i,1)=I_scpvm_out_mpp(i,1)-I_scpvm_out_left(i,1);
    delta_I_scpvm_out_right_to_mpp(i,1)=I_scpvm_out_mpp(i,1)-I_scpvm_out_right(i,1);
    delta_I_scpvm_out_left_to_mpp(i,1)=I_scpvm_out_mpp(i,1)-I_scpvm_out_left(i,1);
elseif (I_scpvm_out_right(i,1)<=I_scpvm_out_mpp(i,1))&&(I_scpvm_out_left(i,1)
>=I_scpvm_out_mpp(i,1))
    delta_I_scpvm_out_ss(i,1)=I_scpvm_out_mpp(i,1)-I_scpvm_out_right(i,1);
    delta_I_scpvm_out_right_to_mpp(i,1)=I_scpvm_out_mpp(i,1)-I_scpvm_out_right(i,1);
    delta_I_scpvm_out_left_to_mpp(i,1)=I_scpvm_out_left(i,1)-I_scpvm_out_mpp(i,1);
end

% steady-state peak-peak variation of the dc-link current
delta_Idc(i,1)=n*delta_I_scpvm_out_ss(i,1);% peak to peak variation in the dc-link
current
deltaD=deltaD+0.01;              %for n units of SCPVM

end
```

APPENDIX E: The Active Filter Algorithm

```matlab
% Active filter controller for four SCPVM units
function [D1_active, D2_active, D3_active, D4_active] = ActiveFilter(D1, D2, D3, D4,
Ipv1, Ipv2, Ipv3, Ipv4,deltaD)
% define initial values
m_init=[0 0 0 0];
I1_avg_init=[0 0 0 0];
I2_avg_init=[0 0 0 0];
I3_avg_init=[0 0 0 0];
I4_avg_init=[0 0 0 0];
D1_save=[0.5 0.5 0.5 0.5];
D2_save=[0.5 0.5 0.5 0.5];
D3_save=[0.5 0.5 0.5 0.5];
D4_save=[0.5 0.5 0.5 0.5];
Dm=[0.5 0.5 0.5 0.5];

persistent m1 m2 Dpair1_old Dpair2_old PV_data;
if isempty(m1)
    m1=m_init; end

if isempty(m2)
    m2=m_init; end

if isempty(PV_data)
    PV_data=[0 0 0 0;0 0 0 0;0 0 0 0;0 0 0 0;0 0 0 0;0 0 0 0;
            Dm(1) Dm(2) Dm(3) Dm(4);Dm(1) Dm(2)Dm(3) Dm(4);
            Ipv1 Ipv2 Ipv3 Ipv4;0 0 0 0;1 2 3 4];end

if isempty(Dpair1_old)
    Dpair1_old=0; end

if isempty(Dpair2_old)
    Dpair2_old=0; end

% P&O avrage duty cycle
D1_save=circshift(D1_save,[0,1]);
D1_save(1,1)=D1;
D1_avg=(D1_save(1,1)+D1_save(1,2)+D1_save(1,3)+D1_save(1,4))/4;
D2_save=circshift(D2_save,[0,1]);
D2_save(1,1)=D2;
D2_avg=(D2_save(1,1)+D2_save(1,2)+D2_save(1,3)+D2_save(1,4))/4;
D3_save=circshift(D3_save,[0,1]);
D3_save(1,1)=D3;
D3_avg=(D3_save(1,1)+D3_save(1,2)+D3_save(1,3)+D3_save(1,4))/4;
D4_save=circshift(D4_save,[0,1]);
D4_save(1,1)=D4;
D4_avg=(D4_save(1,1)+D4_save(1,2)+D4_save(1,3)+D4_save(1,4))/4;
Duty=[D1 D2 D3 D4; D1_avg D2_avg D3_avg D4_avg];
% The avgerage value of the PV modules currents
I1_avg_init=circshift(I1_avg_init,[0,1]);
I1_avg_init(1,1)=Ipv1;
I1_avg=(I1_avg_init(1,1)+I1_avg_init(1,2)+I1_avg_init(1,3)+I1_avg_init(1,4))/4;
I2_avg_init=circshift(I2_avg_init,[0,1]);
I2_avg_init(1,1)=Ipv2;
I2_avg=(I2_avg_init(1,1)+I2_avg_init(1,2)+I2_avg_init(1,3)+I2_avg_init(1,4))/4;
I3_avg_init=circshift(I3_avg_init,[0,1]);
```

```matlab
I3_avg_init(1,1)=Ipv3;
I3_avg=(I3_avg_init(1,1)+I3_avg_init(1,2)+I3_avg_init(1,3)+I3_avg_init(1,4))/4;
I4_avg_init=circshift(I4_avg_init,[0,1]);
I4_avg_init(1,1)=Ipv4;
I4_avg=(I4_avg_init(1,1)+I4_avg_init(1,2)+I4_avg_init(1,3)+I4_avg_init(1,4))/4;
current=[I1_avg I2_avg I3_avg I4_avg];

%%%%%%%%%%%%%%% saving current data
PV_data(9,1)=current(1,PV_data(11,1));
PV_data(9,2)=current(1,PV_data(11,2));
PV_data(9,3)=current(1,PV_data(11,3));
PV_data(9,4)=current(1,PV_data(11,4));
PV_data(8,1)=Duty(2,PV_data(11,1));
PV_data(8,2)=Duty(2,PV_data(11,2));
PV_data(8,3)=Duty(2,PV_data(11,3));
PV_data(8,4)=Duty(2,PV_data(11,4));
PV_data(7,1)=Duty(1,PV_data(11,1));
PV_data(7,2)=Duty(1,PV_data(11,2));
PV_data(7,3)=Duty(1,PV_data(11,3));
PV_data(7,4)=Duty(1,PV_data(11,4));


PV_data(1,1)=100;PV_data(2,2)=100;PV_data(3,3)=100;PV_data(4,4)=100;
PV_data(1,2)=abs(PV_data(9,1)-PV_data(9,2));PV_data(2,1)=abs(PV_data(9,1)-PV_data↵
(9,2));
PV_data(1,3)=abs(PV_data(9,1)-PV_data(9,3)); PV_data(3,1)=abs(PV_data(9,1)-PV_data↵
(9,3));
PV_data(1,4)=abs(PV_data(9,1)-PV_data(9,4)); PV_data(4,1)=abs(PV_data(9,1)-PV_data↵
(9,4));
PV_data(2,3)=abs(PV_data(9,2)-PV_data(9,3)); PV_data(3,2)=abs(PV_data(9,2)-PV_data↵
(9,3));
PV_data(2,4)=abs(PV_data(9,4)-PV_data(9,2)); PV_data(4,2)=abs(PV_data(9,4)-PV_data↵
(9,2));
PV_data(3,4)=abs(PV_data(9,3)-PV_data(9,4)); PV_data(4,3)=abs(PV_data(9,3)-PV_data↵
(9,4));
PV_data_new=PV_data;

% arranging the pair units
if PV_data(8,1)==PV_data(7,1) && PV_data(8,2)==PV_data(7,2)% if D1_pair1_avg=D1_apir1↵
& D2_pair1_avg=D2_pair1
    if PV_data(1,2)>1                               % if Ipv1_pair1_avg -↵
Ipv2_pair1_avg > 1
        PV_data(10,1)=1;  PV_data(10,2)=1;
    else PV_data(10,1)=0; PV_data(10,2)=0;
    end
end
if PV_data(8,3)==PV_data(7,3)&& PV_data(8,4)==PV_data(7,4) % if D1_pair2_avg=D1_apir2↵
& D2_pair2_avg=D2_pair2
    if PV_data(3,4)>1                               % if Ipv1_pair2_avg -↵
Ipv2_pair2_avg > 1
        PV_data(10,3)=1;  PV_data(10,4)=1;
    else PV_data(10,3)=0; PV_data(10,4)=0;
    end
end

if (PV_data(10,1)==1) && (PV_data(10,3)==1)
```

```matlab
    if PV_data(1,3)>PV_data(1,4)
        if PV_data(1,2)> PV_data(1,4)
        PV_data_new(7,2)=PV_data(7,4); PV_data_new(7,4)=PV_data(7,2);
        PV_data_new(8,2)=PV_data(8,4); PV_data_new(8,4)=PV_data(8,2);
        PV_data_new(9,2)=PV_data(9,4); PV_data_new(9,4)=PV_data(9,2);
        PV_data_new(11,2)=PV_data(11,4); PV_data_new(11,4)=PV_data(11,2);
        PV_data(10,1)=0;PV_data(10,2)=0;PV_data(10,3)=0;PV_data(10,4)=0;
        end
    elseif PV_data(1,2)> PV_data(1,3)
        PV_data_new(7,2)=PV_data(7,3); PV_data_new(7,3)=PV_data(7,2);
        PV_data_new(8,2)=PV_data(8,3); PV_data_new(8,3)=PV_data(8,2);
        PV_data_new(9,2)=PV_data(9,3); PV_data_new(9,3)=PV_data(9,2);
        PV_data_new(11,2)=PV_data(11,3); PV_data_new(11,3)=PV_data(11,2);
        PV_data(10,1)=0;PV_data(10,2)=0;PV_data(10,3)=0; PV_data(10,4)=0;
    end
end


%Checking 4 consecutive duty cycles perturbation in the pair units for three step mode
deltaD_Dpair1=abs(PV_data_new(7,1)-PV_data_new(7,2));%deltaD_Dpair1=abs(D1_pair1-
D2_pair1);
deltaD_Dpair2=abs(PV_data_new(7,3)-PV_data_new(7,4));%deltaD_Dpair2=abs(D1_pair2-
D2_pair2);

if (deltaD_Dpair1==Dpair1_old)
    m1=circshift(m1,[0,1]);
    m1(1,1)=1;
else
    m1=circshift(m1,[0,1]);
    m1(1,1)=0;
end
r1=m1(1,1)+m1(1,2)+m1(1,3)+m1(1,4);

if (deltaD_Dpair2==Dpair2_old)
    m2=circshift(m2,[0,1]);
    m2(1,1)=1;
else
    m2=circshift(m2,[0,1]);
    m2(1,1)=0;
end
r2=m2(1,1)+m2(1,2)+m2(1,3)+m2(1,4);

% adjusting perturbation direction to have the duty cycle of a pair out of pahse
% for the first pair
if (r1==4)
    if (PV_data_new(7,1)>PV_data_new(8,1)) && (PV_data_new(7,2)>PV_data_new(8,2))
        Dm(1,PV_data_new(11,1))=PV_data_new(7,1);
        Dm(1,PV_data_new(11,2))=(PV_data_new(7,2))-(2*deltaD);

    elseif (PV_data_new(7,1)<PV_data_new(8,1)) && (PV_data_new(7,2)<PV_data_new(8,2))
        Dm(1,PV_data_new(11,1))=PV_data_new(7,1);
        Dm(1,PV_data_new(11,2))=(PV_data_new(7,2))+(2*deltaD);
    else
        Dm(1,PV_data_new(11,1))=PV_data_new(7,1);
        Dm(1,PV_data_new(11,2))=PV_data_new(7,2);
    end
```

```matlab
else
 Dm(1,PV_data_new(11,1))=PV_data_new(7,1);
 Dm(1,PV_data_new(11,2))=PV_data_new(7,2);
end
% for the second pair
if (r2==4)
    if (PV_data_new(7,3)>PV_data_new(8,3))&&(PV_data_new(7,4)>PV_data_new(8,4))
        Dm(1,PV_data_new(11,3))=PV_data_new(7,3);
        Dm(1,PV_data_new(11,4))=(PV_data_new(7,4))-(2*deltaD);
    elseif (PV_data_new(7,3)<PV_data_new(8,3))&&(PV_data_new(7,4)<PV_data_new(8,4))
        Dm(1,PV_data_new(11,3))=PV_data_new(7,3);
        Dm(1,PV_data_new(11,4))=(PV_data_new(7,4))+(2*deltaD);
    else
        Dm(1,PV_data_new(11,3))=PV_data_new(7,3);
        Dm(1,PV_data_new(11,4))=PV_data_new(7,4);
    end
else
    Dm(1,PV_data_new(11,3))=PV_data_new(7,3);
    Dm(1,PV_data_new(11,4))=PV_data_new(7,4);
end
% sending the new duty cycles to the SCPVM units
D1_active=Dm(1,1); D2_active=Dm(1,2); D3_active=Dm(1,3); D4_active=Dm(1,4);
% update data
Dpair1_old=deltaD_Dpair1;
Dpair2_old=deltaD_Dpair2;
PV_data=PV_data_new;
```